

MONASH UNIVERSITY



Nb–based alloys and their application
for hydrogen permeation membranes

By

Timothy Wong Tek Kong

A dissertation submitted for the degree of
Doctor of Philosophy

Department of Materials Engineering
Monash University

November 2013

Statement of Originality

I hereby declare that this thesis contains no material which has been accepted for the award of any other degree or diploma at any university or equivalent institution and that, to the best of my knowledge and belief, this thesis contains no materials previously published or written by another person, excepted where due reference is made in the text of the thesis.

Signed: _____

Timothy Wong Tek Kong

Date: _____

Under the Copyright Act 1968, this thesis must be used only under the normal conditions of scholarly fair dealing. In particular no results or conclusions should be extracted from it, nor should it be copied or closely paraphrased in whole or in part without the written consent of the author. Proper written acknowledgement should be made for any assistance obtained from this thesis.

Copyright © 2013 by T. Wong Tek Kong. All rights reserved.

Reproduction: Monash University, Melbourne, Australia.

To my wife, parents and grandmother.

Acknowledgements

I would like to thank my supervisor Professor Kiyonori Suzuki of the department of Materials Engineering for his guidance and for the freedom he has given to me to explore areas of my interest during this project. I am grateful for this constant encouragement and financial support. I wish to acknowledge his patience and understanding, and for the invaluable discussions we had over the years. I feel very honoured to have done my dissertation under his supervision.

I would also like to thank my supervisor Dr. Mark Gibson of the Innovation in Process and Production Group at the Commonwealth Scientific and Industrial Research Organisation (CSIRO) for his valuable advice and continuous encouragement over the course of my project. I am grateful for his contribution in the production of the Nb-Ni-Zr wide ribbons and his patience in the critical reading of the draft for my thesis.

I wish to express my sincere thanks to Professor Kiyoshi Aoki and Associate Professor Kazuhiro Ishikawa for their warm welcome and fruitful collaboration during my stay in Japan, and also for their guidance in setting up the hydrogen permeation facilities at Monash University.

I wish to express my sincere thanks to our head of department Professor Nick Birbilis for his generous permission to access his laboratory facilities to carry out the electrochemical hydrogen permeation analysis.

I am also grateful to Distinguished Emeritus Professor John Verhoeven and Dr. Larry Jones of Iowa State University (U.S.A), to Professor Ludovic Thilly of the University of Poitiers, and Dr. Florence Lecouturier of the ‘Laboratoire National des Champs Magnétiques Pulsées’ of CNRS-UPS-INSA (France) for generously providing samples of their Cu-Nb alloys.

I would also like to express my gratitude to Professor Barry Muddle who introduced to me the joys of metallurgy during my undergraduate years and gave me the chance to work in his research group in these early days of my journey as a materials engineer. I am also grateful to Associate Professor Laure Bourgeois for a fruitful collaboration and from whom I learnt a lot about thermo-mechanical processing and electron microscopy.

I would also like to thank Mr. Rod Mackie for his patience in training me on the X-ray apparatus, Mr Silvio Mattievich for his resourcefulness and help in setting up the hydrogen permeation facilities at Monash University, Mr Irek Kozicki and Mr Daniel Curtis for their assistance in sourcing other laboratory supplies and equipment.

I would also like to thank my friends and colleagues; A/Prof. Rimma Lapovok, Ms. Edna Tan, Dr. Naoki Ito, Dr. Aaron Sudholz, Dr. Haiyan Yang, Dr. Isfaaq Timol, Ms. Vann Ly, Dr. Darren Cram, Dr. Hadas Katz, Dr. Andrey Molotnikov, Mr. Mohammad Barati, Dr. Xiaodong Wu, Mr. Hao Zhang, Ms. Wenwen Sun, Mr. Yajie Wu, Ms. Sally Goh, Ms. Jasmine Shih, Mr. Andrew Saldanha, Dr. Chan Seo, Dr. Dulani Heenetigala, Ms. Heiki Krebs, Mr. Cong Qui, Mr. Richard Parsons, Dr. Marie Clancy and Ms. Ezgi Onal, for their support over the years and for the excellent working atmosphere. I also wish to thank Mr. Naoyoshi Ota and Mr. Tetsuya Kato for their friendship and hospitality when I was in Kitami.

I would like to acknowledge the contribution of my past teachers and mentors; Ms. Lilia Pustovoytova, Mr. Jacques Lam Hang, Mr. Donald Lam Hang, Mr. Keith Yeung, Mrs. Suzy, Mrs. Linda, Mr. Kiat fen, Ms. Sien Sien Shi Shun, Mr. John Ip, Mrs. Christine Ip, and Mrs. Emma Fok. I also wish to thank the Chane Yook, Wong Tek Kong, Wong Leung Ki, Shi Shun, Li Kam Cheung, Ng Cheng Hin, Liw Yan Cheong, Chui Hom Lap, Nien Fong and Cheung families for their support and encouragement over the years.

I wish to give a special thanks to God, my parents, Pierre and Chin Chin, my grandmother, and late grandparents, for their love, patience, guidance and support. Without them I would not have been where I am today. I would also like to give special thanks to my siblings Corrie, Emmy and Barny for their encouragement and humour whenever the project did not go my way. I would like to thank my beloved wife Dr. Phillis Jebron for her encouragement, support and love during the difficult periods of my project. Her wonderful cooking, care and incongruous ideas are enough to make me forget all my troubles.

Finally, I would like to thank Monash University and the Australian Government for their financial support through their Monash Graduate Scholarship and Australian Postgraduate Award.

Abstract

The ultimate goal of this work has been to produce some novel and versatile membranes for hydrogen permeation and purification. Nb-alloy membranes were chosen due to their high hydrogen permeability, Φ , and their lower cost when compared to conventional Pd-alloy membranes.

The formation range of amorphous in Nb-Ni-Zr and Nb-Ti-Co alloys produced by melt-spinning was investigated. It was found that the $(\text{Nb}_{90}\text{Zr}_7\text{Ni}_3)_{1-X}(\text{Ni}_{50}\text{Zr}_{50})_X$ alloys with Nb contents below 45 at. % ($X > 0.5$) yielded amorphous ductile ribbons, while those above this Nb content resulted in crystalline brittle ribbons. In the case of the Nb-Ti-Co alloy, the eutectic composition resulted in ductile amorphous ribbons when thin ribbons were spun, however, attempts to prepare wide ribbons failed. The $(\text{Nb}_{90}\text{Zr}_7\text{Ni}_3)_{1-X}(\text{Ni}_{50}\text{Zr}_{50})_X$ alloys with a niobium content, Nb \sim 45 – 20 at. % ($0.5 < X < 0.8$), resulted in NiZr + Nb phases. A nano-scale grain refinement of the NiZr and bcc-Nb microstructure was observed after heating to 923 K. Coarsening of the Nb and NiZr duplex structure was observed in samples heated to 1173 K.

The effect of annealing on the hydrogen permeation properties and microstructure of Nb-Ni-Zr alloys was investigated. These alloys consist of the primary bcc Nb phase surrounded by a Nb+NiZr phase mixture. The hydrogen permeability of $\text{Nb}_{40}\text{Ni}_{30}\text{Zr}_{30}$ was found to increase with increasing annealing temperature and was the highest when annealed at 1123 K for 1 h, resulting in a Φ 3.9 times larger than that of Pd and 2.3 times larger than that in the as-cast state. Two modes of crack propagation were observed, namely transgranular and intergranular cracking. The modes of fracture were found to be composition dependent, with samples with high Nb content suffering from transgranular

ABSTRACT

cracking and those with low Nb content from intergranular cracking. The mode of fracture was found to be unaffected by annealing.

For the first time, the hydrogen permeability, solubility and diffusivity of a chemically identical alloy membrane were investigated in an amorphous, nanocrystalline and crystalline state. It was found that the hydrogen permeability of the Nb₂₀Ni₄₀Zr₄₀ sample with a nanostructure was about twice that of the amorphous sample and one order of magnitude higher than the crystalline sample. Even though the n-sample and the a-sample have higher hydrogen permeabilities, the hydrogen diffusivity and solubility states of each were found to be different. It was shown that the improvement in hydrogen permeation in the samples with a nanostructure was not solely based on improved hydrogen diffusivity, when compared to the amorphous sample, but also due to the improved hydrogen solubility.

The prospect of using Cu-Nb alloys as hydrogen permeation membranes was explored for the first time. The preliminary hydrogen permeation tests on as-cast Cu-15 vol.% Nb and rolled Cu-20 vol.% Nb samples resulted in a Φ of 1.7×10^{-9} and 1.93×10^{-9} molH₂m⁻¹s⁻¹Pa^{-0.5} at 673 K respectively. Both membranes were found to be mechanically strong, hydrogen embrittlement resistant and ductile. An in-situ analysis was conducted by XRD. It was found that Nb was responsible for the permeation of hydrogen and Cu was unaffected by H. The catalytic Pd coating was lost to a Cu rich Cu-Pd phase in areas in direct contact with the Cu matrix at temperatures above 573 K.

To circumvent this issue and also to potentially improve the hydrogen permeability coefficient of the membrane, a modelling exercise was carried out to investigate the effect of altering the morphology of the Nb and Cu phases in Cu-Nb alloys. Based on the simulation, it was found that Nb and Cu phases arranged in parallel to the direction of the flow of hydrogen compared to one arranged in series, would yield gains varying from five to eight orders of magnitude at 723 K and 523 K respectively. The simulation also showed that the Φ of a Cu-15 vol.% Nb alloy membrane following the parallel model would be between 1 to 2 orders of magnitude higher than that of pure Pd membranes at 723 K and 523 K respectively. It was found that arranging the Nb and Cu phases in parallel would

ABSTRACT

yield the most efficient increase in Φ with increasing Nb content. The models of the Cu-Nb alloy with phases arranged in parallel indicate that it follows the unique hydrogen permeation characteristics of Group V elements, which is to have an increasing hydrogen permeability with decreasing temperature. This carries positive implications in improving the efficiency of these membranes. In an attempt to confirm the model, a Cu/Nb/Cu multifilamentary alloy was tested. SEM analysis revealed that the Pd catalyst coating remained intact in areas directly above the Nb filaments at 673 K, thus significantly increasing the operational temperature of the Cu-Nb alloy membrane system.

In summary, the optimum compositions to produce ductile amorphous ribbons in Nb-Ni-Zr and Nb-Ti-Co alloys were identified. The heat treatments to obtain chemically identical alloy membranes in amorphous, nanocrystalline and crystalline state were successfully investigated. The hydrogen permeability, solubility and diffusivity of these membranes were studied. For the first time Cu-Nb superconducting wires were studied for their application as hydrogen permeation membranes and were shown to have a high resistance to hydrogen embrittlement, good durability at high temperature and reasonable hydrogen permeation properties. Further insight into the possible advantages of using Cu-Nb alloys used in the 'parallel mode' was given. Therefore, this study further supports Nb-based alloy membranes as potential alternatives to Pd-based alloy membranes.

List of Publications

T. Wong, K. Suzuki, M. A. Gibson, K. Ishikawa, K. Aoki and L. L. Jones, Scripta Materialia, 62 (2010) 582

T. Wong, Z. Yu, K. Suzuki, M. A. Gibson, K. Ishikawa, K. Aoki, Materials Science Forum, 654 - 656 (2010) 2839

T. Wong, L. Bourgeois, K. Suzuki, K. Ishikawa, K. Aoki, WHEC 2008, Queensland, Proceedings of WHEC 2008, 1080

Other publications

L. Bourgeois, T. Wong, X.Y. Xiong, J.F. Nie and B.C. Muddle, Materials Science Forum, 519 - 521 (2006) 495

Contents

Abstract	i
List of publications	iv
Contents	v
List of figures	xi
List of tables	xxi
Chapter 1. Introduction	1
1.1 Background.....	1
1.2 Objectives of research	2
1.3 Structure of the thesis	3
1.4 References	4
Chapter 2. Literature Review	5
2.1 Background.....	5
2.2 Hydrogen purification techniques	5
2.3 Types of hydrogen separation membranes	7
2.3.1 Polymeric membranes	7
2.3.2 Carbon based membranes	7
2.3.3 Ceramic membranes	8
2.3.4 Metallic membranes	9
2.4 Types of metallic membranes.....	11
2.4.1 Principles of hydrogen permeation in metallic membranes	11
2.4.2 Pure metal membranes.....	14

CONTENTS

2.4.3	Crystalline alloy membranes	16
2.4.4	Amorphous alloy membranes	24
2.4.5	Nanocrystalline alloy membranes	26
2.5	Formation of metallic glasses	27
2.6	Hydrogen embrittlement.....	31
2.6.1	In amorphous alloys.....	31
2.6.2	In crystalline alloys.....	32
2.7	Mechanical behaviour of nanocrystalline alloys	35
2.7.1	Strength.....	35
2.7.2	Ductility	37
2.8	Summary and aims	38
2.9	References	40
Chapter 3. Experimental Methodology		49
3.1	Formation of amorphous alloys	49
3.1.1	Preparation of ingots: argon arc melting	49
3.1.2	Quenching: single roller method	50
3.2	Annealing.....	51
3.2.1	Estimation of the crystallization temperature: DTA.....	51
3.2.2	Annealing: Infrared furnace.....	56
3.2.3	Annealing: convection furnace	56
3.3	Characterization of microstructure	57
3.3.1	Sample preparation: grinding and polishing.....	57
3.3.2	Sample preparation: PIPS	57
3.3.3	Phase identification and degree of crystallinity: XRD	58
3.3.4	Evaluation of grain size: XRD.....	58
3.3.5	Lattice spacing measurements: XRD	61
3.3.6	Characterization of microstructure at the micro scale: SEM.....	62

CONTENTS

3.3.7	Characterization of microstructure at the nano scale: TEM	62
3.4	Characterization of ductility	63
3.5	Sample preparation of Cu-Nb alloys	63
3.5.1	Consumable arc casting	63
3.5.2	Cold drawing of multifilamentary Cu-Nb alloys	65
3.6	References	66

Chapter 4. Formation of Nanostructured Hydrogen Permeation

	Membranes	67
4.1	Introduction	67
4.2	Results	69
4.2.1	Formation of amorphous alloys	69
4.2.1.1	Nb-Ni-Zr alloys	69
4.2.1.2	Nb-Ti-Co alloys	72
4.2.2	Decomposition of as-spun amorphous alloys	74
4.2.2.1	Nb-Ni-Zr alloys	74
4.2.2.2	Nb-Ti-Co alloys	85
4.2.2.3	Effect of annealing on ductility of as-spun amorphous alloys	86
4.3	Discussion	87
4.3.1	Formation of an amorphous phase in Nb-Ni-Zr alloys	87
4.3.2	Formation of an amorphous phase in Nb-Ti-Co alloys	90
4.3.3	Crystallization behaviour of amorphous Nb-Ni-Zr alloys	90
4.3.4	Ductility in Nb-Ni-Zr alloys after annealing	95
4.4	Summary	96
4.5	References	98

CONTENTS

Chapter 5. Implementation of Hydrogen Apparatus and its Application to Investigate the Permeation Behaviour of Nb-Ni-Zr Alloy Membranes	101
5.1 Introduction	101
5.2 Hydrogen permeation measuring technique	103
5.2.1 Palladium coating	103
5.2.2 Implementation of the pressure driven hydrogen permeation measuring technique	105
5.2.3 Calibration of the pressure driven hydrogen permeation apparatus	108
5.3 Results	113
5.3.1 Hydrogen permeation of Nb-Ni-Zr membranes	113
5.3.2 Fracture behaviour of Nb-Ni-Zr membranes.....	116
5.4 Discussion.....	119
5.4.1 Effect of annealing on the hydrogen permeability	119
5.4.2 Failure analysis of the cracked samples	122
5.5 Summary.....	124
5.6 References	125
Chapter 6. Effect of Nano-Scale Grain Refinement on the Hydrogen Permeation Performance of Nb-Ni-Zr Membranes.....	127
6.1 Introduction	127
6.2 Hydrogen permeation measuring technique	128
6.2.1 Implementation of an electrochemical hydrogen permeation measuring apparatus	128
6.2.2 Technique used to estimate the hydrogen diffusivity	131
6.2.3 Calibration of the electrochemical hydrogen permeation apparatus	134
6.2.4 Reliability of the results.....	135

CONTENTS

6.3	Results	137
6.3.1	Hydrogen permeation of the Nb ₂₀ Ni ₄₀ Zr ₄₀ alloy membranes	137
6.4	Discussion.....	145
6.4.1	Effect of microstructure on hydrogen solubility.....	145
6.4.2	Effect of microstructure on hydrogen diffusivity	147
6.4.3	Effect of nanostructure on hydrogen permeability	150
6.4.4	Effect of microstructure on the stability of membranes	151
6.5	Summary.....	153
6.6	References	154

Chapter 7. Potential of Cu-Nb Alloys as Hydrogen Permeation

	Membranes	157
7.1	Introduction	157
7.2	As cast Cu-Nb alloys	158
7.2.1	Sample preparation and methodology	158
7.3	Results	160
7.4	Discussion.....	175
7.4.1	Potential of Cu-Nb alloys for hydrogen permeation applications ...	175
7.4.2	Effect of hydrogen on Nb and Cu phases	177
7.4.3	Factors affecting the hydrogen solubility and diffusivity coefficient	186
7.4.3.1	Pd catalyst coating	186
7.4.3.2	Microstructural arrangement of the Nb particles.....	187
7.4.4	Potential approaches to enhance hydrogen permeability and retain the Pd catalytic layer in Cu-Nb alloy membranes	188
7.4.4.1	Modelling of hydrogen permeability based on models for the thermal conductivity of heterogeneous materials	188
7.4.4.2	Increasing the Nb content in the Cu-Nb alloys.....	194

CONTENTS

7.4.4.3	Changing the morphology of the Nb phases in Cu-Nb alloys	197
7.4.5	Preliminary tests on the potential ways to improve the hydrogen permeation in the Cu-Nb alloy membranes	198
7.5	Summary	205
7.6	References	208
Chapter 8.	Conclusions and Future Work	211
8.1	Conclusions	211
8.2	Future work	214
Appendix		217
	Acronyms	217

List of Figures

Figure 2.1.	The membrane separation system can improve efficiency from 59% to above 75% [3].....	6
Figure 2.2.	Schematic representation of hydrogen separation through a metallic membrane	12
Figure 2.3.	Temperature dependence of hydrogen permeability for pure metals [7, 31, 32]. Metal-hydride formers, in particular with body-centred-cubic (bcc) structure (V, Nb and Ta), exhibit high permeability whereas the non-hydride formers show limited hydrogen permeability	15
Figure 2.4.	A scanning electron micrograph of a Nb ₄₀ Zr ₃₀ Ni ₃₀ alloy for hydrogen permeation [47]. This alloy was prepared by conventional arc melting. The hydrogen permeability (Φ) of this alloy was 2.9 times greater than that of Pd.....	17
Figure 2.5.	CCT diagram with the red line showing the minimum cooling rate required to form an amorphous alloy [100].....	28
Figure 2.6.	Isothermal section of the Ni-Zr-Nb ternary system showing the position of the phase boundaries at 1073 K. The boundaries for ternary amorphous alloy formation (blue dotted line and light blue shaded area) are indicated. In addition, the position of the known binary eutectic compositions (gold arrows) and the established binary glass-forming ranges (yellow bar) are indicated [103]	30
Figure 2.7.	A concept for alloy design of Nb-based hydrogen permeable alloys by Yukawa et al. [108]	33

LIST OF FIGURES

Figure 2.8.	Schematic diagram of the Ni-Nb-Zr ternary system showing the compositions of the fully crystalline alloys investigated by Aoki et al. [109] and the associated hydrogen permeability ($\times 10^{-8} \text{ mol. m}^{-1} \cdot \text{s}^{-1} \cdot \text{Pa}^{-0.5}$).....	34
Figure 2.9.	The 3 regions of the Hall-Petch relationship observed depending on the grain size [116]	36
Figure 3.1.	Isothermal section of the Nb-Ni-Zr equilibrium phase diagram at 773 K [4].....	50
Figure 3.2.	Schematic diagram of the melt-spinning process and how to obtain a nanocrystalline structure	51
Figure 3.3.	Hand made quartz crucibles	51
Figure 3.4.	Schematic of a DTA furnace	52
Figure 3.5.	Estimation of the crystallization temperature by DTA.....	53
Figure 3.6.	Curie temperature of pure Ni at variable heating rates.....	53
Figure 3.7.	A comparison between actual heating rate and programmed heating rate	54
Figure 3.8.	Melting temperature of pure Al at variable heating rate	55
Figure 3.9.	An example of a typical DTA curve used to find the melting point of pure Al at a heating rate is 40 K/min.....	55
Figure 3.10.	Schematic diagram for the measurement of the full width of the half maximum of a reflection peak, B [5].....	59
Figure 3.11.	XRD pattern of pure Si to be used to determine the extent of the optical broadening effect	59
Figure 3.12.	Plots of the FWHM peaks of pure Si at angles 2θ . It shows that the optical broadening effect increases with increasing angle 2θ	60
Figure 3.13.	Schematic of the consumable electrode arc casting furnace [8].....	65
Figure 4.1.	X-ray diffraction traces of as-quenched $(\text{Nb}_{90}\text{Zr}_7\text{Ni}_3)_{1-X} (\text{Ni}_{50}\text{Zr}_{50})_X$ alloys of various compositions produced by melt spinning, where $X =$	

LIST OF FIGURES

	0.3 – 0.9. The red XRD traces represent ductile ribbons and those in black represent brittle ribbons.	70
Figure 4.2.	Ternary phase diagram of Nb-Ni-Zr alloys showing the composition dependence of amorphous melt-spun ribbons [8]. The area highlighted in red denotes the composition range that resulted in ductile amorphous melt-spun ribbons. The compositions highlighted in black resulted in brittle crystalline melt-spun ribbons.	71
Figure 4.3.	Images of as-quenched (a) Nb ₂₀ Ni ₄₀ Zr ₄₀ , (b) Nb ₃₅ Ni _{32.5} Zr _{32.5} and (c) Nb ₅₀ Ni ₂₅ Zr ₂₅ wide ribbons prepared using a single roller melt spinner in an argon atmosphere.....	72
Figure 4.4.	Isothermal section of Nb-Ti-Co system at 1173 K [19]. The green squares denote the compositions that did not yield any melt-spun ribbons. The blue triangles correspond to the compositions that resulted in brittle crystalline melt-spun ribbons and the red dot shows the composition at which an amorphous melt-spun ribbon was obtained	73
Figure 4.5.	X-ray diffraction traces of Nb ₃₀ Ti ₃₅ Co ₃₀ Zr ₅ , Nb ₃₀ Ti ₃₅ Co ₂₅ Zr ₁₀ and Nb ₃₀ Ti ₃₅ Co ₁₅ Zr ₁₅ in the as-quenched state.....	74
Figure 4.6.	DTA curves of amorphous as-quenched Nb-Ni-Zr alloys of various compositions at a heating rate of 40 K/min.....	75
Figure 4.7.	X-ray diffraction traces of Nb-Ni-Zr alloys of various compositions heated to 1200 K at a heating rate of 40 K/min.....	76
Figure 4.8.	DTA curve of amorphous (Nb ₉₀ Zr ₇ Ni ₃) _{1-X} (Ni ₅₀ Zr ₅₀) _X alloy with composition X = 0.55 at a heating rate of 40 K/min	77
Figure 4.9.	X-ray diffraction traces of Nb _{40.5} Ni _{28.85} Zr _{30.65} alloy with composition X = 0.55 after heating to 863 K, 923 K and 1173 K at a heating rate of 40 K/min	78

LIST OF FIGURES

Figure 4.10.	DTA curves of amorphous $(\text{Nb}_{90}\text{Zr}_7\text{Ni}_3)_{1-x}(\text{Ni}_{50}\text{Zr}_{50})_x$ alloy with composition $X = 0.55$ at different heating rates	79
Figure 4.11.	Plot of $\ln C/T^2$ against $1000/T$ for the onset temperatures of the primary and secondary crystallization peaks (T_{X1}) and (T_{X2}) of the amorphous $\text{Nb}_{40.5}\text{Ni}_{28.85}\text{Zr}_{30.65}$ alloy	80
Figure 4.12.	X-ray diffraction trace of the Nb (211) peak of the $\text{Nb}_{40.5}\text{Ni}_{28.85}\text{Zr}_{30.65}$ alloy heated to 923 K at a heating rate of 40 K/min.....	81
Figure 4.13.	Grain size obtained from the estimation of the Nb (211) peak of amorphous Nb-Ni-Zr alloys with varying Nb content after heating to 923 K at a heating rate of 40 K/min	81
Figure 4.14.	Bright field transmission electron micrographs and the corresponding selected area electron diffraction patterns of melt-spun $\text{Nb}_{40.5}\text{Ni}_{28.85}\text{Zr}_{30.65}$ after heating to 863 K ((a) and (b)), 923 K ((c) and (d)), and 1173 K ((e) and (f)) at a heating rate of 40 K/min.....	82
Figure 4.15.	(a) Bright, (b) dark-field TEM images and (c) the corresponding diffraction pattern of as-melt-spun $\text{Nb}_{20}\text{Ni}_{40}\text{Zr}_{40}$ wide ribbon.....	84
Figure 4.16.	(a) Bright, (b) dark-field TEM images and (c) the corresponding diffraction pattern of the $\text{Nb}_{20}\text{Ni}_{40}\text{Zr}_{40}$ melt-spun wide ribbon heated to 923 K	84
Figure 4.17.	(a) Bright, (b) dark-field TEM images and (c) the corresponding diffraction pattern of the $\text{Nb}_{20}\text{Ni}_{40}\text{Zr}_{40}$ melt-spun wide ribbon heated to 1173 K	84
Figure 4.18.	DTA curve of amorphous $\text{Nb}_{30}\text{Ti}_{35}\text{Co}_{35}$ at a heating rate of 40 K/min	85
Figure 4.19.	XRD traces of $\text{Nb}_{30}\text{Ti}_{35}\text{Co}_{35}$ alloy in the as-quenched state, heated to 903 K and 1173 K at a heating rate of 40 K/min.....	86
Figure 4.20.	The ductility ratio of $\text{Nb}_{20}\text{Ni}_{40}\text{Zr}_{40}$ and $\text{Nb}_{36}\text{Ni}_{32}\text{Zr}_{32}$ ribbons in the as-quenched state and after annealing	87

LIST OF FIGURES

Figure 4.21.	Pseudo-binary diagram of Nb-NiZr [18]. The highlighted region indicates the alloy composition range where amorphous and partially crystalline melt-spun ribbons were obtained	88
Figure 4.22.	Schematic diagrams showing the coupled zone and the glass-forming and composite-forming regions related to (1) a symmetric eutectic-coupled zone and (2) an asymmetric eutectic-coupled zone [25]	89
Figure 4.23.	Pseudo-binary diagram of Nb-NiZr [18]. The highlighted region indicates the alloy composition range for type I and II, which resulted in the bcc-Nb + NiZr and NiZr + NiZr ₂ + Ni ₁₁ Zr ₉ , respectively, after heating to 923 K	91
Figure 5.1.	Pd deposition rate with a current of 5 mA	104
Figure 5.2.	Schematic illustration of the hydrogen permeation measuring apparatus [8]	105
Figure 5.3.	Hydrogen permeation measuring apparatus implemented at Monash University	107
Figure 5.4.	Picture of the furnace and a magnified image of the sample holder	108
Figure 5.5.	Temperature variation within the furnace around the neutral position of the sample.....	109
Figure 5.6.	Comparison between the temperature measured and the temperature displayed by the heater's display unit over a 2 h period	110
Figure 5.7.	Estimation of the relationship between the temperature displayed and the real sample temperature for calibration purposes	111
Figure 5.8.	Confirmation of the reliability of the hydrogen permeation data produced at Monash University through a comparison of the Nb ₃₀ Ti ₁₃₅ Co ₃₅ data obtained at the Kitami Institute of Technology in Hokkaido, Japan	112

LIST OF FIGURES

Figure 5.9.	Plots of $(J \times L)$ vs. $(P_{H_2}^{0.5} - P_{D_2}^{0.5})$ at 673 K for the $Nb_{40}Ni_{30}Zr_{30}$ alloy as-cast and after annealing for 1 h between 723 K and 1123 K	113
Figure 5.10.	The hydrogen permeability (Φ) for $Nb_{40}Ni_{30}Zr_{30}$, $Nb_{35}Ni_{32.5}Zr_{32.5}$ and $Nb_{30}Ni_{35}Zr_{35}$ alloys at 673 K in the as-cast state and after annealing for 1 h at different temperatures	114
Figure 5.11.	The XRD traces of the Nb-Ni-Zr alloys in the (a) as-cast state and (b) after annealing for 1 h at 1123 K.....	115
Figure 5.12.	SEM micrographs of $Nb_{40}Ni_{30}Zr_{30}$ alloy in (a) as-cast state and (b) after annealing for 1 h at 1123 K before the hydrogen permeation test	116
Figure 5.13.	SEM images in topographic contrast mode of the (a) $Nb_{40}Ni_{30}Zr_{30}$ and (b) $Nb_{30}Ni_{35}Zr_{35}$ as-cast alloys cracked samples. The cracking occurred within the 30 min waiting period after the Φ measurement at 673 K, during which the hydrogen pressure and temperature were lowered to 0.1 MPa and 623 K respectively.....	118
Figure 5.14.	SEM images in topographic contrast mode of the cracked $Nb_{40}Ni_{30}Zr_{30}$ alloy samples in the (a) as-cast state and (b) after annealing for 1 h at 1123 K. The cracking occurred within the 30 min waiting period after the Φ measurement at 673 K, during which the hydrogen pressure and temperature were lowered to 0.1 MPa and 623 K respectively	119
Figure 5.15.	Temperature dependence of hydrogen permeability Φ of as-cast $Nb_{40}Ni_{30}Zr_{30}$, $Nb_{20}Ni_{40}Zr_{40}$, $Nb_{39}Ti_{31}Ni_{30}$ alloys and pure Pd in the form of an Arrhenius plot as reported by Ishikawa et al. [9].....	121
Figure 6.1.	Schematic diagram of the Devanathan electrochemical cell [4]	129
Figure 6.2.	Electrical circuit of the system [4].....	130
Figure 6.3.	Photo of the electrochemical cell.....	131

LIST OF FIGURES

Figure 6.4.	Effect of current applied on the cathode side of the sample on the Anodic current recorded	135
Figure 6.5.	Anodic current versus time during the hydrogen permeation test.....	136
Figure 6.6.	The measured anodic current during the electrochemical hydrogen permeation test of the as quenched Nb ₂₀ Ni ₄₀ Zr ₄₀ sample at 296 K	137
Figure 6.7.	The measured anodic current during the electrochemical hydrogen permeation test at 296K of the Nb ₂₀ Ni ₄₀ Zr ₄₀ sample heated to 923 K	138
Figure 6.8.	The measured anodic current during the electrochemical hydrogen permeation test at 296K of the Nb ₂₀ Ni ₄₀ Zr ₄₀ sample heated to 1173 K	139
Figure 6.9.	The plots of hydrogen permeability (Φ) for pure Pd, melt-spun Nb ₂₀ Ni ₄₀ Zr ₄₀ ribbons heated to 1173 K and 923 K, compared to experimental values of alloys of the same compositions	140
Figure 6.10.	The plots of hydrogen permeability (Φ) of as-quenched Nb ₂₀ Ni ₄₀ Zr ₄₀ compared to the experimental values of similar alloys from literature.	141
Figure 6.11.	The effect of structural correlation length on the hydrogen diffusion coefficient (D) and solubility coefficient (K). The structural correlation length refers to the grain size in polycrystalline alloys and the inter-atomic separation in amorphous alloys. The dotted lines are added as guide to the eyes	143
Figure 6.12.	The hydrogen permeability (Φ) of the Nb ₂₀ Ni ₄₀ Zr ₄₀ alloy as a function of structural correlation length that refers to the grain size in polycrystalline alloys and the inter-atomic separation in amorphous alloys.....	144
Figure 6.13.	Diffusion coefficient of H, D, and T in Nb [2].....	146

LIST OF FIGURES

Figure 6.14.	Hydrogen diffusivity as a function of hydrogen concentration at room temperature for amorphous Nb ₅₆ Ti ₄₄ and Nb ₆₈ Ti ₃₂ and crystallized Nb ₃₈ Ti ₃₂ alloys [21]	148
Figure 7.1.	Cu-Nb ingot prepared by a conventional arc melting technique	159
Figure 7.2.	X-ray diffraction patterns of (a) Cu–15 vol.% Nb as-cast and (b) Cu–20 vol.% Nb rolled alloys	161
Figure 7.3.	Scanning electron micrographs of (a) as-cast Cu–15 vol. % Nb and (b) rolled Cu–20 vol. % Nb samples. The scanned surfaces correspond to the membrane plane perpendicular to the hydrogen permeation path	162
Figure 7.4.	Temperature dependence of hydrogen permeability Φ for the as-cast Cu–15 vol. % Nb and rolled Cu–20 vol. % Nb alloys. The Φ of pure Pd [12] is also plotted for comparison.....	163
Figure 7.5.	Appearance of the Cu–20 vol.% Nb rolled sample after the hydrogen permeation test. The sample is sandwiched between two silver-coated stainless steel gaskets of 12 mm diameter	164
Figure 7.6.	XRD traces of a Pd coated as-cast Cu–15 vol.% Nb membrane under vacuum with increasing temperature to a maximum of 723 K.....	165
Figure 7.7.	Schematic chronological diagram of the in-situ XRD analysis of the as-cast Cu–15 vol.% Nb membranes to a maximum temperature (T_H) in a hydrogen atmosphere of 0.5 MPa and under vacuum	166
Figure 7.8.	XRD traces of a Pd coated as-cast Cu–15 vol.% Nb membrane with maximum temperature, $T_H = 573$ K in 0.5 MPa hydrogen atmosphere	168
Figure 7.9.	XRD traces of a Pd coated as-cast Cu–15 vol.% Nb membrane with maximum temperature, $T_H = 723$ K in 0.5 MPa hydrogen atmosphere	169

LIST OF FIGURES

Figure 7.10.	Lattice parameter of the Cu phase of the Pd coated as-cast Cu–15 vol.% Nb alloy in vacuum and hydrogen atmosphere when heated to various maximum temperatures (T_H).....	171
Figure 7.11.	Lattice parameters of the bcc-Nb phase for the as-cast Cu–15 vol.% Nb alloy when heated from room temperature to 723 K in vacuum	172
Figure 7.12.	Lattice parameter of the NbH phase for the as-cast Cu–15 vol.% Nb alloys when heated in a 0.5 MPa hydrogen atmosphere to various maximum temperatures (T_H).....	173
Figure 7.13.	Lattice parameter of the Pd phase of the as-cast Cu–15 vol.% Nb alloy in vacuum and hydrogen atmosphere when $T_H = 573$ K. The lattice parameter of PdH _{0.66} phase is observed below 473 K when cooled from $T_H = 573$ K	174
Figure 7.14.	Nb-H phase diagram by J.F. Smith [22]	178
Figure 7.15.	Lattice parameters of α - α' phase boundaries in Nb wire samples at various temperatures [23]. The lattice parameter of the NbH phase observed is in the α' phase region	178
Figure 7.16.	XRD of as-cast Cu-15 vol.% Nb alloy at room temperature before the test, during H permeation test at $T_H = 573$ K and at room temperature after the dehydrogenation procedure after the H permeation test	180
Figure 7.17.	Hydrogen pressure to hydrogen concentration isotherms in Nb-H system by S. Komjathy [24]	181
Figure 7.18.	Schematic PCT diagram of Nb-based and Pd-based hydrogen permeable alloys by Yukawa et al. [26]. The red dot shows the H concentration of the Nb-Cu alloy at 673 K under an isostatic pressure of 0.5 MPa	182
Figure 7.19.	Schematic diagrams of three effective hydrogen permeability structural models for two component materials [34].....	190

LIST OF FIGURES

Figure 7.20.	Temperature dependence of hydrogen permeability for metals, including that of Nb and Cu [1, 35].....	191
Figure 7.21.	The calculated hydrogen permeability of the Cu-Nb alloy with varying Nb content at 523 K and 723 K based on the series, Maxwell Eucken 2 and parallel models	193
Figure 7.22.	The temperature dependence of hydrogen permeability for the series, Maxwell Eucken 2 and parallel models for a Cu-15 vol.% Nb alloy and the experimental results of the as-cast Cu-15 vol.% Nb and pure Pd.....	194
Figure 7.23.	The increase in Φ with increasing Nb content in Cu when compared to Cu-15 vol.% Nb based on the parallel, Maxwell Eucken 2 and series models at 723 K.....	195
Figure 7.24.	Oxygen Free High Conductivity (OFHC) Cu matrix with a bcc Nb tube filled with an OFHC Cu fiber (Cu-f) [41]	199
Figure 7.25.	SEM images of Cu/Nb/Cu conducting wires at different magnifications (a) 20 X (b) 60 X (c) 500 X and (d) 3500 X.....	200
Figure 7.26.	SEM image of Pd coated Cu/Nb/Cu sample after annealing to 673 K in vacuum at a magnification of 3500X	201
Figure 7.27.	SEM image of Pd coated Cu/Nb/Cu sample after annealing to 673 K in vacuum at a magnification of 7000X. The white particles on the surface are the Cu-Pd phases and the darker background is the Pd coating	202
Figure 7.28.	SEM image of cracked Cu/Nb/Cu multifilamentary membrane in secondary electron image mode after the hydrogen permeation test.....	204

List of Tables

Table 2.1. Hydrogen separation technical targets by U. S. DOE's 'Hydrogen from coal' program [4].....	11
Table 2.2. Fundamental properties of pure metals with respect to hydrogen [9, 24, 39, 40].....	16
Table 2.3. Possible second and third metals to be used as alloying elements in crystalline alloys based on V, Nb, Ta, or Zr, while retaining a single phase bcc structure [9, 24, 46]	18
Table 2.4. List of crystalline alloys and their respective hydrogen permeability	20
Table 3.1. Standard conditions for sample preparation using PIPS.....	57
Table 4.1. Activation energy for the self-diffusion of different elements [27, 28, 29].....	93
Table 6.1. The mean grain size for Nb ₂₀ Ni ₄₀ Zr ₄₀ and Nb ₃₅ Ni _{32.5} Zr _{32.5} heated to 923 K and 1173 K. The mean grain size was estimated from the line broadening of the corresponding XRD traces	142
Table 6.2. The hydrogen diffusion coefficient (D), hydrogen permeation rate (V), hydrogen permeability (Φ), hydrogen solubility coefficient (K) and hydrogen concentration (C) in Nb ₂₀ Ni ₄₀ Zr ₄₀ alloys before and after heating, and in pure Pd	142
Table 7.1. Composition of the particles formed on the surface of the Pd coating obtained by energy dispersive X-ray spectroscopy	202

Chapter 1

Introduction

1.1 Background

Global warming is becoming increasingly problematic worldwide and at present the technologies to harness renewable sources of energy are still in the early stages of development, the consensus is to find and implement ways of using the large fossil fuels deposits already at hand and at the same time minimize green house gas emissions. The Australian government announced that Australia would position itself to uphold a strong and internationally competitive economy with lower emissions targets [1] and in December 2007 signed the Kyoto protocol [2]. An oil-free coal based energy cycle has been proposed in a government-led program in Australia called the COAL21 program [3]. The aim of this program is to produce hydrogen, from coal, to generate electricity, capture the CO₂ and store it underground. One such power plant is being implemented in California [4].

A report prepared for the Australian Government predicts that the demand for hydrogen in Australia will be in the order of 11 billion m³ per year in 2030 and of 25 billion m³ per year in 2050 [5]. According to the automotive industry, the biggest obstacle hindering the mass market for hydrogen cars is the lack of infrastructure to support the wide supply of hydrogen and the cost of production of high purity hydrogen [5]. This Ph.D. dissertation looks at one piece of the puzzle, to address the issue related to the high cost of hydrogen production. Currently coal is the cheapest source of energy in Australia, however, the transformation of coal results in large amounts of carbon monoxide and impurity gases [2]. These gases have harmful effects on fuel cells. Therefore, the elimination of these

impurity gases from the gasified coal is extremely important for fuel cell applications, such as in Fuel Cell vehicles (FCVs). Today, there are two major techniques for hydrogen production and separation. The pressure swing adsorption technique is the most widely used, despite the fact that this hydrogen extraction process is more complicated and not as efficient as the second and much simpler, membrane separation technique. Another advantage of membrane separation is the purity of the resultant hydrogen gas, which is as high as or greater than 99.999 mass% [6]. At present, palladium-based alloys are virtually the only available material family for the alloy membrane separation technology. However, palladium-based alloys are not viable due to their prohibitive cost. Therefore, the development of an economically viable alloy membrane for hydrogen separation is a key technological requirement to achieve affordable and efficient hydrogen energy cycles associated with 'clean coal' technology.

However, there are limiting factors in achieving high hydrogen permeability in membranes. Pinholes and cracks form in the membrane structure due to hydrogen embrittlement effects. Hence, much effort in the research community is directed towards the improvement of hydrogen embrittlement. In recent years, the design of a composite microstructure where a niobium-rich high hydrogen permeability phase is reinforced by a structural framework of another phase which has a high resistance to the embrittlement effect has been shown to be an effective solution to this problem [7]. This constitutes a significant progress towards a more viable hydrogen permeation membrane, but more research needs to be done to understand the effect of the microstructure on the hydrogen permeation properties.

1.2 Objectives of research

Although Pd and its alloys currently exist for these purposes today, their cost is prohibitive and there is a need to develop more cost effective alternatives. Nb-based metallic membranes have recently been discovered as a possible alternative to Pd based membranes. However, much work remains to be done in this alloy system to improve its hydrogen

permeation performance and its resistance to hydrogen embrittlement. The objective of this work is to explore and develop an understanding of the effect microstructure has on the hydrogen permeation properties, and potentially identify a novel Nb-based alloy membrane for hydrogen permeation.

1.3 Structure of the thesis

The thesis is divided into eight chapters.

Chapter 2 provides a survey of the literature relevant to hydrogen purification. This includes a brief background on the types of hydrogen separation membranes and more specifically, the different forms of metallic membranes. The advantages, disadvantages and previous studies of pure metallic, amorphous, crystalline and nanocrystalline membranes are summarized. The unique potential of nanocrystalline alloys are discussed based on their effect on hydrogen diffusivity and the formation of their amorphous precursor is reviewed. Factors affecting hydrogen embrittlement resistance and the effect of grain size refinement on the mechanical properties are also summarized. Finally, the aims of the thesis were defined.

Chapter 3 presents various methods used for sample preparation and for the investigation of the structural properties of the samples.

Chapter 4 provides information on the compositional restrictions for the formation of amorphous in the Nb-Ni-Zr and Nb-Ti-Co alloy systems and examines the crystallization behaviour of these amorphous alloys. Observations of grain refinement to the nanoscale are presented.

Chapter 5 presents the implementation of the hydrogen permeation apparatus and examines the effect of annealing on the hydrogen permeation properties of as-cast Nb-Ni-Zr alloy membranes. Observations on the composition dependence of the cracking mechanism are made.

Chapter 6 gives details on an electrochemical hydrogen permeation technique that was implemented due to the brittle nature of the nanocrystalline ribbons. The effect of

microstructure, i.e. in amorphous, crystalline and nanocrystalline states, on the hydrogen permeation properties is investigated for the first time in chemically identical alloy membranes.

Chapter 7 provides for the first time an insight into the potential of Cu-Nb alloys as hydrogen permeation membranes. Their remarkable resistance to hydrogen embrittlement is examined via in-situ XRD analysis. Ways to improve the hydrogen permeation properties of Cu-Nb alloys are also presented through a modelling exercise and experimental investigation.

Chapter 8 contains the conclusions of the thesis and outlines recommendations for future research.

1.4 References

- [1] *Response to President Bush's announcement on climate change* (2002). Retrieved Nov 1, 2013 from http://www.foreignminister.gov.au/releases/2002/fa021j_02.html
- [2] *Kyoto Protocol* (2007), Retrieved Nov 1, 2013 from <http://www.climatechange.gov.au/international/negotiations/history-negotiations/kyoto-protocol>
- [3] *COAL 21* (2006). Retrieved Nov 1, 2013 from <http://www.australiancoal.com.au/coal-21.html>
- [4] *The Project* (2011). Retrieved Nov 1, 2013 from <http://hydrogenenergycalifornia.com/the-project>
- [5] ACIL Tasman and Parsons Brinckerhoff, *National Hydrogen Study* (2003). Retrieved Nov 1, 2013 from http://www.ret.gov.au/energy/Documents/national_hydro_study.pdf
- [6] S. Uemiya, T. Matsuda and E. Kikuchi, *Journal of Membrane Science*, 56 (1991) 315
- [7] K. Hashi, K. Ishikawa, T. Matsuda and K. Aoki, *Journal of Alloys and Compounds*, 368 (2004) 215

Chapter 2

Literature Review

2.1 Background

Australia has large coal deposits and is one of the biggest coal exporters in the world. With the specter of global warming hovering over us, there has been a greater willingness to embrace ‘clean’ energy [1]. Nevertheless coal remains the cheapest source of energy locally and to stop using coal may have a negative impact on Australian society, as many communities are dependent on the coal mining and trade. The government supports the ‘clean coal’ energy initiative such as the production of hydrogen from gasified coal, since hydrogen emits only water as a by-product of combustion. Moreover, high purity hydrogen is required for use in fuel cell applications. This chapter reviews the various purification techniques that are currently available, the relevant literature for this project and concludes with the aims.

2.2 Hydrogen purification techniques

There are three main techniques that can be used to purify hydrogen; these are (1) cryogenic distillation, (2) pressure swing adsorption (PSA) and (3) membrane separation.

Cryogenic distillation is a technique commonly used to separate liquid mixtures that are activated based on the difference in boiling temperatures of the different constituent components. This system has the advantage of high hydrogen recovery, but it also consumes a lot of energy due to the low operating temperature. The hydrogen purity obtained from

this method is average, thus limiting its application for the production of high purity hydrogen. PSA and cryogenic distillation are both used commercially, even if they are both currently not cost-effective and are energetically demanding. PSA is mostly used in petrochemical industries and centres around the capacity of adsorbents to adsorb more impurities at elevated gas pressure. PSA is a batch process, but a continuous flow is possible by using multiple adsorbents, as shown in Figure 2.1. More details on PSA can be found in a review by Sircar and Golden [2].

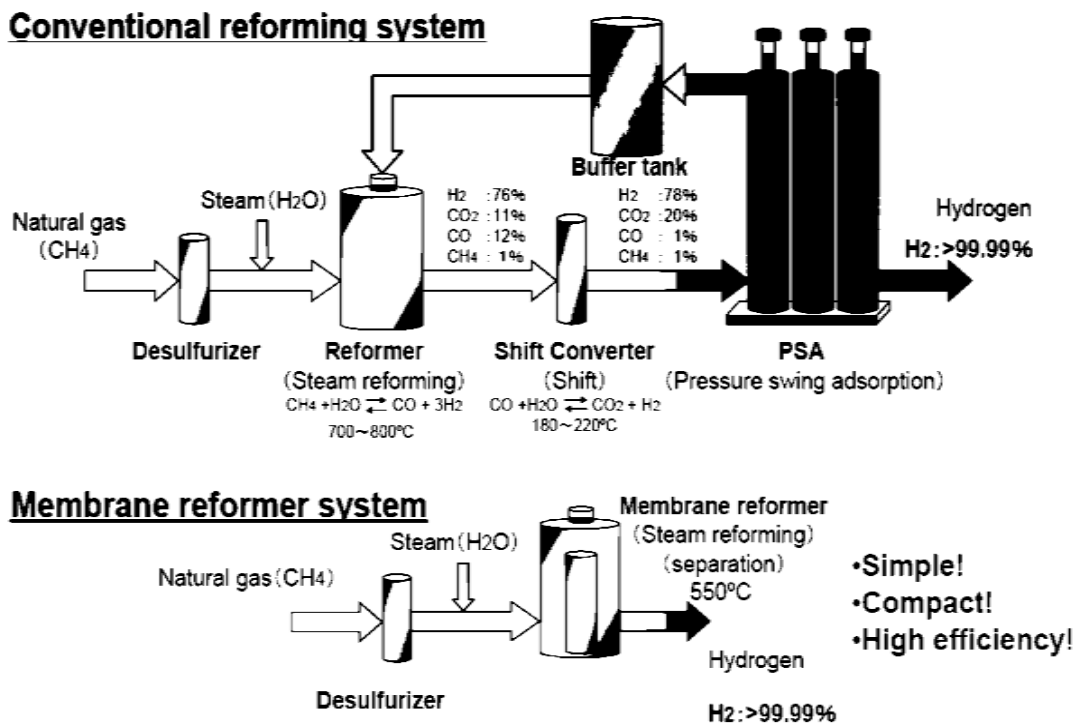


Figure 2.1. The membrane separation system can improve efficiency from 59% to above 75% [3].

The membrane separation technique is the most promising technique. It is based on a barrier that due to its physical and/or chemical nature allows hydrogen to permeate through but not the other constituents. According to a report by the US Department of Energy [4], the efficiency of a typical coal-sourced hydrogen/electricity generation plant can be improved from 59% to greater than 75.5% by employing the membrane separation process instead of PSA. Other advantages of the membrane separation technique are low investment cost, simpler operation, less demand on space due to its more compact nature, and high

purity hydrogen gas that is as high as or greater than 99.99 mass % [5]. This makes the separation membrane technique an ideal candidate for the production of hydrogen from gasified hydrocarbons.

2.3 Types of hydrogen separation membranes

Hydrogen separation membranes can be classified into four different categories based on the material family to which they belong.

2.3.1 Polymeric membranes

Polymeric membranes are used for the separation of hydrogen from gaseous mixtures. There are two main categories of polymer membranes; (1) glassy polymer membranes that have higher hydrogen selectivity but lower hydrogen flux and (2) rubbery polymeric membranes that have higher hydrogen flux but lower hydrogen selectivity [6]. Kluiters believes that the operating temperatures for polymeric membranes are about 373 K [6]. Besides being inexpensive and resistant to high-pressure drops, polymeric membranes have several drawbacks, including limited mechanical strength, susceptibility to certain chemicals commonly present in gasified hydrocarbons, such as sulfur oxides and carbon dioxide, and sensitivity to swelling and compaction. Polymer membranes are currently used for the separation of hydrogen from gaseous mixtures that contain nitrogen, CO or hydrocarbons, and can achieve high hydrogen purity. However, palladium alloys and other inorganic membranes are still required to produce hydrogen of the highest quality. The separation process in polymer membranes occurs according to the solution-diffusion mechanism [7]. A more detailed analysis of polymeric membranes by can be found elsewhere [8].

2.3.2 Carbon based membranes

Non-polymer carbon-based membranes are rejective hydrogen membranes, where hydrogen is rejected and the contaminate species is permeated, unlike conventional methods where hydrogen is permeated and the contaminate species rejected. These membranes are suitable

for operation at high temperatures (773-1173 K) compared to polymer membranes (< 373 K). Carbon-based membranes can be classified into three categories: (1) carbon membranes, (2) carbon molecular sieve membranes and (3) carbon nanotubes [9]. The ability of each of these types of carbon membranes depends on various parameters, such as the chemistry of the material, manufacturing method and morphology. These membranes are usually prepared by heat-treating organic polymers at high temperatures in an inert atmosphere, leading to carbonization. Carbon-based membranes can be prepared by two methods: (1) unsupported such as flat film membranes, capillary tubes or hollow fibers and (2) supported such as flat and tubular membranes on a macroporous material [10, 11]. The reason why carbon-based membranes need support is due to their brittle nature and this has a direct effect on cost and causes difficulties to the multistep material preparation process [12]. Besides the limitations in mechanical properties, carbon-based membranes are also more expensive than polymer membranes and have a poorer performance [13]. The effectiveness of carbon-based membranes will be adversely affected if the incoming mixture of gases contains traces of organic compounds or strong adsorbing vapours such as H₂S and NH₃, as these can clog the pores that are the main transport system. This problem can be avoided by operating at higher temperatures [14], however, the gas permeance is also reported to decrease with increasing temperature due to the increase in the density of the membrane and a reduction in pore size [15]. Carbon-based membranes are a special category of membranes that have some unique permeance characteristics and advantages, but also several disadvantages, which is currently limiting its possible application. This leaves us with the two more promising categories of permeation membranes, ceramic and metallic membranes.

2.3.3 Ceramic membranes

Ceramic membranes have certain properties that make them attractive for membrane separation, such as the ability to sustain high operating temperatures, resistance to hydrogen embrittlement and their inertness to poisoning gases. These membranes have an

interconnected arrangement of micropores that perform the separation of small molecules such as H₂, He, CO, N₂, CO₂ and O₂, and have been reported to have high hydrogen selectivity [16]. Silica membranes are one of the ceramic membranes that are being researched due to their low raw material cost, scalability, low cost of production and ease of manufacturing. Silica membranes usually have two or three layers; (1) a membrane layer, (2) an intermediate layer and (3) a support. Several methods can be used to produce silica membranes but the methods of choice, so far, have been chemical vapor deposition and sol-gel processing [17-19]. Microporous ceramic membranes are also reported to have a hydrogen flux more sensitive to pressure than palladium membranes, as the hydrogen flux is directly proportional to the pressure as opposed to the square root of the pressure in the case of palladium metallic membranes. The permeance is also found to increase significantly with increasing temperature [7]. Therefore, ceramic membranes can permeate a higher flux of hydrogen due to the improved permeance at higher pressure and temperature and their ability to operate in these conditions. However, due to the porous nature of ceramic membranes, they cannot selectively separate only one component, as the separation process occurs as a result of molecules hopping from site to site in the micropore network [20]. Another ceramic that is also being looked at is zeolite, which is a potential candidate for continuous long-term separation process as it provides a combination of pore size and shape selectivity together with mechanical, thermal and chemical stability not observed in many types of membranes. It is also being touted as an interesting candidate for streamlined hydrogen production via natural gas reformation due to its high temperature stability and ability to be regenerated without loss to performance. More details on ceramic membranes and zeolites can be found elsewhere [7, 21, 22].

2.3.4 Metallic membranes

Metallic membranes are dense films or sheets of metal that allow hydrogen to permeate as protons and electrons. When adsorbed within the metal, hydrogen loses its electron and diffuses through the membrane as an ion. Only hydrogen can diffuse through the alloy

membrane as a hydrogen ion, i.e. proton, as the dense membrane prevents larger atoms and molecules such as CO, CO₂, N₂ and O₂ to pass through. This implies that the hydrogen selectivity in metallic membranes is very high and results in high purity hydrogen. Metallic membranes can also sustain operating temperatures well above those of polymer membranes. As part of their '*Hydrogen from Coal*' program, the U.S. Department of Energy have set technical performance targets for hydrogen separation membranes, so that they can be successfully incorporated in membrane separation reactors [23]. These performance targets are shown in Table 2.1. Besides low cost and high hydrogen flux across the membrane, the other performance criteria listed were improved durability, low membrane fabrication cost, operating temperature, low parasitic power requirement, high hydrogen purity and recovery rate [23, 24]. Metallic membranes have two subtypes: (1) the pure metal and alloy membranes, and (2) the hydrogen permeable cermets. The flux of hydrogen flowing across these membranes is proportional to the differences of the square roots of their partial pressure. Pure and alloy membranes are commonly made out of materials such as Pd or Pd-Ag. A more in depth review of types of pure metal and alloy membranes and the mechanism involved for hydrogen permeation can be found in Section 2.4.

Hydrogen permeable cermet membranes are composites of ceramic and metallic membranes, and combine some of the beneficial properties of ceramics with those of metal membranes. They have a dense mixed conducting ceramic matrix phase combined with a hydrogen permeable metallic second phase. The mechanism of hydrogen transfer is a combination of proton and electron conductivity combined with atomic hydrogen transfer. The hydrogen permeable cermet membranes behave like a metallic membrane, as the atomic hydrogen transfer is much greater than the proton and electron conductivity [23]. This metal ceramic composite offers the potential to overcome some of the limitations of both ceramic and metal membranes. These include higher hydrogen purity than ceramic membranes, and in the case of metallic membranes comprise the inhibition of phase change and better tolerance to impurities present in the mixed gas [23]. For the purpose of this dissertation, I will focus solely on pure and alloy metallic membranes.

Table 2.1. Hydrogen separation technical targets by U. S. DOE's 'Hydrogen from coal' program [4].

Properties	Units	2003 status[#]	2007 status[*]	2007 target	2010 target	2015 target
Flux rate	m ³ /h/m ²	18.3	~62	30.5	61	91.5
Temperature	K	573-873	573-673	673-973	573-873	523-773
Cost	\$/m ²	1940	<2150	1615	1076	<1076
ΔP pressure difference across membrane	MPa	0.69	6.89	0.69	<2.76	<6.89
Hydrogen purity	%	99.99 %	>99.999 %	95 %	99.5 %	99.99 %
Durability	Years	<1	0.9	1	3	5

[#]Current status shown for metallic membranes reported by Phair and Donelson [24].

^{*}Current status shown for only the hydrogen permeable cermet separation membrane [23].

2.4 Types of metallic membranes

Pure metal and alloy metal membranes can be classified into four different categories based on their chemical composition and morphology, which are discussed further below.

2.4.1 Principles of hydrogen permeation in metallic membranes

In the case of pure metal and alloy membranes, the permeation of hydrogen happens via pressure driven diffusion across the membrane and occurs through the following steps:

- Dissociation
- Adsorption
- Ionization
- Diffusion
- Desorption
- Re-association

which is illustrated in Figure 2.2. The dissociation and re-association of hydrogen at the surface of the metallic membrane require the presence of a catalyst, usually palladium.

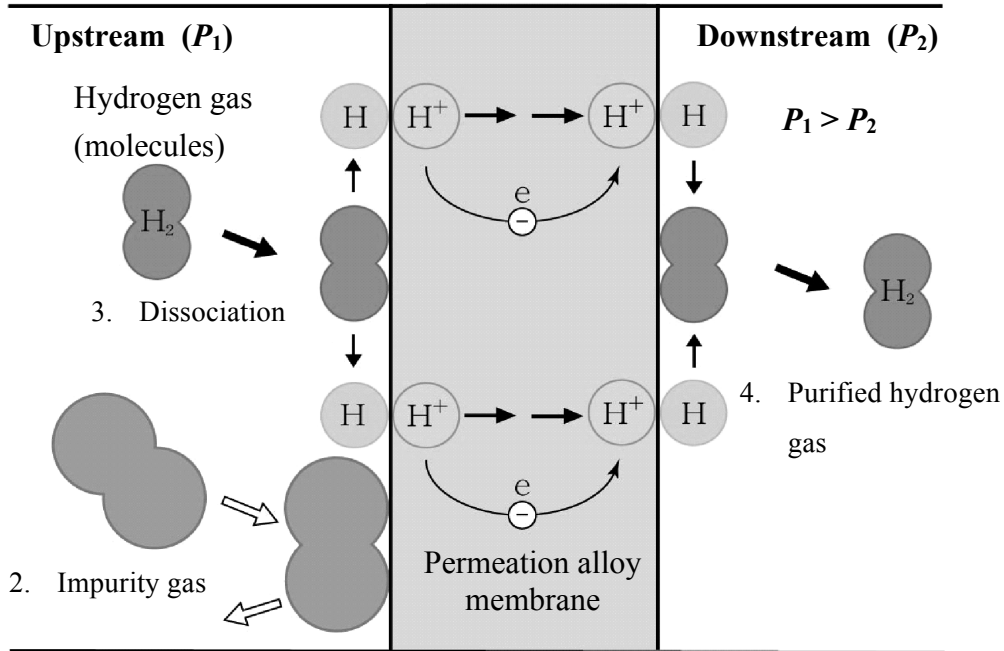


Figure 2.2. Schematic representation of hydrogen separation through a metallic membrane.

An obvious requirement for permeation membranes is that a high steady state flux of hydrogen, J , is induced within the membrane, which can be measured as a mole of hydrogen permeating through a given area of the membrane exposed over a period of time under a certain pressure differential at a given temperature [25]. The flux of hydrogen passing through a membrane is derived from the following Fick's first law that describes the atomic permeation of hydrogen through a metal as a function of concentration gradient and diffusion coefficient, D :

$$J = D \frac{\partial C}{\partial L} \quad (2.1)$$

where $\partial C/\partial L$ is the concentration gradient across the membrane with thickness, L . Pressure can be linked by the following Sievert's law given some conditions are fulfilled:

$$C = K\sqrt{P} \quad (2.2)$$

where K is the Sievert's constant and \sqrt{P} is the term responsible for the link between partial pressure and the dissociation of hydrogen into two ions [26]. The hydrogen flux can then be expressed as:

$$J = \Phi \frac{\sqrt{P_1} - \sqrt{P_2}}{L} \quad (2.3)$$

where P_1 and P_2 are the hydrogen pressures at the upstream and downstream sides of the membrane, Φ is the hydrogen permeability and L is the thickness of the membrane. Φ of hydrogen in the membrane is determined through the following relationship:

$$\Phi = \frac{DS}{2} \quad (2.4)$$

where D is the hydrogen diffusion coefficient and S the hydrogen solubility coefficient. Consequently, a large D , large K , small L and a large pressure difference are preferable for efficient hydrogen permeation through the membrane. The hydrogen permeability, Φ , has been reported to vary exponentially with temperature in an Arrhenius-type relationship which is expressed by

$$\Phi = \Phi_0 \exp\left(\frac{E_a}{RT}\right) \quad (2.5)$$

where Φ_0 is the pre-exponential factor related to the hydrogen permeability of the metal, E_a is the apparent activation energy of the permeation process and T is the temperature during the permeation. Therefore, Equations 2.3 and 2.5 are useful for predicting the hydrogen flux rate for a certain membrane if the parameters such as temperature, membrane thickness, differential pressure, area and permeation rate are known, given that Sievert's law applies. Sievert's law is reported to apply only when the hydrogen to metal atomic ratio is small, and when there is little interaction of the hydrogen atoms [24, 27, 28]. Even though groups doing research on metallic hydrogen permeation membranes commonly use Fick's first law, it has been suggested that it is an oversimplification for the prediction of the hydrogen flux

in amorphous and nanocrystalline materials, and Itoh et al. have proposed other relationships as more appropriate to describe the hydrogen flux in amorphous alloys, which can be found elsewhere [29, 30].

2.4.2 Pure metal membranes

A metal that is crystalline and from a single element is considered 'pure' in this review. The hydrogen permeability through pure metals is attributed to their lattice structure, chemical reactivity to hydrogen and other lattice defects, such as dislocations, vacancies and other atomic impurities. Pd membranes have been conventionally used to separate hydrogen since they have a catalytic effect for the dissociation and re-association of hydrogen on the surface of the membrane and also because they are highly permeable to hydrogen. However, Pd is very expensive and this makes it an unviable option as a stand-alone membrane for large-scale applications. The high cost of Pd encouraged research on other pure metals, mainly from transition metal Group V, which have been reported to have higher hydrogen permeability than Pd, but also on other non-hydride formers such as Ni, which has lower hydrogen permeability than Pd [7, 31-35]. The high hydrogen permeability of transition metals in Group V, such as Nb, is attributed to their body centred cubic (bcc) lattice arrangement as opposed to materials with lower hydrogen permeation such as Pd and Ni, which have a face centered cubic (fcc) lattice arrangement. The high H permeability in metals with a bcc structure is due to their low atomic packing and large interstitial sites that favour hydrogen transport through the membrane. The decrease of the hydrogen permeability of Nb, V, and Ta with increasing temperature is illustrated in Figure 2.3. This phenomenon is due to the faster decrease in hydrogen solubility coefficient than the increase in the diffusion coefficient as the temperature rises [7].

A summary of the properties of pure metals that are relevant to their application as hydrogen permeation membranes is given in Table 2.2. From Equation 2.4, it can be seen that a high hydrogen permeation rate depends on a high hydrogen solubility and high hydrogen diffusivity. A high enthalpy also indicates a more pronounced tendency to form

hydrides, thus a higher susceptibility to hydrogen embrittlement [36]. Changes in the chemical configuration and unit cell aspect ratio when exposed to hydrogen introduce internal stresses that result in hydrogen embrittlement. Consequently, it can be seen in Table 2.2 that certain elements, such as Nb, Ta, V, Zr, and Ti, are likely to suffer from hydrogen embrittlement and degradation in mechanical properties when exposed to high hydrogen partial pressures [36]. Group IV and V elements have other disadvantages. Their rate of dissociation and re-association of hydrogen is too low to achieve high hydrogen flux rates [37], and they are also prone to form oxide layers on their surface that can further hinder the dissociation, dissolution and adsorption of hydrogen atoms within the membrane [31, 37, 38]. Coating a thin layer of Pd on the surface of the membrane can circumvent this problem. However, the tendency of these elements to readily form hydrides imposes a limitation on the use of pure metal membranes due to hydrogen embrittlement.

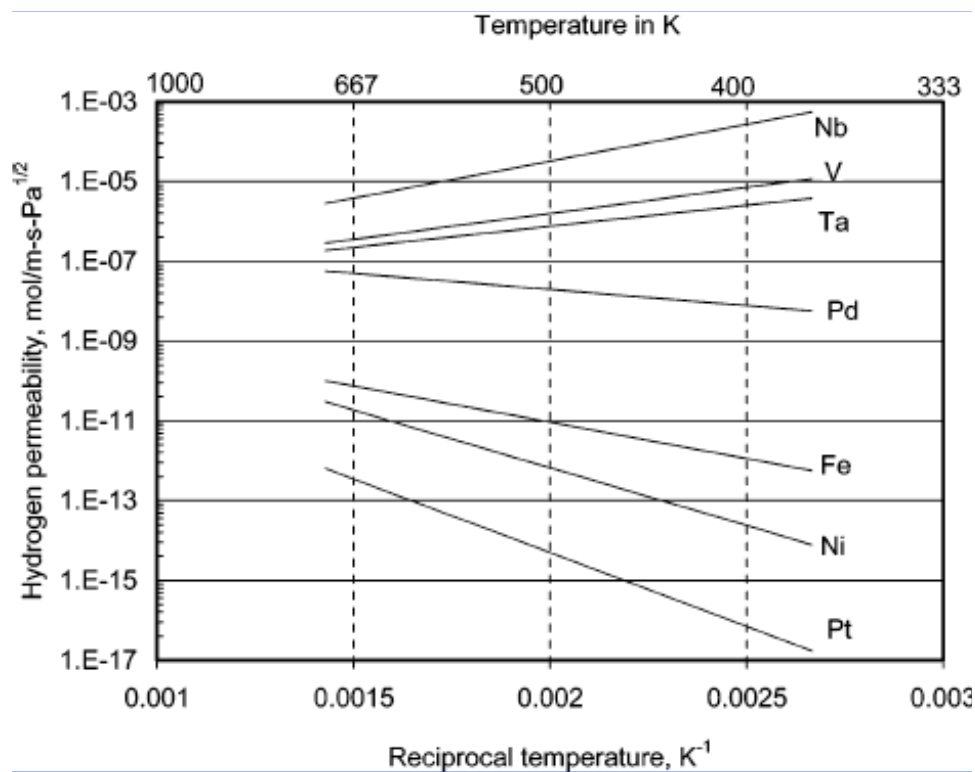


Figure 2.3. Temperature dependence of hydrogen permeability for pure metals [7, 31, 32]. Metal-hydride formers, in particular with body-centred-cubic (bcc) structure (V, Nb and Ta), exhibit high permeability whereas the non-hydride formers show limited hydrogen permeability.

Table 2.2. Fundamental properties of pure metals with respect to hydrogen [9, 24, 39, 40].

Crystal structure	Metal	H solubility at T = 300 K (H/M)	ΔH -Hydride formation (KJ/mol)	H permeability at T = 723 K (mol/m·s·Pa ^{1/2})	Activation energy for bulk diffusion (KJ/mol)
bcc	Nb	0.05	-60 (NbH ₂)	1.6x10 ⁻⁶	10.2
	Ta	0.2	-78 (Ta ₂ H)	1.3x10 ⁻⁷	14.5
	V	0.05	-54 (VH ₂)	1.9x10 ⁻⁷	5.6
	Fe	3x10 ⁻⁸	+14 (FeH)	1.8x10 ⁻¹⁰	44.8
fcc	Cu	<8x10 ⁻⁷		4.9x10 ⁻¹²	38.9
	Ni	<7.6x10 ⁻⁵	-6 (Ni ₂ H)	7.8x10 ⁻¹¹	40
	Pd	0.03	+20 (PdH)	1.9x10 ⁻⁸	24
	Pt	<1x10 ⁻⁵	+26 (PtH)	2.0x10 ⁻¹²	24.7
hcp	Ti	$\alpha \approx 0.0014$	-126 (γ -TiH ₂)		
	Ti	$\beta \approx 1.0$			
	Zr	<0.01	-165 (ZrH ₂)		

2.4.3 Crystalline alloy membranes

Crystalline alloys based on Group 4 (Zr, Ti) and Group 5A (V, Nb, Ta) elements of the periodic table have been reported to have high hydrogen permeabilities [41-46]. As mentioned in the previous section on pure metals, each element possesses both advantages and disadvantages in regards to their behaviour in the presence of hydrogen and their cost. The main aim of alloying is to improve the physical properties of a pure metal, such as resistance to hydrogen embrittlement, while maintaining high hydrogen permeability. For example, Ishikawa et al. reported the successful combination of hydrogen permeability and good hydrogen embrittlement resistance for an alloy consisting of a composite

microstructure where a (Nb,Zr)-rich phase is reinforced by structural frameworks of eutectic (Nb,Zr) + (NiZr) phase that has high resistance to the embrittlement effect [47]. The new membrane had a hydrogen permeability 2.9 times greater than that of pure palladium membranes. Scanning electron micrographs of a $\text{Nb}_{40}\text{Zr}_{30}\text{Ni}_{30}$ alloy showed that the alloy membrane exhibited a two-phase structure, where the bcc-Nb phase was surrounded by the Nb + NiZr matrix, as illustrated in Figure 2.4 [47]. The hydrogen permeability has also been reported to increase with increasing volume fraction of primary bcc-Nb phase [41, 44, 47].

Other alloying elements to Nb include Fe, Mn, Mo, Ni, Ga, Ge, Sn, Si, W, La, Be, Ta, but the most common ones are Ti, Co, Cr and Al [46]. The atomic percentages of the second and third elements to be added while maintaining a bcc-Nb phase that is conducive to hydrogen permeation can be estimated with the help of a binary, pseudo binary or ternary phase diagram [48, 49]. A range and combination of metals that can be used in binary and ternary alloys with Nb, V, Ta, or Zr as base material is shown in Table 2.3.

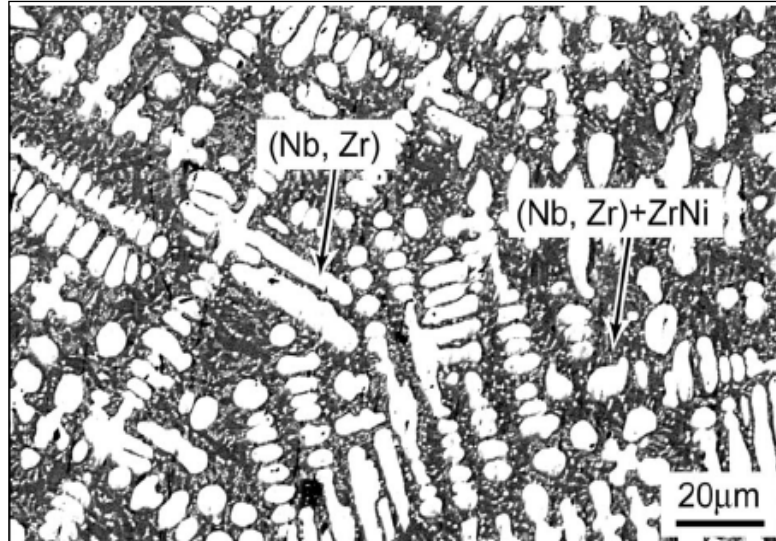


Figure 2.4. A scanning electron micrograph of a $\text{Nb}_{40}\text{Zr}_{30}\text{Ni}_{30}$ alloy for hydrogen permeation [47]. This alloy was prepared by conventional arc melting. The hydrogen permeability (Φ) of this alloy was 2.9 times greater than that of Pd.

Table 2.3. Possible second and third metals to be used as alloying elements in crystalline alloys based on V, Nb, Ta, or Zr, while retaining a single phase bcc structure [9, 24, 46].

Second metal	Atomic %	Third metal	Atomic %
Aluminum	0-40	Cu	0-5
	0-35	Fe	0-40
	0-40	Ga	0-12
	0-40	Ge	0-3
	0-40	Mn	0-53
	0-40	Mo	0-100
	0-40	Nb	0-100
	0-40	Ni	0-8
	0-40	Ta	0-100
	19-25	Sn	0-6
	0-50	Ti	0-90
	0-40	Zr	0-5
Beryllium	0-2	Ti	0-50
Cobalt	0-10	Fe	0-30
	0-12	Ga	0-12
	0-12	Ni	0-10
	0-12	Si	0-7
Chromium	0-100	Fe	0-25
	0-100	Hf	0-2
	0-100	Mo	0-100
	0-100	Nb	0-100
	0-100	Ni	0-9
	0-100	Ta	0-10
	0-100	Ti	0-80

	0-100	W	0-100
	0-100	Zr	0-4
Copper	0-40	Ni	0-12
Iron	0-30	Ga	0-12
	0-30	Mo	0-100
	0-30	Ni	0-5
	0-30	Ti	0-95
Gallium	0-10	Ge	0-4
	0-15	Ln	0-15
	0-10	Mn	0-50
	0-10	Nb	0-100
	0-10	Ni	0-8
	0-10	Si	0-4
Germanium	0-2	Nb	0-100
Hafnium	0-5	Ta	0-5
Manganese	0-50	Si	0-4
Molybdenum	0-100	Nb	0-100
	0-100	Ni	0-22
	0-100	Si	0-4
	0-100	Ta	0-100
	0-100	Ti	0-25
Niobium	0-100	Ni	0-6
	0-100	Ta	0-100
	0-100	Ti	0-100
	0-100	Zr	0-10
Nickel	0-15	Si	0-4
	0-12	Ti	0-100

Table 2.3. (Continued)

Second metal	Atomic %	Third metal	Atomic %
Tantalum	0-100	W	0-100
	0-15	Zr	0-8
	0-100	Si	0-4
	0-100	Sn	0-12
	0-40	Ta	0-10
Titanium	0-80	W	0-100
	0-90	Zr	0-10

Yukawa et al. have reportedly used another approach with the specific addition of a small amount of transition metal, such as Zr, Mo, Ru, Rh and W to alter the stability of hydrides in the Group 5A elements by increasing the hydride formation enthalpies, therefore reducing the risk of hydrogen embrittlement [28, 50-53]. The work of Yukawa is further reviewed in relation to hydrogen embrittlement in Section 2.6.2. Another benefit of alloying with elements such as Cu, Ni, Ag or Fe is that the membrane's surface susceptibility to gaseous impurities and subsequent contamination can be reduced [36, 54, 55]. Table 2.4 provides a list of crystalline alloys and their hydrogen permeabilities for the possible application as hydrogen permeation membranes and brief comments about the findings.

Table 2.4. List of crystalline alloys and their respective hydrogen permeability.

Alloy	H permeability Φ (mol/m·s·Pa ^{1/2})	Comments	Year and Reference
V ₈₅ Ni ₁₅	2-3x10 ⁻⁸ at 473-673 K	H ₂ permeability increase with Ti, Zr, and Y dopants present.	1991 [56], 2002 [57]
INCONEL 718	~2.4x10 ⁻⁹ at 623K	Good ductility and excellent strength.	1994 [58]
GH 761	~1.1x10 ⁻⁹	H ₂ permeability not sensitive to microstructure or chemical composition.	
VCr ₄ Ti ₄	1x10 ⁻⁵ -1.3x10 ⁻⁸	Oxidation prior to annealing	1998 [59]

	at 773-923 K	greatly reduced H ₂ permeability	
Ni ₃ Al-6Fe	4x10 ⁻¹² at 600 K	Fe addition increased permeation rate and protected the surface.	2001 [60]
Ni ₃ Al-Zr	1x10 ⁻¹²	Zr addition of 1.4 at. % protected the Ni ₃ Al surface's function.	
V _{99.98} Al _{0.02}	0.7-1.8x10 ⁻⁹ at 533-673 K	Al is a common impurity in V-based alloys. H ₂ permeability decreased when Al content was increased above 20 at. % due to surface or blocking effects	2002 [61]
V _{99.1} Al _{0.9}	0.7-1.8x10 ⁻⁹		
V _{97.1} Al _{2.9}	0.7-1.8x10 ⁻⁹		
V _{90.2} Al _{9.8}	2-3x10 ⁻⁹		
V _{81.3} Al _{18.7}	3.7-6x10 ⁻⁹		
V _{71.8} Al _{28.2}	0.7-1.8x10 ⁻⁹		
V ₉₀ Al ₁₀	1.3-2x10 ⁻⁷ at 523-673 K	Increase in Al content decreased the H ₂ permeability, which is attributed to the matrix bcc phase as insignificant amounts of precipitates were observed.	2003 [62]
V ₇₀ Al ₃₀	0.7-1.8x10 ⁻⁹		
V ₈₅ Ni ₁₅	3-4x10 ⁻⁷ at 423-673 K	Increase in Al content increased H ₂ permeability due to increase H ₂ solubility. However, H ₂ permeability decreased at lower temperatures due to the presence of Al	2003 [63]
V ₈₅ Ni _{14.91} Al _{0.09}	3-4.5x10 ⁻⁷		
V ₈₅ Ni _{14.1} Al _{0.9}	3-4.5x10 ⁻⁷		
V ₈₅ Ni _{12.4} Al _{2.6}	4-6x10 ⁻⁷		
V ₈₅ Ni _{10.5} Al _{4.5}	5-7x10 ⁻⁷		
Nb ₁₀ Zr ₄₅ Ni ₄₅	~2.73x10 ⁻⁸ at 623 K	Multiphase structure, H ₂ permeability is >Pd above 573 K.	2004 [64]
Nb ₉₅ M ₅ (M=Pd, Zr, Mo, Ru)	~1.3x10 ⁻⁷ at 573 K	H ₂ permeability increased with alloying of Pd and Zr but decreased for Mo and Ru.	2005 [67]
Fe ₃ Al	6x10 ⁻¹¹ -1.01x10 ⁻¹⁰ at 300 K	Two events observed in H ₂ permeation curves; permeation first occurred through α-Fe disordered phase, followed by the ordered B ₂ -phase.	2005 [68]

Table 2.4. (Continued)

Alloy	H permeability Φ (mol/m·s·Pa ^{1/2})	Comments	Year and Reference
Nb ₄₀ Ni ₃₀ Zr ₃₀	4.64x10 ⁻⁸ at 673 K	The microstructure consists of a primary (Nb, Zr) phase surrounded by a fine eutectic microstructure of (Nb, Zr) + (NiZr).	2005 [47]
Nb ₂₀ Ni ₄₀ Zr ₄₀	2.73x10 ⁻⁸ at 673 K		
Nb ₂₉ Ti ₃₁ Ni ₄₀	1.5x10 ⁻⁹ -7x10 ⁻⁹ at 523-673 K	Alloy contains two phases; a bcc (Nb,Ti) solid solution and a B2-TiNi compound or a eutectic ((Nb,Ti)+(TiNi)). The eutectic phase suppressed hydrogen embrittlement, while the bcc phase contributed to H ₂ permeation.	2005 [69, 70]
Nb ₁₇ Ti ₄₂ Ni ₄₁	1.1x10 ⁻⁹ -0.6x10 ⁻⁸		
Nb ₁₀ Ti ₅₀ Ni ₄₀	5.5x10 ⁻¹⁰ -4.5x10 ⁻⁹		
Nb ₃₉ Ti ₃₁ Ni ₃₀	3x10 ⁻⁹ -2x10 ⁻⁸		
Nb ₂₈ Ti ₄₂ Ni ₃₀	2x10 ⁻⁹ -1x10 ⁻⁸		
Nb ₂₁ Ti ₅₀ Ni ₂₉	9x10 ⁻¹⁰ -1x10 ⁻⁸		
Ta ₅₃ Ti ₂₈ Ni ₁₉	~0.25x10 ⁻⁹ -1x10 ⁻⁸ at 523-673 K	The formation of intermetallics compounds led to brittleness. Alloy contained two phases; a bcc (V,Ti) or (Ta,Ti) solid solution and a B2-TiNi compound or a eutectic bcc+B2.	2005 [44]
Ta ₃₉ Ti ₂₇ Ni ₃₄			
Ta ₂₂ Ti ₅₈ Ni ₂₀			
Ta ₁₄ Ti ₃₉ Ni ₄₇			
V ₄₁ Ti ₂₀ Ni ₃₉	~0.5x10 ⁻⁹ -0.5x10 ⁻⁸ at 523-673 K	Ta ₅₃ Ti ₂₈ Ni ₁₉ has a eutectic microstructure and had the highest hydrogen permeability at 673 K, almost equal to that of pure Pd.	
V ₄₁ Ti ₄₀ Ni ₁₉			
V ₄₁ Ti ₃₀ Ni ₂₉			
V ₁₀ Ti ₄₁ Ni ₄₉			
V ₉₀ Ti ₁₀	2.7x10 ⁻⁷ at 673 K	Catalytic Pd coating used on all membranes.	2006 [46]
V ₈₅ Ti ₁₅	3.6x10 ⁻⁷ at 711 K		
V ₈₅ Ni ₁₅	3x10 ⁻⁸ at 673 K		
V ₉₀ Co ₁₀	1.2x10 ⁻⁷ at 673 K		
V ₈₅ Al ₁₅	6x10 ⁻⁸ at 713 K		
Nb ₅₀ Ti ₂₀ Co ₃₀	~2x10 ⁻⁹ – 2.64x10 ⁻⁸ at 523-673 K	The different chemical composition gave different microstructures of bcc (Nb,Ti) embedded in a eutectic matrix of ((Nb,Ti)+TiCo). Nb ₃₀ Ti ₃₅ Co ₃₅ had a fine eutectic ((Nb,Ti)+TiCo)	2006 [71]
Nb ₄₉ Ti ₃₁ Co ₂₀			
Nb ₃₈ Ti ₃₁ Co ₃₁			
Nb ₃₀ Ti ₃₀ Co ₄₀			
Nb ₃₀ Ti ₃₅ Co ₃₅			

Nb ₂₉ Ti ₅₁ Co ₂₀		lamellar structure and had a hydrogen permeability higher than that of pure Pd at 673 K. H embrittlement is suppressed by the eutectic microstructure.	
Nb ₂₉ Ti ₄₀ Co ₃₁			
Nb ₂₀ Ti ₃₉ Co ₄₁			
Nb ₁₉ Ti ₅₀ Co ₃₁			
V ₅₃ Ti ₂₆ Ni ₂₁	1-3.7x10 ⁻⁹ at 295 K	Electrochemical method used to test for hydrogen permeability. (Units in mol H ₂ /ms)	2007 [72]
Nb ₄₀ Ti ₁₈ Zr ₁₂ Ni ₃₀	1.4-3.23x10 ⁻⁸ at 673 K	The effect of rolling had a detrimental effect on the hydrogen permeability of the alloy compared to when in the as-cast state. The H permeability was recovered by annealing at 1273 K for 369 ks. The eutectic microstructure was lost during annealing but the sample maintained good resistance to H embrittlement.	2007 [73]
Pure Nb		This work identified the ductile to brittle transition in Pd coated pure Nb.	2007 [74]
Nb ₁₉ Ti ₄₀ Ni ₄₁	Max of 2.6x10 ⁻⁸ at 673 K	Directionally solidified alloy with a Nb-TiNi microstructure. Alloy with aligned Nb phase showed a two-fold improvement in H permeability over the as-cast eutectic alloy.	2008 [75]
Nb ₁₉ Ti _{40.5} Ni _{40.5}			
Nb ₂₀ Ti ₄₀ Ni ₄₀			
Nb ₁₈ Ti ₄₁ Ni ₄₁			
Nb ₄₀ Ti ₂₀ Zr ₁₂ Ni ₂₈	>3.23x10 ⁻⁸ at 673 K	Hydrogen properties reported to be higher than in Nb ₄₀ Ti ₁₈ Zr ₁₂ Ni ₃₀ .	2008 [76]
Nb ₄₀ Ti ₃₀ Ni ₃₀	0.48-1.8x10 ⁻⁸ at 673 K	Rolling reduced H permeability due to trapping in defects in lattice. H permeability was recovered after annealing at 1373K for 605 ks. The resistance to H embrittlement was retained after the eutectic microstructure was transformed to a duplex microstructure after annealing.	2009 [77]

Table 2.4. (Continued)

Alloy	H permeability Φ (mol/m·s·Pa ^{1/2})	Comments	Year and Reference
Nb ₁₉ Ti ₄₀ Ni ₄₁	2.4-5.7x10 ⁻⁹ at 573 K	Hydrogen permeability of the alloy is found to decrease when the eutectic microstructure changes into a duplex structure after 1 week annealing at 1373 K. This is attributed to a decrease in H diffusivity.	2010 [78]
Nb ₁₆ Ti ₅₃ Fe ₃₁	2.9x10 ⁻⁸ at 673 K	A eutectic microstructure of TiFe and (Nb, Ti) phases was reported. The alloy had a good resistance to hydrogen embrittlement at 673 K.	2013 [124]

2.4.4 Amorphous alloy membranes

Much research work is being done on amorphous alloy membranes as they offer different properties to their crystalline counterparts. Amorphous alloy membranes have been reported to have various advantages over crystalline membranes, such as a higher hydrogen permeability [30, 124], hydrogen solubility [79], ductility and mechanical strength mainly due to their open lattice [25], which also reduce the risk of hydrogen embrittlement during hydrogen purification [80]. In most cases, amorphous and crystalline membranes require a catalytic coating. However, to the credit of amorphous alloys, it has been reported that Zr₃₆Ni₆₄ does not require a catalytic coating due to its unique surface electron structure, chemical homogeneity and high density of low-coordination active sites [80]. This is highly composition dependent as the addition of Ti or Hf, cancelled these surface catalytic properties.

Currently, the work on amorphous membranes has mostly been close to the eutectic compositions of alloy systems that have been reported to have high hydrogen permeability in the crystalline state, namely Nb, V, Zr, Ta, Ni and Fe. One of the successful alloy systems investigated has been Zr- and Ni-based [29, 82, 83]. Hara et al. and Shimpo et al.

reported that the $Zr_{36}Ni_{64}$ and $Zr_{60}Al_{15}Ni_{7.5}Cu_{15}Co_{2.5}$ amorphous membranes had hydrogen permeabilities comparable to that of pure Pd [80, 82]. Nb-Ni-Zr alloy membranes are one of the most promising amorphous metallic membranes. Reports by Yamaura et al. have shown that $Ni_{30}Nb_{20}Zr_{50}$ amorphous membranes had a hydrogen permeability about 67 % higher than that of pure Pd and similar to that of Pd-Ag alloy membranes [83, 84, 125]. They also found that the hydrogen permeability of Nb-Ni-Zr amorphous alloys is dependent on composition, and that the hydrogen permeability increased in a linear fashion with increasing Zr content [83, 84].

Fe-based amorphous membranes investigated to date were not as successful as those based on Ni or Zr, as they resulted in lower hydrogen permeability than their crystalline counterparts due to the presence of metalloids formed on their surface, which hindered the adsorption/desorption process of hydrogen [85, 86]. V-based amorphous alloy membranes have also been much researched due to their high hydrogen solubility and permeability, but these alloys suffer from severe hydrogen embrittlement and require alloying to change their mechanical, thermal and permeability properties [57, 62, 63]. Even if amorphous membranes have been reported to have high hydrogen solubility, which have been credited to the high defect density within their matrix that allows more sites to be occupied by hydrogen over a range of energy levels, the hydrogen permeability of a membrane also depends on its hydrogen diffusivity [87]. Dos Santos et al. have reported that the hydrogen diffusivity in amorphous membranes is lower compared to their crystalline counterpart also due to their high defect content, which is strongly influenced by the manufacturing method [87, 88]. Amorphous alloy membranes have also been reported to display non-Arrhenius behaviour for hydrogen diffusion [24].

Another challenge for amorphous membranes is their tendency to crystallize when exposed to elevated temperatures higher than 773 K, as they are in a thermodynamically metastable state [34]. This could hinder the use of amorphous alloys to low-temperature separation processes where the kinetics for hydrogen permeation is not as favourable. Additional care must also be taken with regard to the maximum temperature the membranes

are exposed to during sample preparation processes, such as grinding and polishing. Even if the necessary care is taken to avoid exposure to high temperatures, the exothermic absorption of H₂ by the amorphous membrane may generate enough heat that could lead to the decomposition, crystallization or a structural change in the membrane [89]. It has been reported that the best performing amorphous membranes in terms of thermal stability are the Zr-Hf-Ni alloys [25, 90]. However, their hydrogen permeability was found to be lower than that of pure Pd [90].

2.4.5 Nanocrystalline alloy membranes

Lately, there has been some interest in the effect of grain size on the hydrogen permeation rate. Gleiter has reported that the high percentage of grain boundary volume due to the smaller grain size in Pd-based nanocrystalline membranes is expected to give alternative paths for the diffusion of hydrogen due to the excess free volume, which can lead to faster rate of diffusion compared to lattice diffusion alone [91, 92]. Bryden and Ying have also reported that the hydrogen fluxes in nano-structured Pd-Fe membranes were higher than those in coarse-grained membranes of similar compositions and also noticed a higher resistance in the nano-structured membranes to hydrogen sulfide poisoning [93-95].

The underlying principle of the present alloy design strategy is based on the effects of grain boundaries on the diffusion coefficient, D , and solubility coefficient, K , of hydrogen. Although the effects of grain boundaries in Nb-based membranes are yet to be studied, it has been shown that the hydrogen permeation of nanocrystalline Ni is larger than that of conventional microcrystalline Ni, even though the grain size of the nanocrystalline Ni was large (~100 nm) [96]. Another study showed that the diffusivity of hydrogen in nanocrystalline Ni, with a grain sizes between 50 – 100 nm, is close to two orders of magnitude greater than that of bulk Ni [97]. The two mechanisms suggested in those studies are (a) a strong segregation of hydrogen at grain boundaries where the diffusivity is dramatically enhanced by the defects and (b) an enhancement of the hydrogen solubility induced by the high volume fraction of grain boundaries. Therefore, a high increase in

hydrogen permeability is expected in the Nb-based alloy membranes with the reduction of the microstructure to the nanoscale. The hydrogen permeation properties of a Nb-based nanocrystalline metallic hydrogen permeation membrane is yet to reported and thus this aspect will be investigated in the current work.

It was also observed that the manufacturing technique also influences the effectiveness of grain size reduction to the nanoscale. Kuji et al. reported a decrease in the hydrogen solubility of nanocrystalline Pd prepared by extrusion and compression, when compared to that of coarse-grained Pd [98]. This is due to the interaction of hydrogen with chemical and/or structural defects within the metal lattice that lead to hydrogen trapping [99]. This is more significant at low hydrogen concentrations as the trapping of hydrogen usually leads to a decrease in hydrogen diffusion due to the entrapment of the hydrogen or through the degradation of the metal matrix by hydrogen embrittlement.

In this project amorphization and subsequent crystallization processes will be used. These are well-established non-equilibrium processes to fabricate nano-structural alloys, but are new to hydrogen permeation membranes. To achieve a nano-structural grain refinement using this method, an alloy system with a good glass forming ability must be identified.

2.5 Formation of metallic glasses

Because the technique of crystallization from amorphous is to be used to produce nanocrystalline alloy membranes, the formation of metallic glasses is also covered in this literature review. The conditions required for amorphization are well understood by following the kinetics of solidification. Figure 2.5 shows a time-temperature- transformation (TTT) diagram of a $Zr_{41.2}Ti_{13.8}Cu_{10.0}Ni_{12.5}Be_{22.5}$ alloy prepared by Y. J. Kim et al. [100]. To form an amorphous phase it is essential to suppress the nucleation and growth reaction of crystalline phases by supercooling the liquid between the melting temperature, T_m , and the glass transition temperature, T_g [101]. Such a large degree of super cooling requires rapid quenching of the melt.

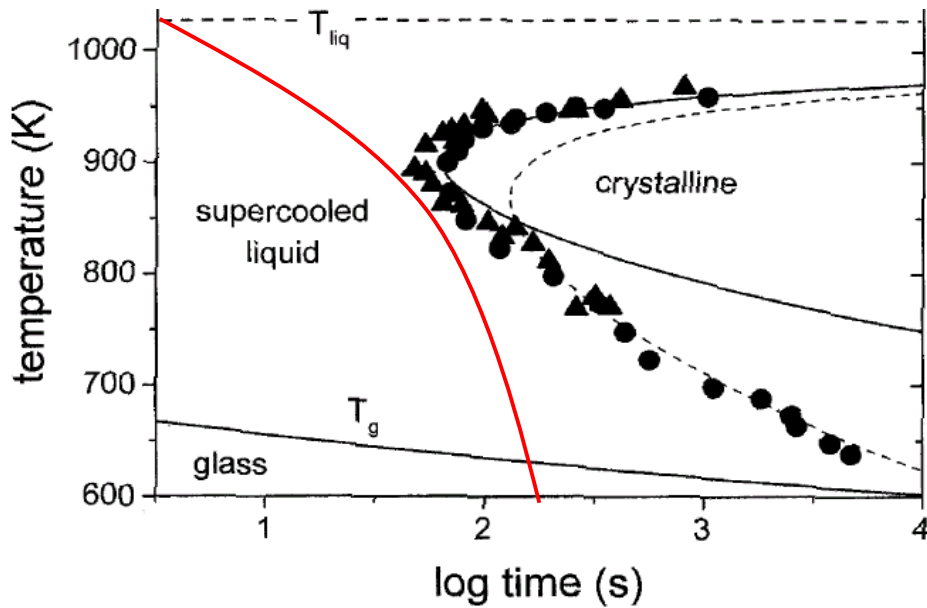


Figure 2.5. TTT diagram with the red line showing the minimum cooling rate required to form an amorphous alloy [100].

The critical cooling rate required to avoid the nucleation and growth processes associated with the equilibrium crystalline phase(s) has been reported to be higher than 10^4 K/s for Ni-based amorphous alloys [101]. Since, the maximum cooling rate in single-roller melt-spinning is in the order of 10^6 K/s, Ni-based amorphous alloys have been prepared by this technique. However, it must be noted that the supercooling required for each alloy system is different and that a high glass forming ability (GFA) can be achieved by taking into account the following two factors (1) high T_g/T_m and (2) large ΔT_x [102], where ΔT_x is the temperature difference between the crystallization temperature and the glass transition temperature. Based on their work on multi-component systems, Inoue et al. suggest three empirical rules for achieving high GFA in bulk amorphous metallic alloys [102]. In the present case we are not dealing with bulk amorphous alloys, but these principles for a high GFA are equally applicable to the formation of amorphous ribbons.

The empirical rules are:

- A multi-component system consisting of more than three elements. However, since it is the fundamental aspect of the formation of a nanostructure that is of interest, the

number of alloying elements will be limited to four and in most cases only three will be used. This will also help in the characterization of the phases that will form during crystallization.

- Significant difference in atomic size ratios (above 12%).
- Negative heats of mixing among their elements.

The rationale behind these three rules can be explained in terms of thermodynamics, topology and kinetics. From a thermodynamic point of view, to obtain a high GFA it is known that a low free energy difference is required for transforming liquid to the crystalline phase. This free energy is represented by the Gibbs free energy, ΔG , where $\Delta G = \Delta H - T\Delta S$, and ΔH is the enthalpy and ΔS the entropy of fusion [19]. The addition of more elements to the alloy system leads to a higher ΔS and the negative heats of mixing and high T_g/T_m ratio lead to a lower ΔH and this therefore results in a low ΔG , which leads to a high GFA.

From a topological point of view, a multi-component system with different atomic sizes will result in denser random packing in the super-cooled liquid. This will result in a higher interfacial energy between liquid and solid interface, higher viscosity and lower atomic diffusivity. From a kinetic point of view, nucleation and growth are the two mechanisms that need to be suppressed to result in a high GFA. The higher interfacial energy between the liquid and solid interface implies that the activation energy required for nucleation will be higher, thus suppressing the nucleation process. A lower atomic diffusivity due to the denser system hinders atomic rearrangement and therefore suppresses crystal growth. The fact that both nucleation and growth are suppressed promotes a high GFA. The same concept of alloying of different elements and limiting atomic diffusivity that is behind the formation of a high GFA also favours the formation and stability of a nanocrystalline system due to the suppression of the growth of crystalline phases.

The work of Yamaura et al. on amorphous Nb-Ni-Zr alloy membranes has reported good hydrogen permeability and this suggests that the Nb-Ni-Zr alloy system may be a potential candidate for the nanocrystalline grain refinement [83, 84]. Kimura et al. has

reported on the glass-forming region in the Nb-Ni-Zr ternary system and the results are shown in Figure 2.6 [103].

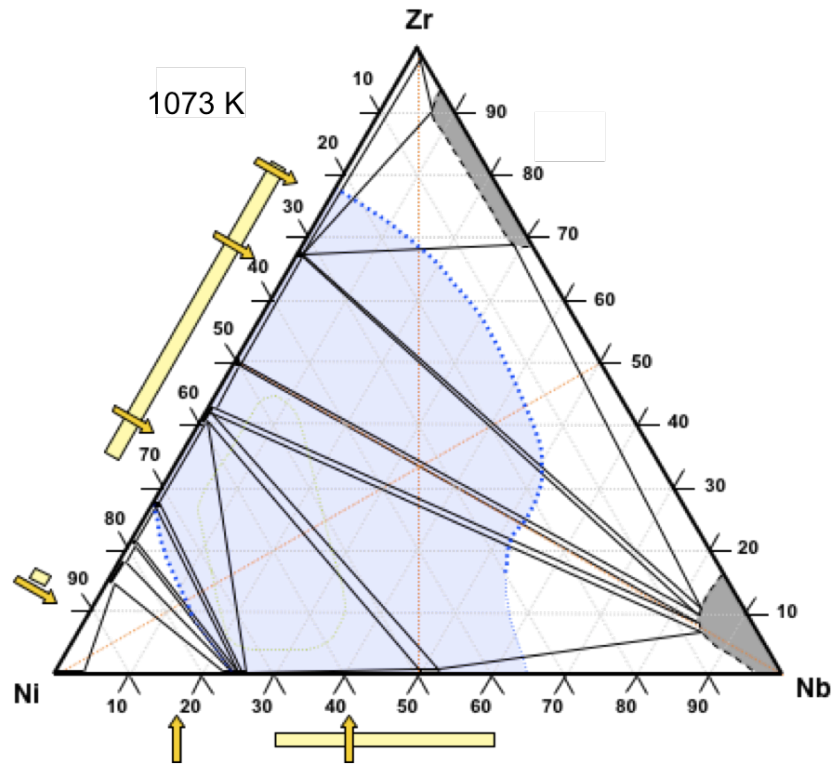


Figure 2.6. Isothermal section of the Ni-Zr-Nb ternary system showing the position of the phase boundaries at 1073 K. The boundaries for ternary amorphous alloy formation (blue dotted line and light blue shaded area) are indicated. In addition, the position of the known binary eutectic compositions (gold arrows) and the established binary glass-forming ranges (yellow bar) are indicated [103].

It can be seen that the extent of the glass-forming region in the ternary phase diagram maps well with the extrapolation of the main glass-forming ranges in both the Ni-Zr and Ni-Nb binary systems. The ability to form amorphous Nb-Ni-Zr metallic membranes at relatively high Nb contents further supports this alloy system as a potential candidate for the nanocrystalline grain refinement, as it was previously reported that the hydrogen permeability increased with increasing Nb content in Nb-Ni-Zr crystalline membranes [41, 44, 47].

2.6 Hydrogen embrittlement

It is well established that the interaction of hydrogen with metals leads to a deterioration of their mechanical properties [104, 105]. This is usually known as hydrogen embrittlement.

This can be classified into four main categories [106]:

- Embrittlement resulting from hydride formation (e.g. zirconium and titanium).
- Embrittlement resulting from reaction between hydrogen and some impurity or alloying addition in the metal (e.g. carbon in steel).
- Embrittlement resulting from hydrogen adsorbed on or absorbed in the metal (e.g. surface cracking in 304L steel).
- Hydrogen blistering or cracking, due to the build up of gas pressure at microcracks and voids. The fact that hydrogen is implicated is secondary.

Sections 2.6.1 and 2.6.2 look further into the effect of hydrogen in amorphous and crystalline alloys.

2.6.1 In amorphous alloys

As it was discussed in Section 2.4.4, amorphous membranes have been shown to have better resistance to hydrogen embrittlement when compared to their crystalline counterpart. However, they are still susceptible to hydrogen embrittlement. The uptake of hydrogen by amorphous membranes can induce considerable changes to the bulk material and this may lead to the failure of the membrane. This hydrogenation process in amorphous alloy membranes usually leads to increased inter-atomic spacing due to hydrogen occupying interstices [89, 107]. A review by Dolan et al. points out that hydrogen occupies polyhedral sites similar to those found in crystalline alloys and prefer ETM_4 sites in early transition metal – late transition metal (ETM-LTM) alloys [90]. The thermal stability of amorphous membranes is reported to decrease with increasing hydrogen concentration past a certain critical value and/or through hydrogen induced phase separation [90]. Thus, the formation of hydrides and high hydrogen concentrations within amorphous membranes should be avoided.

2.6.2 In crystalline alloys

Materials in the Group 5A metals such as Nb and Ta, have high hydrogen solubility and diffusivity, which both are at the same time their strength and Achilles' heel. Nb has a high permeability to hydrogen and is therefore a good candidate for hydrogen permeation membranes. However, Nb is susceptible to form hydrides when exposed to hydrogen at low temperatures and thus suffers from hydrogen embrittlement. Thus, it is difficult to have pure Nb-based metallic membranes that are also resistant to hydrogen embrittlement. By doing an in-situ small punch test at 573-773 K, Yukawa et al. have found that pure Nb has a ductile to brittle transition that occurs at a concentration around $H/M = 0.25$ as shown in Figure 2.7 [28]. It was suggested that to improve the resistance to hydrogen embrittlement of pure Nb, the pressure-composition-isotherms (PCT) curve of niobium should be shifted to the left and have a steeper gradient to minimize the hydrogen concentration in the membrane as shown by the 'designed alloy' curve in Figure 2.7 [28]. Yukawa et al. proposed that designing alloys that can keep the hydrogen concentration within the alloy below the hydrogen concentration for the ductile to brittle transition, would improve the membrane's resistance to hydrogen embrittlement [28]. It is also reported that the addition of alloying elements, such as W, Ru and Mo in Nb to form a solid solution, led to a decrease in the hydrogen solubility but increased the hydrogen diffusivity [53, 126, 127]. The activation energy for the mobility for hydrogen diffusion during hydrogen permeation is reported to decrease with the addition of alloying element [53].

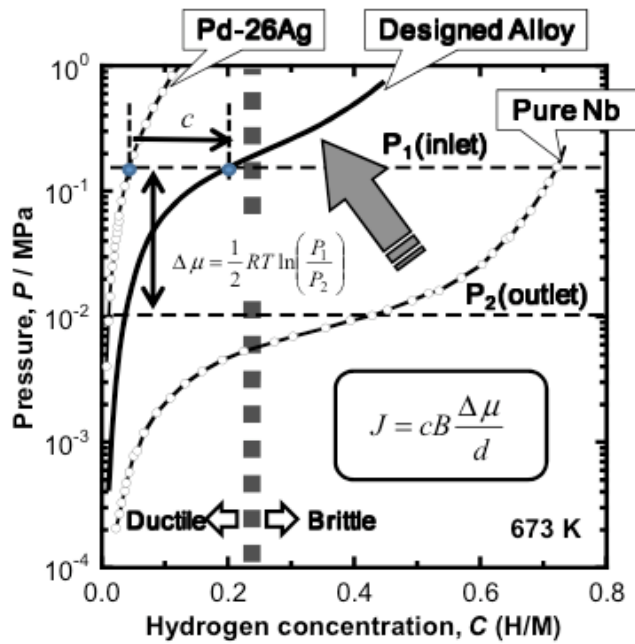


Figure 2.7. A concept for alloy design of Nb-based hydrogen permeable alloys by Yukawa et al. [108].

This approach suggested by Yukawa et al. [28] on limiting the hydrogen concentration within the membrane to improve the resistance to hydrogen embrittlement complements the work done by other research groups on crystalline Nb-based alloy membranes. The approach by these groups involves the design of a microstructure where a Nb-rich phase is surrounded by another phase that is resistant to hydrogen embrittlement [41-44, 47, 70, 71, 73, 76-78, 87, 88, 108]. The hydrogen is reported to permeate through the Nb-rich phase and the other phase acts as a supporting matrix to the Nb-rich phase and restricts the natural lattice expansion when hydrogen is absorbed. The restriction of the expansion in the Nb-rich phase by the supporting matrix is a mechanical way of limiting the amount of hydrogen that can be absorbed in the Nb-rich phase, therefore limiting the hydrogen concentration in the membrane and reducing the likelihood of hydrogen embrittlement. This allows the membranes with a duplex microstructure to have a much higher inlet hydrogen pressure than the ones reported by Yukawa et al. [28, 52, 76-78].

For this project, where the effect of a nanostructural grain refinement on hydrogen permeation is to be investigated, an alloy system of particular interest is the Nb-Ni-Zr alloy system. This alloy system has been reported in Section 2.5 to have a good glass forming

ability and was also reported to have good resistance to hydrogen embrittlement in a crystalline state as shown in Figure 2.8. Since the nano-structural grain refinement is to be obtained by the crystallization from amorphous method, the Nb-Ni-Zr alloy system seems to be ideal. The circles in Figure 2.8 show the alloy compositions that were tested and maintained their structural integrity during hydrogen permeation testing with a hydrogen pressure difference ranging from 0.1 – 0.5 MPa. High hydrogen permeability was also obtained in these crystalline Nb-Ni-Zr alloy membranes. The good resistance to hydrogen embrittlement of the Nb-Ni-Zr alloy membranes in a crystalline state makes this alloy system ideal for the aims of this project. Another promising alloy system with good resistance to hydrogen embrittlement and high hydrogen permeability in a crystalline state is Nb-Ti-Co [110]. Luo et al. have reportedly achieved a hydrogen permeability 2.6 times higher than that of pure Pd in a crystalline Nb₆₀Ti₂₁Co₁₉ alloy membrane [110].

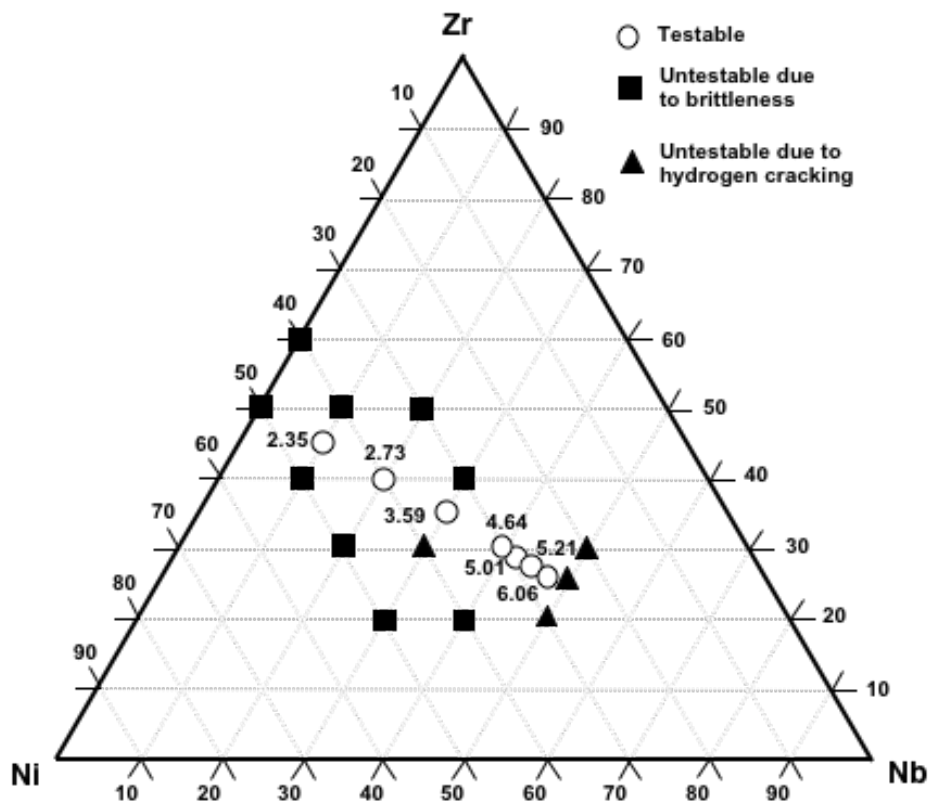


Figure 2.8. Schematic diagram of the Ni-Nb-Zr ternary system showing the compositions of the fully crystalline alloys investigated by Aoki et al. [109] and the associated hydrogen permeability ($\times 10^{-8} \text{ mol. m}^{-1} \cdot \text{s}^{-1} \cdot \text{Pa}^{-0.5}$).

Based on the approach of using a supporting matrix to improve the resistance to hydrogen embrittlement, it has been observed that currently most crystalline alloy systems investigated were ternary or quaternary alloys systems. It would be ideal if a simpler binary alloy system composed of Nb and a secondary phase resistant to hydrogen embrittlement was available to better understand the effect of microstructural changes on the hydrogen permeability and verify models. Cu was identified in Table 2.2 as a potential element for the secondary phase. It is expected that its low hydrogen solubility and permeability will help it maintain its structural integrity during hydrogen permeation. In Section 2.4.3, it was also reported that the alloying of Cu with Group 5A elements led to the membrane surface being less susceptible to gaseous impurities and contamination.

2.7 Mechanical behavior of nanocrystalline alloys

2.7.1 Strength

It is recognized that the yield strength of conventional polycrystalline alloys follows the Hall-Petch relationship:

$$\sigma = \sigma_0 + kd^{1/2} \quad (2.6)$$

where σ is the yield strength, d is the average grain size in diameter, σ_0 the frictionless stress representing the overall resistance of the crystal lattice to dislocation movement and k is a material constant representing the Hall-Petch slope. If this equation is extrapolated to the nanocrystalline alloys, materials with great strength are to be expected. There are experimental observations of nanocrystalline alloys with grain sizes well below 100 nm that follow the Hall-Petch relationship [111, 112].

The strengthening due to grain refinement has been explained by the concept of dislocation pile-ups at grain boundaries [113]. However, the rationale for the continued Hall-Petch type strengthening is still not fully understood as the dislocation sources are not expected to operate within the small nanocrystalline grains and there are no experimental confirmations of dislocation pile-ups in deformed nanocrystalline specimens.

A subject of significant debate has been the experimental evidence of a negative Hall-Petch slope [114, 115]. One of the arguments related to the negative Hall-Petch slope is the one linking the experimental methods used and their influence on the Hall-Petch curve. Sanders et al. argued that even at the low end of the nanocrystalline scale the Hall-Petch relation is roughly obeyed if the yield stress values are collected from hardness measurement or by testing in compression, but that when tested in tension the trend is less well established and a negative Hall-Petch relationship may be observed [112]. Apart from this argument, the variations in yield strength as a function of grain size has been constructed by several authors and three regions have been identified [111, 116]. These three regions can be seen in Figure 2.9, which shows the experimental data of yield stress as a function of the inverse square root of the average grain size in copper samples [116].

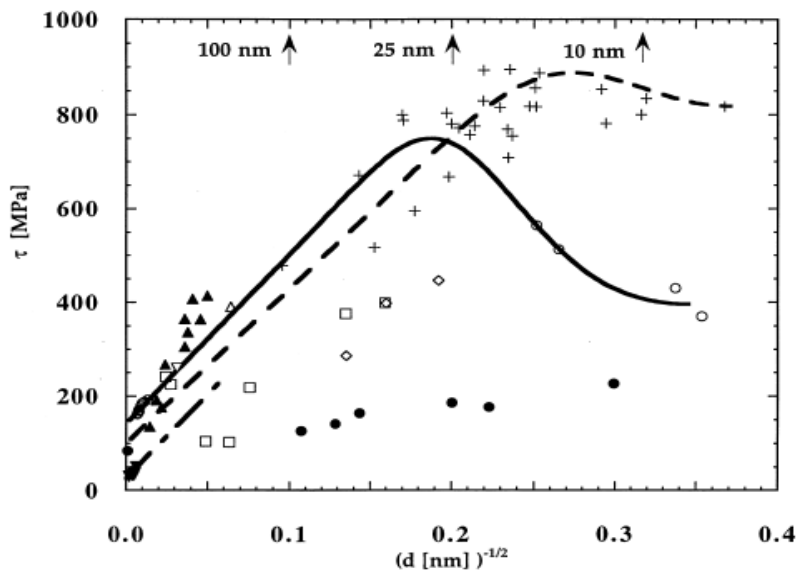


Figure 2.9. The 3 regions of the Hall-Petch relationship observed depending on the grain size [116].

The first region is from the micro-scale to about 100 nm where the strengthening with grain refinement follows the traditional Hall-Petch relationship. The second region still keeps a linear relationship between σ and $d^{1/2}$ and ranges from about 100 to 10 nm. However, the gradient of the slope is lower than that of the microcrystalline region, indicating that the efficacy of the grain boundaries as dislocation barriers may be

decreasing. The last region corresponds to the sub 10 nm grain sizes, where the Hall-Petch relationship is lost. It has been proposed that grain boundary softening may be occurring [111].

Therefore, as seen in Section 2.4.5, the potential benefit of the nanoscale grain refinement does not reside only in increased hydrogen permeability, but may also improve the yield strength. This improvement in yield strength has been reported by several groups [112, 117, and 118]. The theoretical study by Schiotz et al. has predicted that the yield strength in typical polycrystalline metals reaches a maximum when their grain size is reduced to about 10 to 15 nm [118, 119]. Experimental results by Sanders et al. have shown that nanocrystalline Cu and Pd had yield stresses 10-15 times those of coarse-grained annealed samples [112]. The possible implication of an improved strength in the material due to the nanoscale grain refinement would be that membranes could be made into thinner wall thickness. Therefore, potentially leading to an increased hydrogen flux across the membrane.

2.7.2 Ductility

A large number of nanocrystalline alloys have tensile elongations to failure below ~ 10 % according to Koch and sometimes exhibit a brittle behaviour [120]. In some cases the materials fail at low stresses before yielding has time to occur. It is now generally accepted that this type of premature failure is mainly due to processing flaws, such as residual porosity, poor interparticle bonding, impurities, internal stresses or contaminations from H, S, O, etc, or sometimes due to a form of plastic instability, such as shear banding or necking in the early stage of straining [121]. Intrinsically, nanocrystalline alloys appear to be ductile for grain sizes above 15 nm [122].

From a mechanical properties perspective, the reduction in grain size to the nanoscale bears the potential to increase the yield strength of the alloy significantly. Copper with an the average grain size of approximately 100 nm has been shown to be as ductile as to coarse-grained copper, with an elongation greater than 8 % [112].

2.8 Summary and aims

The review of relevant research has highlighted the need to investigate the effect of the microstructure on the hydrogen permeation properties of Nb-based alloy membranes. Currently, there has been much study on amorphous, crystalline and single-phase membranes, but there is a distinct lack of research on nanocrystalline alloy membranes given the potential these membranes have on improving the hydrogen permeability. The potential application and benefits of these Nb-based membranes have been discussed in the literature review. At this time, there has been no study conducted to compare the effect of changing microstructure, i.e. from amorphous to nanocrystalline and to crystalline, in a chemically identical Nb-Ni-Zr or Nb-Ti-Co alloy membrane. A major challenge is to produce nanocrystalline membranes, and the melt-spinning technique is proposed as an effective way to produce amorphous ribbons that will be subsequently annealed at various temperatures to produce nanocrystalline and crystalline membranes. Therefore, one of the main aims in this study is to explore nanocrystalline Nb-based alloy membranes.

The specific aims of my Ph.D. research project are as follows:

- The Nb-Ni-Zr alloy system is to be investigated as it has been reported to have high hydrogen permeability performance in a crystalline state and are known to have good glass forming ability over a broad composition range. Therefore, one of the aims is to investigate the formation of nanocrystalline Nb-Ni-Zr membranes produced by the subsequent crystallization of amorphous ribbons produced by a melt-spinning technique. The formation of nano-structural grain refinement in the Nb-Ti-Co alloy system by the crystallization from amorphous technique is also to be investigated.
- To study the effect of varying microstructure, i.e. from amorphous to nanocrystalline and to conventional crystalline, on the hydrogen permeation properties of a chemically identical Nb-based alloy membrane. This work can potentially deepen the understanding on how the microstructure influences the hydrogen permeation process

and help in the optimisation of the microstructure of the alloy membranes to better suit the hydrogen permeability required.

- To study the effect of annealing in as-cast Nb-Ni-Zr alloy membranes in an attempt to improve their hydrogen permeability. An improvement in hydrogen permeability has been reported in Nb-Ti-Ni-Zr alloy membranes after annealing. The effect of annealing on conventional as cast crystalline Nb-Ni-Zr alloys are yet to be investigated. Given that the Nb-Ni-Zr alloy system has one of the highest hydrogen permeability reported to date, it would be interesting to observe whether annealing help further improve their hydrogen permeability.
- To explore a binary Nb-based hydrogen permeation membrane with good resistance to hydrogen embrittlement. In this case, the Cu-Nb alloy has been identified as a potential candidate due to the low interaction of Cu with H and also due to its immiscibility with Nb.

2.9 References

- [1] *National Hydrogen Study* – a report generated by ACIL Tasman and Parsons Brinckerhoff for the department of Industry, Tourism and Resources, (Commonwealth of Australia, Canberra, 2003)
- [2] S. Sircar and T. C. Golden, *Separation Science and Technology*, 35 (2000) 667.
- [3] *Development of highly efficient membrane reformer system for hydrogen production from natural gas* – a presentation by I. Yasuda from Tokyo Gas at the 17th World Hydrogen Energy conference (Brisbane 2008)
- [4] *Clean Coal_Gasification R&D*, Office of Fossil Energy, U.S. department of Energy, viewed 28 October 2013, <<http://energy.gov/fe/science-innovation/clean-coal-research/gasification>>
- [5] S.Uemiya, T. Matsuda and E. Kikuchi, *Journal of Membrane Science*, 56 (1991) 315
- [6] Kleuiters, S. C. A. *Status review on membrane systems for hydrogen separation*, Energy center of Netherlands; (Petten, The Netherlands, 2004)
- [7] S. Adhikari and S. Fernando, *Industrial and Engineering Chemistry Research*, 45 (2006) 875
- [8] W. J. Koros and G. K. Fleming, *Journal of Membrane Science*, 83 (1993) 1
- [9] N. W. Ockwig and T. M. Nenoff, *Chemical Reviews*, 107 (2007) 4078
- [10] L. J. Wang and F. C. N. Hong, *Applied Surface Science*, 240 (2005) 161
- [11] A. F. Ismail and L. I. B. David, *Journal of Membrane Science*, 193 (2001) 1.
- [12] C. Liang, G. Sha and S. Guo, *Carbon* 37 (1999) 1391
- [13] S. M. Saufi and A. F. Ismail, *Carbon* 42 (2004) 241
- [14] J. E. Koresh and A. Soffer, *Separation Science and Technology*, 22 (1987) 973
- [15] H. Keta, K. Nambu, H. Maeda and K. I. Okamoto, *Advanced Materials for Membrane Separations*, I. Pinnau., (B. D. Eds; ACS Symposium series 876; American Chemical Society, Washington, DC, 2004, pp 203-217)

- [16] A. K. Prabhu, R. Radhakrishnan and S. T. Omayya, *Applied Catalysis A*, 183 (1999) 241
- [17] A. K. Prabhu and S. T. Omayya, *Journal of Membrane Science* 176 (2000) 233
- [18] S. Morooka and K. Kusakabe, *Materials Research Society Bulletin*, 24 (1999) 25
- [19] R. M. de Vos, W. F. Maier and H. Verweij, *Journal of Membrane Science*, 158 (1999) 277
- [20] H. Verweij, *Journal of Materials Science*, 38 (2003) 4677
- [21] T. Masuda, N. Fukumoto, M. Kitamura, S. R. Mukai, K. Hahimoto, T. Tanaka and T. Funabiki, *Microporous Mesoporous Materials*, 48 (2001) 239
- [22] X. Gu, J. H. Dong, T. M. Nenoff and D. E. Ozokwelu, *Journal of Membrane Science*, 280 (2006) 624
- [23] *Hydrogen from Coal Program – Research, Development and Demonstration Plan*; Office of Fossil Energy, U. S. Department of Energy: Washington, DC, September 2007
- [24] J. W. Phair and R. Donelson, *Industrial and Engineering Chemistry Research*, 45 (2006) 5657
- [25] S. Hara, N. Hatakeyama, N. Itoh, H. M. Kimura and A. Inoue, *Journal of Membrane Science*, 211 (2003) 149
- [26] R. Kirchheim, *Solid State Physics*, 59 (2004) 203
- [27] H. Frieske, E. Wicke and Ber. Bunsen-Ges. Physical Chemistry, 77 (1973) 48
- [28] H. Yukawa, M. Morinaga, T. Nambu and Y. Matsumoto, *Materials Science Forum* 654-656 (2010) 2827
- [29] N. Itoh, W. C. Xu, S. Hara, H. M. Kimura and T. Masumoto, *Journal of Membrane Science*, 126 (1997) 41
- [30] N. Itoh, W. C. Xu, S. Hara, H. M. Kimura and T. Masumoto, *Journal of Membrane Science*, 139 (1998) 29
- [31] R. E. Buxbaum and T. L. Marker, *Journal of Membrane Science*, 85 (1993) 29
- [32] R. E. Buxbaum and A.B Kinney, *Industrial and Engineering Chemistry Research*, 35 (1996) 530

- [33] S. N. Paglieri, J. D. Way, *Separation and Purification Methods*, 31 (2002) 1
- [34] K. Lu and J. T. Wei, *Journal of Physics D: Applied Physics*, 25 (1992) 808
- [35] B. S. Liu, H. X. Li, Y. Cao, J. F. Deng, C. Sheng and S. Y. Zhou, *Journal of Membrane Science*, 135 (1997) 33
- [36] H. K. Birnbaum, *Journal of the Less Common Metals*, 104 (1984) 31
- [37] K. S. Rothenberger, B. H. Howard, R. P. Killmeyer, A. V. Cugini, R. M. Enick, F. Bustamante, M. V. Ciocco, B. D. Morreale and R. E. Buxbaum, *Journal of Membrane Science*, 218 (2003) 19
- [38] B. D. Morreale, M. V. Ciocco, R. M. Enick, B. I. Morsi, B. H. Howard, A. V. Cugini and K. S. Rothenberger, *Journal of Membrane Science*, 212 (2003) 87
- [39] K. H. J. Buschow, P.C. P. Bouten and A. R. Miedema, *Reports on Progress in Physics*, 9 (1982) 937
- [40] K. F. Kelton, T. K. Croat, A. K. Gangopadhyay, L. Q. Xing, A. L. Greer, M. Weyland, X. Li and K. Rajan, *Journal of Non-Crystalline Solids*, 317 (2003) 71
- [41] K. Hashi, K. Ishikawa, T. Matsuda and K. Aoki, *Journal of Alloys and Compounds*, 368 (2004) 215
- [42] W. Luo, K. Ishikawa and K. Aoki, *Materials Transactions*, 46 (2005) 2253
- [43] W. Luo, K. Ishikawa and K. Aoki, *Journal of Alloys and Compounds*, 407 (2006) 115
- [44] K. Hashi, K. Ishikawa, T. Matsuda and K. Aoki, *Journal of Alloys Compounds*, 404 (2005) 273
- [45] M. V. Mundschau. *Hydrogen transport membranes*. U. S. Patent 6,899,744. (2005)
- [46] S. E. Roark, R. Mackay and M. V. Mundschau. *Dense layered membranes for hydrogen separation*. U. S. Patent 7,001,446. (2006)
- [47] K. Ishikawa, T. Takano, T. Matsuda and K. Aoki, *Applied Physics Letters*, 87 (2005) 081906
- [48] P. Villars, A. Prince, H. Okamoto, *Handbook of Ternary Alloy Phase Diagrams*; ASM International, Materials Park, OH, 1995

- [49] T. B. Massalski, H. Okamoto, P. R. Subramanian and L. Kacprzak, *Binary Alloy Phase Diagrams*; (ASM International, Materials Park, OH, 1990)
- [50] G. X. Zhang, H. Yukawa, T. Nambu, Y. Matsumoto and M. Morinaga, *International Journal of Hydrogen Energy*, 35 (2010) 1245
- [51] C. Marte and R. Kirchheim, *Scripta Materialia*, Vol. 37 No. 8 (1997) 1171
- [52] H. Yukawa, G. X. Zhang, N. Watanabe, M. Morinaga, T. Nambu and Y. Matsumoto, *Journal of Alloys and Compounds* 476 (2009) 102
- [53] H. Yukawa, T. Nambu and Y. Matsumoto, *Defect and Diffusion Forum*, 297-301 (2010) 1091
- [54] H. Y. Gao, Y. S. Lin, Y. D. Li and B. Q. Zhang, *Industrial and Engineering Chemistry Research*, 43 (2004) 6920
- [55] S. E. Dorris, T. H. Lee and U. Balachandran, *Metal/ceramic composites with high hydrogen permeability*. U. S. Patent 6,569,226.
- [56] M. Amano, M. Komaki and C. Nishimura, *Journal of Less Common Metals*, 172 (1991) 727
- [57] C. Nishimura, M. Komaki, S. Hwang and M. Amano, *Journal of Alloys and Compounds*, 330-332 (2002) 902
- [58] J. Xu, X. K. Sun, Q. Q. Liu and W. X. Chen, *Metallurgical Materials Transactions A*, 25 (1994) 539
- [59] I. V. Shkolnik, T. V. Kulsartov, I. L. Tazhibaeva and V. P. Shestakov, *Fusion Technology*, 34 (1998) 868
- [60] J. Cermak and V. Rothova, *Intermetallics* 9 (2001) 403
- [61] Y. Zhang, T. Ozaki, M. Komaki and N. Nishimura. *Scripta Materialia*. 47 (2002) 601
- [62] C. Nishimura, T. Ozaki, M. Komaki and Y. Zhang, *Journal of Alloys and Compounds*, 356-357 (2003) 295
- [63] T. Ozaki, Y. Zhang, M. Komaki, C. Nishimura, *International Journal of Hydrogen Energy*, 28 (2003) 1229

- [64] T. Takano, K. Ishikawa, T. Matsuda and K. Aoki, *Materials Transactions*, 45 (2004) 3360
- [67] K. Komiya, Y. Shinzato, Y. Yukawa, M. Morinaga and I. Yasudam, *PRICM5: The fifth Pacific Rim International Conference on Advanced Materials and Processing*, 475-479 (2005) 2497
- [68] X. Y. Cheng, Q. Y. Wu and Y. K. Sun, *Journal of Alloys and Compounds*, 389 (2005) 198
- [69] K. Hashi, K. Ishikawa, T. Matsuda and K. Aoki, *Materials Transactions*, 46 (2005) 1026
- [70] K. Aoki, T. Matsuda and K. Ishikawa. '*Multiple phase alloys and metal membranes for hydrogen separation-purification and method for preparing the alloys and the metal membranes*'. U. S. Patent 0,217,480. A1 (2005)
- [71] K. Hashi, K. Ishikawa, T. Matsuda and K. Aoki, *Journal of Alloys and Compounds*, 425 (2006) 284
- [72] T.M. Adams and J. Mickalonis, *Materials Letters*, 61 (2007) 817
- [73] H. Tang, K. Ishikawa and K. Aoki, *Materials Transactions*, 48 (2007) 2454
- [74] T. Nambu, K. Shimizu, Y. Matsumoto, R. Rong, N. Watanabe, H. Yukawa, M. Morinaga and I. Yasuda, *Journal of Alloys and Compounds*, 446–447 (2007) 588
- [75] K. Kishida, Y. Yamaguchi, K. Tanaka, H. Inui, S. Tokui, K. Ishikawa and K. Aoki, *Intermetallics*, 16 (2008) 88
- [76] H. Tang, K. Ishikawa and K. Aoki, *Materials Transactions*, 49 (2008) 2220
- [77] K. Ishikawa, S. Tokui and K. Aoki, *Intermetallics*, 17 (2009) 109
- [78] H. Tang, K. Ishikawa and K. Aoki, *Journal of Membrane Science*, 351 (2010) 65
- [79] A. V. Gapontsev and V. V. Kondrat'ev, *Physics Uspekhi*, 46 (2003) 1077
- [80] S. Hara, S. Sakaki, N. Itoh, H. M. Kimura, K. Asami and A. Inoue, *Journal of Membrane Science*, 164 (2000) 289
- [81] B. S. Liu, W. D. Zhang, W. L. Dai and J. F. Deng, *Journal of Membrane Science*, 244 (2004) 243

- [82] Y. Shimpo, S. I. Yamaura, H. Okouchi, M. Nishida, O. Kajita, H. Kimura and A. Inoue, *Journal of Alloys and Compounds*, 372 (2004) 197
- [83] S. I. Yamaura, Y. Shimpo, H. Okouchi, M. Nishida, O. Kajita and A. Inoue, *Materials Transactions*, 45 (2004) 330
- [84] S. I. Yamaura, M. Sakurai, M. Hasegawa, K. Wakoh, Y. Shimpo, M. Nishida, H. Kimura, E. Matsubara and A. Inoue, *Acta Materialia*, 53 (2005) 3703
- [85] E. A. Evard, N. I. Sidorov and I. E. Gabis, *Technical Physics*, 45 (2000) 377
- [86] E. A. Evard, A. A. Kurdumov, F. N. Berseneva and I. E. Gabis, *International Journal of Hydrogen Energy*, 26 (2001) 457
- [87] D. S. Dos Santos and P. E. V. Miranda, *International Journal of Hydrogen Energy*, Vol. 23 Iss. 11 (1998) 1011
- [88] D. S. Dos Santos and P. E. V. Miranda, *Journal of Materials Science*, 32 (1997) 6311
- [89] D. Zander, H. Leptien, U. Koster, N. Eliaz and D. Eliezer, *Journal of Non-Crystalline Solids*, 252 (1999) 893
- [90] M. D. Dolan, N. C. Dave, A. Y. Ilyushechkin, L. D. Morpeth and K. G. McLennan, *Journal of Membrane Science*, 285 (2006) 30
- [91] H. Gleiter, *Physica Status Solidi B*, 172 (1992) 41
- [92] H. Gleiter, *Progress in Materials Science*, 33 (1989) 223
- [93] K. J. Bryden and J. Y. Ying, *Journal of Membrane Science*, 203 (2002) 29
- [94] K. J. Bryden and J. Y. Ying, *Materials Science and Engineering A*, 204 (1995) 1
- [95] K. J. Bryden and J. Y. Ying, *Nanostructured Materials*, 9 (1997) 485
- [96] D. R. Arantes, X. Y. Huang, C. Marte and R. Kirchheim, *Acta Metallurgica et Materialia*. 41 (1993) 3215
- [97] C. Marte and R. Kirchheim, *Scripta Materialia*, 37 (1997) 1171
- [98] T. Kuji, Y. Matsumura, H. Uchida, and T. Aizawa, *Journal of Alloys and Compounds*, 330 (2002) 718
- [99] K. Yang, M. Z. Cao, *Scripta Metallurgica et Materialia*, 25 (1991) 2139

- [100] Y. J. Kim, W.L. Johnson, A. J. Rulison and W. K. Rhim, *Applied Physics Letters*, 68 (1996) 1057
- [101] H. A. Davies: *Amorphous Metallic Alloys*, Ed. F.E. Luborsky (Butterworths, London 1983) p. 14
- [102] A. Inoue, K. Hashimoto, *Amorphous and nanocrystalline materials* (Springer, Heidelberg 2001)
- [103] H. Kimura, A. Inoue, S.I. Yamaura, K. Sasamori, M. Nishida, Y. Shinpo and H. Okouchi, *Materials. Transactions*, 44 (2003) 1167
- [104] B. A. Kolachev and R. M. Gabidullin, *Material Science*, Vol. 12 No. 5 (1977) 463
- [105] G. V. Karpenko, *Material Science*, Vol. 11 No. 6 (1976) 621
- [106] M. R. Louthan Jr., G. R. Caskey Jr., J. A. Donovan and D. E. Rawl Jr., *Materials Science and Engineering*, 10 (1972) 357
- [107] D. Zander, U. Koster, N. Eliaz and D. Eliezer, *Materials Science and Engineering A*, 294-296 (2000) 112
- [108] T. Wong, K. Suzuki, M. A. Gibson, K. Ishikawa, K. Aoki and L. L. Jones, *Scripta Materialia*, 62 (2010) 582
- [109] K. Aoki, T. Matsuda and K. Ishikawa, *Crystalline dual phase hydrogen-permeation alloy for film, contains eutectic structure containing compound phase comprising cobalt-titanium phase and titanium-niobium phase*, Japan Patent JP2006118035-A, 11th May 2006
- [110] W. Luo, K. Ishikawa, K. Aoki, *International Journal of Hydrogen Energy*, 37 (2012) 12793
- [111] K.S. Kumar, H. Van Swygenhoven and S. Suresh, *Acta Materialia*, 51 (2003) 5743
- [112] P. G. Sanders, J. A. Eastman and J. R. Weertman, *Acta Materialia*, 45 (1997) 4019
- [113] A. W. Thompson, *Acta Metallurgica*, 23 (1975) 1337
- [114] C. A. Schuh, T. G. Nieh and H. Iwasaki, *Acta Materialia*, 51 (2003) 431
- [115] D. H. Jeong, U. Erb, K. T. Aust and G. Palumbo, *Scripta Materialia*, 48 (2003) 1067
- [116] R. A. Masumura, P. M. Hazzledine, and C. S. Pande, *Acta Materialia*, 46 (1998) 4527
- [117] A. Inoue, *Nanostructured Materials*, 6 (1995) 53

- [118] J. Schiøtz, F. D. Di Tolla and K. W. Jacobsen, *Nature*, 391 (1998) 561
- [119] J. Schiøtz, and K. W. Jacobsen, *Science*, 301 (2003) 135
- [120] C. C. Koch, *Scripta Materialia*, 49 (2003) 657
- [121] E. Ma, *Scripta Materialia*, 49 (2003) 663
- [122] F. Ebrahimi, G. R. Bourne, M. S. Kelly and T. E. Matthews, *Nanostructured Materials*, 11 (1999) 343
- [123] K. Ishikawa, S. Watanabe and K. Aoki, *Journal of Alloys and Compounds*, 566 (2013) 68
- [124] S. L. I. Chan and C. I. Chiang, *Journal of Alloys and Compounds*, 253 (1997) 370
- [125] S. Jayalakshmi, V. S. Vasantha, E. Fleury and M. Gupta, *Applied Energy*, 90 (2012) 94
- [126] K. Tsuchimoto, H. Yukawa, T. Nambu, Y. Matsumoto and Y. Murata, *Journal of Alloys and Compounds*, 580 (2013) S391
- [127] H. Yukawa, C. Tsukada, T. Nambu and Y. Matsumoto, *Journal of Alloys and Compounds*, 580 (2013) S386

Chapter 3

Experimental Methodology

3.1 Fabrication of amorphous alloys

Nanocrystalline Nb-Ni-Zr and Nb-Ti-Co hydrogen permeation membrane alloys were fabricated by the primary crystallization of amorphous precursor alloys. The ingots of Nb-Ni-Zr and Nb-Ti-Co were first prepared in an argon arc furnace. The ingots were then crushed and melt-spun into amorphous ribbons. The melt-spun ribbons were punched into a disc shape or mechanically cut into a rectangular shape.

3.1.1 Preparation of ingots: argon arc melting

Samples were prepared to investigate the composition range for the formation of an amorphous phase in melt-spun Nb-Ni-Zr and Nb-Ti-Co alloys. Alloy ingots with nominal compositions of $(\text{Nb}_{90}\text{Zr}_7\text{Ni}_3)_{1-X}(\text{Ni}_{50}\text{Zr}_{50})_X$ ($X = 0.3, 0.4, 0.45, 0.5, 0.55, 0.6, 0.7, 0.8$ and 0.9) and $\text{Nb}_{1-X}(\text{Ti}_{50}\text{Co}_{50})_X$ ($X = 0.55, 0.6, 0.65, 0.7, 0.75$ and 0.8) were prepared in an argon atmosphere by arc melting. Both alloy systems are known to show a high hydrogen permeability and resistance to hydrogen embrittlement in their crystalline form, which has been attributed to their duplex microstructure [1-3]. Figure 3.1 shows an isothermal section of the Nb-Ni-Zr equilibrium phase diagram at 773 K [4]. The chemical compositions of the Nb-Ni-Zr ingots prepared lie on the tie-line between the bcc-Nb and NiZr phases. In a

similar way, the Nb-Ti-Co alloy ingots lie on the tie-line between the bcc-Nb and TiCo phases.

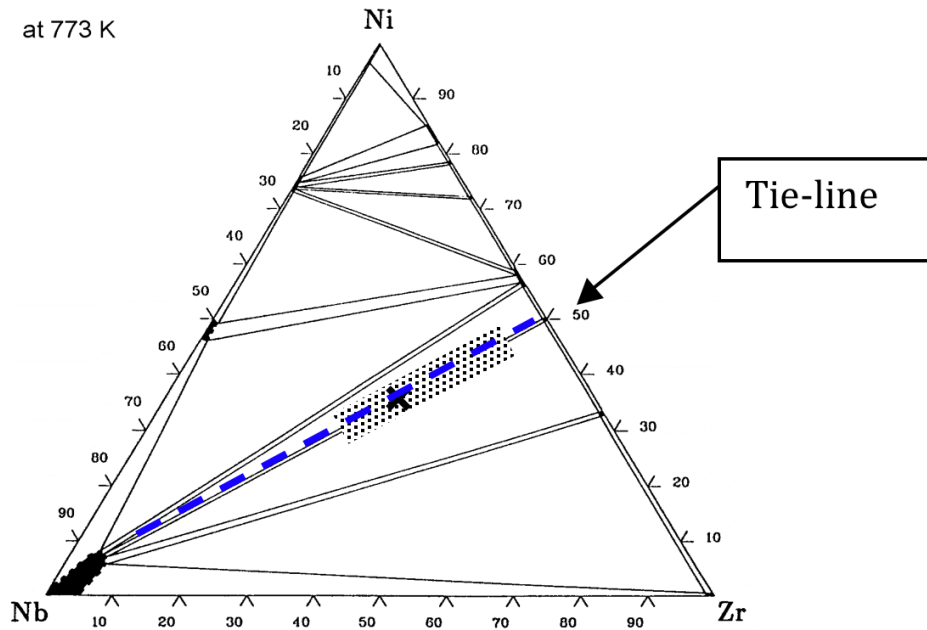


Figure 3.1. Isothermal section of the Nb-Ni-Zr equilibrium phase diagram at 773 K [4].

As starting materials, high purity elemental metals of Nb (> 99.8 wt.%), Ni (> 99.9 wt.%), Ti (> 99.5 wt.%), Co (> 99.5 wt.%) and Zr (> 99.5 wt.%) were used. The mixtures of elements are melted on a water-cooled copper hearth in a controlled argon atmosphere in the presence of a titanium target that was melted prior to alloying to reduce oxygen impurity present. In order to ensure homogeneity, the elemental Nb and Ti were pre-alloyed before alloying with Co and the alloys were turned and remelted several times.

3.1.2 Quenching: single roller method

The ingots were broken into pieces using a hydraulic press so that the alloy can fit into the quartz nozzles used for the melt spinning process. The melt-spun ribbons were produced by a single-roller melt-spinning technique in an argon atmosphere with a cooling rate of 10^6 K/s, as shown schematically in Figure 3.2. The circumferential speed of the copper wheel was set to 30 m/s. Figure 3.3 shows the small handmade quartz crucible where the ingot pieces were placed prior to the melt spinning process. All the narrow ribbons were prepared

at Monash University while the wider ribbons were prepared using a different carbon crucible at the CSIRO Clayton laboratory in Melbourne, Australia.

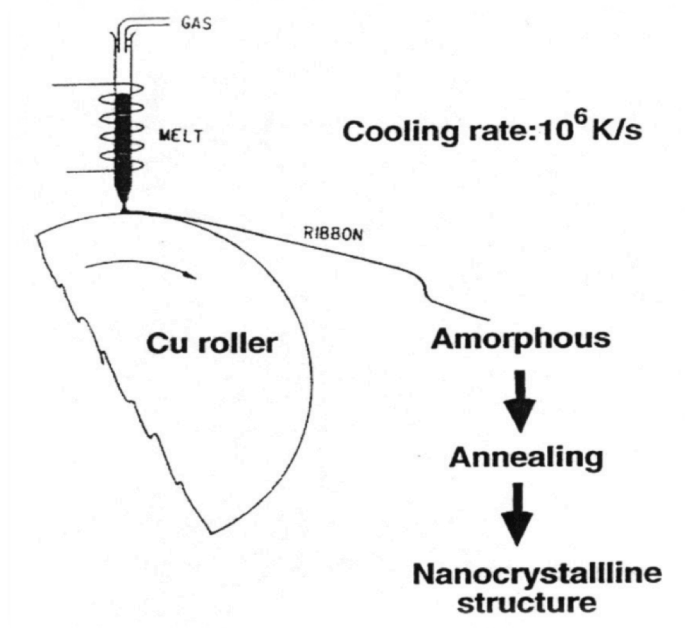


Figure 3.2. Schematic diagram of the melt-spinning process and how to obtain a nanocrystalline structure.

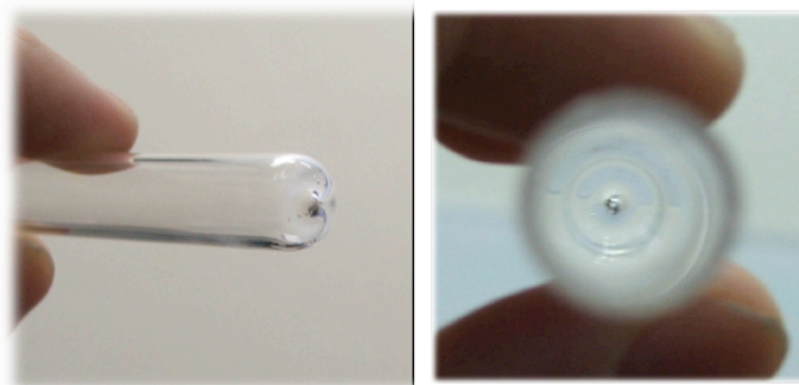


Figure 3.3. Hand made quartz crucibles.

3.2 Annealing

There were a few annealing techniques used to anneal the samples and to determine the crystallization behaviour of the samples.

3.2.1 Estimation of the crystallization temperature: DTA

The crystallization temperatures of the melt-spun amorphous ribbons were estimated by using a differential thermal analyzer (DTA). Figures 3.4 and 3.5 show a schematic of the

sample holder inside the furnace and a picture of the PerkinElmer DTA used respectively. DTA measurements are a standard method of determining thermally activated transformation behaviour of materials. It consists of two cups that are each connected to a thermocouple. One of them is the reference cup and the other the sample cup. The thermocouples in the furnace are connected to a computer that monitors and records the temperature change in each cup. The computer also monitors the temperature inside the furnace through other sensors. The alumina chamber is purged with argon or nitrogen gas during the experiment to reduce the risk of oxidation of the samples. The accuracy of the measurements is affected by the details of heat transfer within the measurement cell and by transformation kinetics.

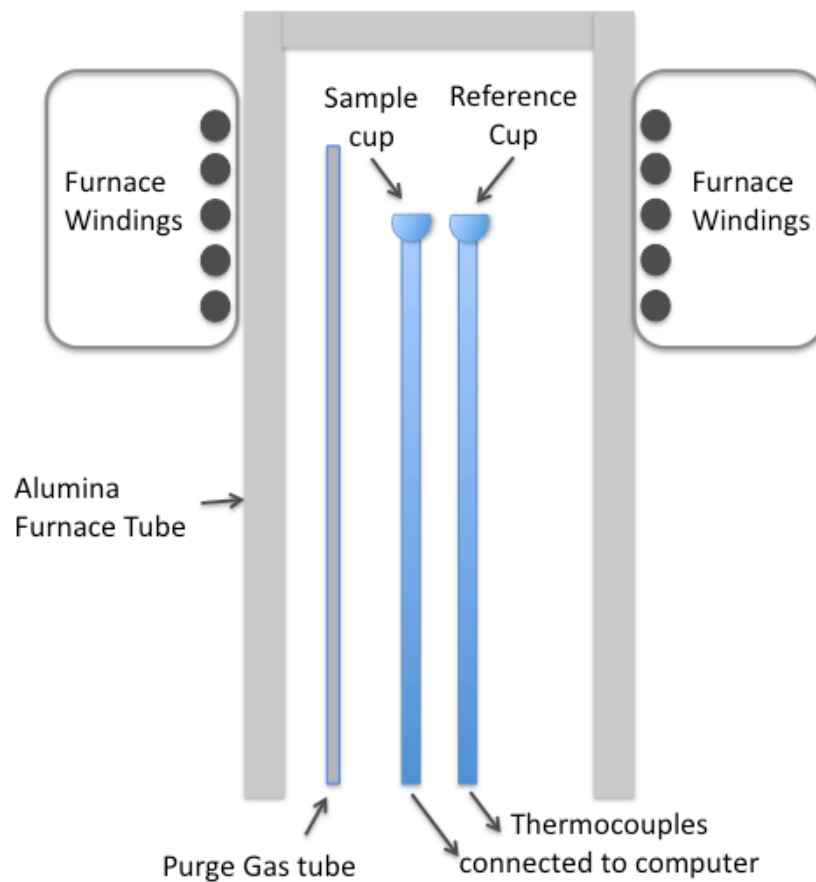


Figure 3.4. Schematic of a DTA furnace.

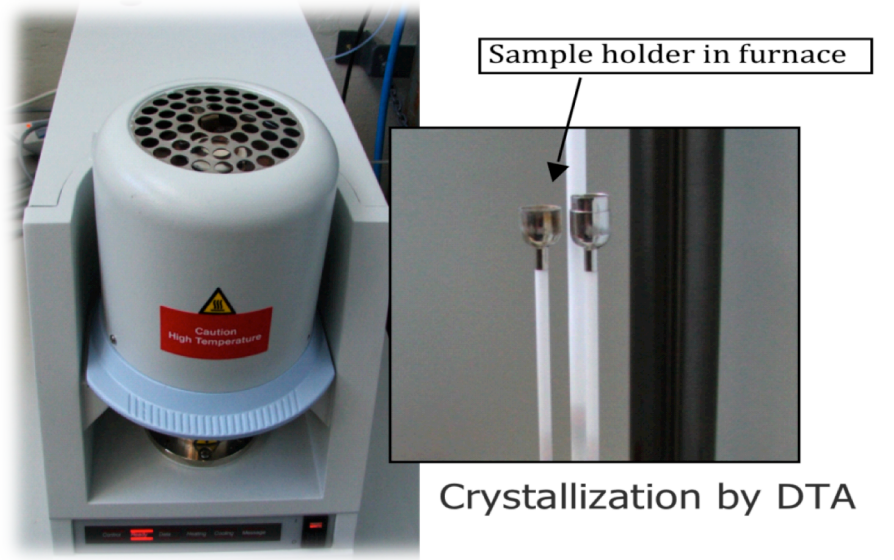


Figure 3.5. Estimation of the crystallization temperature by DTA.

The DTA was calibrated by looking into how the heating rate affects the temperature measurements by measuring the Curie temperature of pure Ni at various heating rates. The Curie temperature of pure Ni as a function of the heating rate is shown in Figure 3.6 and Figure 3.7 shows the programmed heating rate as a function of the actual heating rate.

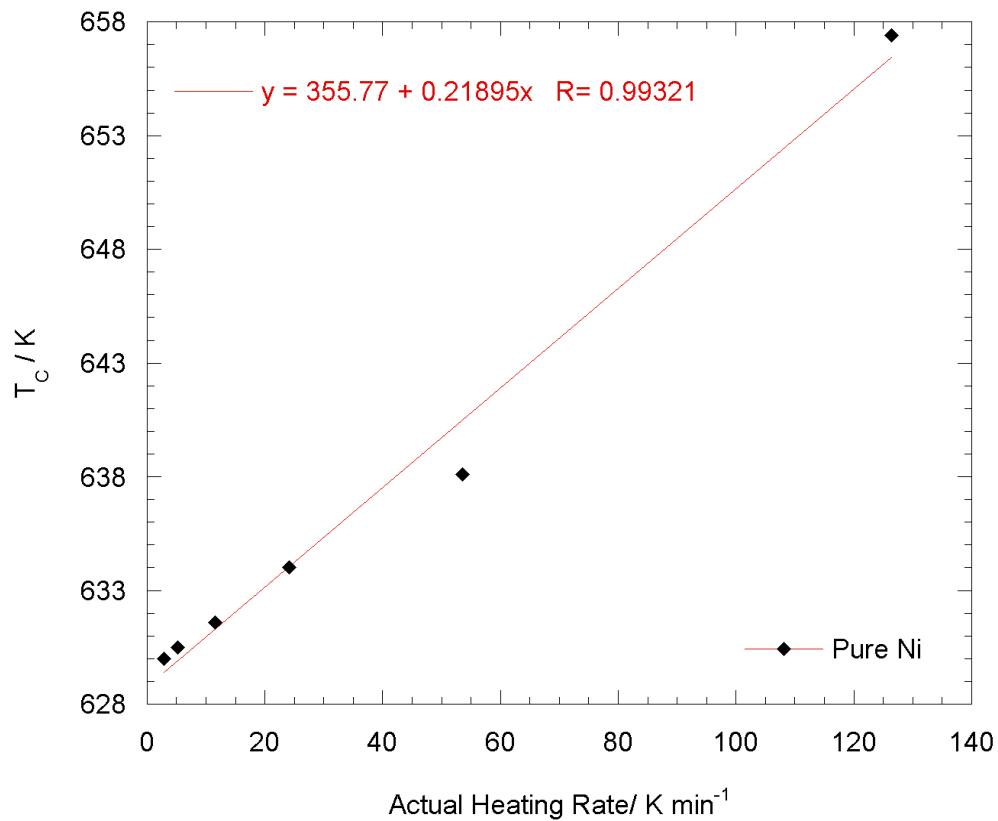


Figure 3.6. Curie temperature of pure Ni at variable heating rates.

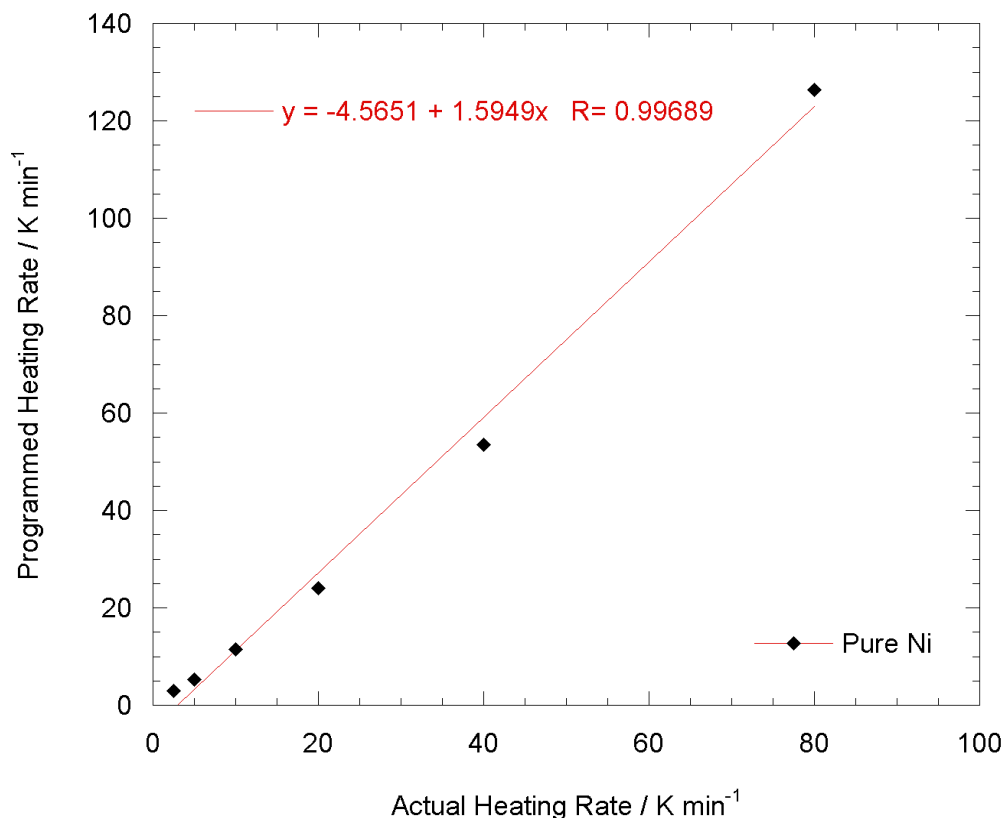


Figure 3.7. A comparison between actual heating rate and programmed heating rate.

To assess whether the DTA was calibrated, the preferred method was to check the melting point of pure Al at a heating rate of 40 K/min and compare it with the calibration data obtained previously. The melting temperature of pure Al at various heating rates is shown in Figures 3.8 and 3.9, and the endothermic reaction that occurs at the melting point of pure Al from which the melting temperature can be determined, respectively. The melt-spun ribbons were cut into small pieces and placed in the sample holder before being heated to a temperature of 1173 K so that the crystallization process could take place. A heating rate of 40 K/min was used and the DTA recorded data at a rate of two points per second.

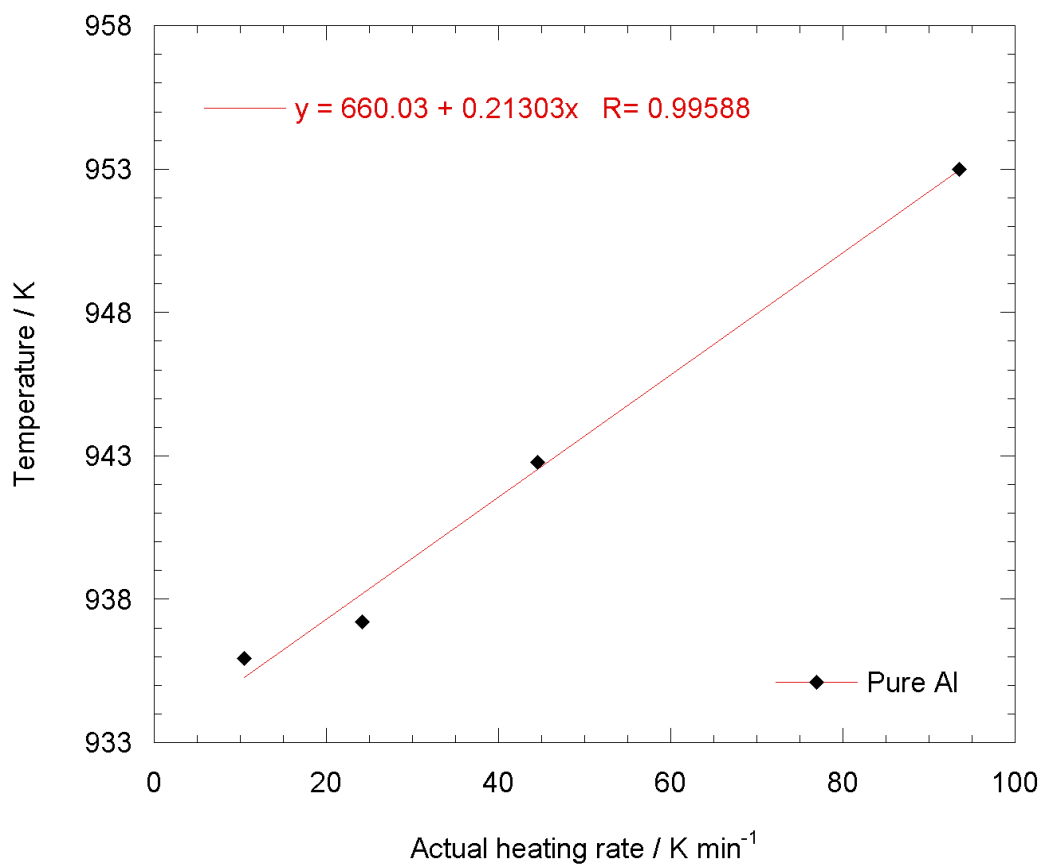


Figure 3.8. Melting temperature of pure Al at variable heating rate.

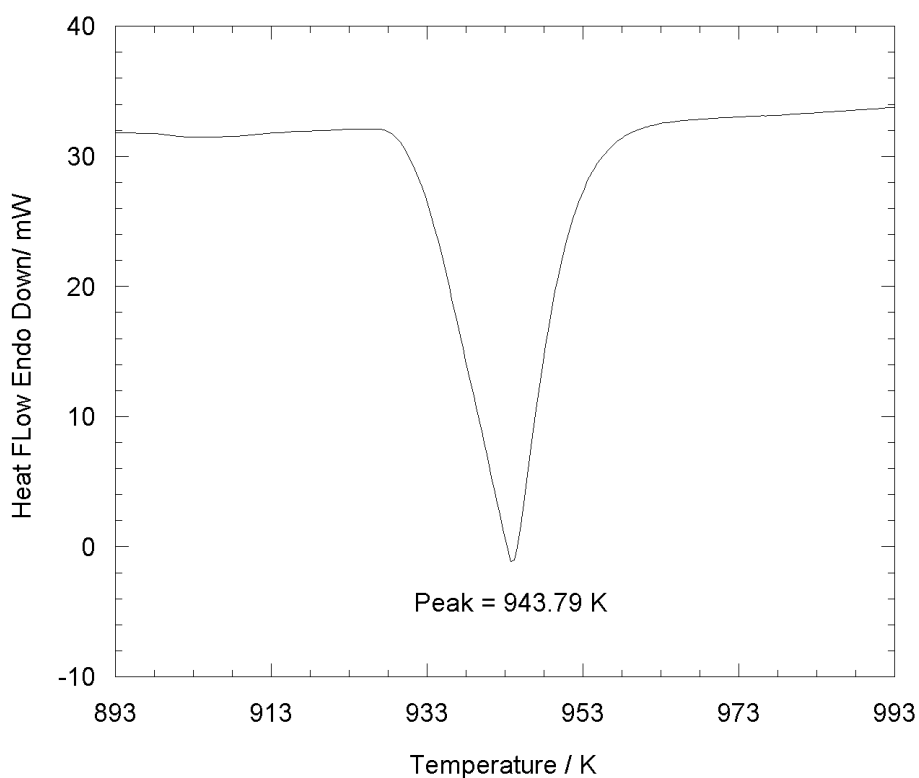


Figure 3.9. An example of a typical DTA curve used to find the melting point of pure Al at a heating rate is 40 K/min.

3.2.2 Annealing: infrared furnace

After the crystallization behaviour of the ribbons has been established, samples were annealed isochronally in an infrared furnace under a vacuum of 1×10^{-5} mbar. This technique was used to obtain ribbons with a microstructure in the nano and micro scale for hydrogen permeation characterization. The samples were annealed at temperatures just above their phase transformations temperatures, observed from the DTA scans, and at a higher temperature. A Ulvac Mila - 3000 infrared furnace was used for the annealing process, the heating rate was 0.5 K/s. Two vacuum pumps were used to achieve the desired vacuum. The rotary pump used was a Leybovac PT 150/4 and the turbo molecular pump used was a Leybold-Heraeus Turbotronik NT 120/150.

3.2.3 Annealing: convection furnace

To investigate the effect of long term annealing on the mechanical properties of the ribbons, the amorphous ribbons were wrapped in small batches of about six to ten in tantalum foil before being vacuum-sealed in quartz tubes. For vacuum-sealing the samples, the quartz tubes were sealed at one end before the samples were inserted. The open end of the quartz tube was then connected to a vacuum system that consists of a rotary pump and a diffusion pump. The tubes were then evacuated until a pressure of 1×10^{-5} mbar was reached. While the tubes were still connected and still under vacuum, an oxy-fuel torch was used to seal and separate the ampoule containing the ribbon samples. These quartz ampoules were then annealed isothermally at temperatures of 923 K, 1073 K, 1123 K, 1173 K, 1223 K and 1273 K in a conventional convection furnace for 60 s, 3.6 ks and 10.8 ks.

3.3 Characterization of microstructure

3.3.1 Sample preparation: grinding and polishing

The melt-spun amorphous ribbons were mechanically cut with scissors in a rectangular shape and lightly sanded prior to carrying out XRD scans. The SEM samples were polished by mechanical grinding using SiC papers of 320 grit for planar grinding, 600 grit, 1000 grit, 1200 grit and 2400 grit in ascending order. To avoid burring and scratching the sample surface, it was important to have a consistent water flow to clear debris away from the surface. The SEM samples were then polished on a soft cloth pad with 0.5 μm α -alumina paste.

3.3.2 Sample preparation: PIPS

The TEM specimens were prepared by using a Gatan 691 precision ion polishing system (PIPS) at room temperature under a vacuum of 1×10^{-3} mbar, using low angles to minimize damage and improve the quality of the specimen. The conditions for PIPS are shown in Table 3.1. The PIPS conditions vary depending on the thickness of the ribbons and the time it took for a hole to appear in the sample. As soon as a hole appeared, the angle of the beam was changed to lower angles at 5 KeV before shifting to angles of 3° and 2° at 3 KeV for the final stage of polishing to obtain a nice finish.

Table 3.1. Standard conditions for sample preparation using PIPS.

Energy of Ion beam (KeV)	Angle of gun from the top	Angle of gun from the bottom	Time (Hour: minute)
5	6°	4°	2:00
5	4°	2°	0:30
3	3°	2°	0:30

3.3.3 Phase identification and degree of crystallinity: XRD

After annealing, the ribbons obtained by melt-spinning were examined by X-ray diffraction (XRD) with Cu-K_α radiation for their degree of crystallinity and identify the phases present. A Philips PW 140/90 XRD machine was used with a 2-theta configuration. The ribbons were cut into small strips that were then secured by double-sided sticky tape to a flat piece of glass for the XRD scans. Care was taken to avoid oxides on the surface of the tested sample by gently sanding and cleaning the surface prior to the XRD scan. The 2θ angle scan range is between 30° and 90° with a scanning speed of 2°/min and a step size of 0.05°. The voltage used was at 40 kV and the current was 25 mA.

3.3.4 Evaluation of grain size: XRD

The XRD is conducted on several specimens, including those that were crystallized from an amorphous phase. To determine the grain size, an isolated peak from the bcc Nb phase was chosen from the scan so as to avoid interference from other phases. The grain size is determined using the same settings as previously used except that the scanning speed was reduced to 0.5°/min and the step size to 0.02 to get a more accurate scan. The slit divergence angle was set to 1°, the slit-receiving angle was set to 0.2° and the slit scatter angle to 1°.

The grain size was calculated from the half width of the maximum of the Nb (211)_{bcc} peak by using Scherrer's equation [2],

$$B = \frac{0.9\lambda}{t \cos \theta} \quad (3.1)$$

where B is the full width of half maximum (FWHM) of the peak at angle $2\theta_B$, t is the grain size and λ is the wavelength of the source. A schematic diagram of where to measure the FWHM of the peak being investigated is shown in Figure 3.10.

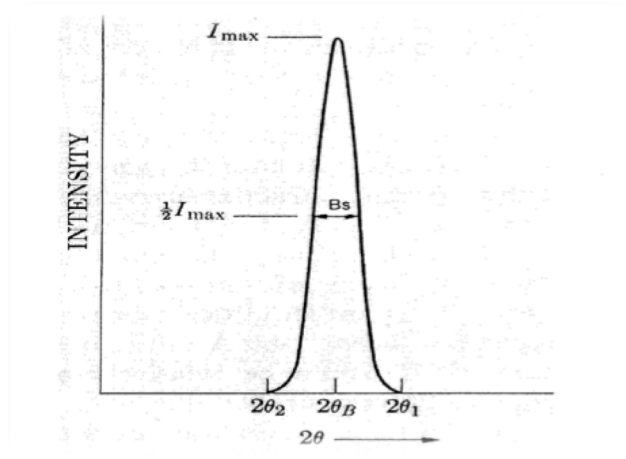


Figure 3.10. Schematic diagram for the measurement of the full width of the half maximum of a reflection peak, B [5].

Prior to measuring the grain size, the optical broadening effect was estimated by using the XRD pattern of a single crystal silicon wafer. According to Equation 3.1 the XRD patterns of the single crystal silicon wafer is supposed to give single line peaks with no broadening effect, however, this is not the case due to optical broadening. This optical broadening effect can be observed in Figure 3.11.

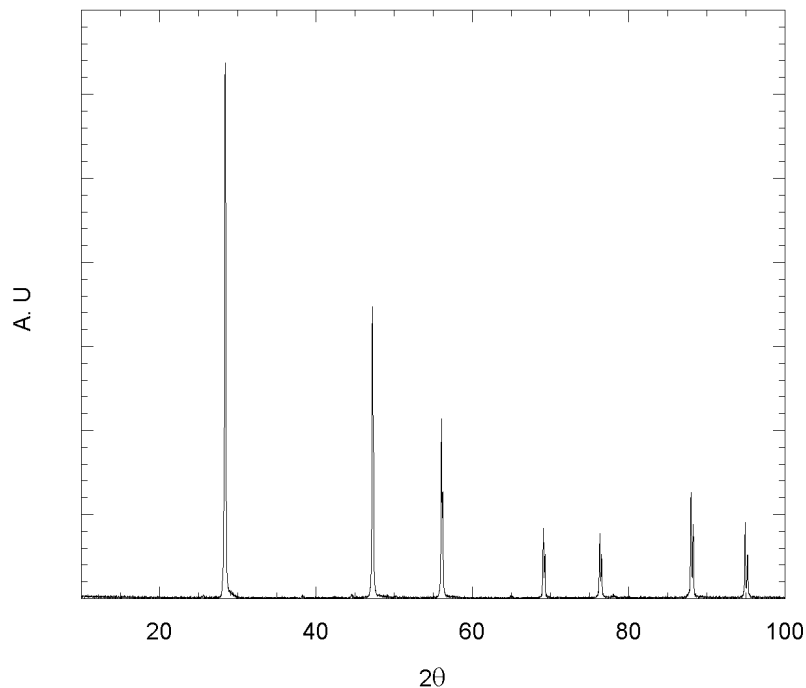


Figure 3.11. XRD pattern of pure Si to be used to determine the extent of the optical broadening effect.

The XRD pattern of the single crystal Si wafer in Figure 3.12 shows that the optical broadening effect increases with increasing 2θ angle. When measuring the grain size, the optical broadening associated with a peak can be subtracted from the experimental values by using the following formula;

$$B = \sqrt{B_{ex}^2 - B_{st}^2} \quad (3.2)$$

where B_{ex} is the FWHM of the experimental peak and B_{st} is the inherent optical broadening effect associated with the set up. B_{st} can be estimated for the peaks being measured based on the calibration data obtained in Figure 3.12.

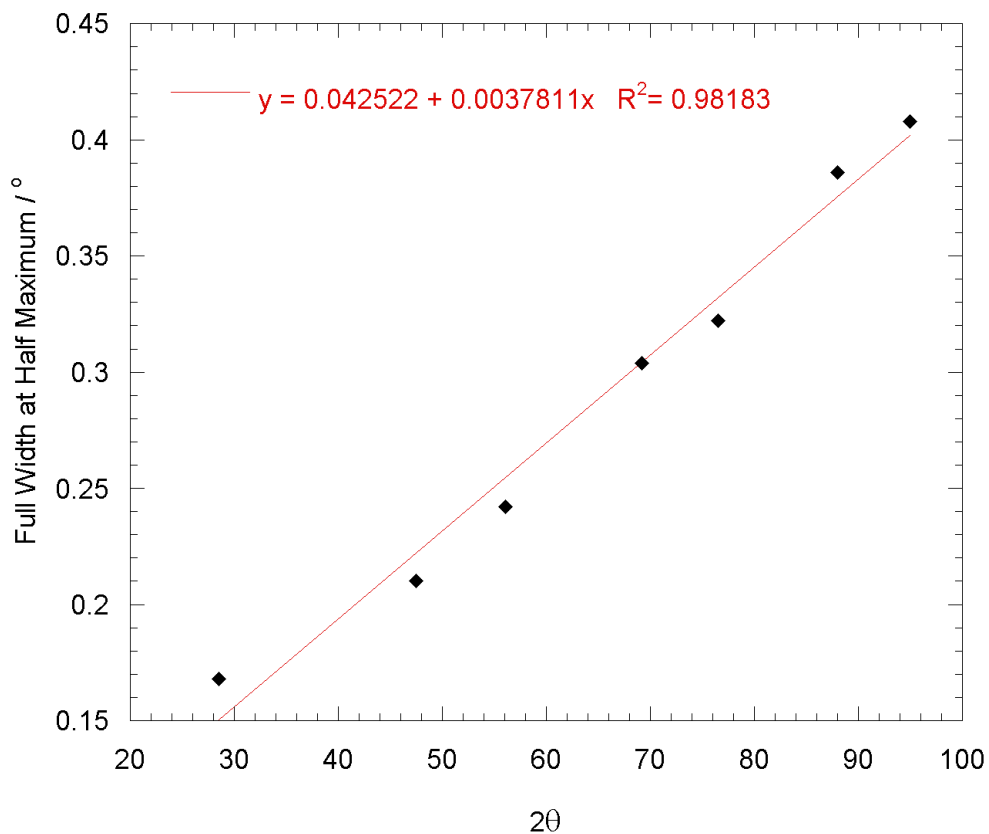


Figure 3.12. Plots of the FWHM peaks of pure Si at angles 2θ . It shows that the optical broadening effect increases with increasing angle 2θ .

3.3.5 Lattice spacing measurements: XRD

The lattice spacing of the crystal is obtained by Bragg's equation shown below

$$n\lambda = 2d \sin \theta \quad (3.3)$$

where λ is the wavelength of the Cu-K α X-ray ($\lambda = 0.15405$ nm), d , is the lattice spacing and θ is the Bragg angle. The lattice parameter, a , can be found by using the following equation;

$$d = \frac{a}{\sqrt{h^2 + k^2 + l^2}} \quad (3.4)$$

where h , k , and l are the miller indices. The hydrogen concentration is estimated from the change in lattice parameter based on the work of Zabel and Peisl [6], who found that the hydrogen concentration varies linearly with the change in lattice parameter. They reported that there was no indication of a deviation from the linear relationship at various concentrations. The hydrogen concentration c can be estimated based on the following equation:

$$\left(\frac{1}{a}\right)\left(\frac{\Delta a}{c}\right) = 0.058 \quad (3.5)$$

where a is the lattice parameter and Δa is the change in lattice parameter.

3.3.6 Characterization of microstructure at the micro scale: SEM

The microstructural observations were carried out using a FEI Phenom scanning electron microscope (SEM) and a JEOL JSM 7001F FEG SEM, which is also equipped for X-ray analysis. The samples were characterized mostly in the backscattered electron mode on the SEM to distinguish the phases present through compositional contrast. It was also operated using the topological mode at 15 kV.

3.3.7 Characterization of microstructure at the nano scale: TEM

The prepared samples were sandwiched in between two copper grids before being mounted on the sample holder and placed in the TEM. The TEMs used were a Philips EM420 and a Philips CM20 TEM. The TEM were operated at 100 kV and 200 kV respectively and images were taken in bright field, dark field and diffraction pattern modes. The centred beam of electrons was used to produce the bright field images while the dark field images were produced by an off-centred beam.

From the diffraction pattern obtained, the following formulas were used to find the interplanar spacing and therefore identify the phases present.

$$d_{hkl} = \frac{a}{\sqrt{(h^2 + k^2 + l^2)}} \quad (3.6)$$

$$d_{hkl} = \frac{\lambda L}{R_{hkl}} \quad (3.7)$$

where d_{hkl} is the interplanar spacing of a ring that represents a set of crystalline planes (hkl), λ is the wavelength of the electron and is estimated to be 0.037° , L is the camera length used and in the present case is 472 mm, R_{hkl} is the radius of each ring, in mm, from which one can deduce the interplanar spacing of the set of planes (d_{hkl}) and a is the lattice parameter of the phase (e.g. the a of bcc Nb is 3.307 \AA). The grain size was also measured from the bright and dark field, where appropriate. The grain size measured is an average of at least 50 grains measured along the horizontal and vertical axis.

3.4 Characterization of ductility

The ductility of the Nb-based alloy foils was measured by a micrometer bend test that is standard practice for measuring the ductility in electrodeposits. This ASTM international standard is issued under the fixed designation B 490-92 [7]. This test consisted of measuring the bend of a foil held between the jaws of a micrometer. These were closed until fracture or cracks appear. In an attempt to provide a more replicable condition for the test, such as a more constant strain rate, an Instron apparatus was used instead of a micrometer. The thickness of the foil was measured with a micrometer at the point of bending. The sample was then bent in a ‘U’ shape with the side of the foil that was in contact with the copper wheel during melt-spinning facing inwards in the ‘U’. The bent foil was then placed between then jaws. The jaws were then gradually closed until the foils cracked. The ductility could then be estimated by using the following formulas,

$$Ductility, percentage = \frac{100T}{(2R - T)} \quad (3.8)$$

The maximum value is 100%

$$Ductility, ratio = \frac{T}{2R} \quad (3.9)$$

The maximum value is 0.5

where $2R$ is the recorded micrometer reading and T the thickness of the foil. A minimum of three samples were tested and the average taken.

3.5 Sample preparation of Cu-Nb alloys

3.5.1 Consumable arc casting

The alloy preparation of the cast Nb-Cu alloys, which were investigated at a later stage of the project, was done in collaboration with the Materials Preparation Center of Ames Laboratory USDOE at the University of Iowa (U.S.). The samples were provided by Dr. L.

L. Jones and the Distinguished Emeritus Professor J. D. Verhoeven. Due to the immiscible nature of Nb and Cu, it was not possible to manufacture the ingots by the conventional arc melting technique at Monash University. The ingots were produced by using the consumable arc casting technique. While plasma melting by Stark has been demonstrated, the resulting ingot had inferior homogeneity when compared to consumable arc casting processed alloys [8].

The main differences with the conventional arc melting technique are that the consumable arc casting technique consumes the electrode, which is made of Nb and Cu, and uses a double melt process that enhances homogeneity. The electrode rods are prepared from an oxygen free high conductivity (OFHC) copper rod stock before the niobium is fixed in place in the milled slots. The electrode is then loaded in a vertical position in the melting apparatus as shown in the schematic diagram of the consumable arc casting furnace in Figure 3.13. The whole chamber is placed under high vacuum before being backfilled with argon. The process of evacuation and backfilling with argon is repeated several times to ensure low oxygen contamination. Prior to casting, the chamber is backfilled with argon. The arc casting is started by striking the electrode against copper turnings at the bottom of the copper mold. The high amperage arc is established and maintained by lowering the electrode in the copper mold. This melting condition is maintained until the electrode is consumed and the melt terminated. The ingot obtained is then sealed by electron beam welding in an OFHC copper extrusion can and extruded at 923-1023 K. The extruded rod is then used as an electrode for a second melt, which performed in the same way as the first one. This technique allows for enhanced ingot homogeneity of niobium and copper binary alloys. More details of the preparation technique have been given elsewhere [8].

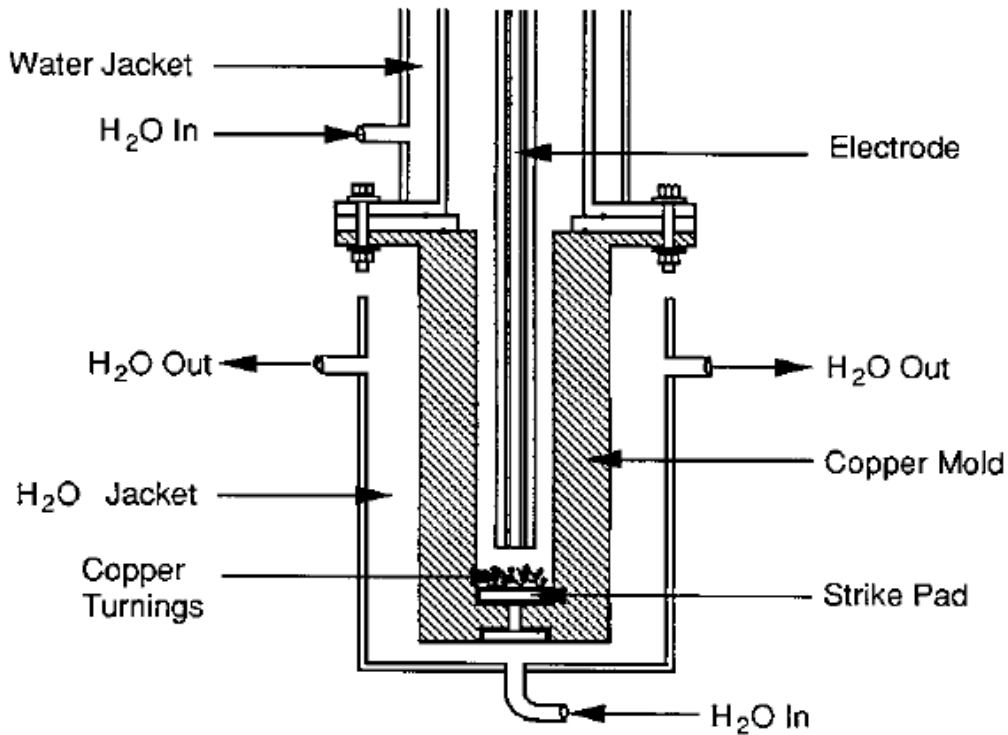


Figure 3.13. Schematic of the consumable electrode arc casting furnace [8].

3.5.2 Cold drawing of multifilamentary Cu-Nb alloys

The Cu/Nb/Cu multifilamentary wires are produced by SPD via the ADB process. The alloy preparation of the Cu/Nb/Cu multifilamentary alloys investigated was done in collaboration with the University of Poitiers and CNRS of France. The initial billet is composed of an OFHC copper jacket containing a core consisting of a Cu rod inserted in a Nb tube. This billet is hot extruded after annealing and cold drawn to a hexagonal shape. To obtain finer microstructure, the hexagonal composite wire is cut into 85 segments and bundled into a can of OFHC Cu and reduced as in the first stage. The series of hot-extrusion/cold drawing/bundling of 85 Cu/Nb/Cu tubes are repeated 3 times to obtain Cu-Nb alloys containing $N = 85^3$ Nb nanotubes filled with Cu filaments [9].

3.6 References

- [1] K. Ishikawa, T. Takano, T. Matsuda and K. Aoki, *Applied Physics Letters*, 87 (2005) 081906
- [2] W. Luo, K. Ishikawa, and K. Aoki, *International Journal of Hydrogen Energy* 37 (2012) 12793
- [3] K. Hashi, K. Ishikawa, T. Matsuda, and K. Aoki, *Journal of Alloys and Compounds*, 425 (2006) 284
- [4] *Handbook of Ternary Alloy phase diagrams*, edited by P. Villars, A. Princes and H. Okamoto (ASM International, Materials Park, 1997)
- [5] B. D. Cullity, *Elements of X-ray Diffraction*, (Addison-Wesley publishing company, United States, 1972)
- [6] H. Zabel and J. Peisl, *Journal of Physics F: Metal Physics*, Vol. 9 No. 7 (1979) 1461
- [7] *Standard Practice for Micrometer Bend Test for Ductility of Electrodeposits*, ASTM standard, B 490-92 (Reapproved 2003)
- [8] L. L. Jones, F. A. Schmidt, and J. D. Verhoeven, '*Consumable Electrode Arc Casting Of Copper-Refractory Metal Composites in 'Refractory Metals'*', edited by D. Sadoway (The Minerals, Metals & Materials Society, Warrendale, Pa., 1991)
- [9] V. Vidal, L. Thilly, F. Lecouturier, P. O. Renault, *Scripta Materialia* 57 (2007) 245

Chapter 4

Formation of Nanostructured Hydrogen Permeation Membranes

4.1 Introduction

At the present time, Pd based alloys are the main material used for metallic alloy membrane separation technology. However, Pd-based alloys are not viable economically due to their high material cost [1]. Therefore, the development of an economically viable membrane for hydrogen separation is important to realize efficient hydrogen energy cycles. Two families of metallic membranes known so far are amorphous and crystalline alloy membranes. Much work has been done on ways to improve the hydrogen permeability of crystalline Nb-based alloy membranes through the control of microstructure and its optimization [2-9]. The crystalline membranes have shown good hydrogen permeation, however, the manufacturing method used is less suitable for mass production due to the time required for making the membranes and the limitations associated with the thickness into which the membranes can be cut. The relatively thick membranes are not as favourable for the permeation of hydrogen. On the other hand amorphous Nb-based alloys produced by melt-spinning have shown promise, even if their hydrogen permeability is lower compared to that of their crystalline counterparts. The melt-spinning technique results in very thin membranes that

CHAPTER 4. FORMATION OF NANOSTRUCTURED HYDROGEN PERMEATION MEMBRANES

can be mass-produced. However, since amorphous alloys are in a non-equilibrium state, their long term stability in a contaminated hydrogen atmosphere at high temperature is yet to be proven and this aspect needs to be looked into further [10-13]. Combined with the fact that the hydrogen diffusivities of amorphous membranes are also often lower than crystalline membranes, the focus has shifted to redesigning crystalline alloys for hydrogen separation. A possible way of improving the hydrogen permeation is to reduce the grain size to the nanoscale since the diffusivity of hydrogen could be enhanced dramatically by grain refinement [14, 15].

The main aim of this chapter is to identify a suitable alloy system to produce nanocrystalline hydrogen permeation membranes through the process of amorphization and subsequent annealing. The advantage of a nanostructure is that the hydrogen permeability may be greatly improved, as these properties are highly microstructure sensitive [14, 15]. The melt-spinning technique through which the nanostructure is to be produced has another potential benefit, as the ribbons produced will be about 30 μm in thickness, which is beneficial to the hydrogen flux performance of the membrane. In light of the different advantages mentioned above, nanoscale grain refinement has the potential to make the Nb-based hydrogen permeation membrane a viable and efficient option for the purification of hydrogen.

4.2 Results

The details of the experimental techniques used in this chapter are given in Chapter 3. The results section will look into the formation of amorphous Nb-Ni-Zr and Nb-Ti-Co alloys and investigate their crystallization behaviour upon annealing, with particular attention to the formation of a nanocrystalline structure.

4.2.1 Formation of amorphous alloys

4.2.1.1 Nb-Ni-Zr alloys

The XRD traces from the Nb-Ni-Zr alloys of various compositions produced by melt-spinning in an as-quenched state are shown in Figure 4.1. The XRD traces for $(\text{Nb}_{90}\text{Zr}_{7}\text{Ni}_3)_{1-X}(\text{Ni}_{50}\text{Zr}_{50})_X$ alloy composition where $X > 0.5$ show a main broad maximum around 39° and a second faint broad maximum around 66° , which are characteristic of an amorphous alloy. The samples where $X = 0.3 - 0.5$ show broad Bragg peaks of the bcc-Nb phase. In addition to the bcc-Nb phase, broad Bragg peaks of NiZr and $\text{Ni}_{11}\text{Zr}_9$ phases are also identified at the base of the Nb (110) peak in the XRD trace of the sample with the composition where $X = 0.45$.

The ductility of a hydrogen permeation membrane is of prime significance as the membrane is exposed to a pressure difference when operated. Hence, the ductility of the melt-spun ribbons was investigated by the micrometer bend test (ASTM B490-492) described in Chapter 3. The melt-spun ribbons were considered ductile only when the ductility ratio, calculated from the experiment, achieved the maximum value of 0.5. Figure 4.2 shows the Nb-Ni-Zr ternary phase diagram. The area highlighted in red denotes the composition range that resulted in ductile amorphous melt-spun ribbons and the compositions highlighted in black resulted in brittle crystalline melt-spun ribbons.

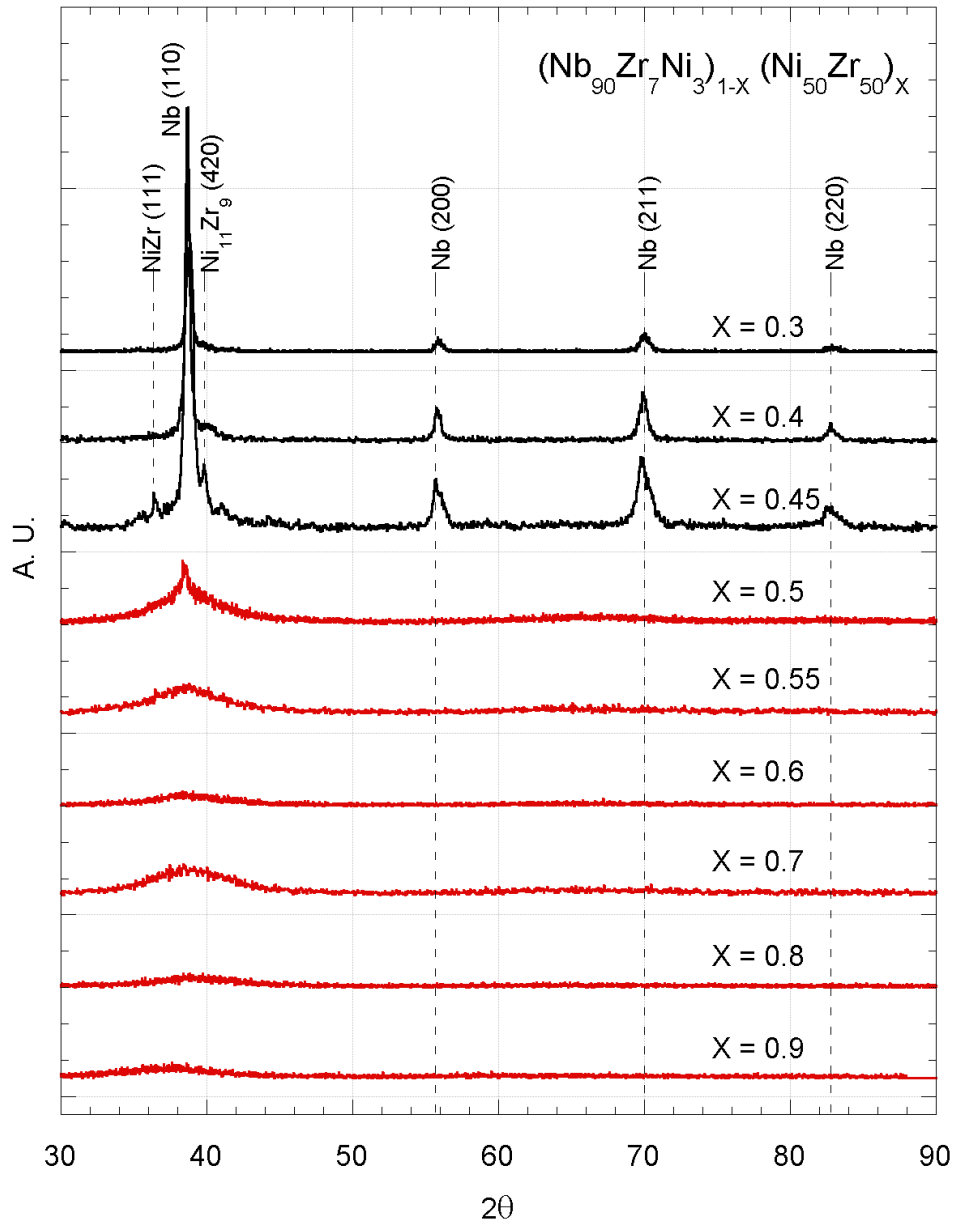


Figure 4.1. X-ray diffraction traces of as-quenched $(\text{Nb}_{90}\text{Zr}_7\text{Ni}_3)_{1-x}(\text{Ni}_{50}\text{Zr}_{50})_x$ alloys of various compositions produced by melt spinning, where $X = 0.3 - 0.9$. The red XRD traces represent ductile ribbons and those in black represent brittle ribbons.

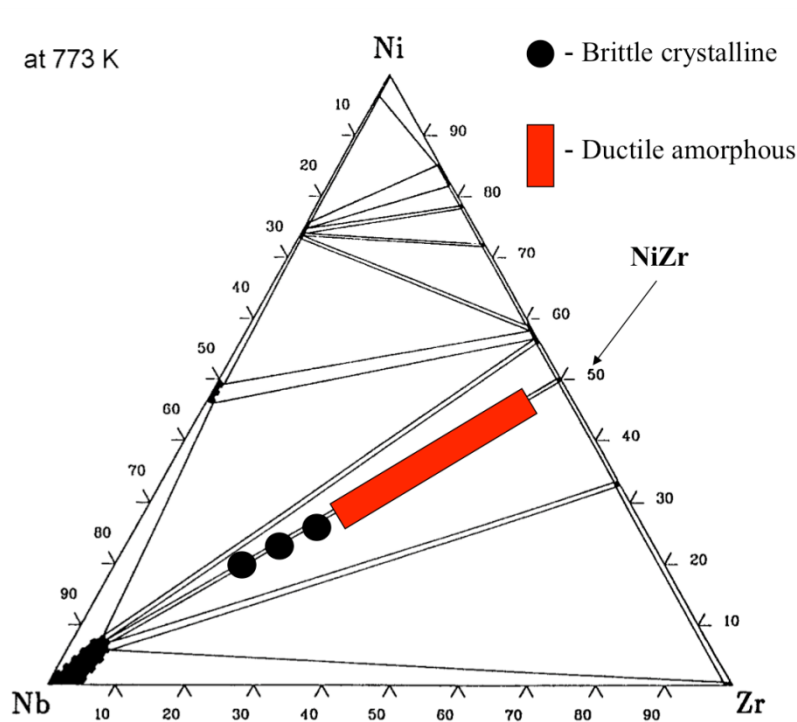


Figure 4.2. Ternary phase diagram of Nb-Ni-Zr alloys showing the composition dependence of amorphous melt-spun ribbons [8]. The area highlighted in red denotes the composition range that resulted in ductile amorphous melt-spun ribbons. The compositions highlighted in black resulted in brittle crystalline melt-spun ribbons.

Figure 4.3 shows the images of as-quenched $\text{Nb}_{20}\text{Ni}_{40}\text{Zr}_{40}$, $\text{Nb}_{35}\text{Ni}_{32.5}\text{Zr}_{32.5}$ and $\text{Nb}_{50}\text{Ni}_{25}\text{Zr}_{25}$ wide ribbons prepared using a single roller melt spinner in an argon atmosphere. The $\text{Nb}_{20}\text{Ni}_{40}\text{Zr}_{40}$ ribbon was successfully prepared without cracks and voids. The ribbons were about 23 – 28 mm wide and 30 – 40 μm thick. The ribbon samples of $\text{Nb}_{20}\text{Ni}_{40}\text{Zr}_{40}$ and $\text{Nb}_{35}\text{Ni}_{32.5}\text{Zr}_{32.5}$ had sufficient ductility and flexibility at room temperature. However, there were some cracks and voids present in the $\text{Nb}_{50}\text{Ni}_{25}\text{Zr}_{25}$ ribbons, which made them unsuitable for the hydrogen permeation test.

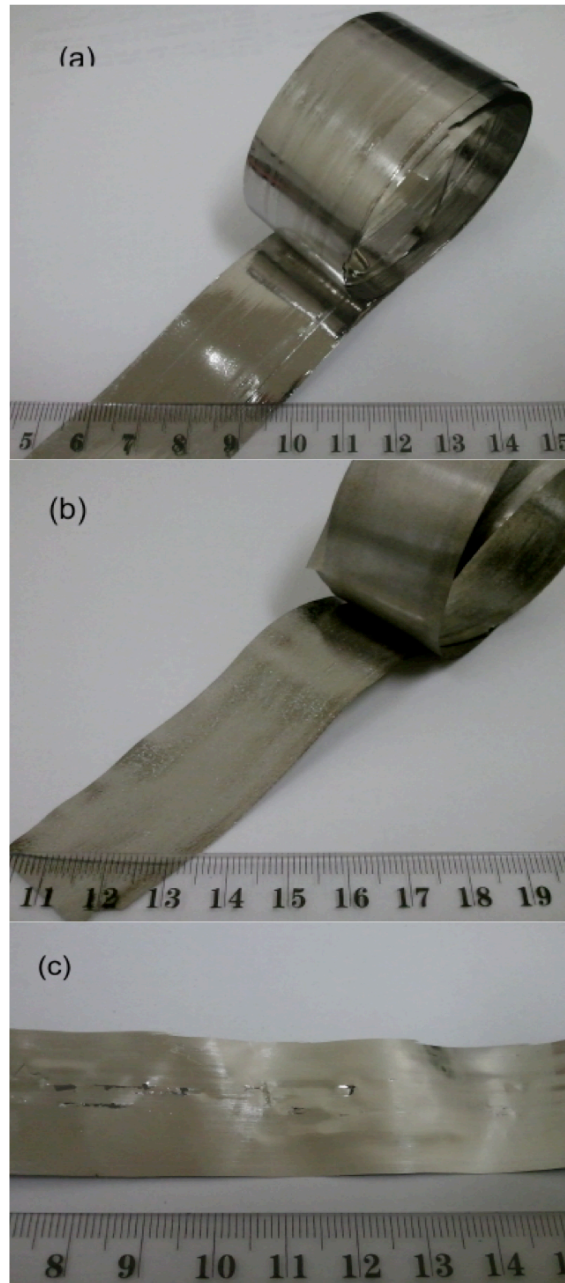


Figure 4.3. Images of as-quenched (a) $\text{Nb}_{20}\text{Ni}_{40}\text{Zr}_{40}$, (b) $\text{Nb}_{35}\text{Ni}_{32.5}\text{Zr}_{32.5}$ and (c) $\text{Nb}_{50}\text{Ni}_{25}\text{Zr}_{25}$ wide ribbons prepared using a single roller melt spinner in an argon atmosphere.

4.2.1.2 Nb-Ti-Co alloys

The isothermal section of the Nb-Ti-Co phase diagram at 1173 K is shown in Figure 4.4 [19]. The orange line denotes the tie line along which the compositions in the present study were chosen. The melt-spinning of the Nb-Ti-Co alloys proved to be more challenging than

those of the Nb-Ni-Zr alloys. The eutectic $\text{Nb}_{30}\text{Ti}_{35}\text{Co}_{35}$ alloy, shown as a red dot, produced the only amorphous and ductile ribbon from the Nb-Ti-Co system under the processing conditions investigated. The $\text{Nb}_{35}\text{Ti}_{32.5}\text{Co}_{32.5}$ and $\text{Nb}_{25}\text{Ti}_{37.5}\text{Co}_{37.5}$ alloys, shown as blue triangles, yielded ribbons but were found to be crystalline and brittle. The other Nb-Ti-Co alloy compositions, shown as green squares, did not yield any ribbon upon melt-spinning but rather a flaky residue. To be able to test for hydrogen permeation, wide ribbons of $\text{Nb}_{30}\text{Ti}_{35}\text{Co}_{35}$ were melt-spun. However, no ribbons were obtained, indicating the level of difficulty in the production of amorphous wide ribbons from this system. Subsequently, Zr was added to the $\text{Nb}_{30}\text{Ti}_{35}\text{Co}_{35}$ alloy in an attempt to improve the GFA, based on the criteria required for a high GFA summarized in Section 2.5.

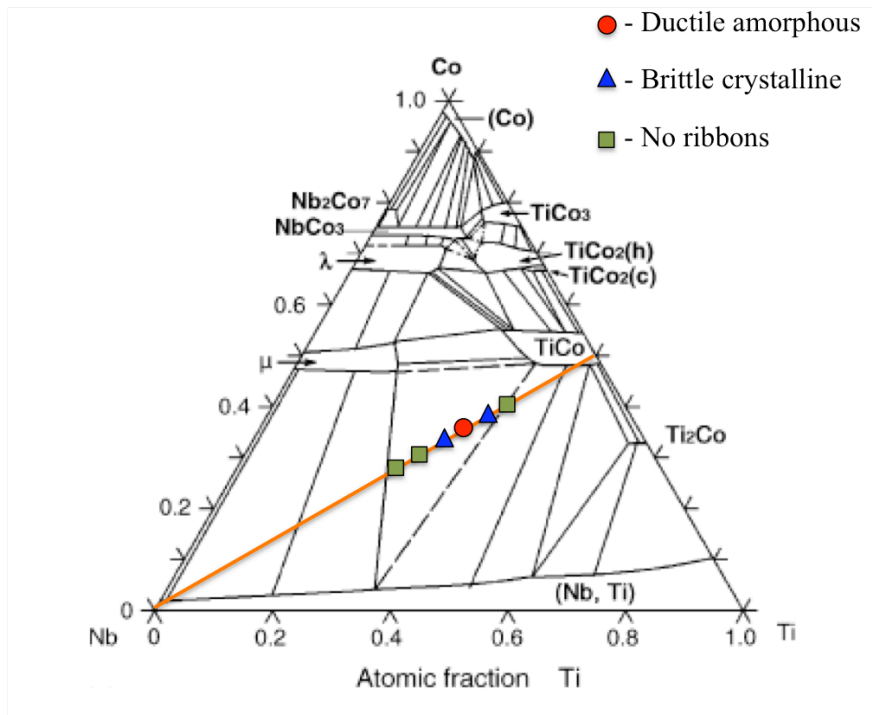


Figure 4.4. Isothermal section of Nb-Ti-Co system at 1173 K [19]. The green squares denote the compositions that did not yield any melt-spun ribbons. The blue triangles correspond to the compositions that resulted in brittle crystalline melt-spun ribbons and the red dot shows the composition at which an amorphous melt-spun ribbon was obtained.

The addition of Zr showed promising improvements to the GFA of the Nb-Ti-Co system and yielded amorphous ribbons, as shown in Figure 4.5, which shows the XRD traces of the $\text{Nb}_{30}\text{Ti}_{35}\text{Co}_{30}\text{Zr}_5$, $\text{Nb}_{30}\text{Ti}_{35}\text{Co}_{25}\text{Zr}_{10}$, and $\text{Nb}_{30}\text{Ti}_{35}\text{Co}_{15}\text{Zr}_{15}$ ribbons in an as-

quenched state. All three XRD traces show a main broad maximum around 40° and a second faint broad maximum around 70° , which are characteristic of amorphous alloys. Therefore it can be concluded that all three Nb-Ti-Co-Zr alloys resulted in amorphous ribbons. However, even though the addition of Zr helped to form amorphous ribbons, the ductility was reduced and the ribbons were found to be very brittle. Therefore, due to the manufacturing challenges in the Nb-Ti-Co and Nb-Ti-Co-Zr alloy systems by melt-spinning, further testing of their hydrogen permeation properties were not carried out.

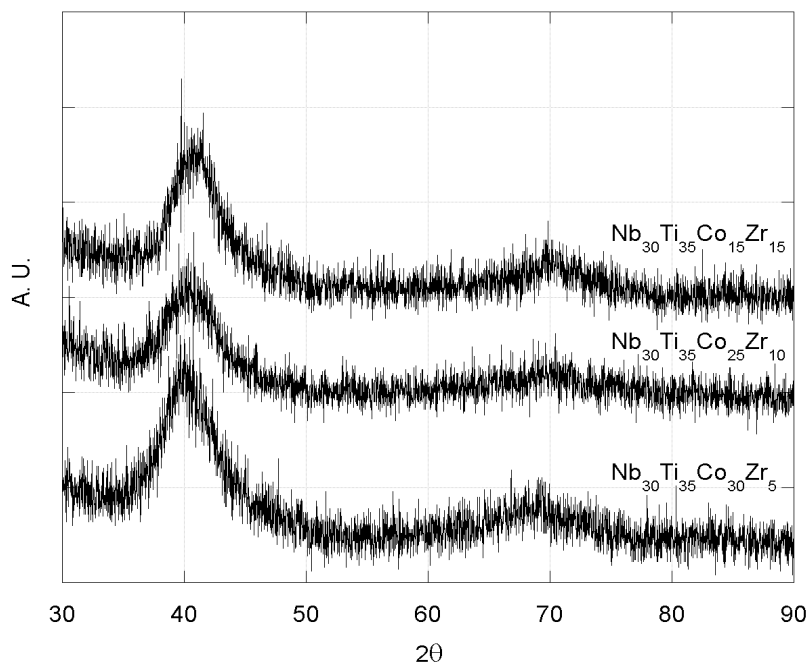


Figure 4.5. X-ray diffraction traces of $\text{Nb}_{30}\text{Ti}_{35}\text{Co}_{30}\text{Zr}_5$, $\text{Nb}_{30}\text{Ti}_{35}\text{Co}_{25}\text{Zr}_{10}$ and $\text{Nb}_{30}\text{Ti}_{35}\text{Co}_{15}\text{Zr}_{15}$ in the as-quenched state.

4.2.2 Decomposition of as-spun amorphous alloys

4.2.2.1 Nb-Ni-Zr alloys

Figure 4.6 shows the DTA curves of as-quenched amorphous $(\text{Nb}_{90}\text{Zr}_7\text{Ni}_3)_{1-x}(\text{Ni}_{50}\text{Zr}_{50})_x$ ribbons of various compositions ($X = 0.55 - 0.9$) that were acquired at a heating rate of 40 K/min. The crystallization behaviour of the ribbons was found to be composition dependent. The Nb-Ni-Zr alloys with a higher Nb content, shown in red (where $X = 0.5 - 0.7$) and

identified as ‘Type I’, show two exothermic peaks between 800 and 930 K, while those with lower Nb content, shown in black (where $X = 0.8 - 0.9$) and identified as ‘Type II’, show one sharp exothermic peak between 830 and 880 K.

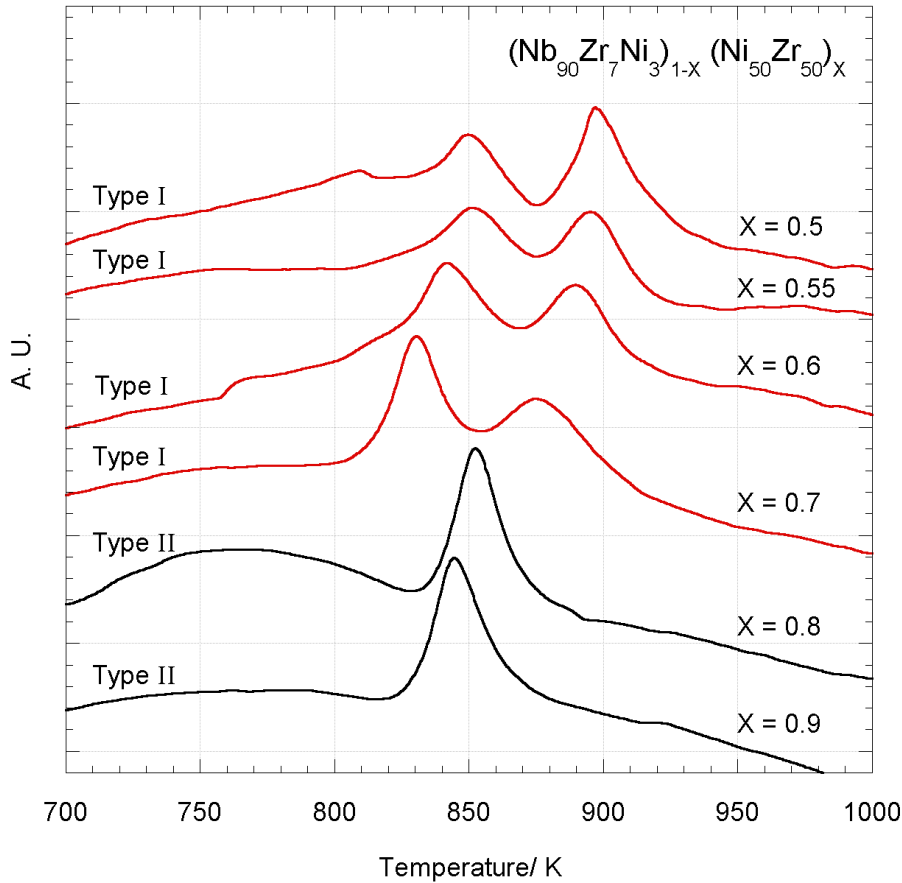


Figure 4.6. DTA curves of amorphous as-quenched Nb-Ni-Zr alloys of various compositions at a heating rate of 40 K/min.

The XRD traces of amorphous $(\text{Nb}_{90}\text{Zr}_7\text{Ni}_3)_{1-X}(\text{Ni}_{50}\text{Zr}_{50})_X$ alloys of various compositions that were heated to 1200 K at a heating rate of 40 K/min in an infrared furnace under vacuum are contained in Figure 4.7. The XRD traces of the alloys with higher Nb content that showed two exothermic crystallization peaks on the DTA curve, shown in red ($X = 0.5 - 0.7$), show sharp Bragg peaks of bcc-Nb and orthorhombic NiZr phases in higher proportions and faint Bragg peaks of NiZr₂ and Ni₁₁Zr₉ phases in smaller proportions. On the other hand the XRD patterns of the alloys with lower Nb content, that showed one

CHAPTER 4. FORMATION OF NANOSTRUCTURED HYDROGEN PERMEATION MEMBRANES

exothermic crystallization peak on the DTA curve, shown in black ($X = 0.8 - 0.9$), show sharp Bragg peaks of NiZr, NiZr₂ and Ni₁₁Zr₉ phases, and no Bragg peaks of the bcc-Nb phase were observed.

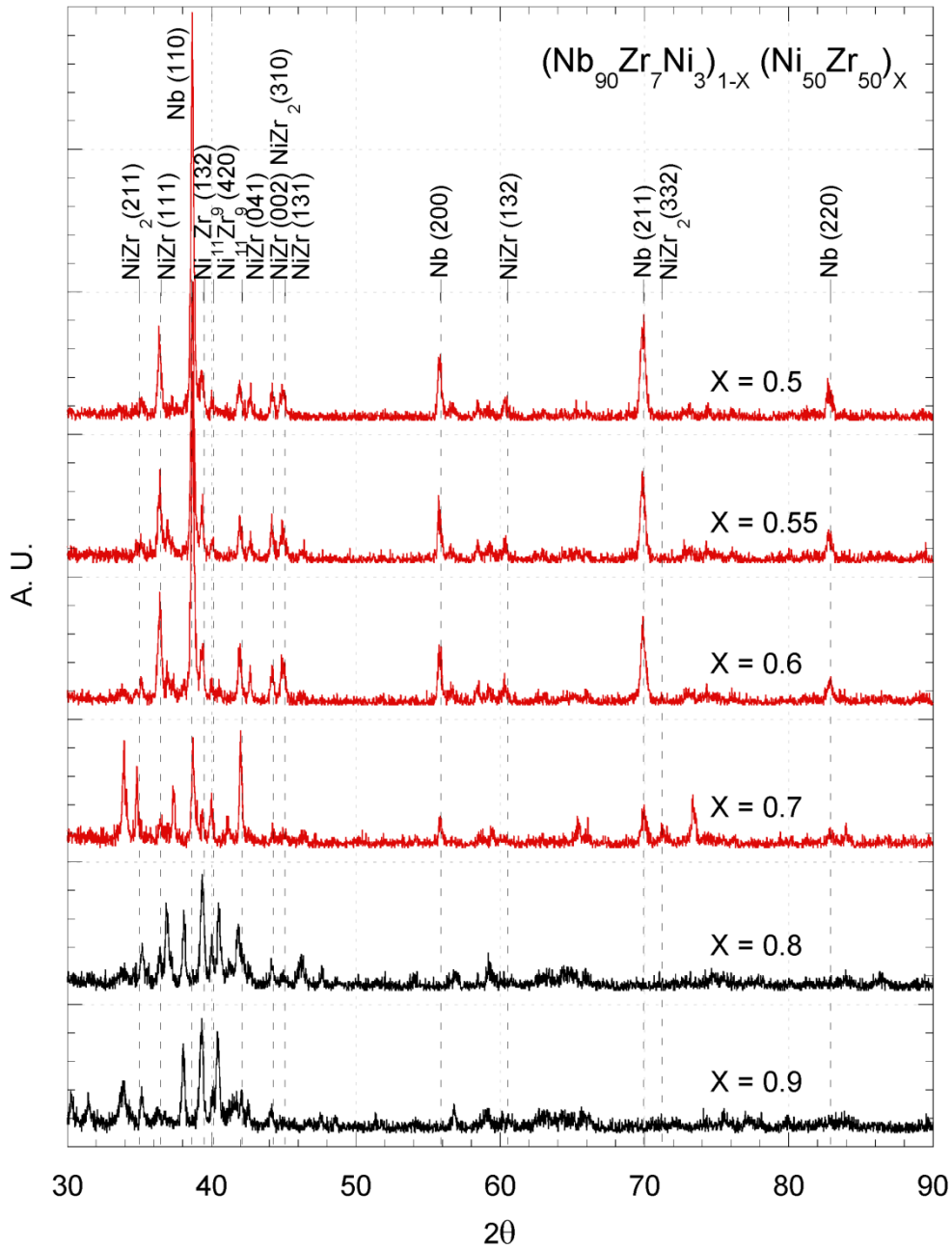


Figure 4.7. X-ray diffraction traces of Nb-Ni-Zr alloys of various compositions heated to 1200 K at a heating rate of 40 K/min.

To further investigate the crystallization behaviour in detail, the $(\text{Nb}_{90}\text{Zr}_7\text{Ni}_3)_{1-X}(\text{Ni}_{50}\text{Zr}_{50})_X$ alloy with composition $X = 0.55$ was chosen. Figure 4.8 shows the DTA curve

of the as-spun $\text{Nb}_{40.5}\text{Ni}_{28.85}\text{Zr}_{30.65}$ ribbon that was acquired at a heating rate of 40 K/min. A two-stage crystallization process similar to what is seen in Figure 4.6 is observed. For this alloy, the onset temperatures of the primary and secondary crystallization peaks were observed to be at $T_{X1} = 851$ K and $T_{X2} = 897$ K, respectively. The first exothermic peak corresponds to the formation of NiZr and $\text{Ni}_{11}\text{Zr}_9$ phases and the second crystallization peak results in bcc Nb and NiZr phases, which were determined by XRD analysis, as shown in Figure 4.9. The XRD traces were taken from samples heated to temperatures just after each exothermic peak and these temperatures are indicated by the red, blue and black crosses on the DTA curve.

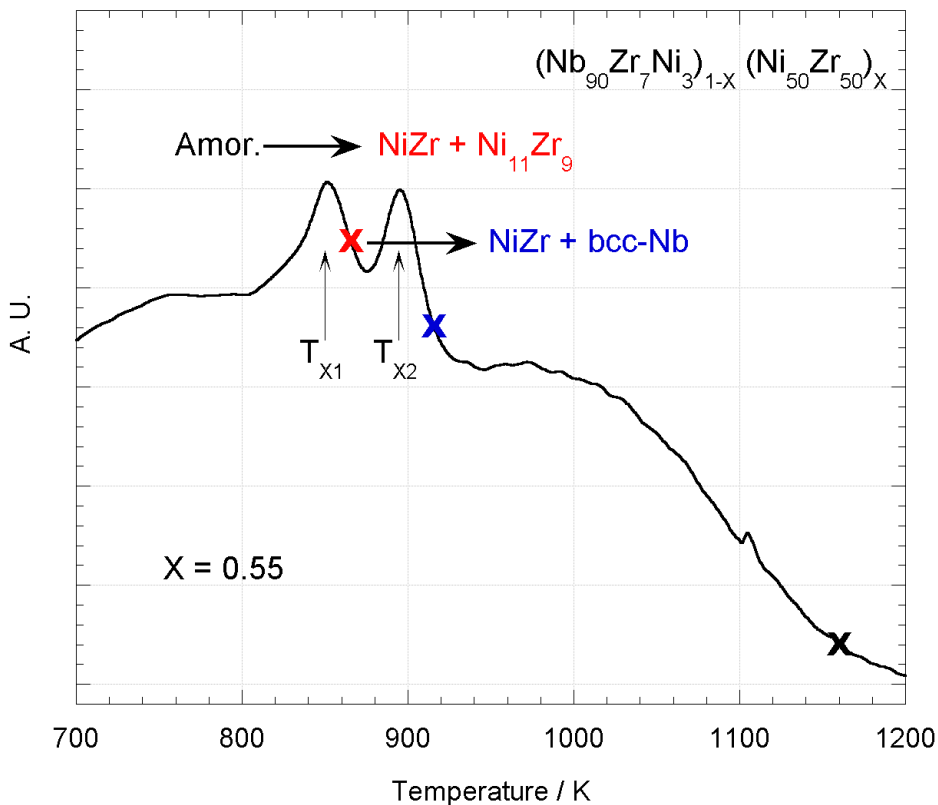


Figure 4.8. DTA curve of amorphous $(\text{Nb}_{90}\text{Zr}_7\text{Ni}_3)_{1-x}(\text{Ni}_{50}\text{Zr}_{50})_x$ alloy with composition $X = 0.55$ at a heating rate of 40 K/min.

The XRD traces of $(\text{Nb}_{90}\text{Zr}_7\text{Ni}_3)_{1-x}(\text{Ni}_{50}\text{Zr}_{50})_x$ alloy with composition $X = 0.55$ that was heated at a rate of 40 K/min to 863, 923 and 1173 K are shown in Figure 4.9. The XRD traces of the sample heated to 863 K show faint broad Bragg peaks of NiZr and $\text{Ni}_{11}\text{Zr}_9$

phases and show a main broad maximum around 39° and a second faint broad maximum around 66° , which are characteristic of amorphous alloys. This indicates the presence of NiZr and $\text{Ni}_{11}\text{Zr}_9$ phases forming while the ribbon remained mostly amorphous. The sample heated to 923 K shows broad Bragg peaks of bcc-Nb and NiZr phases, and after heating to 1173 K, sharp Bragg peaks of bcc-Nb, NiZr and $\text{Ni}_{11}\text{Zr}_9$ phases are found to be present. The sharper Bragg peaks after heating to 1173 K indicate a coarsening of the microstructure.

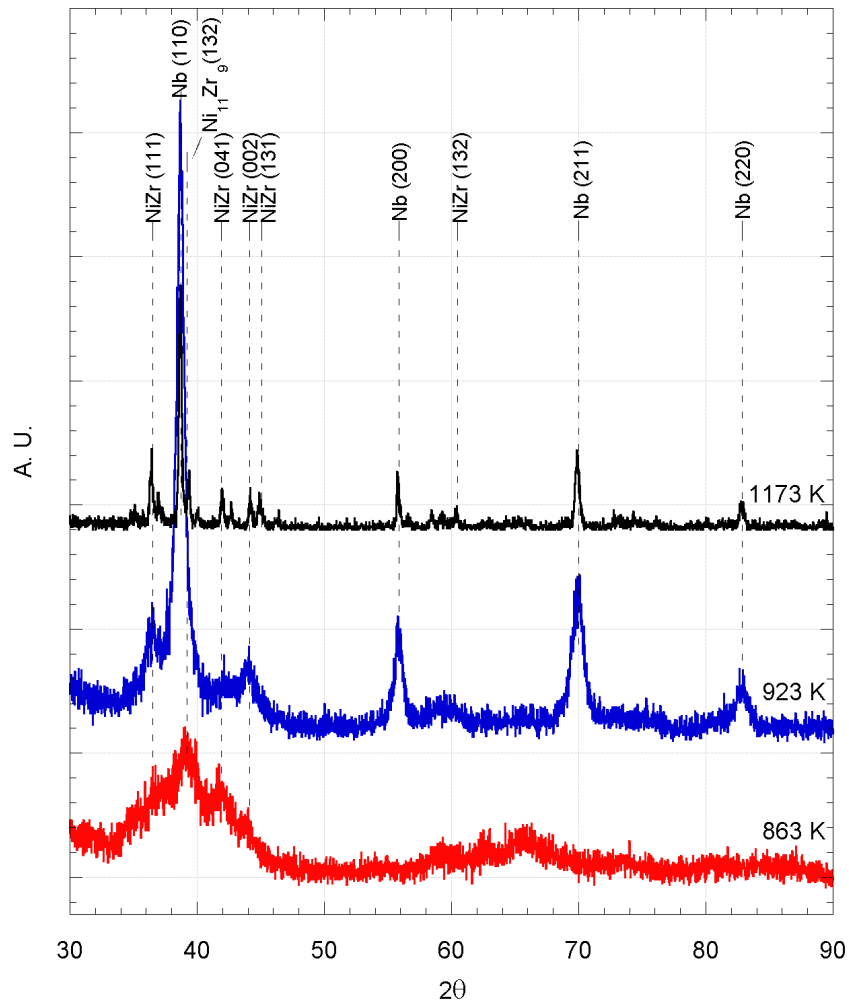


Figure 4.9. X-ray diffraction traces of $\text{Nb}_{40.5}\text{Ni}_{28.85}\text{Zr}_{30.65}$ alloy with composition $X = 0.55$ after heating to 863 K, 923 K and 1173 K at a heating rate of 40 K/min.

In an attempt to calculate the activation energy of the crystallization reactions observed for the $(\text{Nb}_{90}\text{Zr}_7\text{Ni}_3)_{1-X}(\text{Ni}_{50}\text{Zr}_{50})_X$ alloy with composition $X = 0.55$ in Figure 4.8, the crystallization reaction was traced by DTA at different heating rates. Figure 4.10 shows

the DTA curves obtained at five different heating rates. The peak temperatures of the primary and secondary crystallization reactions were recorded. The experimental variations associated with the machine and the heating rates were taken into consideration prior to the Kissinger analysis.

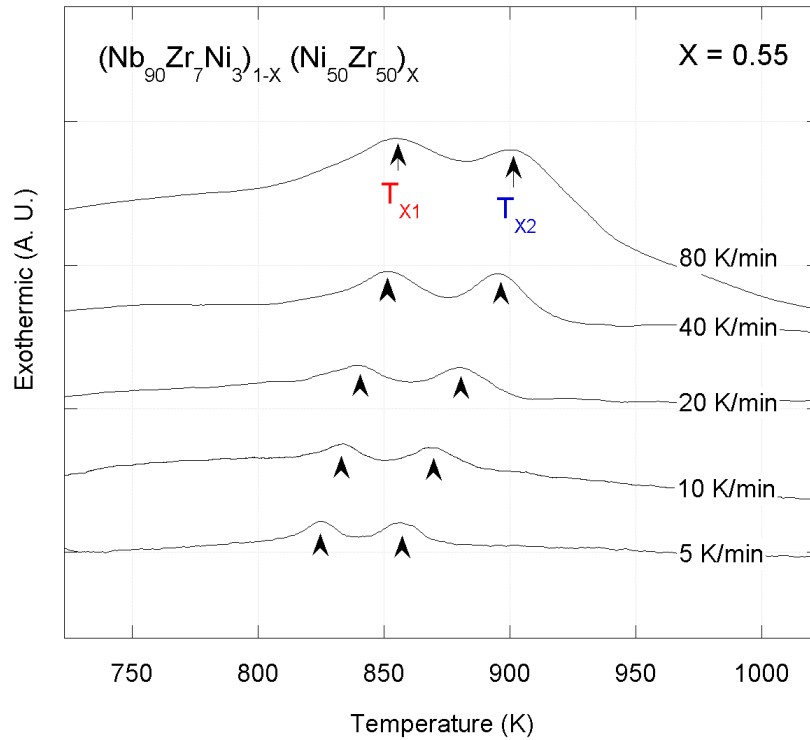


Figure 4.10. DTA curves of amorphous $(\text{Nb}_{90}\text{Zr}_7\text{Ni}_3)_{1-X}(\text{Ni}_{50}\text{Zr}_{50})_X$ alloy with composition $X = 0.55$ at different heating rates.

The crystallization kinetics was examined from the DTA curves obtained at different heating rates using the following Kissinger equation:

$$C = AT^2 \exp\left(\frac{-E_a}{k_B T}\right) \quad (4.1)$$

where C is the heating rate, T is the crystallization peak temperature, E_a the apparent activation energy for the crystallization reaction and k_B is the Boltzmann constant [15, 16]. Figure 4.11 shows the plot of $\ln C/T^2$ against $1000/T$ for the peak temperatures of the

CHAPTER 4. FORMATION OF NANOSTRUCTURED HYDROGEN PERMEATION MEMBRANES

primary and secondary crystallization peaks (T_{X1}) and (T_{X2}) of the amorphous $(\text{Nb}_{90}\text{Zr}_7\text{Ni}_3)_{1-X}(\text{Ni}_{50}\text{Zr}_{50})_X$ alloy with composition $X = 0.55$. The activation energies for the primary and secondary crystallization reactions were found to be 7.7 eV and 4.6 eV respectively. The experimental errors associated with the increasing heating rate during the DTA test were taken into account. It was found that a lower heating rate resulted into a lower deviation as the temperature is given more time to stabilize, which is crucial for the accuracy of the data transmitted.

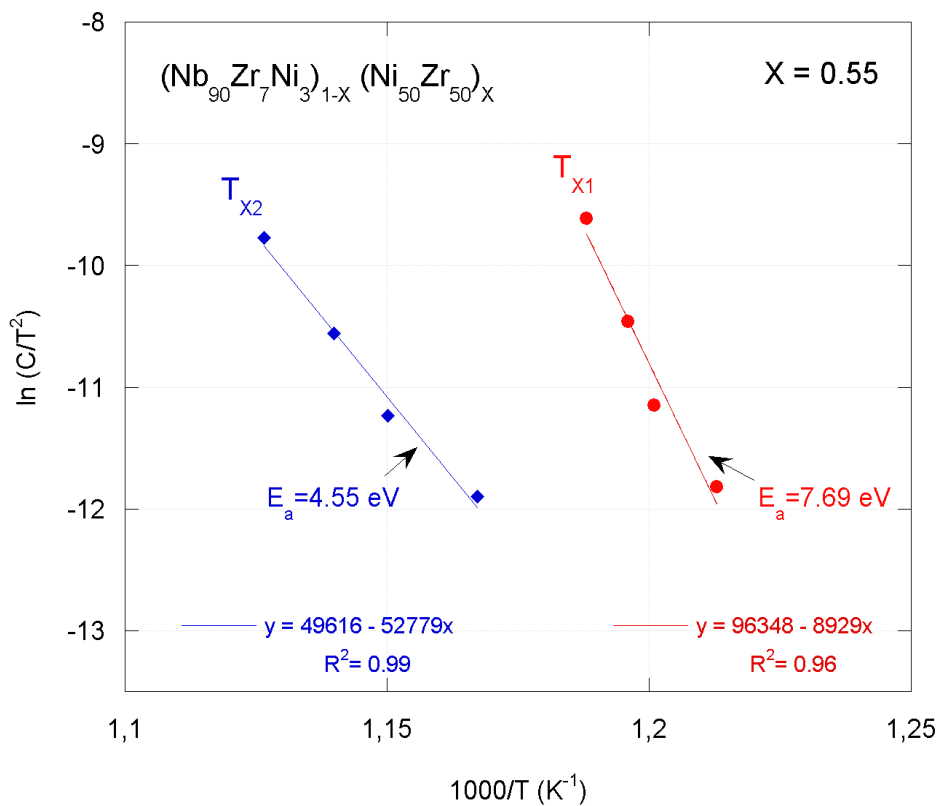


Figure 4.11. Plot of $\ln C/T^2$ against $1000/T$ for the onset temperatures of the primary and secondary crystallization peaks (T_{X1}) and (T_{X2}) of the amorphous $\text{Nb}_{40.5}\text{Ni}_{28.85}\text{Zr}_{30.65}$ alloy.

The X-ray diffraction trace of the Nb (211) peak of the $\text{Nb}_{40.5}\text{Ni}_{28.85}\text{Zr}_{30.65}$ alloy heated to 923 K at a rate of 40 K/min, from which the preliminary grain size was calculated by using Scherrer's equation (Eq. 3.1.) is shown in Figure 4.12.

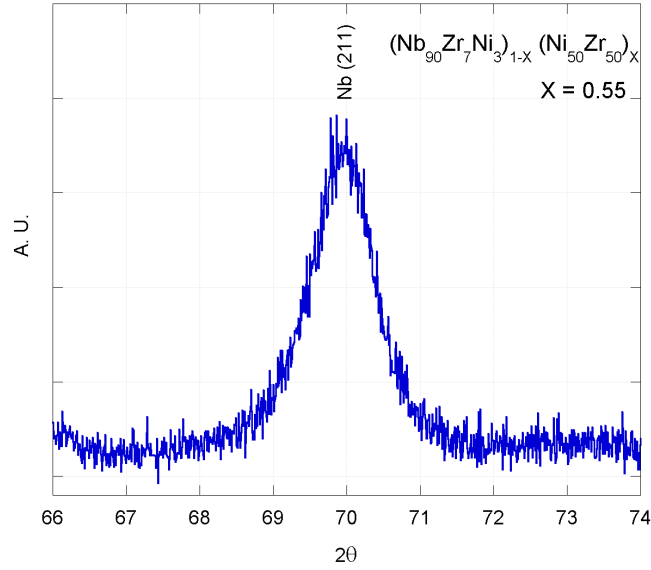


Figure 4.12. X-ray diffraction trace of the Nb (211) peak of the $\text{Nb}_{40.5}\text{Ni}_{28.85}\text{Zr}_{30.65}$ alloy heated to 923 K at a heating rate of 40 K/min.

The grain size of the amorphous $(\text{Nb}_{90}\text{Zr}_7\text{Ni}_3)_{1-X}(\text{Ni}_{50}\text{Zr}_{50})_X$ alloys that were heated to 923 K are contained in Figure 4.13. The average grain size is found to be approximately 15 ± 1 nm for the composition range $X = 0.5 - 0.7$, where Nb $\sim 45 - 27$ at. %.

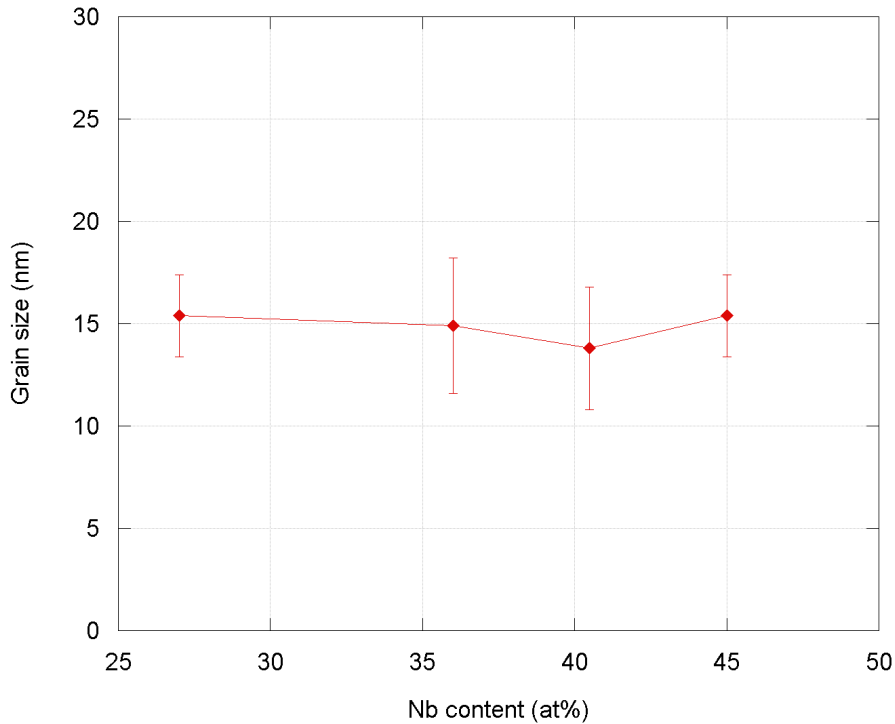


Figure 4.13. Grain size obtained from the estimation of the Nb (211) peak of amorphous Nb-Ni-Zr alloys with varying Nb content after heating to 923 K at a heating rate of 40 K/min.

CHAPTER 4. FORMATION OF NANOSTRUCTURED HYDROGEN PERMEATION MEMBRANES

Bright field TEM images and the corresponding diffraction patterns of melt-spun $\text{Nb}_{40.5}\text{Ni}_{28.85}\text{Zr}_{30.65}$ heated to 863 K ((a) and (b)), 923 K ((c) and (d)), and 1173 K ((e) and (f)) at a heating rate of 40 K/min are shown in Figure 4.14. The TEM micrographs confirm that the grain size of the sample $X = 0.55$ is at a nanoscale after the first and second crystallization reactions.

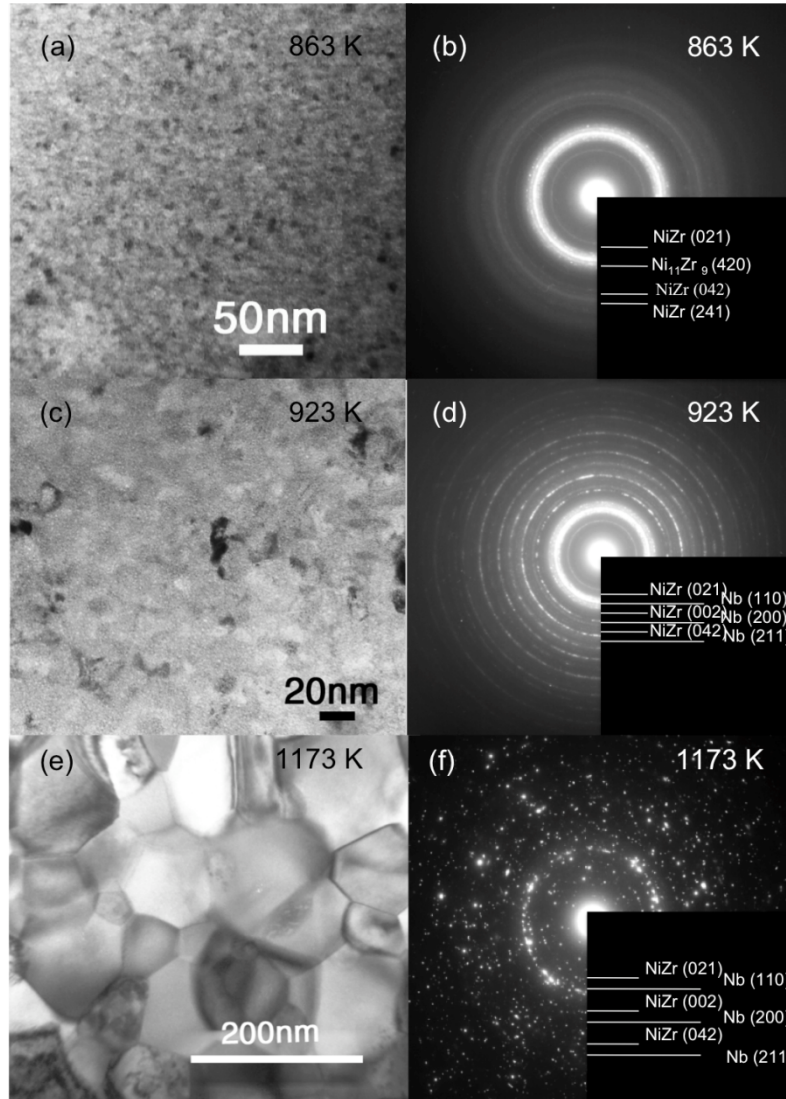


Figure 4.14. Bright field transmission electron micrographs and the corresponding selected area electron diffraction patterns of melt-spun $\text{Nb}_{40.5}\text{Ni}_{28.85}\text{Zr}_{30.65}$ after heating to 863 K ((a) and (b)), 923 K ((c) and (d)), and 1173 K ((e) and (f)) at a heating rate of 40 K/min.

After heating to 863 K, a nanostructure of NiZr and $\text{Ni}_{11}\text{Zr}_9$ phases with an average grain size of 7 ± 2 nm is observed. Heating to 923 K resulted in a nanostructure of NiZr and

bcc-Nb phases with an average grain size of 13 ± 4 nm. The grain size estimations were based on the measurement of at least 50 grains from the TEM micrographs. The grain size of the sample heated to 1173 K was found to be about 75 ± 20 nm. The diffraction patterns of the three samples confirmed the presence of the bcc-Nb, NiZr and $\text{Ni}_{11}\text{Zr}_9$ phases, similar to those identified by XRD in Figure 4.9.

To verify whether or not the grain refinement to the nanoscale is achievable at the other end of the compositional spectrum, which contains a lower Nb concentration, the crystallization behaviour of the $\text{Nb}_{20}\text{Ni}_{40}\text{Zr}_{40}$ wide ribbon was investigated by TEM. Figure 4.15 shows the bright field, dark field TEM images and the corresponding diffraction pattern of as-spun $\text{Nb}_{20}\text{Ni}_{40}\text{Zr}_{40}$ wide ribbons. The absence of obvious grains in the TEM images and the presence of diffuse rings in the diffraction pattern confirm the formation of an amorphous phase in the as-quenched $\text{Nb}_{20}\text{Ni}_{40}\text{Zr}_{40}$ wide ribbon.

The bright field, dark field images and the corresponding diffraction pattern of the $\text{Nb}_{20}\text{Ni}_{40}\text{Zr}_{40}$ melt-spun wide ribbon heated to 923 K are shown in Figure 4.16. From the TEM images, the average grain size is found to be 19 ± 4 nm. The diffraction rings from the diffraction pattern confirm the presence of bcc-Nb and orthorhombic NiZr phase.

The bright field image, dark field image and the corresponding diffraction pattern of the $\text{Nb}_{20}\text{Ni}_{40}\text{Zr}_{40}$ melt-spun wide ribbon heated to 1173 K are given in Figure 4.17. Grain coarsening can be observed in the bright field and dark field images. The average grain size is found to be 100 ± 20 nm. Bcc-Nb and orthorhombic NiZr phase are identified despite the fact that the coarsening of the grain size led to poorly defined rings on the diffraction pattern. The bcc-Nb structure was found to have a lattice parameter of 3.307 Å.

CHAPTER 4. FORMATION OF NANOSTRUCTURED HYDROGEN PERMEATION MEMBRANES

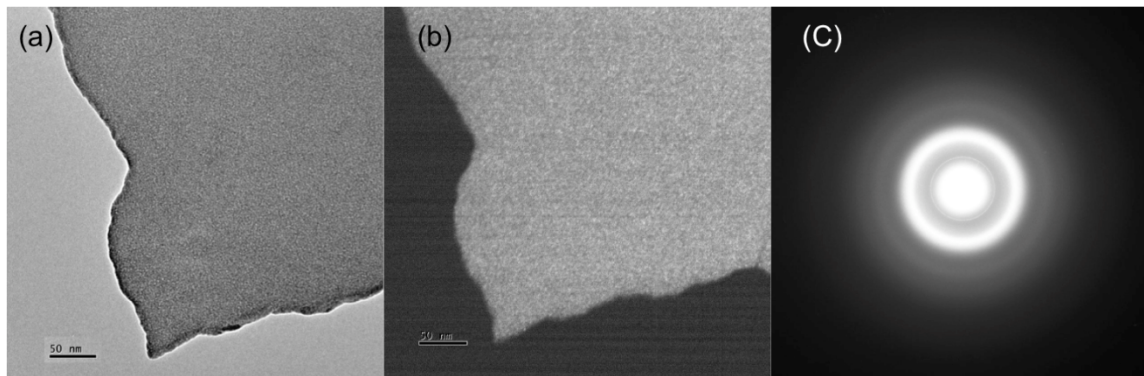


Figure 4.15. (a) Bright, (b) dark-field TEM images and (c) the corresponding diffraction pattern of as-melt-spun $\text{Nb}_{20}\text{Ni}_{40}\text{Zr}_{40}$ wide ribbon.

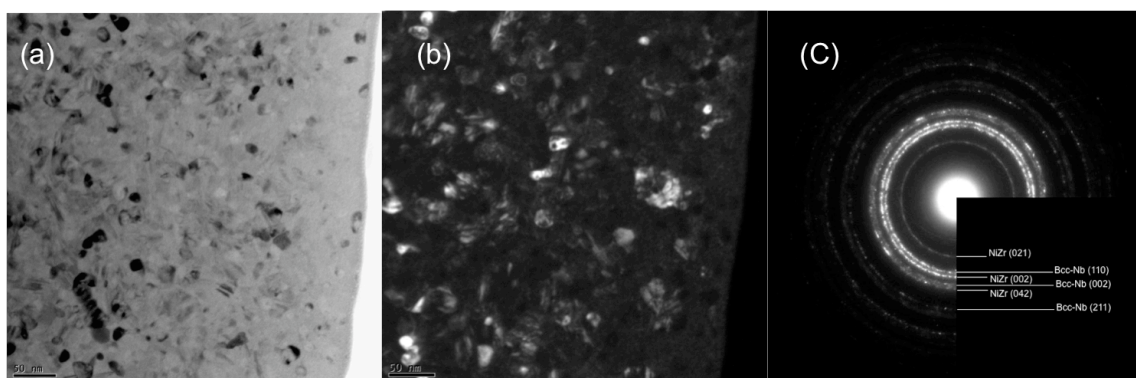


Figure 4.16. (a) Bright, (b) dark-field TEM images and (c) the corresponding diffraction pattern of the $\text{Nb}_{20}\text{Ni}_{40}\text{Zr}_{40}$ melt-spun wide ribbon heated to 923 K.

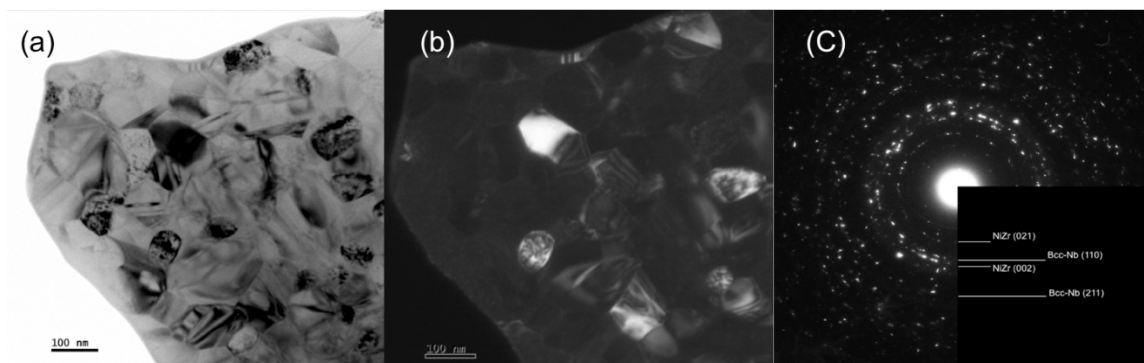


Figure 4.17. (a) Bright, (b) dark-field TEM images and (c) the corresponding diffraction pattern of the $\text{Nb}_{20}\text{Ni}_{40}\text{Zr}_{40}$ melt-spun wide ribbon heated to 1173 K.

4.2.2.2 Nb-Ti-Co alloys

The DTA curve of the $\text{Nb}_{30}\text{Ti}_{35}\text{Co}_{35}$ alloy that was acquired at a heating rate of 40 K/min is illustrated in Figure 4.18. A single exothermic peak is observed. For this alloy, the onset temperature of this crystallization peak is observed at 895 K. The crystallization peak corresponds to the formation of TiCo and bcc-Nb, which were determined by XRD analysis as shown in Figure 4.19. The XRD patterns were taken from the sample heated to just after the crystallization peak.

The XRD traces of the $\text{Nb}_{30}\text{Ti}_{35}\text{Co}_{35}$ alloy in the as-quenched state in black, and after heating to 905 K and 1173 K at a heating rate of 40 K/min; these are shown in red and blue respectively in Figure 4.19. The XRD trace of the as-quenched ribbon shows a main broad maximum around 40° and a second faint broad maximum around 70° , which are characteristic of an amorphous phase. The XRD trace of the sample heated to 905 K shows broad Bragg peaks of TiCo and bcc-Nb phases, and sharp Bragg peaks of the same phases were observed for the sample heated to 1173 K. This indicates a coarsening of the TiCo and bcc-Nb microstructure in the sample heated to 1173 K.

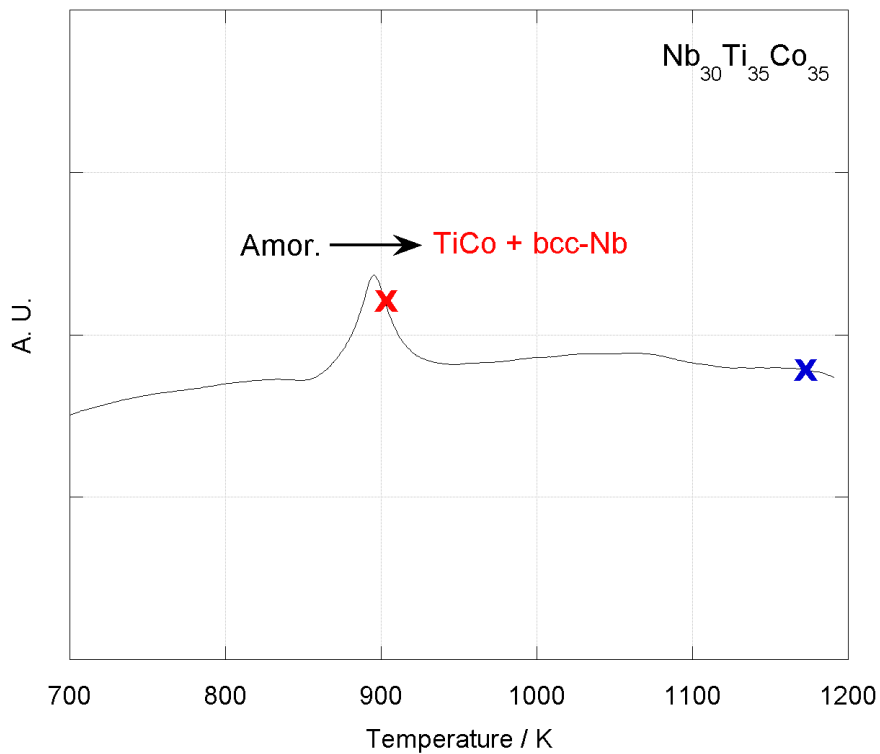


Figure 4.18. DTA curve of amorphous $\text{Nb}_{30}\text{Ti}_{35}\text{Co}_{35}$ at a heating rate of 40 K/min.

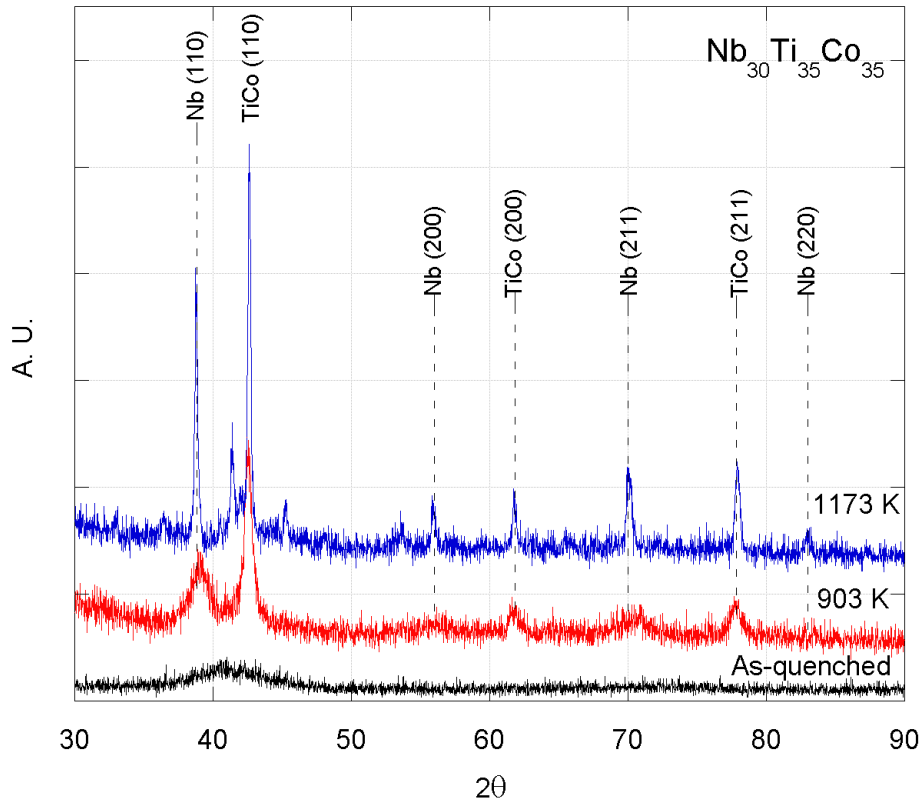


Figure 4.19. XRD traces of $\text{Nb}_{30}\text{Ti}_{35}\text{Co}_{35}$ alloy in the as-quenched state, heated to 903 K and 1173 K at a heating rate of 40 K/min.

4.2.2.3 Effect of annealing on ductility of as-spun amorphous alloys

A plot of the ductility ratio of the $\text{Nb}_{20}\text{Ni}_{40}\text{Zr}_{40}$ and $\text{Nb}_{36}\text{Ni}_{32}\text{Zr}_{32}$ ribbons in their as-quenched state and against their annealing temperatures for periods of 1 min, 1 h and 3 h is illustrated in Figure 4.20. The ductility ratio can be defined as the thickness of the membrane, T , divided by the reading on the micrometer, $2R$, when the ribbon cracks. It can be seen in both alloys that annealing for 1 min at 923 K leads to a loss in ductility. This loss in ductility is observed to recover with increasing annealing temperature. This phenomenon can be clearly observed in the $\text{Nb}_{20}\text{Ni}_{40}\text{Zr}_{40}$ ribbons annealed for 1 h that shows increased ductility ratio with increasing annealing temperature. The annealing time is also observed to have a positive impact on the recovery of the ductility of both alloy compositions.

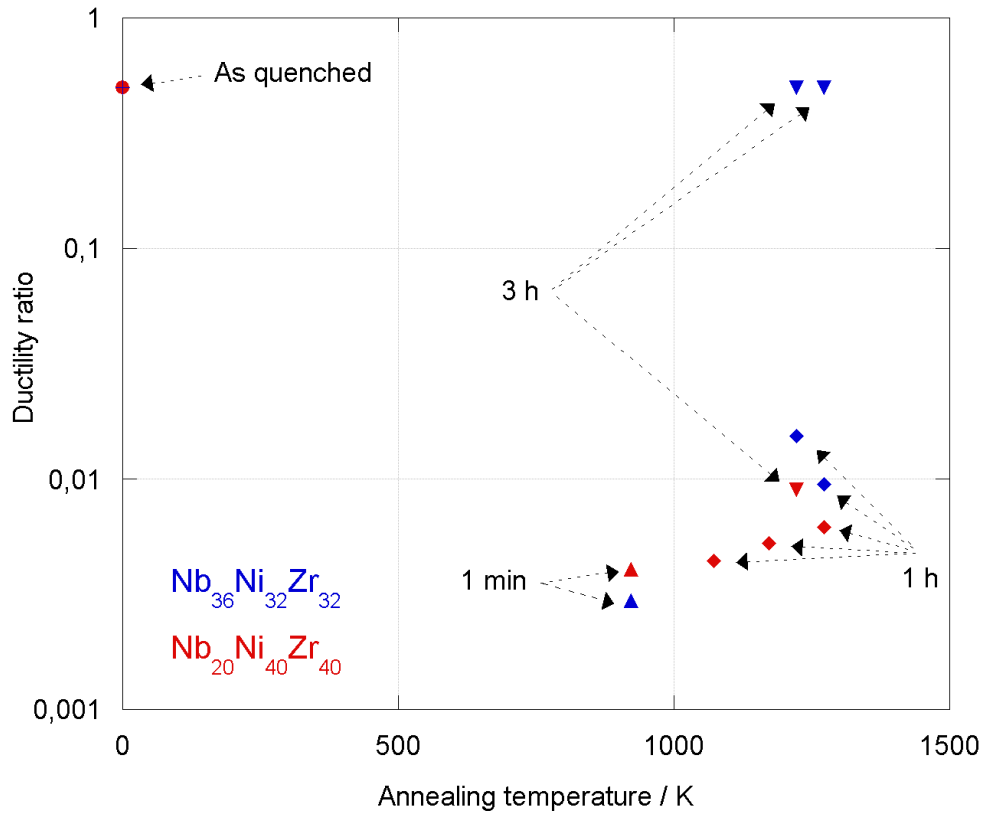


Figure 4.20. The ductility ratio of $\text{Nb}_{20}\text{Ni}_{40}\text{Zr}_{40}$ and $\text{Nb}_{36}\text{Ni}_{32}\text{Zr}_{32}$ ribbons in the as-quenched state and after annealing.

4.3 Discussion

4.3.1 Formation of an amorphous phase in Nb-Ni-Zr alloys

The formation of amorphous in 1.6 mm wide ribbons obtained by melt-spinning $(\text{Nb}_{90}\text{Zr}_{7}\text{Ni}_3)_{1-x}(\text{Ni}_{50}\text{Zr}_{50})_x$ alloys were found to be composition dependent. The alloys with Nb contents below 45 at. %, where $X = 0.5 - 0.9$, yielded ductile amorphous ribbons while those above 45 at. % resulted in brittle crystalline ribbons, indicating that the formation of the nanostructure by crystallization of an amorphous precursor is not possible for those compositions, due to the lack of glass formability. The formation of an amorphous phase at high Ni-Zr contents is consistent with the literature as the Ni-Zr alloy system is a well-known glass former [20]. Figure 4.21 shows a pseudo-binary phase diagram of a Nb-NiZr system [18] where the microstructures after melt-spinning in the present study are also

shown. It is observed that bcc-Nb forms near the eutectic composition while the formation of an amorphous phase is limited to the hypereutectic region away from the eutectic composition. This observation is unusual as it is well established that the formation of amorphous is the easiest at the eutectic composition where the melting point is the lowest and thus, the supercooled melt becomes stable upon the rapid solidification process.

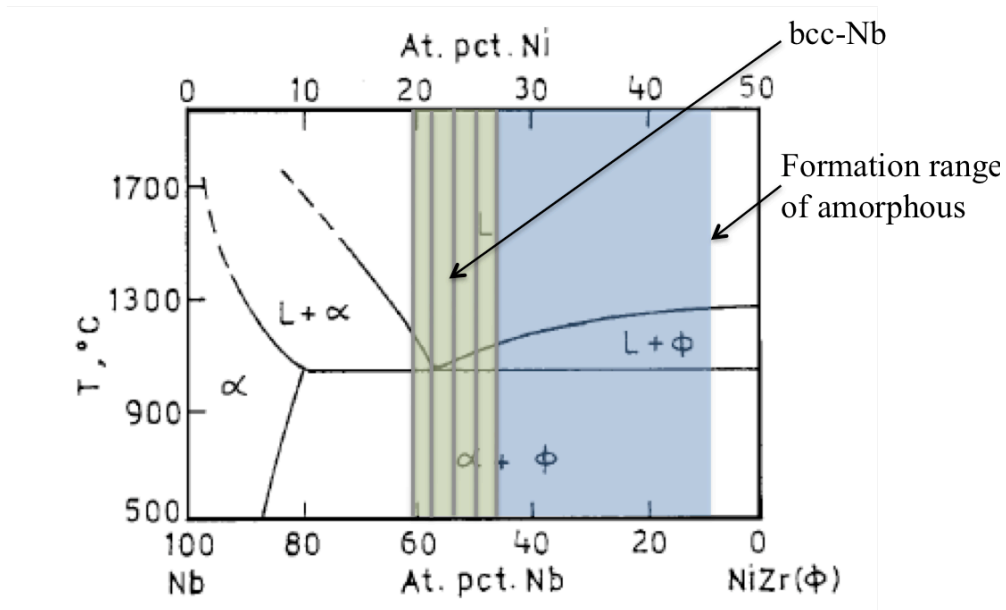


Figure 4.21. Pseudo-binary diagram of Nb-NiZr [18]. The highlighted region indicates the alloy composition range where amorphous and partially crystalline melt-spun ribbons were obtained.

Gibson and Delamore [21], Suk et al. [22], and Kurz and Fisher [23] have reported that the shift of the glass formation range from the eutectic composition can be explained by taking into account an asymmetrical coupled zone. A coupled zone represents the growth temperature/composition region where an entirely coupled eutectic-like microstructure forms [23]. Figure 4.22 shows the glass-forming and composite-forming regions of the two types of coupled zones. These two types are (1) the symmetric coupled zone where the terminal eutectic phases are non-faceted, and (2) the asymmetric coupled zone where a non-faceted phase and a faceted phase are involved in the eutectic reaction [24]. The asymmetric coupled zone is skewed towards the faceted phase as growth velocity is increased [24].

According to Kurz, Fisher and Li [23, 25], if the amorphous phase is treated as one of the competing phases together with eutectic, primary α and β phases, it is believed that glass will form when the glass transition temperature, T_g (represented by the dotted line), of the alloy is higher than the growth temperature of any crystalline phases at a critical growth rate. In the present case of alloys with high GFA, the T_g is expected to be relatively high compared to the melting temperature, T_m , and this implies that the T_g intercepts the growth-temperature/growth-rate curves of crystalline phases at a relatively low growth rate and therefore enables glass formation in the hypereutectic region. The skewed coupled zone concept in Figure 4.22 (2) is consistent with the off-eutectic amorphous formation range observed in Figure 4.21. The presence of bcc-Nb phase in the as-quenched ribbons at compositions near the eutectic composition, where Nb = 63 – 49.5 at. %, further confirms the presence of the skewed coupled zone. Based on the current observations on the composition range for the formation of amorphous and the presence of the bcc-Nb phase in the as-spun ribbons at the eutectic composition, it can be concluded that an asymmetric coupled zone is present in this Nb-Ni-Zr alloy system and is skewed towards the composition of the NiZr phase.

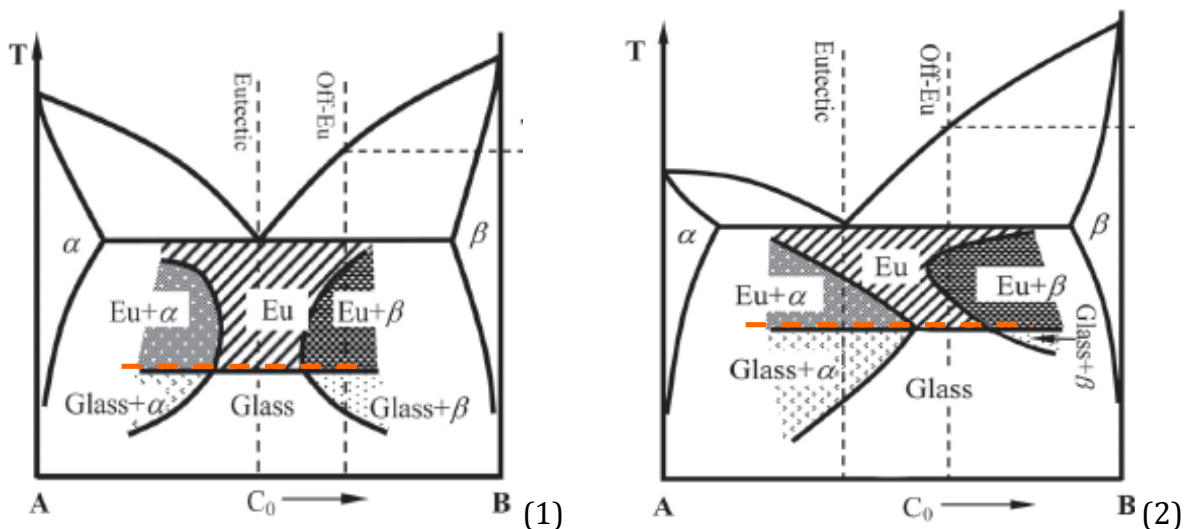


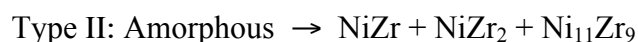
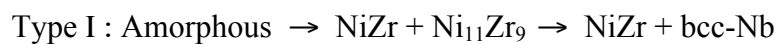
Figure 4.22. Schematic diagrams showing the coupled zone and the glass-forming and composite-forming regions related to (1) a symmetric eutectic-coupled zone and (2) an asymmetric eutectic-coupled zone [25].

4.3.2 Formation of an amorphous phase in Nb-Ti-Co alloys

The melt-spinning of the Nb-Ti-Co alloys was proved to be more challenging than that of the Nb-Ni-Zr alloys. The Nb₃₀Ti₃₅Co₃₅ alloy produced the only amorphous and ductile ribbon from the Nb-Ti-Co system under the processing conditions investigated. Hashi et al. have reported the Nb₃₀Ti₃₅Co₃₅ as the eutectic composition in the Nb-Ti-Co alloy system and showed that it had a fine lamellar microstructure consisting of (Nb,Ti) + TiCo phases, which is consistent with alloys with a eutectic composition [3]. The formation of the amorphous ribbons at the eutectic composition indicates that the Nb-Ti-Co alloy system is consistent with a symmetrical eutectic-coupled zone where the terminal eutectic phases are non-faceted. This symmetric eutectic-coupled zone can be seen in Figure 4.22 (1), where the glass formation zone is symmetric and directly below the eutectic point. Our attempt of preparing wider ribbons of the Nb₃₀Ti₃₅Co₃₅ alloy by melt-spinning was unsuccessful, indicating the level of difficulty in the production of amorphous wide ribbons from this system. Zr was added to the system in an attempt to improve the GFA. Subsequently, amorphous ribbons were produced but the addition of Zr rendered the ribbons very brittle.

4.3.3 Crystallization behaviour of amorphous Nb-Ni-Zr alloys

The crystallization of the amorphous ribbons, as investigated by DTA, showed that the number of crystallization reactions depends on the alloy composition. Two types of crystallization reactions were observed in Figure 4.6 which are described as follows:



The Nb-Ni-Zr alloys with a Nb content of $\sim 45 - 20$ at. % displayed the type I crystallization behaviour and resulted in the desired bcc-Nb + NiZr phases. The type II reaction was confirmed for alloys with a Nb content of $\sim 18 - 9$ at. %. The composition

ranges where the two types of crystallization reactions were confirmed are shown in Figure 4.23.

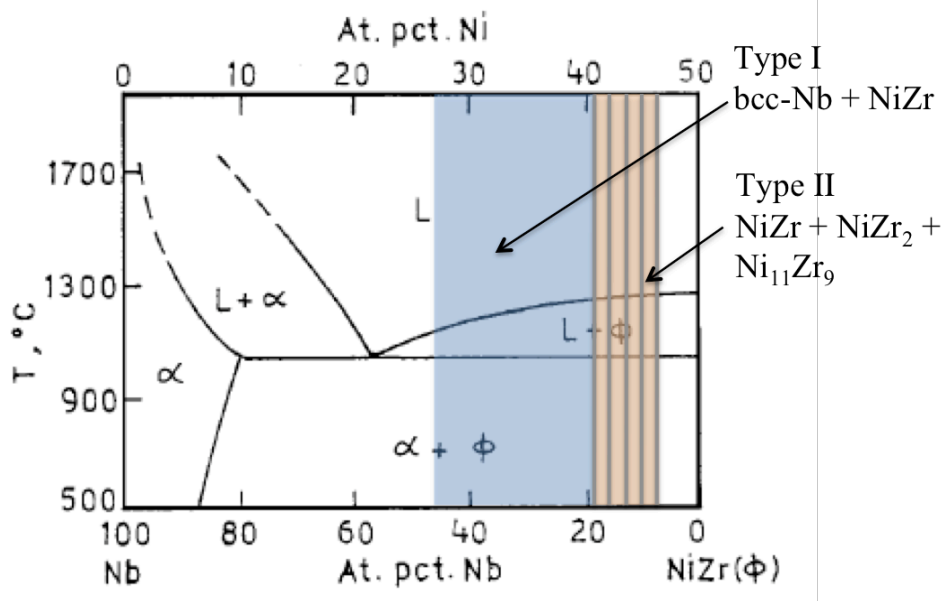


Figure 4.23. Pseudo-binary diagram of Nb-NiZr [18]. The highlighted region indicates the alloy composition range for type I and II, which resulted in the bcc-Nb + NiZr and NiZr + NiZr₂ + Ni₁₁Zr₉, respectively, after heating to 923 K.

The phase constituents for the melt-spun amorphous alloys after heating to 923 K are also summarized in this diagram. The desired Nb + NiZr duplex microstructure is obtained via the type I reaction. The formation of the Nb + NiZr microstructure after heating to 923 K is consistent with the pseudo-binary phase diagram. It was observed that the type II crystallization reaction for alloys with a Nb content of ~ 18 – 9 at. % resulted in a microstructure of NiZr + NiZr₂ + Ni₁₁Zr₉. According to Figure 4.23, this composition range is expected to yield a Nb + NiZr microstructure when heated to 923 K. This implies that even after heating to 923 K, these alloys remained in a metastable state.

Therefore, we have been able to identify the composition range in the Nb-Ni-Zr alloy system that can lead to grain refinement by the amorphization and subsequent crystallization processes, and yield the desired bcc-Nb + NiZr microstructure that is conducive to hydrogen permeation. Heating the amorphous precursors to 923 K resulted in an average grain size of 15 ± 1 nm for the composition range with $X = 0.5 - 0.7$ (where Nb

CHAPTER 4. FORMATION OF NANOSTRUCTURED HYDROGEN PERMEATION MEMBRANES

~ 45 – 20 at. %), as shown in Figures 4.12 and 4.13. Although the desired mixed structure of NiZr + bcc-Nb is preserved even after heating to 1173 K, grain coarsening was clearly evident through the sharpening of the XRD peaks and the direct microstructural observation by TEM.

The nanoscale grain refinement of the $(\text{Nb}_{90}\text{Zr}_7\text{Ni}_3)_{1-x}(\text{Ni}_{50}\text{Zr}_{50})_x$ alloys after heating to 823 K was confirmed by TEM analysis. Heating to 863 K resulted in an average grain size of 7 ± 2 nm and the presence of NiZr and $\text{Ni}_{11}\text{Zr}_9$ phases were confirmed by analysis of the Debye rings on the electron diffraction pattern. The nanoscale grain refinement for a microstructure comprising of bcc-Nb + NiZr phases was also confirmed by TEM imaging of the $\text{Nb}_{40.5}\text{Ni}_{28.8}\text{Zr}_{30.65}$ and $\text{Nb}_{20}\text{Ni}_{40}\text{Zr}_{40}$ samples after heating to 923 K, where the average grain sizes were found to be 13 ± 4 and 19 ± 4 nm respectively. The presence of bcc-Nb and NiZr phases were confirmed by the corresponding electron diffraction patterns. Grain coarsening was observed for the sample heated to 1173 K. The average grain size for the $\text{Nb}_{40.5}\text{Ni}_{28.8}\text{Zr}_{30.65}$ sample and $\text{Nb}_{20}\text{Ni}_{40}\text{Zr}_{40}$ samples heated to 1173 K was 75 ± 20 and 100 ± 20 nm, respectively.

To have a better understanding of the formation of the nanostructure upon crystallization in the Nb-Ni-Zr system, the Kissinger analysis was carried out. The apparent activation energy of the primary crystallization peak (T_{X1}) and the secondary crystallization peak (T_{X2}) was found to be of 7.7 ± 0.8 eV and 4.6 ± 0.6 eV respectively. To achieve a nanostructure, it is known that a high nucleation rate and a low growth rate are required. It is important to realize that the crystallization reactions in amorphous alloys may not be described by a simple thermal activation process with a single activation energy. Rather, the apparent activation energy, E_a , reflects the activation energies for nucleation, E_n , and growth, E_g , which can be expressed by the following equation [26], assuming linear growth.

$$E_a = \frac{aE_n + bE_g}{a+b} \quad (4.1)$$

CHAPTER 4. FORMATION OF NANOSTRUCTURED HYDROGEN PERMEATION MEMBRANES

where a is the nucleation variable.

$a = 0$ for no nucleation

$a = 1$ for constant nucleation rate

$a > 1$ for increasing nucleation rate

$0 < a < 1$ for decreasing nucleation rate.

and where b is a morphology index.

$b = 1$ for one-dimensionally growing particle.

$b = 2$ for two-dimensionally growing particle.

$b = 3$ for three-dimensionally growing particle.

Table 4.1. Activation energy for the self-diffusion of different elements [27, 28, 29]

Element	Activation energy for self-diffusion / eV
Ni	2.77 – 3.03
Zr	0.74 – 1.305
Nb	3.62 – 5.21

The high apparent activation energy for the primary crystallization reaction T_{X1} ($E_a = 7.7 \pm 0.8$ eV) in the $\text{Nb}_{40.5}\text{Ni}_{28.8}\text{Zr}_{30.65}$ alloy, which lies at the high end of the activation energies for amorphous alloys reported to date, is an indication of the thermal stability of this alloy [30-32]. As described in Equation 4.1, the apparent activation energy is influenced by both the nucleation and growth processes. Since both the nucleation and growth are observed to occur concurrently during the first crystallization reaction T_{X1} , it is not possible to draw significant conclusions related to the value of the activation energy. Table 4.1 shows the activation energy for the self-diffusion of Nb, Ni and Zr in a crystalline state. The activation energy for self-diffusion in a crystalline state is not directly applicable to the present case where the diffusion is occurring in an amorphous state. However, according to the work of Kronmuller et al., the self-diffusion enthalpies of transition metals in amorphous metal-metalloid alloys are smaller by 0.5 to 1 eV than the self-diffusion enthalpies of crystalline metals in the Fe group [33]. This is consistent with the diffusion of

CHAPTER 4. FORMATION OF NANOSTRUCTURED HYDROGEN PERMEATION MEMBRANES

Fe in Fe₉₁Zr₉ amorphous alloy where the activation energies in amorphous and crystalline state were obtained by radioactive tracer diffusion and were found to be 1.5 and 2.5 eV respectively [33]. Assuming that this applies in the present case, the activation energies in Table 4.1 can be used to give an indicative idea of the activation energies for the diffusion of these elements in an amorphous alloy. Thus, it can be observed that the apparent activation energy for the primary crystallization reaction obtained is larger than that expected for a simple diffusion process. This large apparent activation energy confirms that the crystallization process is governed by more than one thermal activation process. For example, the nucleation rate is governed by at least two thermal activation barriers, i.e. the one for atomic transport by diffusion and the free energy barrier at the critical radius. Hence, it is perfectly natural that the apparent activation energy of crystallization is higher than that for diffusion. The first crystallization reaction is assumed to be a combination of both nucleation and growth, with nucleation having a bigger influence. Kim et al. and Collins et al. have reported similarly high activation energies for the primary crystallization reaction during the decomposition of (Ni_{0.6}Nb_{0.4})₇₀₋₉₀Zr₃₀₋₁₀ and Ni₆₀Nb₄₀ amorphous alloys, respectively [30, 31].

The secondary crystallization reaction, had a much lower apparent activation energy (4.6 ± 0.6 eV) and was found to lead to the formation of bcc-Nb. Given that the primary crystallization reaction was dominated by the nucleation, it can be assumed that the nucleation rate in second crystallization would be much lower. According to Equation 4.1, this would imply that the nucleation variable a would be close to zero and if this is the case, then $E_a \approx E_g$. Based on the earlier argument by Kronmuller et al. that the activation energy for self-diffusion in amorphous is about 0.5 to 1 eV lower than that in crystalline and the data in Table 4.1, it can be seen that the apparent activation energy for the secondary crystallization reaction is approximately equal to that of the self-diffusion of Nb in amorphous (3.12 – 4.71 eV). This is consistent with the formation of bcc-Nb after the second crystallization reaction and suggests that the second crystallization reaction is governed by the diffusion of Nb. The first crystallization reaction is believed to facilitate the

second crystallization reaction, as the formation of NiZr and Ni₁₁Zr₉ phases implies that Nb atoms are being diffused out to the matrix adjacent to the NiZr and Ni₁₁Zr₉ phases. This Nb rich matrix is thought to subsequently assist the nucleation and growth of the bcc-Nb phase.

4.3.4 The ductility in Nb-Ni-Zr alloys after annealing

From Figure 4.20, it can be seen that annealing of Nb₂₀Ni₄₀Zr₄₀ and Nb₃₆Ni₃₂Zr₃₂ amorphous alloys for 1 min at 923 K leads to a loss in ductility. From the TEM image of the amorphous Nb₂₀Ni₄₀Zr₄₀ alloy heated to 923 K in Figure 4.16, it was found that the annealing process leads to a nanocrystalline microstructure. The brittleness of these nanocrystalline alloys is not unexpected. There have been several reports on the tensile elongation of nanocrystalline metals being lower relative to their crystalline counterparts [34-36] According to Koch a large number of nanocrystalline alloys have tensile elongations to failure below 10 % and sometimes exhibit a brittle behaviour [37]. In some cases, the materials fail at low stresses before yielding has time to occur. It is now generally accepted that this type of premature failure is mainly due to processing defects or to a form of plastic instability, such as shear banding or necking in the early stage of straining, due to a lack of effective hardening mechanism [38]. During the experiment, it was not possible to observe these plastic instability due to the speed at which the samples failed. The initial loss in ductility observed in the Nb₂₀Ni₄₀Zr₄₀ and Nb₃₆Ni₃₂Zr₃₂ alloys after the formation of nanocrystalline microstructures is consistent with other reports in the literature as discussed earlier.

The initial loss in ductility upon annealing is observed to recover with increasing annealing temperature. This recovery in ductility after annealing at 1200 K was found to correlate with a coarsening in the microstructure of the Nb₂₀Ni₄₀Zr₄₀ alloy from 19 ± 4 nm to 100 ± 20 nm, as shown in Figures 4.16 and 4.17. This link between an improvement in ductility and the coarsening of the microstructure is consistent with the literature, which reported that nanocrystalline alloys appear to be ductile for grain sizes above 15 nm and 100 nm according to Ebrahimi et al. [36] and Sanders et al. [34], respectively. Tang et al. also reported an analogous finding regarding the coarsening of the microstructure after

increasing annealing time of a rolled $\text{Nb}_{40}\text{Ti}_{18}\text{Zr}_{12}\text{Ni}_{30}$ alloy, which led to a reduction in the Vickers hardness [7]. In the present experiment, the annealing time is also observed to have a positive impact on the recovery of the ductility of both alloy compositions. It was found that annealing the $\text{Nb}_{36}\text{Ni}_{32}\text{Zr}_{32}$ alloy at 1223 K and 1273 K for 3 h resulted in a full recovery of the ductility.

4.4 Summary

The preliminary research segment showed that the formation of amorphous by the melt-spinning technique was found to be highly dependent on the composition of the alloys in both the Nb-Ni-Zr and the Nb-Ti-Co systems. The $(\text{Nb}_{90}\text{Zr}_7\text{Ni}_3)_{1-x}(\text{Ni}_{50}\text{Zr}_{50})_x$ alloys with Nb contents below 45 at. % yielded amorphous ductile ribbons while those above this Nb content resulted in crystalline brittle ribbons. The eutectic Nb-Ti-Co alloy resulted in ductile amorphous ribbons when thin ribbons were spun, however, attempts to prepare wide ribbons failed. The Nb-Ni-Zr alloy system was found to be an easier alloy system to produce amorphous and ductile wide ribbons.

The formation range of amorphous in the $(\text{Nb}_{90}\text{Zr}_7\text{Ni}_3)_{1-x}(\text{Ni}_{50}\text{Zr}_{50})_x$ alloy system was observed to be in the hypereutectic region. The rationale behind the formation of amorphous in an off eutectic region in the Nb-Ni-Zr alloys, was the presence of an asymmetric coupled zone that is skewed towards the NiZr phase.

Two decomposition behaviors were observed in the Nb-Ni-Zr alloys. The $(\text{Nb}_{90}\text{Zr}_7\text{Ni}_3)_{1-x}(\text{Ni}_{50}\text{Zr}_{50})_x$ alloys with a higher niobium content, Nb ~ 45 – 20 at. %, had a two-step crystallization reaction while those with a Nb content of ~ 18 – 9 at. % showed a single-step crystallization reaction. For the Nb-Ni-Zr alloys with a two-step crystallization reaction, the primary crystallization peak corresponds to the formation of NiZr + $\text{Ni}_{11}\text{Zr}_9$ phases prior to the formation of bcc-Nb phase at the secondary crystallization peak. The nanoscale grain refinement of a NiZr and bcc-Nb microstructure was obtained for $(\text{Nb}_{90}\text{Zr}_7\text{Ni}_3)_{1-x}(\text{Ni}_{50}\text{Zr}_{50})_x$ ribbons with Nb content between 45 – 20 at. % after heating to

CHAPTER 4. FORMATION OF NANOSTRUCTURED HYDROGEN PERMEATION MEMBRANES

923 K. Coarsening of the Nb and NiZr duplex structure was observed in samples heated to 1173 K.

After the initial annealing of amorphous $\text{Nb}_{20}\text{Ni}_{40}\text{Zr}_{40}$ and $\text{Nb}_{36}\text{Ni}_{32}\text{Zr}_{32}$ ribbons for 1 min, a drop in ductility was observed. The ductility recovered in both alloys with increasing annealing time and temperature. A full recovery was achieved in the $\text{Nb}_{36}\text{Ni}_{32}\text{Zr}_{32}$ alloy after annealing at 1223 K and 1273 K for 3 h. This improvement in ductility is likely to be due to grain coarsening. In this chapter it was confirmed that the formation of a nanostructure by amorphization and crystallization is possible in the $(\text{Nb}_{90}\text{Zr}_7\text{Ni}_3)_{1-x}(\text{Ni}_{50}\text{Zr}_{50})_x$ alloy system and the compositional restrictions for the formation of amorphous and the formation of the desired microstructure containing bcc-Nb in a NiZr or TiCo matrix were also identified.

4.5 References

- [1] S. N. Paglieri and J. D. Way, *Separation and Purification Methods*, 31 (2002) 1
- [2] K. Ishikawa, S. Tokui and K. Aoki, *Intermetallics*, 17 (2009) 109
- [3] K. Hashi, K. Ishikawa, T. Matsuda and K. Aoki, *Journal of Alloys and Compounds*, 425 (2006) 284
- [4] K. Hashi, K. Ishikawa, T. Matsuda and K. Aoki, *Journal of Alloys and Compounds*, 368 (2004) 215
- [5] W. Luo, K. Ishikawa and K. Aoki, *Journal of Alloys and Compounds*, 407 (2006) 115
- [6] K. Kishida, Y. Yamaguchi, K. Tanaka, H. Inui, S. Tokui, K. Ishikawa and K. Aoki, *Intermetallics*, 16 (2008) 88
- [7] H. Tang, K. Ishikawa and K. Aoki, *Materials Transactions*, 48 (2007) 2454
- [8] K. Ishikawa, T. Takano, T. Matsuda and K. Aoki, *Applied Physics Letters*, 87 (2005) 081906
- [9] T. Takano, K. Ishikawa, T. Matsuda and K. Aoki, *Materials Transactions*, 45 (2004) 3360
- [10] M. D. Dolan, *Journal of Membrane Science*, 362 (2010) 12
- [11] M. D. Dolan, N. C. Dave, A. Y. Ilyushechkin, L. D. Morpeth and K. G. McLennan, *Journal of Membrane Science*, 385 (2006) 30
- [12] S. Jayalakshmi, V. S. Vasantha, E. Fleury and M. Gupta, *Applied Energy*, 90 (2012) 94
- [13] S. Hara, K. Sakaki, N. Itoh, H.M. Kimura, K. Asami and A. Inoue, *Journal of Membrane Science*, 164 (2000) 289
- [14] C. Marte and R. Kirchheim, *Scripta Materialia*, 37 (1997) 1171
- [15] D. R. Arantes, X. Y. Huang, C. Marte and R. Kirchheim, *Acta Metallurgica et Materialia*, 41 (1993) 3215
- [16] H.E. Kissinger, *Analytical Chemistry*, Vol. 29 No. 11 (1957) 1702
- [17] N. S. Prasad and K. B. R. Varma, *Journal of the American Ceramic Society*, Vol. 88 No.2 (2005) 357

CHAPTER 4. FORMATION OF NANOSTRUCTURED HYDROGEN
PERMEATION MEMBRANES

- [18] K. P. Gupta, *Journal of Phase Equilibria*, Vol. 21 No. 5 (2000) 485
- [19] H. Xua, Y. Dua, C. Tang, Y. Hea, Z. Yuan, B. Huang and S. Li, *Materials Science and Engineering A*, 412 (2005) 336
- [20] A. Inoue, K. Hashimoto, *Amorphous and nanocrystalline materials*, (Springer-Verlag, Berlin Heidelberg, 2001)
- [21] M. A. Gibson and G. W. Delamore, *Materials Science and Engineering A*, 101 (1988) 135
- [22] M. J. Suk, I. S. Ahn and I. H. Moon, *Journal of Materials Science*, 21 (1986) 451
- [23] W. Kurz and D. J. Fisher, *Fundamentals of Solidification*, 4th Ed. (Trans Tech Publications, Switzerland, 1998)
- [24] M. Li, S. Yoda, and K. Kuribayashi, *Philosophical Magazine*, Vol. 85 No. 23, (2005) 2581
- [25] M. Li, S. Yoda, and K. Kuribayashi, *Bulk Metallic Glasses: Eutectic Coupled Zone and Amorphous Formation JOM*, March 2005
- [26] S. Ranganathan and M. Von Heimendhal, *Journal of Materials Science*, 16 (1981) 2401
- [27] Pierre Guiraldenq, (1978) *Diffusion dans les métaux, Techniques de l'ingénieur* (Translation of the title from French: *Diffusion in metals*), (Editions T.I., 1978)
- [28] N. L. Peterson, *Journal of Nuclear Materials*, 69 & 70 (1978) 3
- [29] G. Neumann and C. Tuijn, *Self-diffusion and impurity diffusion in pure metals: Handbook of experimental data*, (Pergamon Science Series Volume 14, Elsevier Oxford U.K., 2009)
- [30] S. M. Kim, D. Chandra, N. K. Pal, M. D. Dolan, W. M. Chien, A. Talekar, J. Lamb, S. N. Paglieri and T. B. Flanagan, *International Journal of Hydrogen Energy*, 37 (2012) 3904
- [31] L. E. Collins, N. J. Grant and J. B. Vander Sande, *Journal of Materials Science*, 18 (1983) 804
- [32] N. Zarubova, N. Moser and H. Kronmuller, *Materials Science and Engineering A*, 151 (1992) 205

CHAPTER 4. FORMATION OF NANOSTRUCTURED HYDROGEN
PERMEATION MEMBRANES

[33] H. Kronmuller, W. Frank and A. Horner, *Materials Science and Engineering A*, 133 (1991) 410

[34] P. G. Sanders, J. A. Eastman and J. R. Weertman, *Acta Materialia*, Vol. 45 No. 10 (1997) 4019

[35] F. Dalla Torre, H. Van Swygenhoven and M. Victoria, *Acta Materialia*, 50 (2002) 3957

[36] F. Ebrahimi, G.R. Bourne, M.S. Kelly and T.E. Matthews, *NanoStructured Materials*, Vol. 11 No. 3 (1999) 343

[37] C. C. Koch, *Scripta Materialia*, 49 (2003) 657

[38] E. Ma, *Scripta Materialia*, 49 (2003) 663

Chapter 5

Implementation of Hydrogen Permeation Apparatus and its Application to Investigate the Permeation Behaviour of Nb-Ni-Zr Alloy Membranes

5.1 Introduction

In this chapter we look into (1) the hydrogen permeation measuring apparatus that the author built during the course of his Ph.D, and (2) the effect of annealing on the hydrogen permeation of as-cast Nb-Ni-Zr alloy membranes. Monash University did not have the facilities required to measure the hydrogen permeation of metallic membranes via the pressure difference method and therefore one of the essential tasks was to implement such an apparatus. Hydrogen gas produced by chemical processes such as steam reforming of hydrocarbons contains a large amount of CO gas that is harmful to the Pt electrode of fuel cells. There is therefore a need to purify hydrogen prior to its use in fuel cells. Currently, there are two methods used, namely the pressure swing absorption method and the membrane separation method. Even though the membrane separation method is known to

CHAPTER 5. IMPLEMENTATION OF HYDROGEN PERMEATION
APPARATUS AND ITS APPLICATION TO INVESTIGATE
THE PERMEATION BEHAVIOUR OF Nb-Ni-Zr ALLOY MEMBRANES

be more efficient, the cost of Pd-Ag alloys that are currently used as hydrogen permeation membrane is prohibitive to the production of low cost and high purity hydrogen gas. The recent discovery of Nb-Ni-Zr alloys with high hydrogen permeability has provided a boost for the many attempts to develop palladium free permeation membranes [1-3, 9]. The Nb-Ni-Zr hydrogen permeation alloys have a composite microstructure where a niobium-rich bcc phase is reinforced by structural frameworks of a nickel/zirconium phase. The current work looks into the effect of annealing on the hydrogen permeability of Nb-Ni-Zr alloy samples. Nb has been reported to be the hydrogen permeable phase [1, 4, 9], and the process of annealing after rolling has been reported to restore and even enhance hydrogen permeability [5]. The effect of annealing on as-cast Nb-Ni-Zr alloys has not been reported to date but annealing after casting is known to improve ductility in other as-cast alloys [6]. Hence, it is important to clarify the effect of annealing on the hydrogen permeation and mechanical behaviour of Nb-Ni-Zr alloy membranes. The as-cast Nb-Ni-Zr permeation alloy membranes were prepared using the same sample preparation techniques as described in Chapter 3. For the annealing process, the test specimens were encapsulated in quartz tubes under a vacuum of 5×10^{-4} Pa prior to annealing in a furnace at a predetermined temperature for 1h. The samples were then removed from the furnace and left to cool before the quartz tubes were opened for subsequent characterization.

In this chapter, details on the implementation of the hydrogen permeation technique used to test the samples are given and the effects of annealing on the hydrogen permeation properties are investigated.

5.2 Hydrogen permeation measuring technique

Due to the unavailability of a hydrogen permeation measuring apparatus at Monash University, it was required to build such a device. This was made possible through the training provided by the research group of Professors K. Aoki and K. Ishikawa from the Kitami Institute of technology, Japan. Professors Aoki and Ishikawa are pioneers in the field of Nb-based hydrogen permeation membranes and have published numerous well-cited papers on the subject [1-3, 5, 7-9]. Section 5.2 provides details on the techniques involved in the preparation of the samples and in the measurement of the hydrogen permeation that had to be implemented and tested before use.

5.2.1 Palladium coating

A palladium (Pd) coating is required on the surface of the membrane for hydrogen permeation testing because of its catalytic effect on the adsorption of H on the membrane surface. A Pd coating also reduces the risk of oxidation at elevated temperature. For this purpose a high purity Pd target was purchased and used in an ULVAC sputter coater. The system was operated under an Ar atmosphere after being evacuated.

To establish the time required to coat a layer of 190 nm using a sputtering current of 5 mA, a small disc shape sample of known dimensions was coated with Pd. The weight of the sample was measured at 5 min intervals when coating, for a total period of 20 min. The calculations were made based on the relationship between density, mass and volume shown below;

$$\rho = \frac{m}{v} = \frac{m}{A \times l} \quad (5.1)$$

$$\Delta l = \frac{\rho \times A}{\Delta m} \quad (5.2)$$

CHAPTER 5. IMPLEMENTATION OF HYDROGEN PERMEATION APPARATUS AND ITS APPLICATION TO INVESTIGATE THE PERMEATION BEHAVIOUR OF Nb-Ni-Zr ALLOY MEMBRANES

where m is the mass, Δm the change in mass, ρ the density of pure Pd, A the area of the sample being coated, l the thickness of Pd, and Δl the change in thickness of the Pd coating. The area of the sample was 4.52 cm^2 and the density of Pd was taken to be 12.02 g/cm^3 .

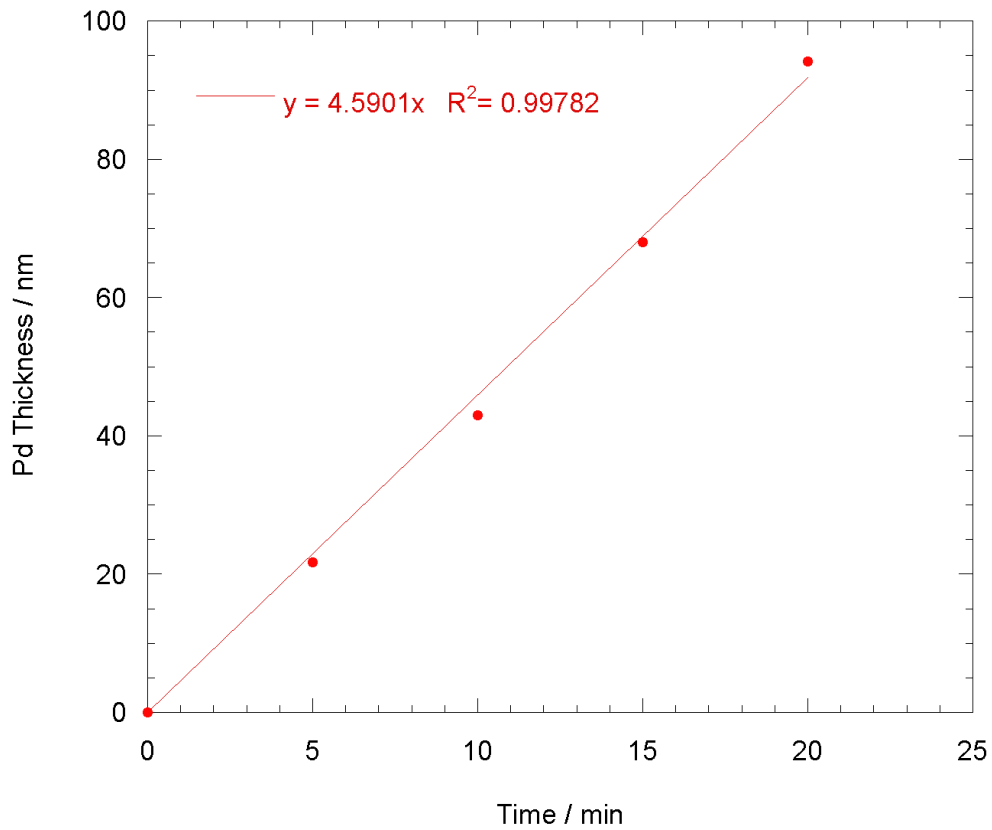


Figure 5.1. Pd deposition rate with a current of 5 mA.

The relationship between the Pd layer thickness and sputtering time is illustrated in Figure 5.1. Based on the equation of the line of best fit shown in Figure 5.1, the time required for coating the sample can be expressed by the equation below,

$$y = 4.59x \quad (5.3)$$

where y is the thickness of Pd coating in nm and x is the time in minutes.

5.2.2 Implementation of the pressure driven hydrogen permeation measuring technique

The first technique to be established for the hydrogen permeation was the pressure driven hydrogen permeation apparatus, which took about 12 months to complete. More details on the implementation of an electrochemical method used to measure hydrogen permeation are given in Chapter 6. This pressure driven system is similar to the one reported by Hashi et al. [8]. A schematic illustration of the hydrogen permeation measuring apparatus that was built is shown in Figure 5.2. Two silver coated stainless steel gaskets are used to seal the Pd coated sample disk. The system built has been modified to also have an argon inlet. The hydrogen permeation testing apparatus is designed with an extra cross-connect valve to allow the use of the argon sweep gas on the feed side, sweep side or both. After the sample has been sealed between the two gaskets, the feed and sweep sides are isolated and an argon pressure test is used to check the integrity of the sample and the seal. In the event of a leak, which involves a flow of argon being detected by the mass flow meter, the sample needs to be changed and new gaskets used.

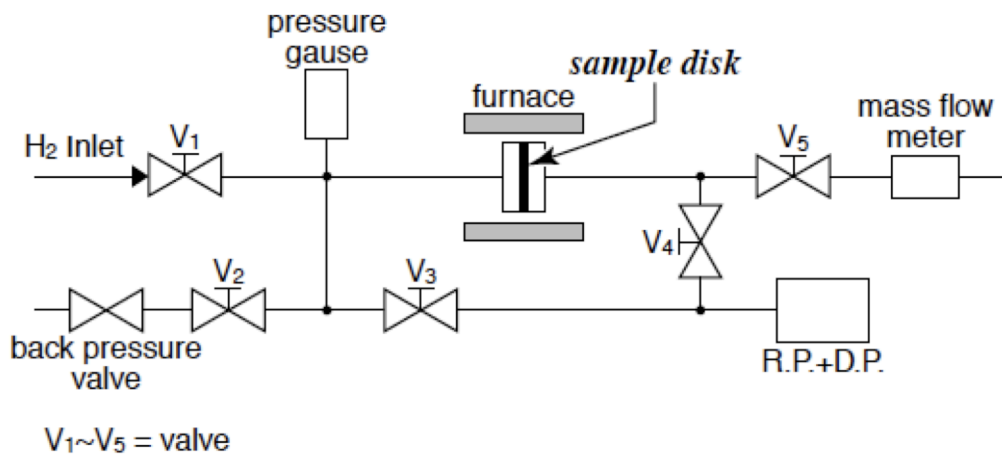


Figure 5.2. Schematic illustration of the hydrogen permeation measuring apparatus [8].

After the pressure test was complete, the chambers on both sides of the sample were evacuated using a diffusion pump to a pressure below 5×10^{-3} Pa. The sample was then

CHAPTER 5. IMPLEMENTATION OF HYDROGEN PERMEATION
 APPARATUS AND ITS APPLICATION TO INVESTIGATE
 THE PERMEATION BEHAVIOUR OF Nb-Ni-Zr ALLOY MEMBRANES

heated to the temperature of 673 K. The furnace was kept at this temperature until the temperature at the sample became stabilized. Note that the calibrations of the tube furnace will be discussed further below. High purity hydrogen gas (99.9999%) of 0.1 and 0.2 MPa was introduced into the downstream and upstream sides respectively. After the stabilization of the hydrogen flow rate, the experiment was started. At 673 K, the feed hydrogen pressure was increased from 0.2 to 0.5 MPa by 0.05 MPa increments and the hydrogen flux was recorded. The temperature was then reduced from 673 K to 523 K by 50 K increments and the hydrogen flux measured at each temperature. The hydrogen flux J was measured using the mass flow meter. In the ideal case of a solid solution state and if the hydrogen permeation rate Φ is dependent on the hydrogen diffusion coefficient through the membrane, then J can be expressed by using Fick's first law,

$$J = -D \cdot \frac{\Delta C}{\Delta x} = D \cdot \frac{C_u - C_d}{L} \quad (5.4)$$

where D and L are the hydrogen diffusion coefficient and the thickness of the membrane respectively. C_u and C_d are the H concentrations in the upstream and downstream side of the membrane respectively. Equation (5.4) shows that J is proportional to the H concentration gradient $\Delta C/\Delta x$. If H absorption obeys Sieverts' law, then the H concentration C is expressed as follows;

$$C = K \cdot P^{0.5} \quad (5.5)$$

where K and P are the H solubility coefficient and hydrogen pressure respectively.

The following equation is obtained by combining Equations 5.4 and 5.5.

$$J \times L = \Phi (P_u^{0.5} - P_d^{0.5}) \quad (5.6)$$

CHAPTER 5. IMPLEMENTATION OF HYDROGEN PERMEATION APPARATUS AND ITS APPLICATION TO INVESTIGATE THE PERMEATION BEHAVIOUR OF Nb-Ni-Zr ALLOY MEMBRANES

where P_u and P_d are the hydrogen pressure at upstream and downstream relative to the sample respectively. This relationship can be verified by plotting $(J \times L)$ versus $(P_u^{0.5} - P_d^{0.5})$. The hydrogen permeability can then be found by doing a linear regression analysis of the results. The hydrogen permeability, Φ , is the product of hydrogen diffusion coefficient, D , and hydrogen solubility coefficient, K . The unit of Φ is $\text{molH}_2\text{m}^{-1}\text{s}^{-1}\text{Pa}^{-0.5}$.



Figure 5.3. Hydrogen permeation measuring apparatus implemented at Monash University.

CHAPTER 5. IMPLEMENTATION OF HYDROGEN PERMEATION APPARATUS AND ITS APPLICATION TO INVESTIGATE THE PERMEATION BEHAVIOUR OF Nb-Ni-Zr ALLOY MEMBRANES



Figure 5.4. Picture of the furnace and a magnified image of the sample holder.

5.2.3 Calibration of the pressure driven hydrogen permeation apparatus

Before the apparatus could be used, a series of calibration experiments and tests were carried out to ensure the reliability of the device. The furnace was the first to be calibrated. The temperature homogeneity within the furnace was investigated with by using a thermocouple that was placed at various positions from the exact sample location within the furnace along the upstream and downstream feed lines. Figure 5.5 shows that the temperature around the location of the sample was quite consistent, with a variation of ± 0.35 K within a distance of 25 mm.

CHAPTER 5. IMPLEMENTATION OF HYDROGEN PERMEATION APPARATUS AND ITS APPLICATION TO INVESTIGATE THE PERMEATION BEHAVIOUR OF Nb-Ni-Zr ALLOY MEMBRANES

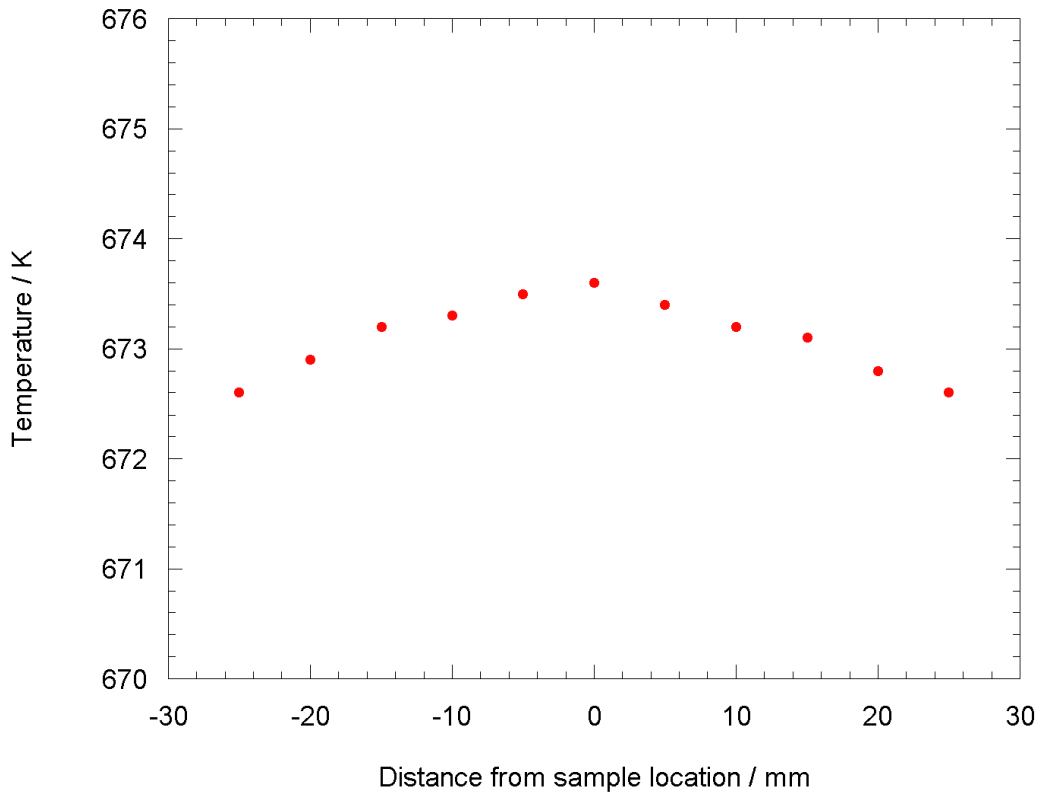


Figure 5.5. Temperature variation within the furnace around the neutral position of the sample.

The second furnace calibration looked into was the difference between the temperature displayed and the real sample temperature. Figure 5.6 shows the temperature of the heater's display unit and the simultaneous temperature at the exact sample position in the furnace at regular time intervals for a period of 2 hours. The temperature at the sample location was monitored with the help of a digital thermocouple. The temperature range surveyed was between 523 K and 823 K, which encompass the common experimental temperature range of hydrogen permeation tests. It was observed that at higher temperatures the sample would reach equilibrium more rapidly when compared to lower temperatures. The time varied from 45 minutes at higher temperatures, increasing to 60 minutes at the lower end of the thermal spectrum.

CHAPTER 5. IMPLEMENTATION OF HYDROGEN PERMEATION APPARATUS AND ITS APPLICATION TO INVESTIGATE THE PERMEATION BEHAVIOUR OF Nb-Ni-Zr ALLOY MEMBRANES

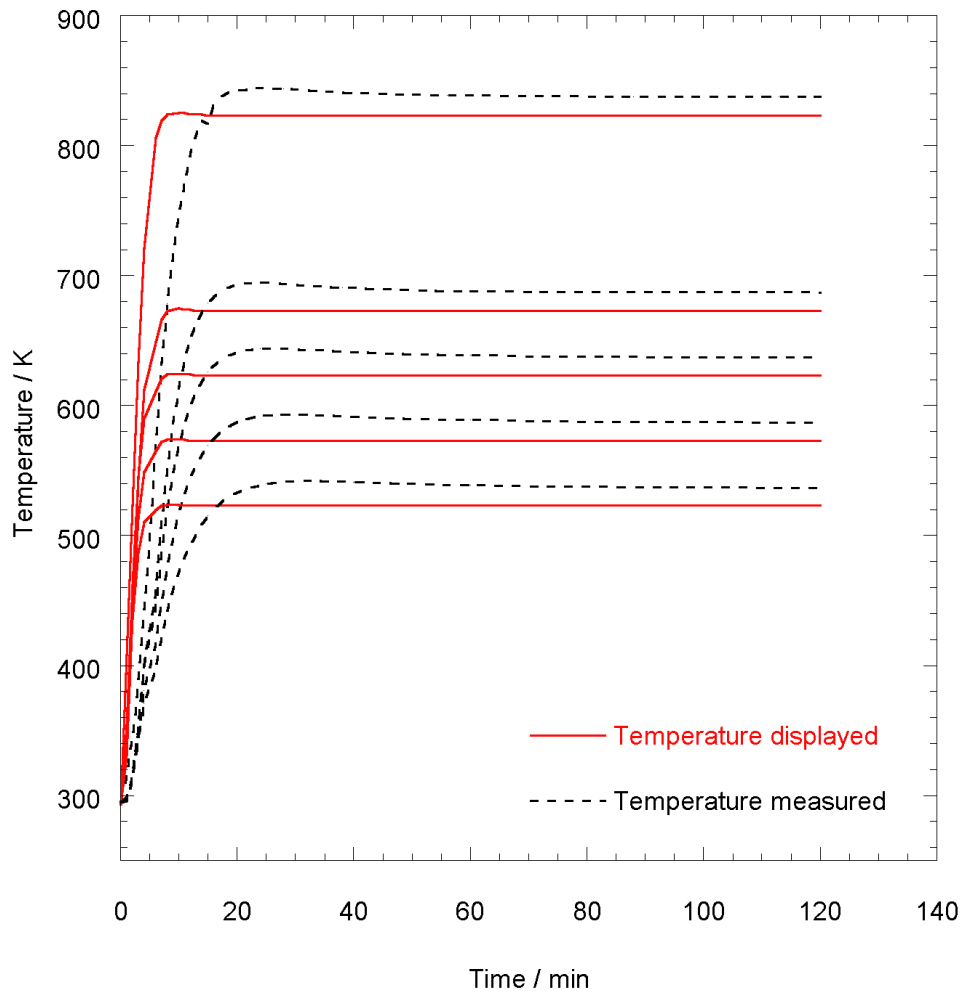


Figure 5.6. Comparison between the temperature measured and the temperature displayed by the heater's display unit over a 2 h period.

The relationship between the displayed temperature and the actual sample temperature was established by a linear regression of the two sets of data, see Figure 5.7. The relationship is given by,

$$y = 0.998x - 12.8 \quad (5.5)$$

where y is the temperature which needs to be set on the furnace control unit and x is the required temperature at the sample.

CHAPTER 5. IMPLEMENTATION OF HYDROGEN PERMEATION APPARATUS AND ITS APPLICATION TO INVESTIGATE THE PERMEATION BEHAVIOUR OF Nb-Ni-Zr ALLOY MEMBRANES

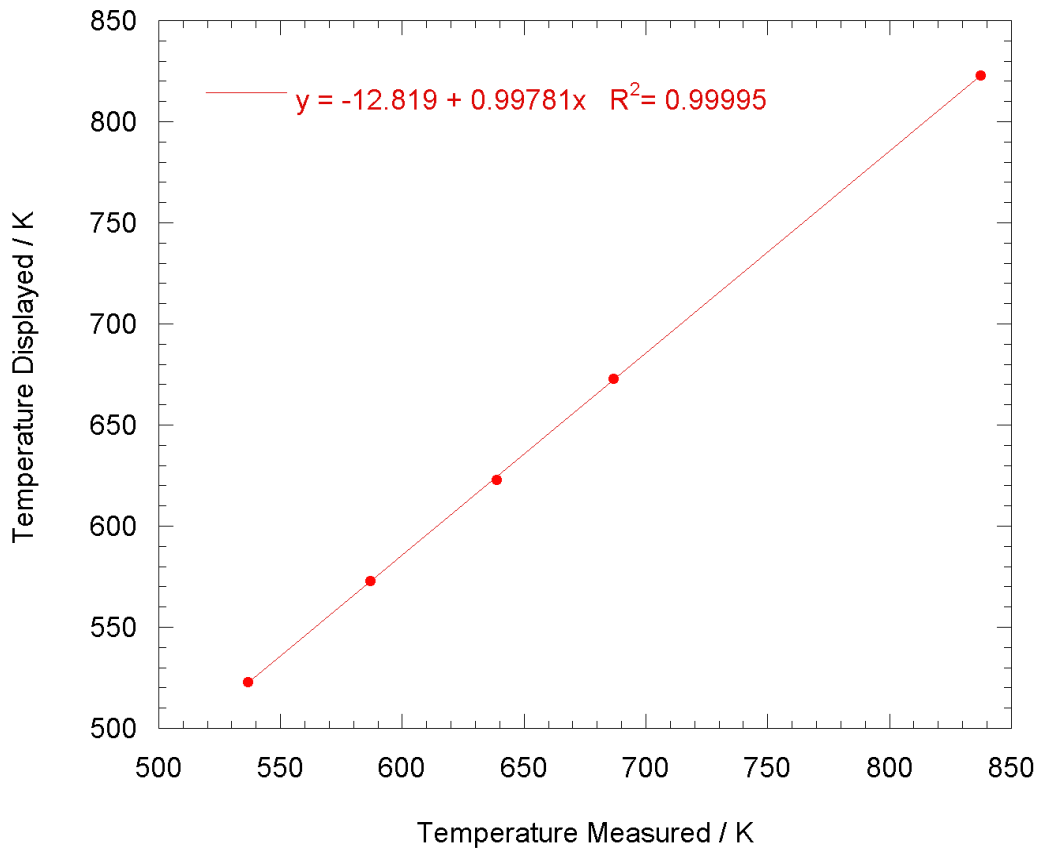


Figure 5.7. Estimation of the relationship between the temperature displayed and the real sample temperature for calibration purposes.

The hydrogen permeability of the pressure driven hydrogen permeation apparatus was verified based on the permeation results of the exact same samples that were tested previously at the laboratory of Professor Aoki at the Kitami Institute of Technology (KIT). The samples tested at KIT were $\text{Nb}_{30}\text{Ti}_{35}\text{Co}_{35}$ samples. The hydrogen permeation results obtained from the locally made apparatus were then compared to the results obtained from the well-established research laboratory at the Kitami Institute of Technology. It can be seen in Figure 5.8 that the hydrogen permeation results obtained at Monash University were consistent with the ones done at KIT. Therefore, the hydrogen permeation testing apparatus built at Monash University was deemed reliable.

CHAPTER 5. IMPLEMENTATION OF HYDROGEN PERMEATION APPARATUS AND ITS APPLICATION TO INVESTIGATE THE PERMEATION BEHAVIOUR OF Nb-Ni-Zr ALLOY MEMBRANES

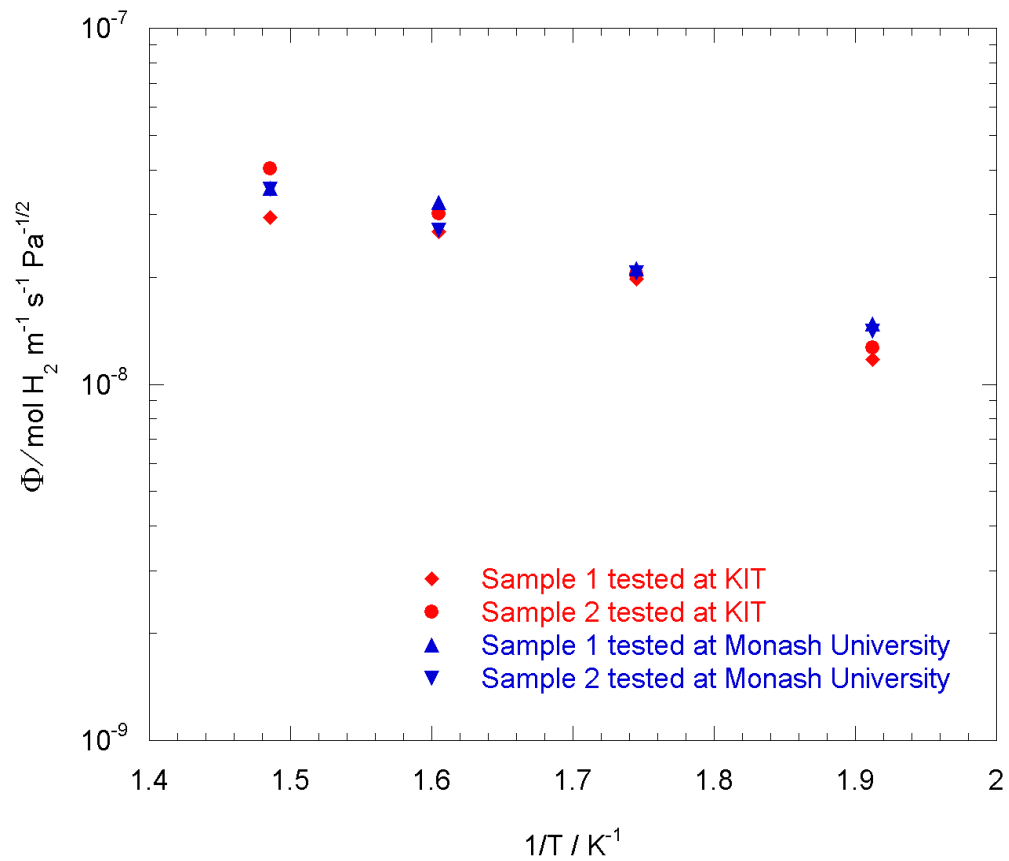


Figure 5.8. Confirmation of the reliability of the hydrogen permeation data produced at Monash University through a comparison of the $\text{Nb}_{30}\text{Ti}_{35}\text{Co}_{35}$ data obtained at the Kitami Institute of Technology in Hokkaido, Japan.

5.3 Results

5.3.1 Hydrogen permeation of annealed Nb-Ni-Zr membranes

The plots of $(J \times L)$ vs. $(P_u^{0.5} - P_d^{0.5})$ at 673 K for the Nb₄₀Ni₃₀Zr₃₀ alloy in the as-cast state and after annealing for 1 h between 723 K and 1123 K are shown in Figure 5.9. From this plot, it can be observed that annealing for 1 h at higher temperatures leads to an increase in the hydrogen flux passing through the membrane. It is evident that the relationship of the hydrogen flux at 673 K to the square root of the pressure difference between the upstream and downstream sides for the as-cast and annealed Nb₄₀Ni₃₀Zr₃₀ samples obeys Sievert's law and is well described by Equation 2.3. Hence, the hydrogen permeability is obtained from the gradient of the line of best fit.

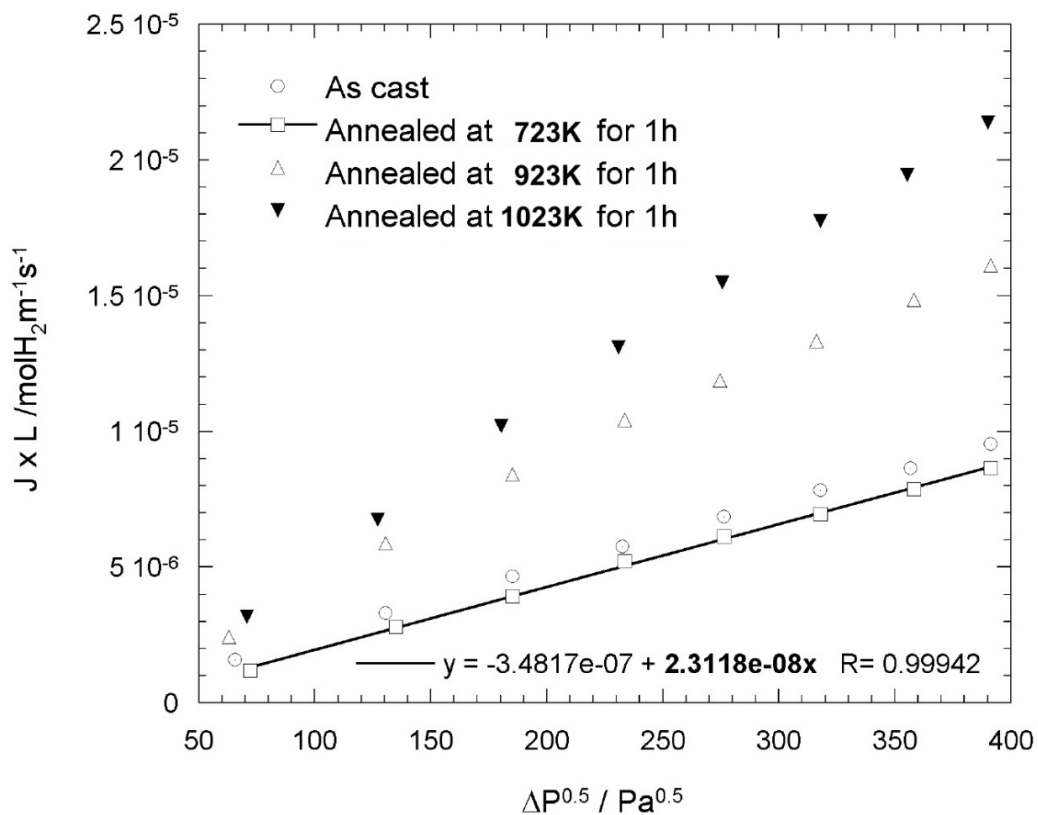


Figure 5.9. Plots of $(J \times L)$ vs. $(P_u^{0.5} - P_d^{0.5})$ at 673 K for the Nb₄₀Ni₃₀Zr₃₀ alloy as-cast and after annealing for 1 h between 723 K and 1123 K.

CHAPTER 5. IMPLEMENTATION OF HYDROGEN PERMEATION APPARATUS AND ITS APPLICATION TO INVESTIGATE THE PERMEATION BEHAVIOUR OF Nb-Ni-Zr ALLOY MEMBRANES

The hydrogen permeability (Φ) for Nb₄₀Ni₃₀Zr₃₀, Nb₃₅Ni_{32.5}Zr_{32.5} and Nb₃₀Ni₃₅Zr₃₅ alloys in the as-cast state and after annealing for 1 h at different temperatures is given in Figure 5.10. These values were obtained from the $(J \times L)$ vs. $(P_u^{0.5} - P_d^{0.5})$ plots. The permeability values of the Nb₄₀Ni₃₀Zr₃₀, Nb₃₅Ni_{32.5}Zr_{32.5} and Nb₃₀Ni₃₅Zr₃₅ alloys annealed for 1 h at 1123 K were consistently higher than those of the as-cast samples, indicating that annealing is beneficial to the improvement of hydrogen permeation behaviour in these alloys. It can also be observed that the hydrogen permeability of the samples annealed at 1123 K shows a tendency to increase with increasing Nb content.

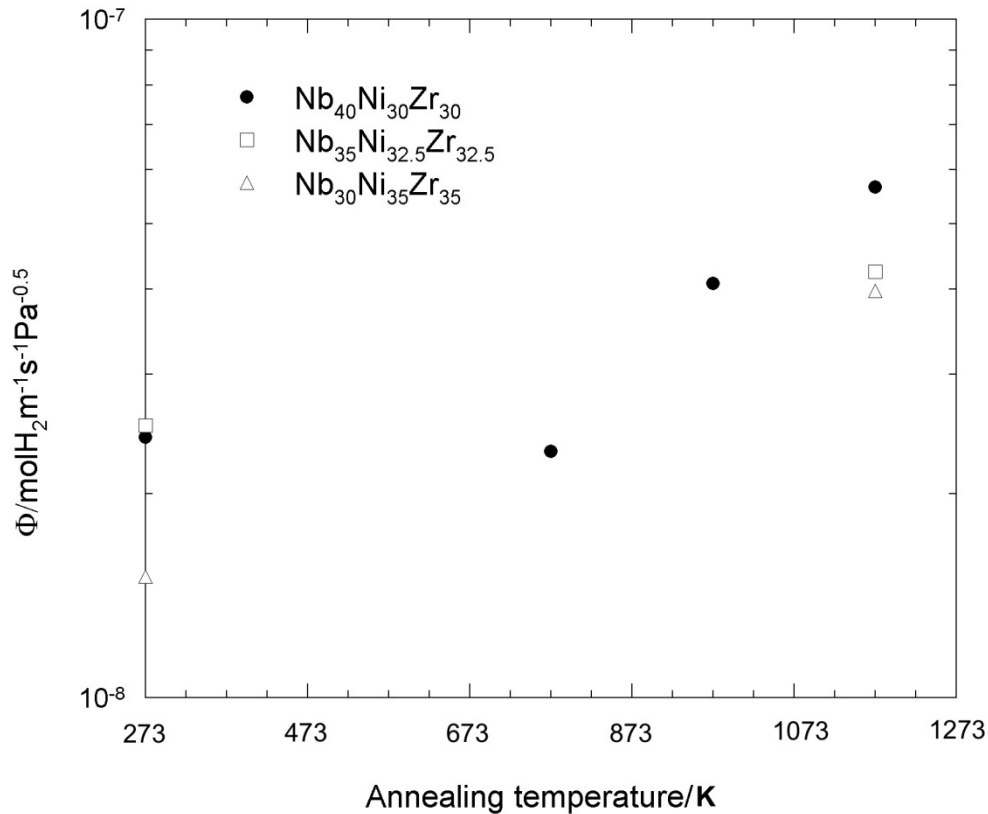


Figure 5.10. The hydrogen permeability (Φ) for Nb₄₀Ni₃₀Zr₃₀, Nb₃₅Ni_{32.5}Zr_{32.5} and Nb₃₀Ni₃₅Zr₃₅ alloys at 673 K in the as-cast state and after annealing for 1 h at different temperatures.

The XRD traces of the Nb-Ni-Zr alloys in the as-cast state and after annealing for 1 h at 1123 K is shown in Figure 5.11. The phase constituent of these alloys is consistent with that of the phase diagram. The presence of the desired microstructure comprised of Nb and NiZr phase is confirmed.

CHAPTER 5. IMPLEMENTATION OF HYDROGEN PERMEATION APPARATUS AND ITS APPLICATION TO INVESTIGATE THE PERMEATION BEHAVIOUR OF Nb-Ni-Zr ALLOY MEMBRANES

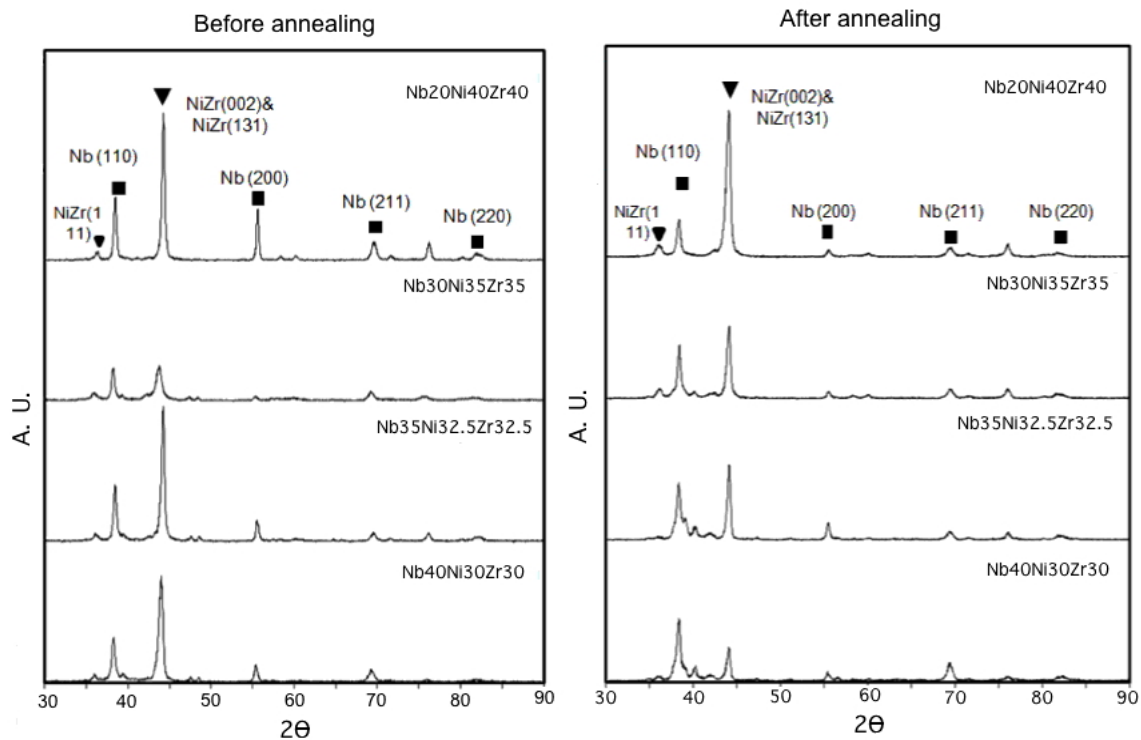


Figure 5.11. The XRD traces of the Nb-Ni-Zr alloys in the (a) as-cast state and (b) after annealing for 1 h at 1123 K.

The SEM micrographs of Nb₄₀Ni₃₀Zr₃₀ alloy in (a) as-cast state and (b) after annealing for 1 h at 1123 K before the hydrogen permeation test can be observed in Figure 5.12. It can be observed that there is no discernable microstructural change in the alloys after a short annealing period of 1 h at 1123 K.

CHAPTER 5. IMPLEMENTATION OF HYDROGEN PERMEATION APPARATUS AND ITS APPLICATION TO INVESTIGATE THE PERMEATION BEHAVIOUR OF Nb-Ni-Zr ALLOY MEMBRANES

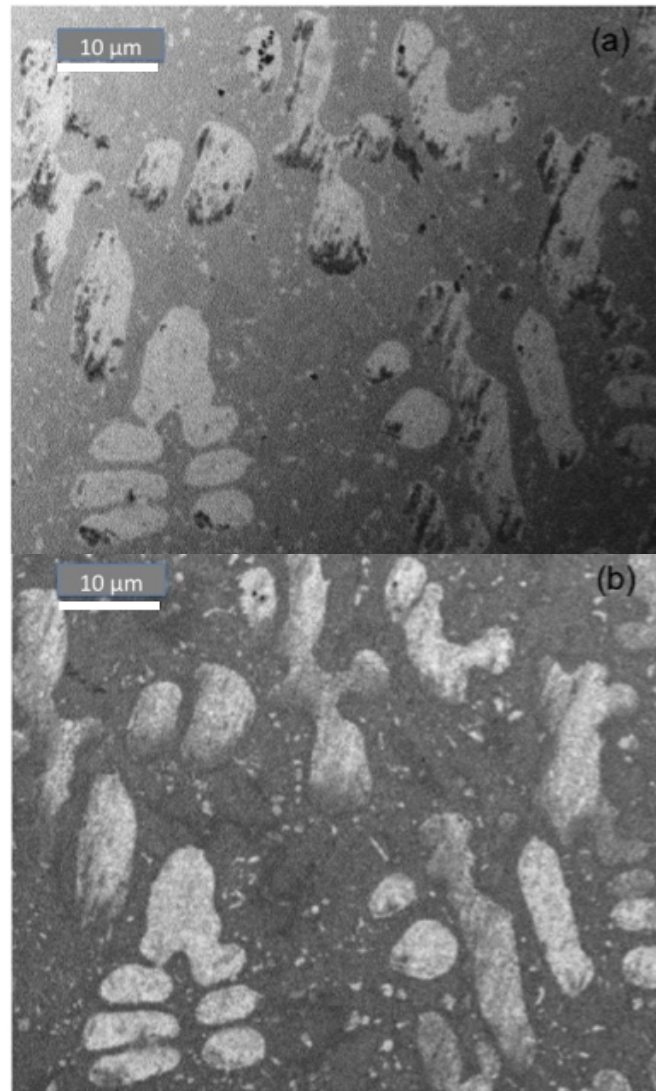


Figure 5.12. SEM micrographs of Nb₄₀Ni₃₀Zr₃₀ alloy in (a) as-cast state and (b) after annealing for 1 h at 1123 K before the hydrogen permeation test.

5.3.2 Fracture behaviour of annealed Nb-Ni-Zr membranes

During the hydrogen permeability test of the samples at 673 K, there was no evidence of cracking in the membrane. After the measurements at 673 K, the hydrogen pressure and temperature were lowered to 0.1 MPa and 623 K respectively. After waiting 30 min for the temperature to stabilize, the hydrogen permeability test was repeated. However, it was clearly evident that the samples had cracked during cooling to 623 K, as an instant large hydrogen flux was evident when the upstream H pressure was increased. Figure 5.13 shows the SEM micrographs of the samples after the hydrogen permeation test at 623 K for (a)

CHAPTER 5. IMPLEMENTATION OF HYDROGEN PERMEATION
APPARATUS AND ITS APPLICATION TO INVESTIGATE
THE PERMEATION BEHAVIOUR OF Nb-Ni-Zr ALLOY MEMBRANES

Nb₄₀Ni₃₀Zr₃₀ and (b) Nb₃₀Ni₃₅Zr₃₅ as-cast alloys. On both images a clear gap is seen on the surface of the sample, indicating that cracking took place during the permeation test at 623 K. The cracking paths observed seem to vary between samples with high Nb content and low Nb content. It can be seen that in the Nb₄₀Ni₃₀Zr₃₀ alloy the crack propagates through the region with a lighter contrast, which corresponds to the Nb phase. Hence, this can be described as transgranular. On the other hand the crack in the Nb₃₀Ni₃₅Zr₃₅ sample propagates mostly in the matrix along and around the Nb and NiZr particles and can therefore be described as intergranular.

CHAPTER 5. IMPLEMENTATION OF HYDROGEN PERMEATION APPARATUS AND ITS APPLICATION TO INVESTIGATE THE PERMEATION BEHAVIOUR OF Nb-Ni-Zr ALLOY MEMBRANES

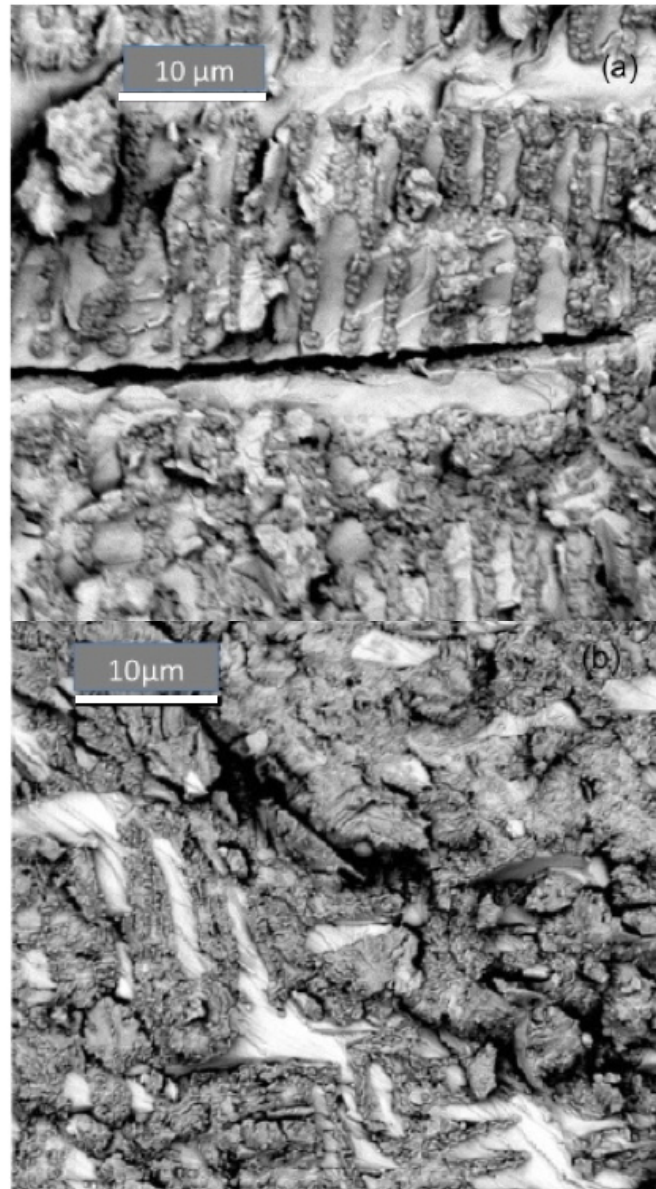


Figure 5.13. SEM images in topographic contrast mode of the (a) Nb₄₀Ni₃₀Zr₃₀ and (b) Nb₃₀Ni₃₅Zr₃₅ as-cast alloys cracked samples. The cracking occurred within the 30 min waiting period after the Φ measurement at 673 K, during which the hydrogen pressure and temperature were lowered to 0.1 MPa and 623 K respectively.

The SEM images of cracked samples after the hydrogen permeation test of Nb₄₀Ni₃₀Zr₃₀ alloy in the (a) as-cast state and (b) after annealing for 1 h at 1123 K can be observed in Figure 5.14. It can be observed that in both cases the crack propagation is transgranular.

CHAPTER 5. IMPLEMENTATION OF HYDROGEN PERMEATION APPARATUS AND ITS APPLICATION TO INVESTIGATE THE PERMEATION BEHAVIOUR OF Nb-Ni-Zr ALLOY MEMBRANES

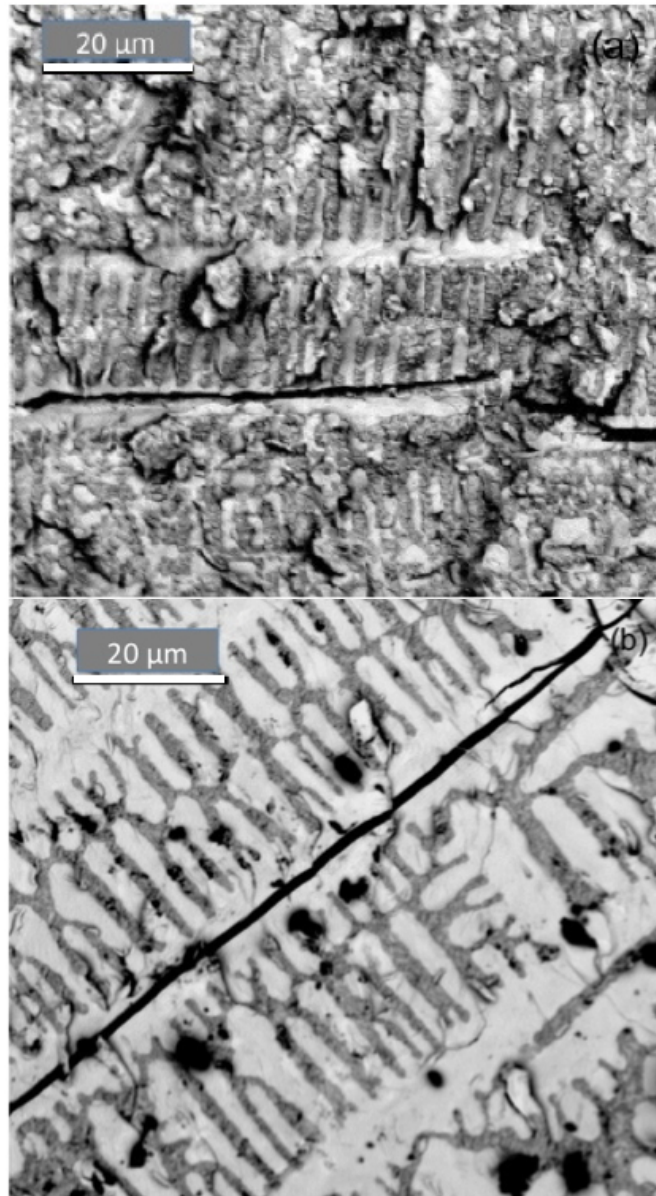


Figure 5.14. SEM images in topographic contrast mode of the cracked Nb₄₀Ni₃₀Zr₃₀ alloy samples in the (a) as-cast state and (b) after annealing for 1 h at 1123 K. The cracking occurred within the 30 min waiting period after the Φ measurement at 673 K, during which the hydrogen pressure and temperature were lowered to 0.1 MPa and 623 K respectively.

5.4 Discussion

5.4.1 Effect of annealing on the hydrogen permeability

The hydrogen permeability of the Nb₄₀Ni₃₀Zr₃₀ sample annealed at 723 K for 1 h is found to be 2.31×10^{-8} [molH₂m⁻¹s⁻¹Pa^{-0.5}], which is 1.6 times higher than that of Pd. This annealed

CHAPTER 5. IMPLEMENTATION OF HYDROGEN PERMEATION
APPARATUS AND ITS APPLICATION TO INVESTIGATE
THE PERMEATION BEHAVIOUR OF Nb-Ni-Zr ALLOY MEMBRANES

sample showed little improvement in hydrogen permeability over its as-cast counterpart. Annealing of the Nb₄₀Ni₃₀Zr₃₀ samples at 923 K and 1123 K for 1 h resulted in Φ of 4.24×10^{-8} and 5.66×10^{-8} [molH₂m⁻¹s⁻¹Pa^{-0.5}], respectively, which are 1.8 and 2.3 times higher than that of their as-cast equivalent. A similar increase in Φ after isochronal annealing of the as-cast sample is also observed in Nb-Ni-Zr alloys with lower Nb content, as illustrated in Figure 5.10. The Φ of Nb₄₀Ni₃₀Zr₃₀, Nb₃₅Ni_{32.5}Zr_{32.5} and Nb₃₀Ni₃₅Zr₃₅ alloys annealed at 1123 K for 1 h are 5.66×10^{-8} , 4.25×10^{-8} and 3.98×10^{-8} [molH₂m⁻¹s⁻¹Pa^{-0.5}], respectively, which is an improvement of 2.3, 1.7 and 2.6 times, respectively, over the Φ of their corresponding as-cast samples at a test temperature of 673 K. Tang et al. has reported an improvement of 1.4 times in the Φ of a Nb₄₀Ti₁₈Zr₁₂Ni₃₀ alloy membrane annealed at 673 K for 605 ks when compared to its as-cast counterpart [5]. Even though an improvement in Φ of the as-cast alloy has been reported after annealing, the reasons for this effect remain unclear. The Φ of 2.32×10^{-8} [molH₂m⁻¹s⁻¹Pa^{-0.5}] for the Nb₄₀Ni₃₀Zr₃₀ as-cast alloy in the current experiment was found to be half the value reported by Ishikawa et al. on an identical as-cast Nb₄₀Ni₃₀Zr₃₀ alloy as shown in Figure 5.15. The Φ value reported was 4.64×10^{-8} [molH₂m⁻¹s⁻¹Pa^{-0.5}] [9]. From Figure 5.10, the Φ of the Nb₄₀Ni₃₀Zr₃₀ sample annealed at 1123 K for 1 h shows a recovery and a slight improvement on the Φ of 4.64×10^{-8} [molH₂m⁻¹s⁻¹Pa^{-0.5}] reported by Ishikawa et al. [9].

Given the fact that lattice strains have an impact on hydrogen diffusion, the discrepancy between the Φ values of two chemically identical Nb₄₀Ni₃₀Zr₃₀ alloy membranes in as-cast state may be attributed to the possible difference in the magnitudes of residual stresses within each membrane. Residual stresses are described as self-equilibrating internal stresses in a material that is free of applied forces, external constraints and temperature gradients [10]. They are mostly the undesired byproduct of processing and are commonly found in cast, welded, forged and extruded parts [11, 12]. James et al. described residual stresses as ‘an inescapable consequence of manufacturing and fabrication processes’ in their analysis of residual stresses in aluminium and steel welds via synchrotron

CHAPTER 5. IMPLEMENTATION OF HYDROGEN PERMEATION APPARATUS AND ITS APPLICATION TO INVESTIGATE THE PERMEATION BEHAVIOUR OF Nb-Ni-Zr ALLOY MEMBRANES

and neutron diffraction [11], while Ladoss and Apelian stated that residual stresses are present in all alloy systems [13]. Residual stresses are highly dependent on the processing conditions and it is difficult to predict the residual stress levels, but it is known that the most common cause of severe residual macrostresses is non-uniform cooling [11]. The arc-melting technique used to melt the Nb₄₀Ni₃₀Zr₃₀ sample tested involves non-uniform cooling of the ingot. The bottom of the ingot in contact with the copper hearth will cool at a much faster rate than the rest of the surface. This non-uniform cooling condition is likely to cause severe residual stresses within the Nb₄₀Ni₃₀Zr₃₀ alloys to varying degrees depending on the arc-melting conditions. Based on the work of Lewis et al., it is known that lattice strains have an impact on hydrogen diffusion and permeation through membranes [14-16].

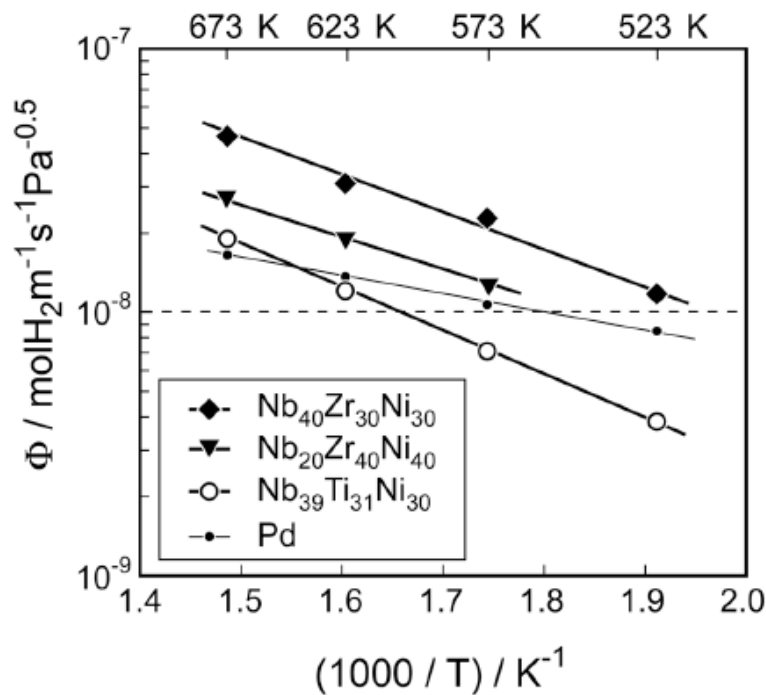


Figure 5.15. Temperature dependence of hydrogen permeability Φ of as-cast Nb₄₀Ni₃₀Zr₃₀, Nb₂₀Ni₄₀Zr₄₀, Nb₃₉Ti₃₁Ni₃₀ alloys and pure Pd in the form of an Arrhenius plot as reported by Ishikawa et al. [9].

Therefore, it is likely that the difference in Φ of the two chemically identical as-cast Nb₄₀Ni₃₀Zr₃₀ alloy membranes is due to the difference in residual stress levels from variations in the arc-melting conditions. The improvement in Φ after the annealing at 973

CHAPTER 5. IMPLEMENTATION OF HYDROGEN PERMEATION
APPARATUS AND ITS APPLICATION TO INVESTIGATE
THE PERMEATION BEHAVIOUR OF Nb-Ni-Zr ALLOY MEMBRANES

and 1173 K for 1h of the as-cast Nb₄₀Ni₃₀Zr₃₀ sample could be attributed to the relieving of some of the residual stresses present in the membrane. This is further supported by Figures 5.12 (a) and (b), which show the SEM micrographs of the same area of the Nb₃₅Ni_{32.5}Zr_{32.5} alloy in the as-cast state and after annealing at 1123 K for 1 h. Even though Tang et al. reported a microstructural change and an increase in Φ after annealing at 1273 K for 360 ks for a Nb₄₀Ti₁₈Zr₁₂Ni₃₀ alloy, no microstructural change is observed in the present case. It can be seen that both micrographs of the Nb₃₅Ni_{32.5}Zr_{32.5} alloy in Figure 5.12 are consistent with the one reported by Ishikawa et al. [9], where the large primary bcc-Nb phase (brighter contrast on SEM images) is surrounded by a Nb + NiZr matrix. The absence of microstructural change after annealing further supports the possibility of the lowering of residual stress levels, leading to improved Φ .

5.4.2 Failure analysis of the cracked samples

Even though the Φ is improved after annealing, the samples were more prone to suffer from hydrogen embrittlement and the membranes exhibited cracks. It must be noted that the Φ data come from samples that were not cracked. Figures 5.13 (a) and (b) show the SEM images of the as-cast Nb₄₀Ni₃₀Zr₃₀ and Nb₃₀Ni₃₅Zr₃₅ samples after they cracked during the hydrogen permeation tests. The cracking can be attributed to the formation of Nb hydrides as the temperature is reduced. The initial microstructure of large dendritic primary Nb phases surrounded by a NiZr + Nb matrix can be clearly seen in both micrographs. It can be seen that in the Nb₄₀Ni₃₀Zr₃₀ sample, the crack propagates through the Nb phase and can therefore be described as transgranular cracking. The crack in the Nb₃₀Ni₃₅Zr₃₅ sample on the other hand propagates mostly along and around the Nb particles and can therefore be described as intergranular cracking. From the current results, it can be deduced that the Nb content of the as-cast Nb-Ni-Zr alloys influenced the crack propagation path, with the alloys with a higher Nb content exhibiting transgranular cracking within the Nb phase, those with lower Nb content (Nb < 40 at.%) showed intergranular cracking within the interface with the NiZr + Nb matrix. This observation is supported by a report by Chin et al. who reported

CHAPTER 5. IMPLEMENTATION OF HYDROGEN PERMEATION
APPARATUS AND ITS APPLICATION TO INVESTIGATE
THE PERMEATION BEHAVIOUR OF Nb-Ni-Zr ALLOY MEMBRANES

intergranular cracking in a $\text{Ni}_{42}\text{Nb}_{28}\text{Zr}_{25}\text{Ta}_5$ crystalline membrane, which had a similar Nb content as the $\text{Nb}_{30}\text{Ni}_{35}\text{Zr}_{35}$ sample tested herein [18].

The transgranular cracking of the Nb phase in the $\text{Nb}_{40}\text{Ni}_{30}\text{Zr}_{30}$ crystalline sample indicates that the presence of H within the Nb phase. The presence of H in Nb lattice usually leads to the expansion of the lattice and the formation of Nb hydrides. The formation of these hydrides and the crystallographic changes associated with their formation could therefore have contributed to the crack initiation and propagation within the Nb phase during hydrogen permeation. Alloys with a higher Nb content have a lower volume of Ni-Zr matrix to support the expansion of bcc-Nb. Therefore, whenever Nb absorbs H there is a lower isostatic force exerted on the Nb phase by the matrix to minimize the lattice expansion required for the formation of Nb hydrides. For alloys with a lower Nb content, a higher volume of the hydrogen embrittlement resistant Ni-Zr matrix is present. This larger volume of supporting matrix hinders the lattice of Nb from expanding freely and therefore restricts the hydrogen concentration within the Nb phase and reduces the likelihood of producing hydrides. The easiest path for the crack to propagate in alloys with low Nb content is at the interface between the Nb and Ni-Zr phases, leading to intergranular cracking. A report by Owen et al., who reported on the effect of grain size and H concentration on the ductility of a Nb-based refractory alloy, suggests that grain boundaries in alloys act as traps for hydrogen and once the hydrogen concentration at these grain boundaries reaches a critical concentration, they may act as the intergranular crack initiators [18]. Owen et al. also suggested that H within the grains seems to be necessary to facilitate the mixed transgranular-intergranular crack propagation they observed [18]. This argument supports the transgranular crack propagation observed in Nb-rich Nb-Ni-Zr alloy membranes and the common knowledge that Nb has a high H permeability. Owen et al. also reported that intergranular cracks always act as initiators, followed by transgranular cracking [18].

CHAPTER 5. IMPLEMENTATION OF HYDROGEN PERMEATION
APPARATUS AND ITS APPLICATION TO INVESTIGATE
THE PERMEATION BEHAVIOUR OF Nb-Ni-Zr ALLOY MEMBRANES

The SEM images of the fractured surfaces of Nb₄₀Ni₃₀Zr₃₀ in the as-cast state and after annealing for 1 h at 1123 K are shown in Figures 5.14 (a) and (b), respectively, after cracking during the permeation test. It can be observed that transgranular cracking occurred through the Nb rich phase in both cases. Thus, it can be said that annealing has little effect on altering the path of crack propagation in this particular alloy. However, the mode of fracture is found to be composition dependent, particularly on the Nb content of the alloy.

5.5 Summary

The effect of annealing on the hydrogen permeation properties and microstructure of Nb-Ni-Zr alloys has been investigated. These alloys consist of the primary bcc-Nb phase surrounded by a Nb+NiZr phase mixture. The hydrogen permeability of Nb₄₀Ni₃₀Zr₃₀ was found to increase with increasing annealing temperature and was the highest when annealed at 1123 K for 1 h with a Φ 3.9 times larger than that of Pd and 2.3 times larger than that in the as-cast state. Annealing for 1 h at 1123 K was found to be beneficial to the Φ of all three Nb-Ni-Zr alloys tested, which was on average two times greater than that of their respective as-cast samples. The microstructure of the samples showed little change after annealing and the resistance to hydrogen embrittlement showed no marked improvement. SEM analysis of the fracture surface revealed that there were two main mechanisms of crack propagation, namely transgranular and intergranular cracking. The modes of fracture were found to be composition dependent with samples with high Nb content suffering from transgranular cracking and those with low Nb content from intergranular cracking. The mode of fracture was found to be unaffected by annealing.

CHAPTER 5. IMPLEMENTATION OF HYDROGEN PERMEATION
APPARATUS AND ITS APPLICATION TO INVESTIGATE
THE PERMEATION BEHAVIOUR OF Nb-Ni-Zr ALLOY MEMBRANES

5.6 References

- [1] K. Hashi, K. Ishikawa, T. Matsuda and K. Aoki, *Journal of Alloys and Compounds*, 425 (2006) 284
- [2] T. Takano, K. Ishikawa, T. Matsuda and K. Aoki; *Materials Transactions*, Vol. 45, No. 12 (2004) 3360
- [3] T. Wong, K. Suzuki, M. Gibson, K. Ishikawa, K. Aoki and L. L. Jones; *Scripta Materialia*, 62 (2010) 582
- [4] R. E. Buxbaum and A. B. Kinney; *Industrial and Engineering Chemistry Research*, 35 (1996) 530
- [5] H. Tang, K. Ishikawa and K. Aoki; *Materials Transactions*, Vol. 48, No.9 (2007) 2454
- [6] Y. A. Filip'eva, M. Volin, G. S. Baeva, N. Ya. Volina and A. E. Lokshina; *Metal Science and Heat Treatment*, Vol . 14, No.1 (1972) 3
- [7] K. Ishikawa, S. Tokui, K. Aoki, *Intermetallics*, 17 (2009) 109
- [8] K. Hashi, K. Ishikawa, T. Matsuda and K. Aoki, *Journal of Alloys and Compounds*, 368 (2004) 215
- [9] K. Ishikawa, T. Takano, T. Matsuda and K. Aoki, *Applied Physics Letters*, 87, (2005) 081906
- [10] G.E. Dieter: *Engineering Design*, 3rd ed., McGraw-Hill Book Co., New York, NY, 2000
- [11] M. N. James, D. J. Hughes, Z. Chen, H. Lombard, D. G. Hattingh, D. Asquith, J. R. Yates, and P. J. Webster, *Engineering Failure Analysis*, 14 (2007) 384
- [12] E. M. Johnson, T. R. Watkins, J. E. Schmidlin, and S. A. Dutler, *Metallurgical and Materials Transactions A*, Vol. 43A (2012) 1487
- [13] D. A. Lados and D. Apelian, *Metallurgical and Materials Transactions A*, 37A (1006) 133

CHAPTER 5. IMPLEMENTATION OF HYDROGEN PERMEATION
APPARATUS AND ITS APPLICATION TO INVESTIGATE
THE PERMEATION BEHAVIOUR OF Nb-Ni-Zr ALLOY MEMBRANES

- [14] F. A. Lewis, K. Kandasamy, and X. Q. Tong, *International Journal of Hydrogen Energy*, 27 (2002) 687
- [15] F. A. Lewis, X. Q. Tong, and K. Kandasamy, *International Journal of Hydrogen Energy*, 18 (1993) 481
- [16] F. A. Lewis, X. Q. Tong, K. Kandasamy, R. V. Bucur, and Y. Sakamoto, *Thermochimica Acta*, 218 (1993) 57
- [17] F. A. Lewis, Y. Sakamoto and X. Q. Tong, *International Journal of Hydrogen Energy*, 20 (1995) 365
- [18] C. V. Owen, D. S. Cheong, and O. Buck, *Metallurgical Transactions A*, Vol. 18A (1987) 857

Chapter 6

Effect of Nano-Scale Grain Refinement on the Hydrogen Permeation Performance of Nb-Ni-Zr Membranes

6.1 Introduction

In this chapter the effect of microstructure on the hydrogen permeation properties of chemically identical alloy membranes is investigated. The novelty of this work lies in the ability to isolate the effect of structural properties from other parameters affecting hydrogen permeation. The hydrogen permeation properties of the alloy are compared between chemically identical samples in amorphous, conventional crystalline, and nanocrystalline state.

Particular attention is given to the effect of nanostructural grain refinement on hydrogen permeation. Although the effects of grain boundaries in Nb-based membranes are yet to be studied, the hydrogen diffusivity in nanocrystalline Ni has been investigated. Arantes et al. [1] have shown that the hydrogen permeation of nanocrystalline (~100 nm) Ni is larger than that of microcrystalline Ni, due to improved hydrogen solubility and diffusivity, and another report by Marte and Kirchheim [2] has shown that the diffusivity of

CHAPTER 6. EFFECT OF NANO-SCALE GRAIN REFINEMENT
ON THE HYDROGEN PERMEATION PERFORMANCE
OF Nb-Ni-Zr MEMBRANES

hydrogen in nanocrystalline Ni, with a grain size of 50-100 nm, is about two orders of magnitude greater than that of bulk Ni. The hydrogen permeability of nickel in of itself is too low to be used as a hydrogen permeation membrane. However, there is substantial scope in the Nb-Ni-Zr alloy system, which has been reported to have hydrogen permeabilities as high and even greater than that of pure Pd [6]. As described in Chapters 2 and 4, melt-spun Nb-Ni-Zr alloys can be nanostructured by crystallization of an amorphous precursor phase. The ingots of Nb-Ni-Zr were first prepared in an argon arc furnace. The ingots were then melt-spun into amorphous ribbons. The melt-spun ribbons were punched into a disc shape or mechanically cut into a rectangular shape for annealing prior to the permeation test. More details on the implementation of the methodology and the formation of the nanostructure can be found in Chapters 3 and 4.

In this section, the effect of microstructural changes on the hydrogen permeation properties are investigated, with particular attention paid to the hydrogen solubility and hydrogen diffusivity in the alloys.

6.2 Hydrogen permeation measuring technique

The following techniques were required for the preparation of the samples and the measurement of the hydrogen permeation. They had to be implemented and tested, before being calibrated and the level of uncertainty assessed.

6.2.1 Implementation of an electrochemical hydrogen permeation measuring apparatus

An electrochemical hydrogen permeation testing apparatus was built for the hydrogen permeation measurements for alloy membranes that were too brittle to be tested by the pressure driven hydrogen permeation apparatus. The design of the cell is similar to that described by Devanathan and Stachurski [4]. This type of cell is widely used in studies of

CHAPTER 6. EFFECT OF NANO-SCALE GRAIN REFINEMENT
ON THE HYDROGEN PERMEATION PERFORMANCE
OF Nb-Ni-Zr MEMBRANES

hydrogen permeation and diffusion in metals and alloys. The apparatus implemented consists of two Pyrex compartments, each ending with a standard pipe flange. Each flange has a Teflon gasket with the side facing the sample polished flat. When the thin sample is loaded between the two gaskets, the two compartments are clamped together, which results in a watertight seal. Each unit carried a titanium mesh working electrode and a saturated calomel reference electrode, similar to the diagram shown in Figure 6.1. In the figure, the working electrodes are denoted by 1 and 4, the reference electrodes by 5 and 7, and the sample by number 6. The test solution consisted of 0.1 M NaOH solution. Inlets for the bubbling of nitrogen were also present. The experiment was carried out at a constant laboratory temperature of 296 K.

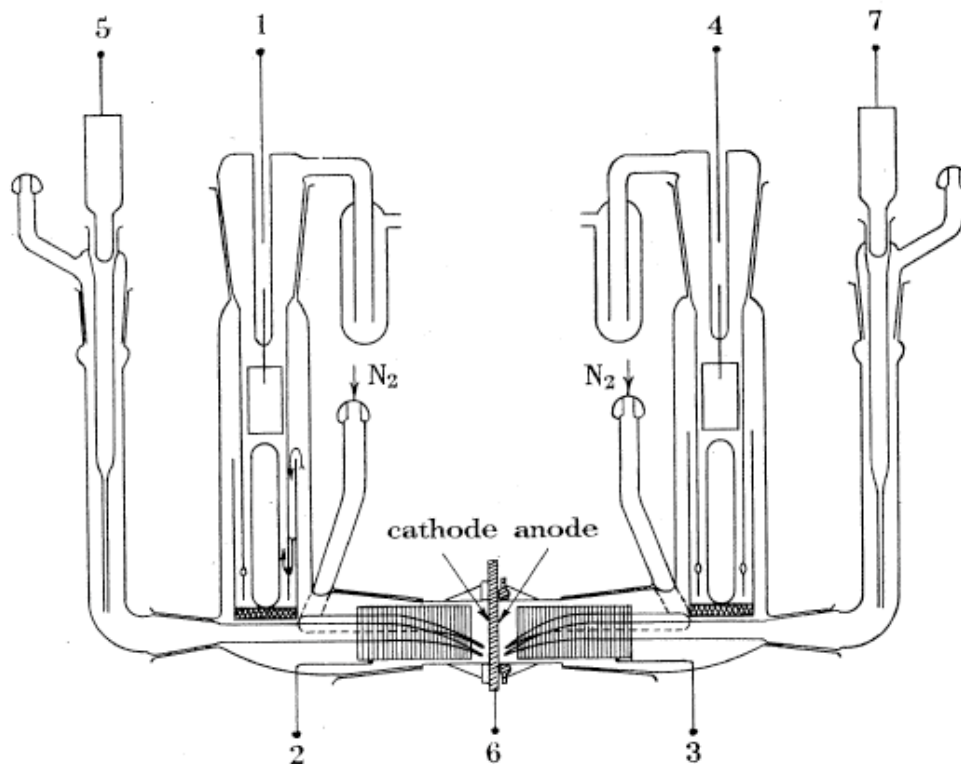


Figure 6.1. Schematic diagram of the Devanathan electrochemical cell [4].

This method requires that the adsorbed atomic hydrogen on one side of the sample be maintained at a fixed level, while on the other side it should always be negligibly small. These conditions are fulfilled by the cathodic polarization of one side and anodic

CHAPTER 6. EFFECT OF NANO-SCALE GRAIN REFINEMENT
ON THE HYDROGEN PERMEATION PERFORMANCE
OF Nb-Ni-Zr MEMBRANES

polarization of the opposite side as shown in Figure 6.2. The current in the anodic circuit that maintains zero coverage on one side of the membrane is by Faraday's law a direct measure of the instantaneous hydrogen permeation rate [4], which allows for the measurement of the rate of hydrogen permeation in the membrane concerned. This method has a high sensitivity and is ideal to measure membranes susceptible to hydrogen embrittlement. Fig. 6.3 shows the electrochemical hydrogen permeation apparatus cell.

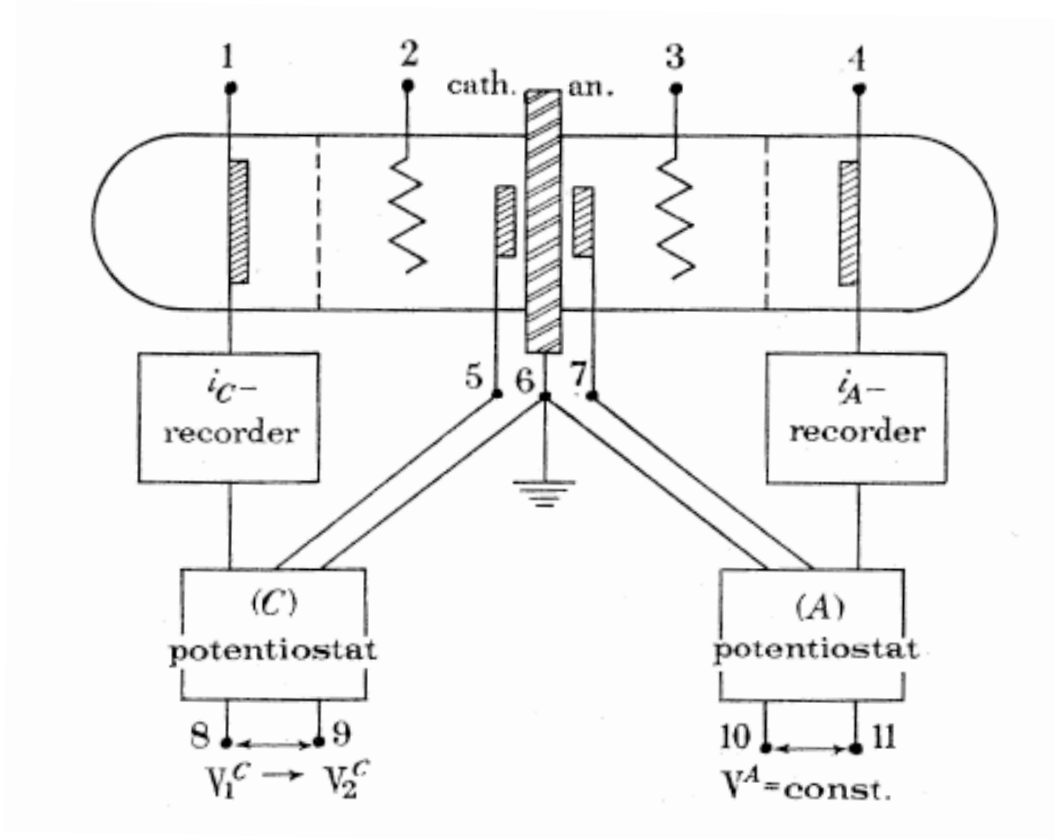


Figure 6.2. Electrical circuit of the system [4].

CHAPTER 6. EFFECT OF NANO-SCALE GRAIN REFINEMENT
ON THE HYDROGEN PERMEATION PERFORMANCE
OF Nb-Ni-Zr MEMBRANES

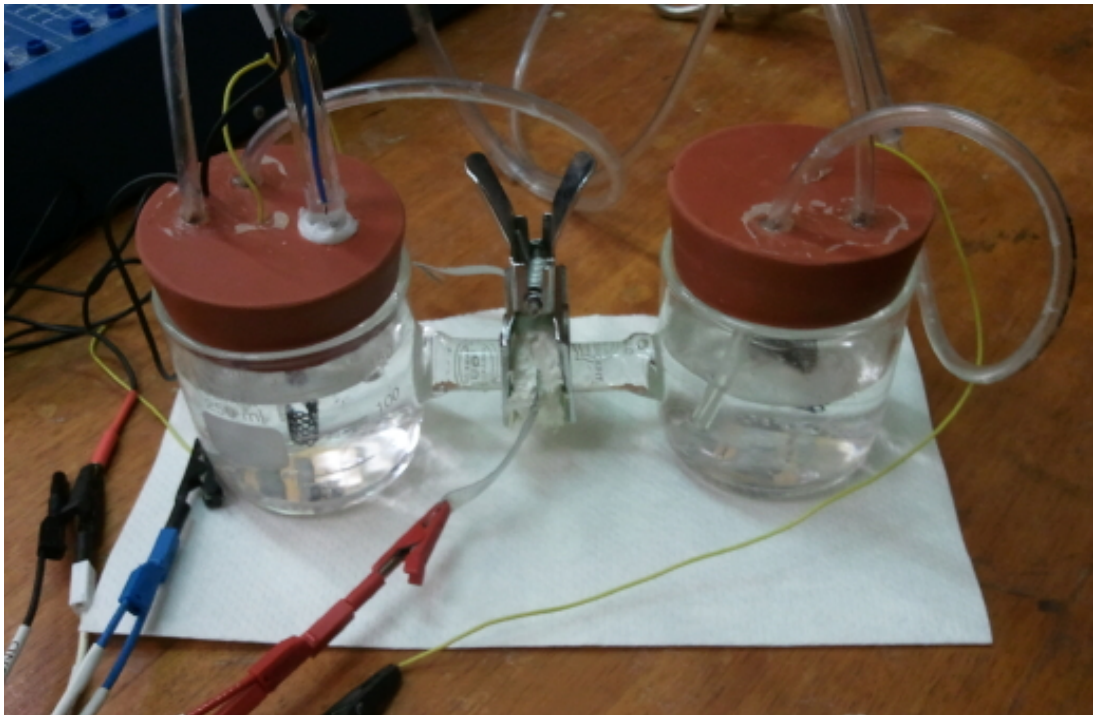


Figure 6.3. Photo of the electrochemical cell.

Before the commencement of each experiment, the anodic current is zero as the hydrogen concentrations on both the cathodic and anodic sides are identical. After the cathodic potential is applied, the current recorded on the anodic side initially remains unchanged, but soon increases rapidly before reaching a steady state. When the cathodic current is removed, the recorded anodic current decreases to zero exponentially.

6.2.2 Technique used to estimate the diffusivity of hydrogen

The diffusivity of hydrogen in the membrane can be calculated using several different techniques. The method used here is called the time lag method, which relies on the current readings of the increasing amount of hydrogen that has permeated through the membrane prior to a steady state permeation being achieved. The classical method of obtaining the diffusion constant by the time lag method required the integration of the rising transient. However, Devanathan has shown that the same value can be obtained by measuring the time at which the rate of permeation is 0.6299 times the steady-state current [4, 5]. The time lag

CHAPTER 6. EFFECT OF NANO-SCALE GRAIN REFINEMENT
ON THE HYDROGEN PERMEATION PERFORMANCE
OF Nb-Ni-Zr MEMBRANES

was evaluated by both methods and the results were found to be within 2 % of one another [5]. However, it must be noted that the lag time obtained by either method will be in error by an amount equal to the relaxation time, therefore in the case of membranes with larger thicknesses, the diffusion constant could be as much as 20 % smaller than the value calculated from the time constant method.

In the present experiment the thickness of the samples tested are very small and in a similar range as the ones reported by Devanathan and Stachurski [4]. The lag time method is also commonly used to determine the diffusion rate of hydrogen in hydrogen permeation membranes [6-9]. The diffusion coefficient, D , is related to the sample thickness, L , and lag time, $t_{0.6299}$, by the following equation. The units for D are $\text{m}^2 \text{s}^{-1}$.

$$D = \frac{L^2}{6t_{0.6299}} \quad (6.1)$$

The steady state hydrogen permeation flux, J , ($\text{mol H}_2/\text{m}^2 \text{ s}$) can be determined by the steady state current density through the following relationship. Where n is the number of electrons transferred, I_p is the steady-state current density, and F is Faraday's constant.

$$J = \frac{I_p}{nF} \quad (6.2)$$

The steady state hydrogen permeation rate, V , ($\text{mol H}_2/\text{m s}$) can be defined according to Equation 6.3.

$$V = J \times L = \frac{LI_p}{nF} \quad (6.3)$$

The hydrogen permeability, Φ , ($\text{mol H}_2/\text{m s Pa}^{1/2}$) can be obtained from the hydrogen permeation rate, by Equation 6.4, where P_{up} and P_{down} are the applied pressure of hydrogen up and down stream, respectively.

$$\Phi = \frac{V}{\sqrt{P_{\text{up}}} - \sqrt{P_{\text{down}}}} \quad (6.4)$$

CHAPTER 6. EFFECT OF NANO-SCALE GRAIN REFINEMENT
ON THE HYDROGEN PERMEATION PERFORMANCE
OF Nb-Ni-Zr MEMBRANES

In this particular case, the main driving force is not the hydrogen pressure but the hydrogen concentration. With the assumption that the gaseous hydrogen and the hydrogen atom in the metal are in an equilibrium condition at the surface of the metal membrane, the difference in the hydrogen chemical potential, $\Delta\mu$, can be expressed as shown in Equation 6.5.

$$\Delta\mu = \frac{1}{2}RT \ln\left(\frac{P_{up}}{P_{down}}\right) \quad (6.5)$$

Where R is the gas constant and T is the temperature (K). Therefore, the hydrogen permeability can be arranged as follows:

$$\Phi = \frac{V}{e^{\frac{\Delta\mu}{RT}}} \quad (6.6)$$

To find $\Delta\mu$, the equation for Fick's law is rearranged with the well-established Equation (6.7) for the H flux diffusion through a membrane in the light of the H chemical potential, to give Equation (6.8).

$$J = -cB \frac{\Delta\mu}{L} \quad (6.7)$$

$$J = -D \frac{\Delta\mu}{L} \quad (6.8)$$

Where J is the hydrogen flux, c is the H concentration, B is the hydrogen mobility, D the hydrogen diffusion coefficient and L is the thickness of the membrane.

CHAPTER 6. EFFECT OF NANO-SCALE GRAIN REFINEMENT
ON THE HYDROGEN PERMEATION PERFORMANCE
OF Nb-Ni-Zr MEMBRANES

By rearranging Equations 6.2 and 6.8, the following relationship can be found.

$$\Delta\mu = \frac{I_p L}{nFD} \quad (6.9)$$

Where n is the number of electrons transferred, I_p is the steady-state current density, and F is Faraday's constant.

6.2.3 Calibration of the electrochemical hydrogen permeation apparatus

To ensure that the hydrogen permeation and hydrogen diffusivity data from the recorded current on the anodic side of the membrane is not affected by hydrogen trapping within the membrane and that the current recorded is large enough to be distinguished from the baseline current, the constant cathodic current applied to the sample was varied between 1 and 50 μA to determine the effect it had on the steady state current as shown in Figure 6. 4. A 50 μA cathodic current was used for an area with a diameter of 8 mm, which is equivalent to a current density of approximately 100 $\mu\text{A}/\text{cm}^2$. This current density was not exceeded to avoid an elevated hydrogen concentration within the membrane, which may lead to the formation of hydrides. The constant voltage applied to the anodic side of the membrane was of -0.85 V.

CHAPTER 6. EFFECT OF NANO-SCALE GRAIN REFINEMENT
ON THE HYDROGEN PERMEATION PERFORMANCE
OF Nb-Ni-Zr MEMBRANES

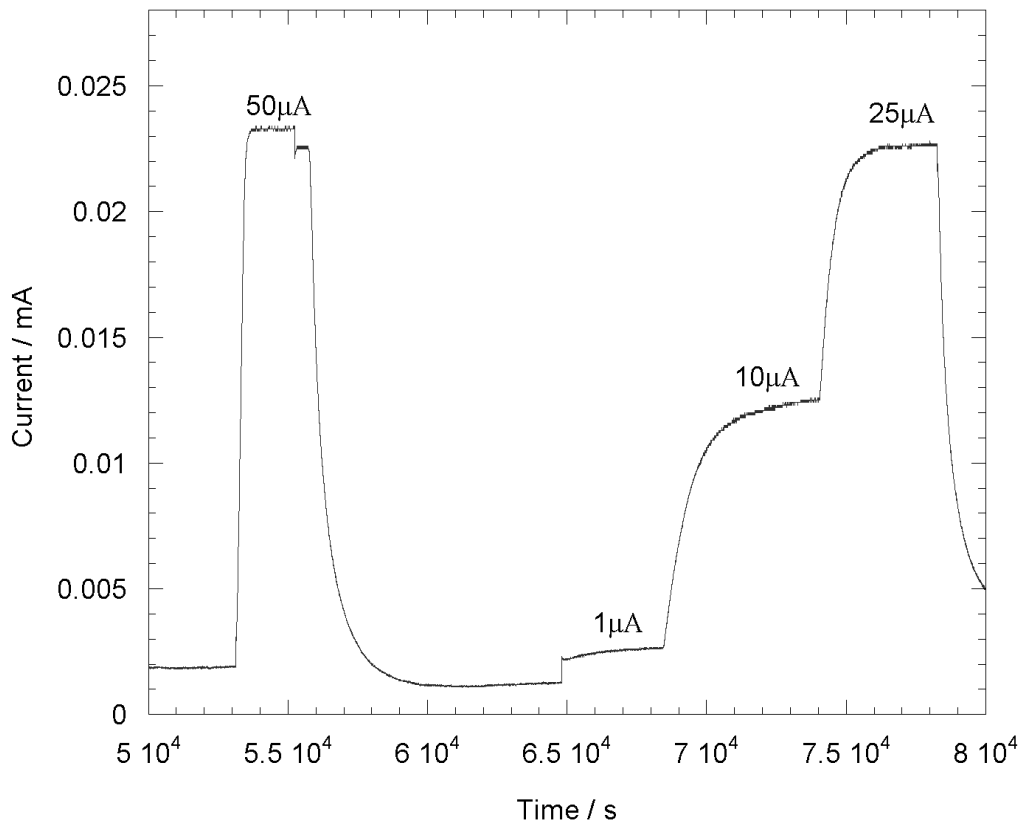


Figure 6.4. Effect of current applied on the cathode side of the sample on the Anodic current recorded.

6.2.4 Reliability of the results

To verify whether the apparatus was working reliably, a pure Pd sample was tested. The anodic current recorded during hydrogen permeation under a constant charging current of $50 \mu\text{A}$ on the cathode side is shown in Figure 6.5. The $t_{0.6299}$ of the pure Pd samples tested was in the range of 160 - 210 s, resulting in a hydrogen diffusion rate of $3.7 - 5.7 \times 10^{-12} \text{ m}^2/\text{s}$ and the steady state current density I_p was $21.5 \mu\text{A}$, resulting in a permeation rate, V , of $2.4 - 3.6 \times 10^{-10} \text{ mol H}_2/\text{ms}$, which is within the range of $3.3 - 4.3 \times 10^{-10} \text{ mol H}_2/\text{ms}$ reported by Adams and Mickalonis who used a similar electrochemical apparatus [9]. The current set up was therefore deemed reliable enough to perform hydrogen permeation measurements on the membranes.

CHAPTER 6. EFFECT OF NANO-SCALE GRAIN REFINEMENT
ON THE HYDROGEN PERMEATION PERFORMANCE
OF Nb-Ni-Zr MEMBRANES

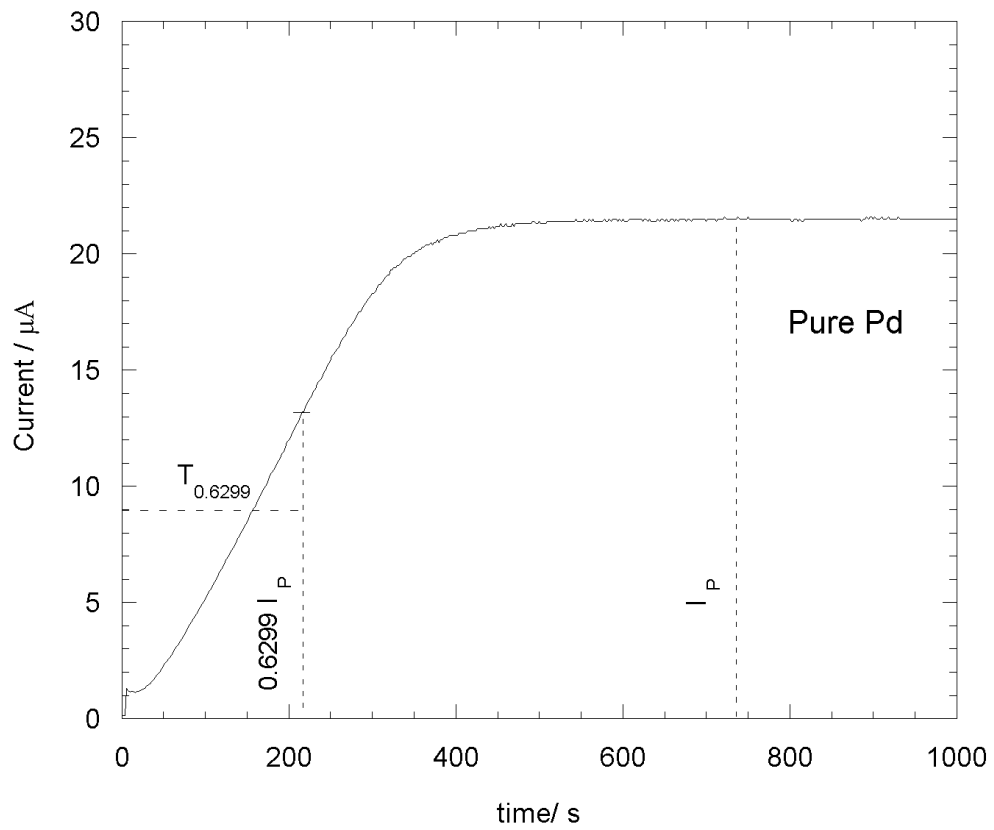


Figure 6.5. Anodic current versus time during the hydrogen permeation test.

6.3 Results

6.3.1 Hydrogen permeation of the Nb₂₀Ni₄₀Zr₄₀ alloy membranes

The measured anodic current during the electrochemical hydrogen permeation test of the as-quenched Nb₂₀Ni₄₀Zr₄₀ sample at 296 K is shown in Figure 6.6. From this curve, the hydrogen permeation and hydrogen diffusion coefficient can be calculated from Equation 6.1 and 6.4 from the earlier section in the chapter. Note that Figures 6.6, 6.7 and 6.8 are typical curves for each of the different alloy membranes.

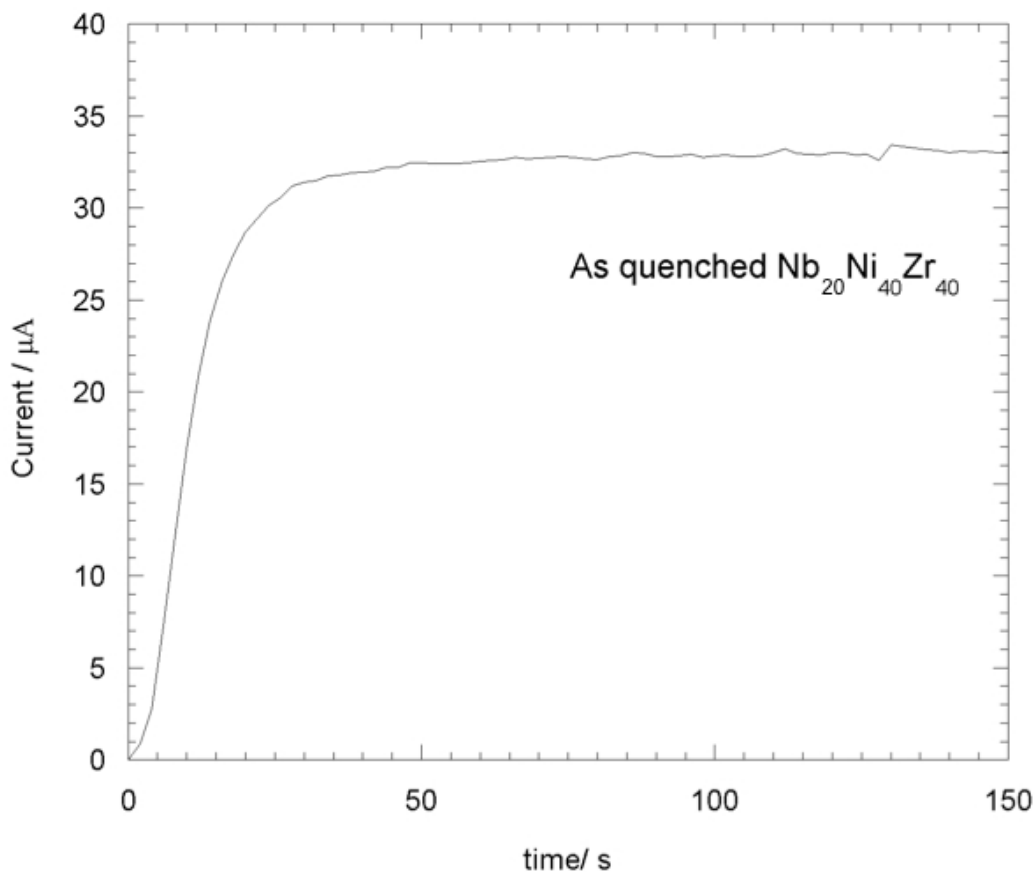


Figure 6.6. The measured anodic current during the electrochemical hydrogen permeation test of the as quenched Nb₂₀Ni₄₀Zr₄₀ sample at 296 K.

CHAPTER 6. EFFECT OF NANO-SCALE GRAIN REFINEMENT
ON THE HYDROGEN PERMEATION PERFORMANCE
OF Nb-Ni-Zr MEMBRANES

The measured anodic current during the electrochemical hydrogen permeation test at 296 K of the Nb₂₀Ni₄₀Zr₄₀ sample heated to 923 K is shown in Figure 6.7. The hydrogen permeation data, which is based on the measured saturation current, is close to that of the as-quenched sample. The main difference is the higher diffusion rate of hydrogen in the sample heated to 923 K with the nanoscale microstructure.

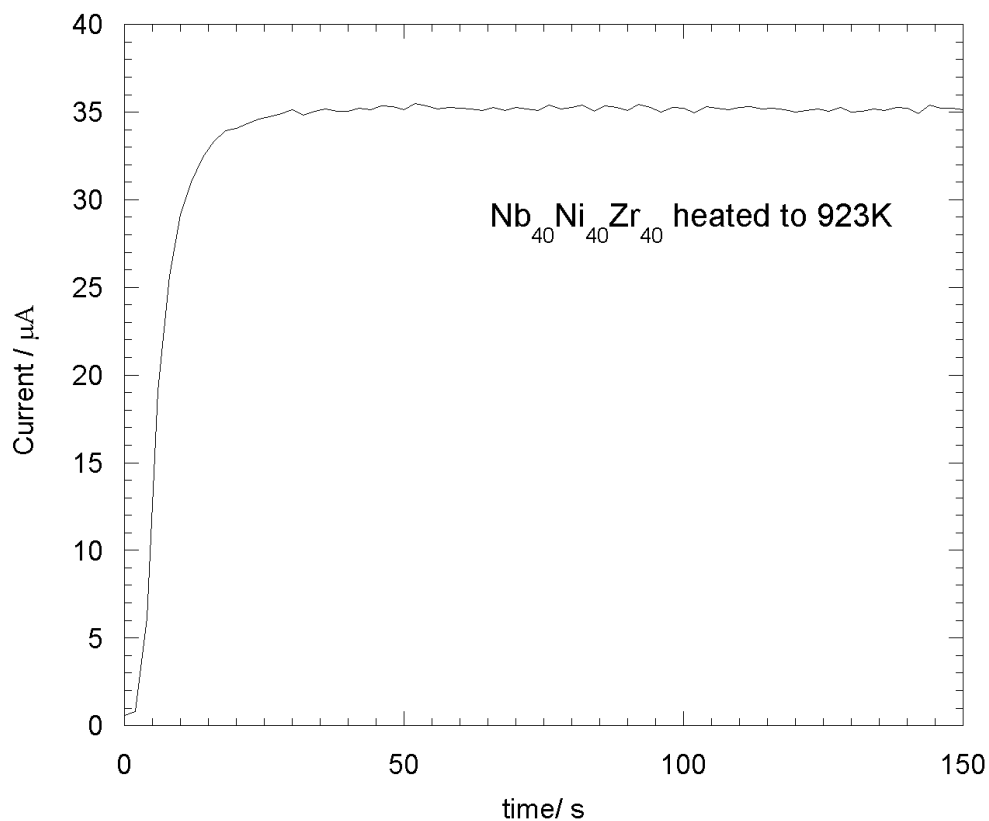


Figure 6.7. The measured anodic current during the electrochemical hydrogen permeation test at 296K of the Nb₂₀Ni₄₀Zr₄₀ sample heated to 923 K.

The measured anodic current during the electrochemical hydrogen permeation test at 296 K of the Nb₂₀Ni₄₀Zr₄₀ sample heated to 1173 K is illustrated in Figure 6.8. The hydrogen permeation in this sample is lower to that of the as-quenched sample and the one heated to 923 K.

CHAPTER 6. EFFECT OF NANO-SCALE GRAIN REFINEMENT
ON THE HYDROGEN PERMEATION PERFORMANCE
OF Nb-Ni-Zr MEMBRANES

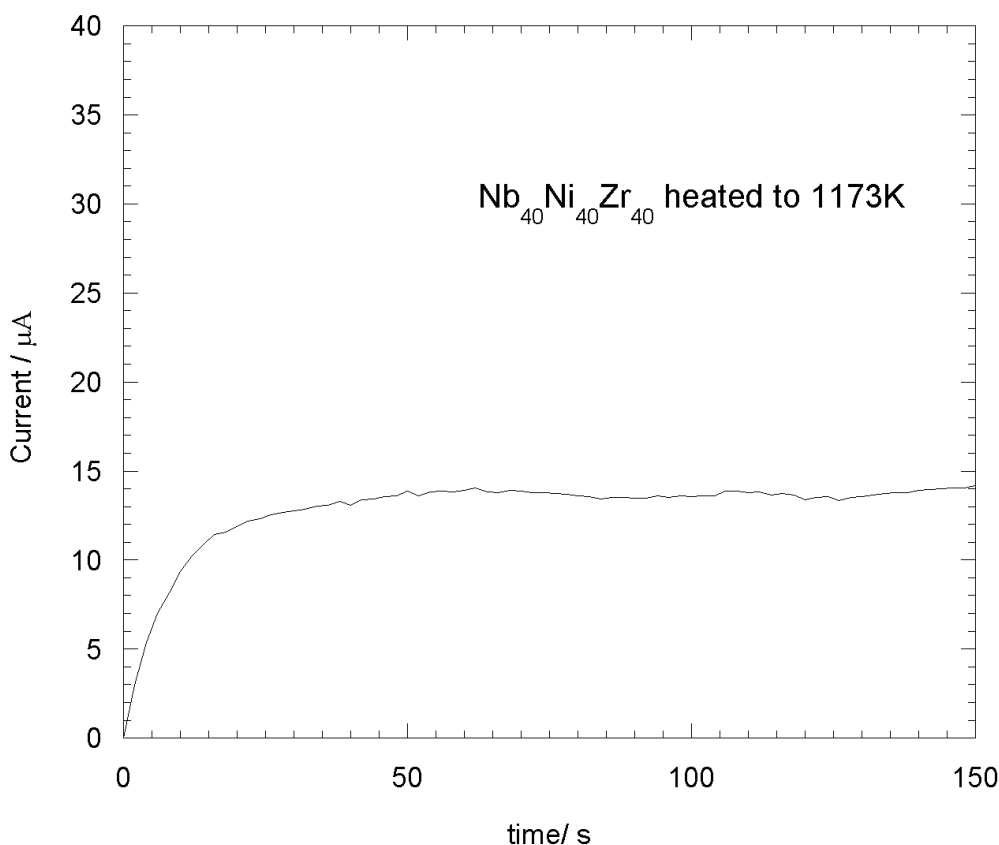


Figure 6.8. The measured anodic current during the electrochemical hydrogen permeation test at 296K of the $\text{Nb}_{20}\text{Ni}_{40}\text{Zr}_{40}$ sample heated to 1173 K.

The plots of hydrogen permeability (Φ) for pure Pd, melt-spun $\text{Nb}_{20}\text{Ni}_{40}\text{Zr}_{40}$ ribbons heated to 1173 K and 923 K, compared to experimental values of alloys of the same compositions are shown in Figure 6.9. The hydrogen permeability of the crystalline $\text{Nb}_{20}\text{Ni}_{40}\text{Zr}_{40}$ sample heated to 1173 K, obtained by the electrochemical method, can be seen to follow the Arrhenius relationship of the as-cast $\text{Nb}_{20}\text{Ni}_{40}\text{Zr}_{40}$ data published by Ishikawa et al. [10]. This can be observed through the extrapolation of the line obtained by the mean square fitting of the hydrogen permeation data points in a higher temperature range where the results were obtained using the pressure difference method. The $\text{Nb}_{20}\text{Ni}_{40}\text{Zr}_{40}$ sample heated to 923 K is found to have a significantly higher Φ value as compared to the one heated to 1173 K. The Φ of the experimental value of pure Pd in this work is close to the literature values published by Adams and Mickalonis [9] who used a similar electrochemical technique. The Φ of the experimental value of pure Pd can also be

CHAPTER 6. EFFECT OF NANO-SCALE GRAIN REFINEMENT
ON THE HYDROGEN PERMEATION PERFORMANCE
OF Nb-Ni-Zr MEMBRANES

compared by extrapolating the line of the mean square fitting of the Φ data points of pure Pd obtained at higher temperature by the pressure-difference method [10].

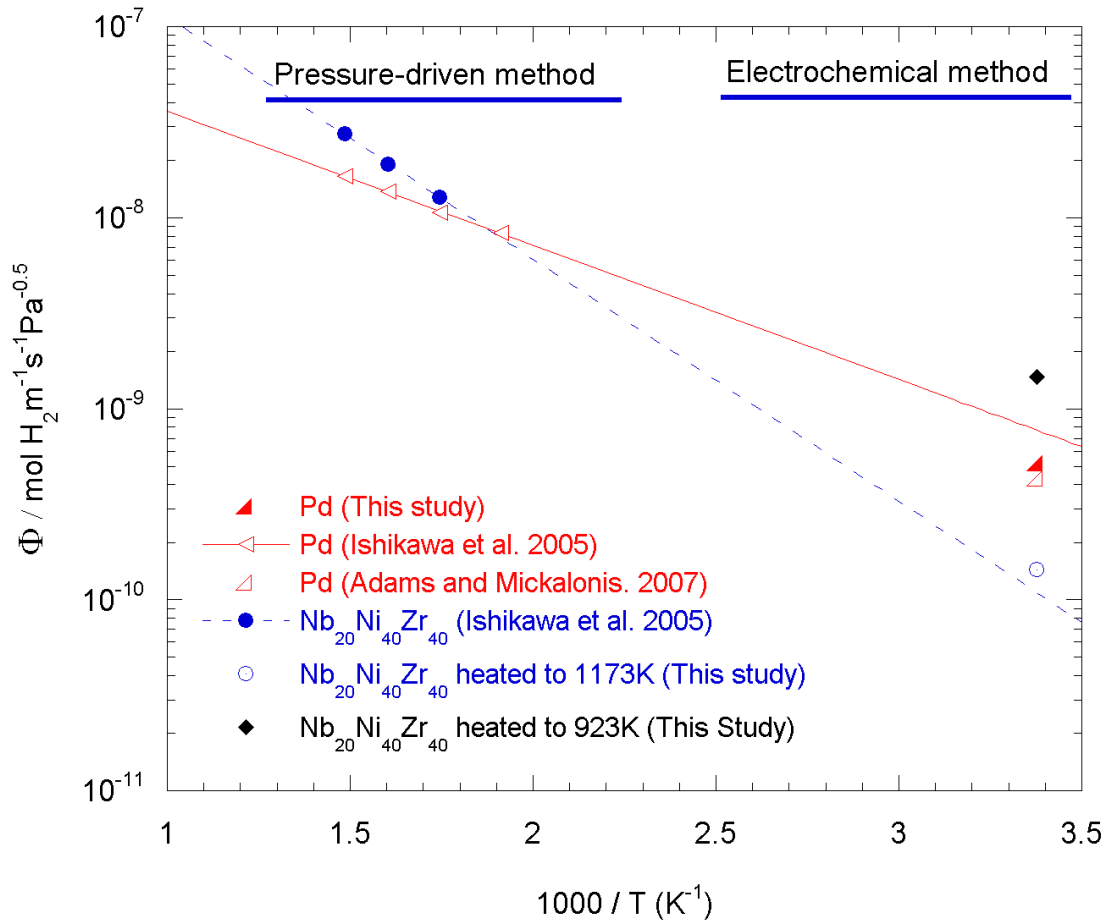


Figure 6.9. The plots of hydrogen permeability (Φ) for pure Pd, melt-spun Nb₂₀Ni₄₀Zr₄₀ ribbons heated to 1173 K and 923 K, compared to experimental values of alloys of the same compositions.

The plots of hydrogen permeability (Φ) of as-quenched Nb₂₀Ni₄₀Zr₄₀ compared to the experimental values of similar alloys from literature is illustrated in Figure 6.10. The extrapolated line of the mean square fitting of the literature values of amorphous Nb₂₈Ni₄₂Zr₃₀ alloys show that the value obtained by the present electrochemical method falls within a consistent range, assuming that the permeation rate in amorphous alloy membranes does not deviate from an Arrhenius relationship. This assumption is reasonable

CHAPTER 6. EFFECT OF NANO-SCALE GRAIN REFINEMENT
ON THE HYDROGEN PERMEATION PERFORMANCE
OF Nb-Ni-Zr MEMBRANES

as it has been reported that below 873 K the diffusion of hydrogen in Pd follows an Arrhenius correlation [3]

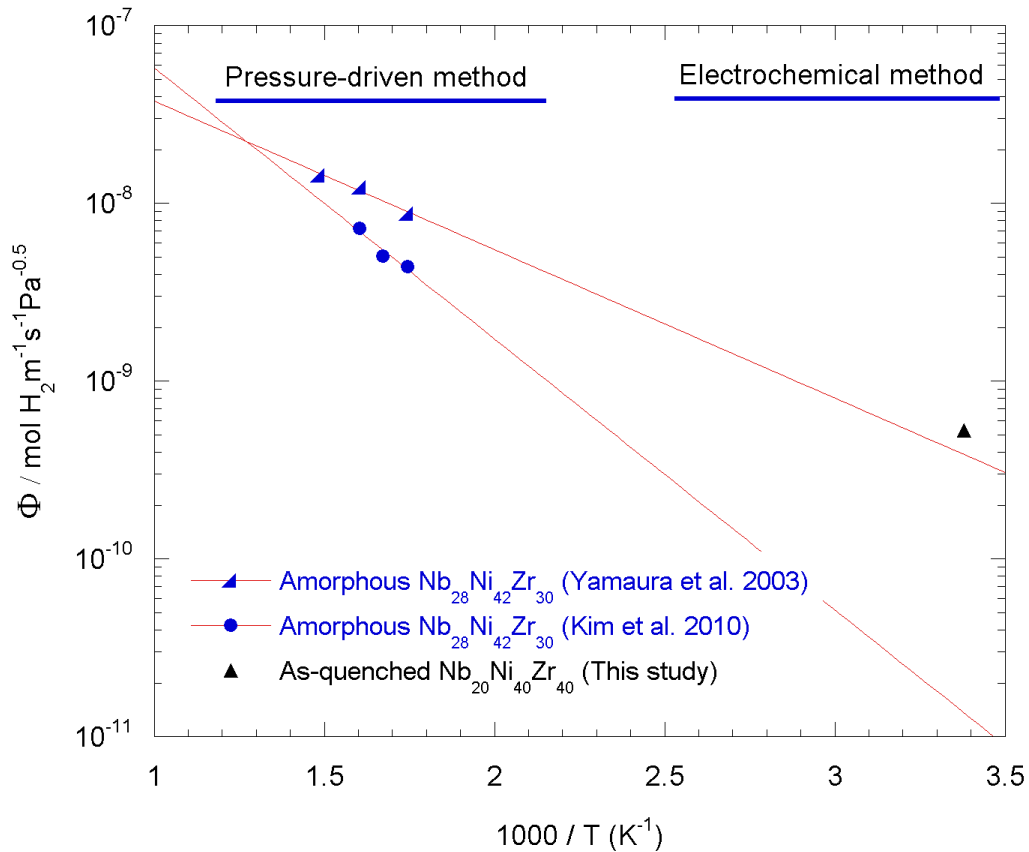


Figure 6.10. The plots of hydrogen permeability (Φ) of as-quenched $\text{Nb}_{20}\text{Ni}_{40}\text{Zr}_{40}$ compared to the experimental values of similar alloys from literature.

The mean grain size for $\text{Nb}_{20}\text{Ni}_{40}\text{Zr}_{40}$ and $\text{Nb}_{35}\text{Ni}_{32.5}\text{Zr}_{32.5}$ heated to 923 K and 1173 K is summarized in Table 6.1. More details on the microstructure and the techniques used can be found in Chapter 3 and 4. The $\text{Nb}_{35}\text{Ni}_{32.5}\text{Zr}_{32.5}$ sample was not used due to the deterioration in ribbon quality after annealing. The grain size when heated to 1173 K was found to be larger, about 200 nm, when measured from TEM micrographs. The larger grain size by TEM is deemed more reliable due to the larger errors involved in estimating the larger grain size from the sharper XRD peaks.

CHAPTER 6. EFFECT OF NANO-SCALE GRAIN REFINEMENT
ON THE HYDROGEN PERMEATION PERFORMANCE
OF Nb-Ni-Zr MEMBRANES

Table 6.1. The mean grain size for Nb₂₀Ni₄₀Zr₄₀ and Nb₃₅Ni_{32.5}Zr_{32.5} heated to 923 K and 1173 K. The mean grain size was estimated from the line broadening of the corresponding XRD traces.

Sample	Nb ₂₀ Ni ₄₀ Zr ₄₀ heated to 923 K	Nb ₃₅ Ni _{32.5} Zr _{32.5} heated to 923 K	Nb ₂₀ Ni ₄₀ Zr ₄₀ heated to 1173 K	Nb ₃₅ Ni _{32.5} Zr _{32.5} heated to 1173 K
Grain size (nm)	44	40	101	116

The hydrogen diffusion coefficient, (D), hydrogen permeation rate (V), hydrogen permeability (Φ), hydrogen solubility coefficient (K) and hydrogen concentration (C) in the Nb₂₀Ni₄₀Zr₄₀ alloy before and after heating and in pure Pd are shown in Table 6.2. D is obtained from Equation 6.1, V from Equation 6.2, Φ from Equation 6.4, and S from Equation 2.4. It can be seen that the nanocrystalline Nb₂₀Ni₄₀Zr₄₀ has the highest Φ , while the crystalline membrane has the highest hydrogen diffusivity, D , and the amorphous membrane the highest hydrogen solubility coefficient, K . The amorphous and nanocrystalline samples have a lower hydrogen concentration than the crystalline sample. The results for pure Pd are included for comparison.

Table 6.2. The hydrogen diffusion coefficient (D), hydrogen permeation rate (V), hydrogen permeability (Φ), hydrogen solubility coefficient (K) and hydrogen concentration (C) in Nb₂₀Ni₄₀Zr₄₀ alloys before and after heating and in pure Pd.

Nb ₂₀ Ni ₄₀ Zr ₄₀	D (m ² /s)	V (mol H ₂ /m s)	Φ (mol H ₂ /m s Pa ^{0.5})	K (mol H ₂ /m ³ Pa ^{0.5})	C (H/M)
As-quenched	9.47x10 ⁻¹²	5.18x10 ⁻¹⁰	5.16x10 ⁻¹⁰	54.5	0.103
Heated to 923 K	3.70x10 ⁻¹¹	1.47x10 ⁻⁹	1.47x10 ⁻⁹	39.7	0.097
Heated to 1173 K	4.24x10 ⁻¹¹	1.43x10 ⁻¹⁰	1.43x10 ⁻¹⁰	3.4	0.232
Pure Pd	5.05x10 ⁻¹²	3.00x10 ⁻¹⁰	3.00x10 ⁻¹⁰	64.1	0.046

The effect of structural correlation length on the hydrogen diffusion coefficient (D) and solubility coefficient (K) is shown in Figure 6.11. The structural correlation length

CHAPTER 6. EFFECT OF NANO-SCALE GRAIN REFINEMENT
ON THE HYDROGEN PERMEATION PERFORMANCE
OF Nb-Ni-Zr MEMBRANES

refers to the grain size in polycrystalline alloys and the inter-atomic separation in amorphous alloys.

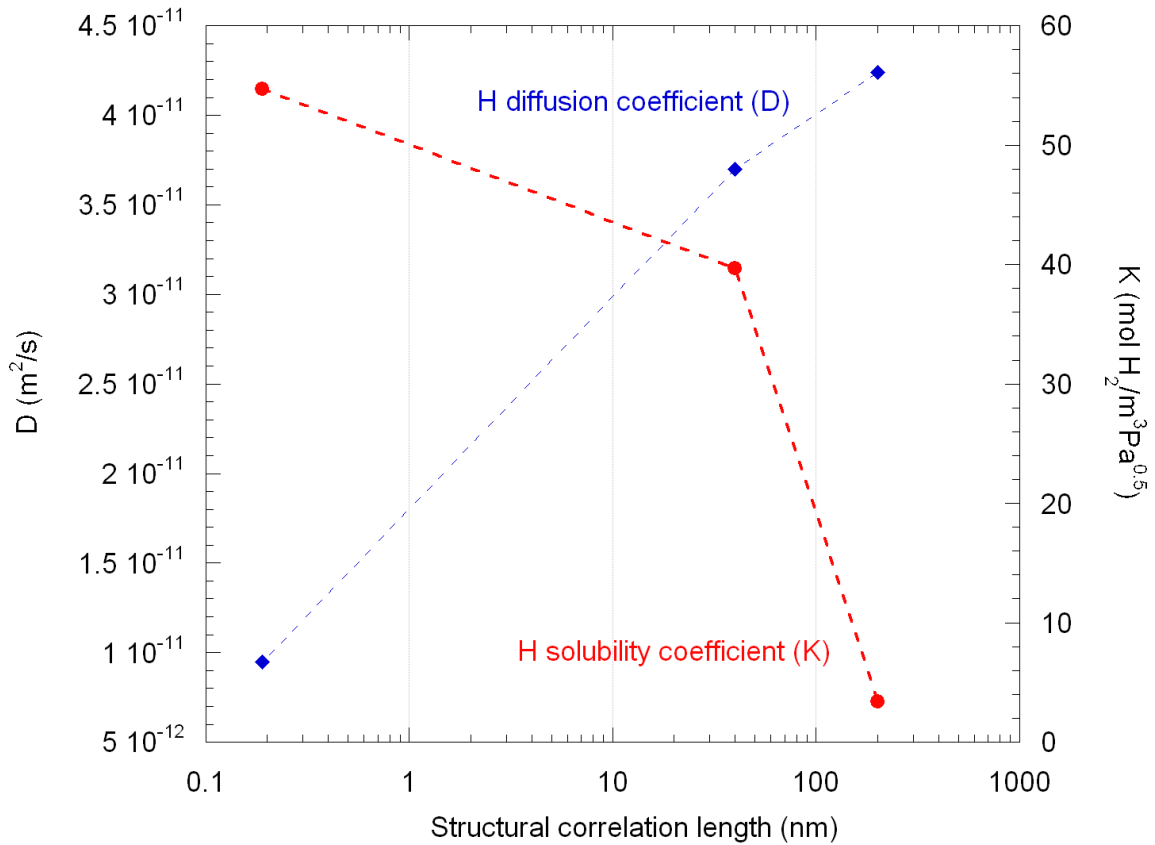


Figure 6.11. The effect of structural correlation length on the hydrogen diffusion coefficient (D) and solubility coefficient (K). The structural correlation length refers to the grain size in polycrystalline alloys and the inter-atomic separation in amorphous alloys. The dotted lines are added as guide to the eyes.

The hydrogen permeability (Φ) of the Nb₂₀Ni₄₀Zr₄₀ alloy as a function of structural correlation length that refers to the grain size in polycrystalline alloys and the interatomic separation in amorphous alloys is illustrated in Figure 6.12.

CHAPTER 6. EFFECT OF NANO-SCALE GRAIN REFINEMENT
ON THE HYDROGEN PERMEATION PERFORMANCE
OF Nb-Ni-Zr MEMBRANES

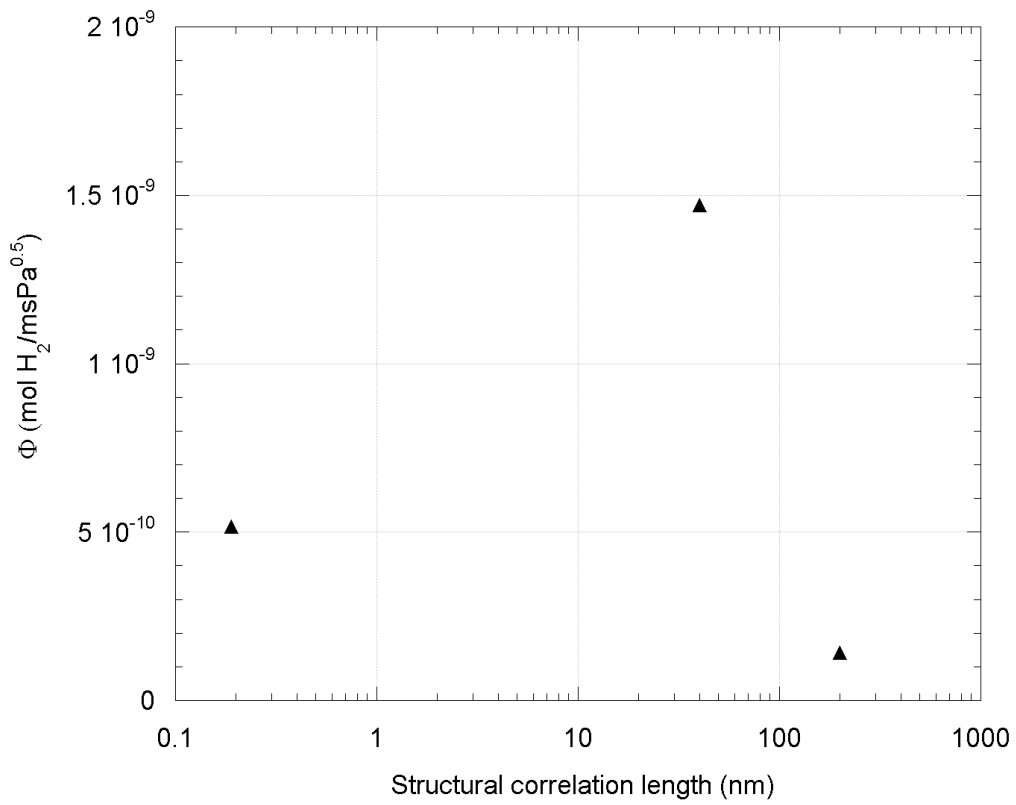


Figure 6.12. The hydrogen permeability (Φ) of the $\text{Nb}_{20}\text{Ni}_{40}\text{Zr}_{40}$ alloy as a function of structural correlation length that refers to the grain size in polycrystalline alloys and the inter-atomic separation in amorphous alloys.

6.4 Discussion

It is well established that the hydrogen permeation of a membrane is highly dependent on its hydrogen solubility coefficient and diffusivity. The following discussion section will look into the effect of varying the microstructure on each of these properties. The last section of this discussion looks into the effect of the microstructure on the hydrogen concentration within the membrane, as this has a direct correlation to the resistance to hydrogen embrittlement in Nb-based membranes.

6.4.1 Effect of microstructure on hydrogen solubility

The electrochemical hydrogen permeation data from the Nb₂₀Ni₄₀Zr₄₀ alloy sample annealed at 1173 K (c-crystalline) follows an Arrhenius relationship similar to the results published by Ishikawa et al. [10]. Based on Equation 2.5, the activation energy for the permeation of hydrogen in the c-Nb₂₀Ni₄₀Zr₄₀ alloy sample was found to be 24.3 kJmol⁻¹, which is close to the activation energies (28.5 - 35.7 kJmol⁻¹) reported for several alloys of the Nb-Ni-Zr-Ti alloy system by Tang et al. [11]. The activation energy for the diffusion of hydrogen in pure Nb has been reported by Volkl and Alefeld to be 10.2 kJmol⁻¹ [12]. The effect of alloying different elements to increase the resistance to hydrogen embrittlement of Nb seems to lead to a higher activation energy for the diffusion of hydrogen. The diffusion coefficient was reported not to show a deviation from an Arrhenius relation for temperatures above 273 K as shown in the Figure 6.13 [2].

CHAPTER 6. EFFECT OF NANO-SCALE GRAIN REFINEMENT
ON THE HYDROGEN PERMEATION PERFORMANCE
OF Nb-Ni-Zr MEMBRANES

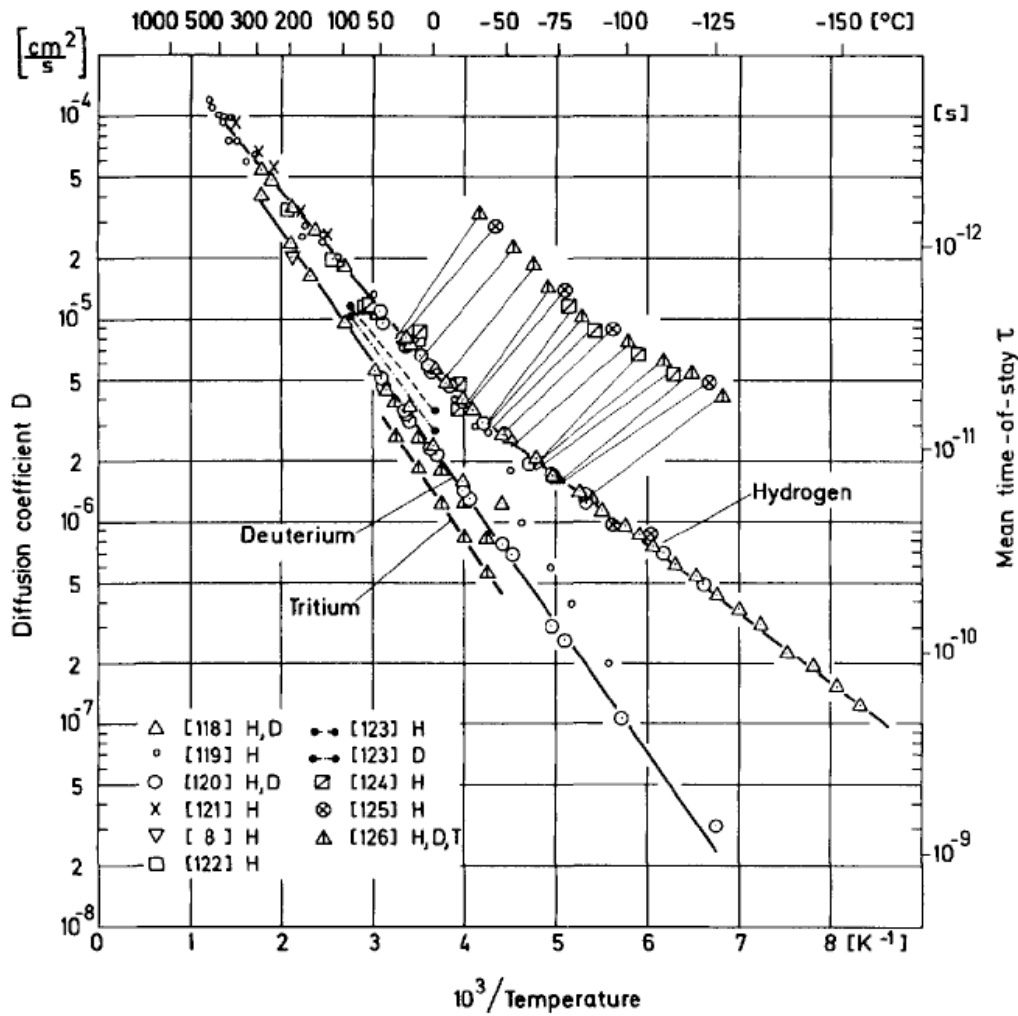


Figure 6.13. Diffusion coefficient of H, D, and T in Nb [2].

The high hydrogen solubility coefficient obtained for the amorphous sample is expected as the solubility can be quantified by the hydrogen absorption capacity of the alloy, which has been reported to be larger for amorphous alloys compared to their corresponding crystalline counterpart [12-15]. This high hydrogen solubility coefficient is attributed to the ‘defects’ present in its matrix. Each defect possesses a specific hydrogen binding energy. The wide range of sites to be occupied by hydrogen, over a range of potential energy levels, leads to an increase in hydrogen solid solubility [16].

Another possible reason for the high hydrogen solubility is the high catalytic activities at the surface of the amorphous alloys due to their unique surface electron structures, high density of low-coordination active sites and chemical homogeneity [17].

CHAPTER 6. EFFECT OF NANO-SCALE GRAIN REFINEMENT
ON THE HYDROGEN PERMEATION PERFORMANCE
OF Nb-Ni-Zr MEMBRANES

These are highly composition dependent, and it has been reported that $\text{Ni}_{64}\text{Zr}_{36}$ amorphous alloy did not require a catalytic coating but after additions of Hf or Ti, a catalytic coating was required [18, 19].

The hydrogen solubility coefficient of the as-quenched sample is the closest to pure Pd. The sample annealed at 923 K, with a nanocrystalline structure has a hydrogen solubility coefficient about 30 % less than that of the amorphous alloy, but about one order of magnitude higher than that of the conventional crystalline $\text{Nb}_{20}\text{Ni}_{40}\text{Zr}_{40}$ sample. This trend of decreasing hydrogen solubility coefficient with increasing grain size has parallels with the work of Hirscher et al. who reported an increasing hydrogen desorption temperature with increasing grain size in hydrogen-charged heterogeneous Co-Zr alloys [20].

6.4.2 Effect of microstructure on hydrogen diffusivity

In the present work, the amorphous alloy was found to have the lowest hydrogen diffusivity. Even though the exact mechanisms involved are not clear, Dos Santos et al. [13, 16] suggest that the decreasing hydrogen diffusivity observed in amorphous alloys is due to the high density of ‘defects’ within its structure. Metallic glasses do not possess long-range atomic order and have a varied spectrum of site energies. This results in a large amount of hydrogen trapping sites that hinder hydrogen diffusion [13,16].

The hydrogen concentration in the membrane is also important, as the hydrogen diffusivity could potentially be higher at more elevated hydrogen concentrations. It must be noted that at low hydrogen concentration, hydrogen behaves as an ideal gas. It has been reported that the hydrogen diffusivity in an amorphous binary Ti-Ni alloy increased by two orders of magnitude with increasing hydrogen concentration as shown in Figure 6.14. [21]. Wu et al. have attributed this phenomenon to the weakening of metal-metal bonds that leads to an increase of low-energy sites and increased hydrogen mobility, which have been reported elsewhere [21-24]. From this perspective, the amorphous alloys are promising.

CHAPTER 6. EFFECT OF NANO-SCALE GRAIN REFINEMENT
ON THE HYDROGEN PERMEATION PERFORMANCE
OF Nb-Ni-Zr MEMBRANES

However, in the current case the hydrogen concentration in the amorphous alloy is 0.103, which is not low and thus the potential increase in hydrogen diffusivity with increasing hydrogen concentration is mitigated. Amorphous alloys are also thermodynamically metastable and therefore tend to crystallize when exposed to elevated temperatures for long periods of time, which raise concerns regarding the durability of amorphous membranes.

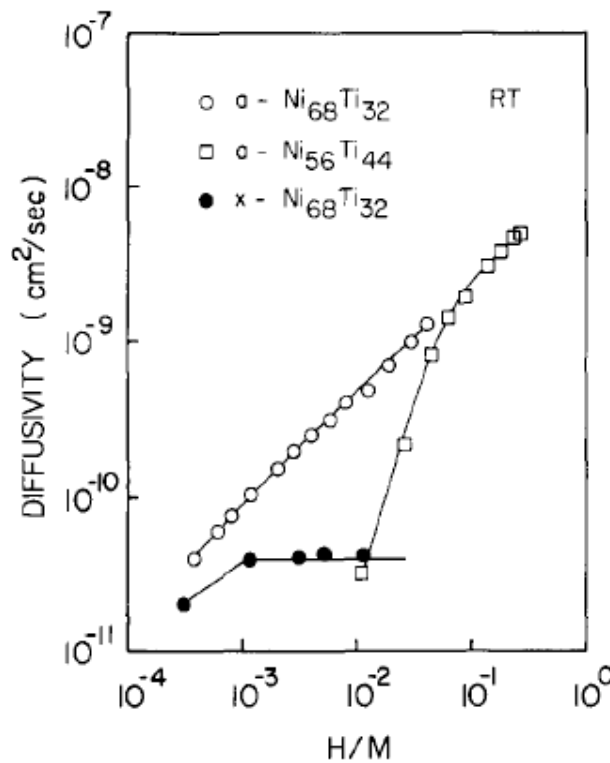


Figure 6.14. Hydrogen diffusivity as a function of hydrogen concentration at room temperature for amorphous Nb₅₆Ti₄₄ and Nb₆₈Ti₃₂ and crystallized Nb₃₈Ti₃₂ alloys [21].

The conventional crystalline Nb₂₀Ni₄₀Zr₄₀ sample on the other hand has the highest hydrogen diffusivity (4.24 × 10⁻¹¹ m²/s at RT), which is attributed to its bcc structure and the hydrogen travelling through lattice diffusion. As it can be seen in Table 6.2, the hydrogen diffusivity of the nanocrystalline sample is only marginally lower than the crystalline sample (3.70 × 10⁻¹¹ m²/s at RT) and higher than the amorphous sample (9.47 × 10⁻¹² m²/s at RT). The introduction of long-range atomic order in the nanocrystalline sample by the annealing of the amorphous sample has enhanced the hydrogen diffusivity. It was shown by

CHAPTER 6. EFFECT OF NANO-SCALE GRAIN REFINEMENT
ON THE HYDROGEN PERMEATION PERFORMANCE
OF Nb-Ni-Zr MEMBRANES

Kelton et al. that the activation energy for the bulk diffusion of hydrogen in 5A Group metals such as Nb, Ta and V, were lower than that of pure bcc Fe, other fcc metals such as Cu, Ni, Pd and Pt, and other hcp metals such as Ti and Zr [25].

Despite having the highest hydrogen diffusivity, the crystalline sample did not have high hydrogen permeability due to its low hydrogen solubility even with the presence of the catalytic Pd coating. The diffusion coefficient of the conventional crystalline Nb₂₀Ni₄₀Zr₄₀ alloy sample (4.24×10^{-11} m²/s at RT) is also one order of magnitude lower than the diffusion coefficient of hydrogen in pure Nb (6×10^{-10} m²/s at RT), which can be seen in Figure. 6.13 [2]. It can be concluded that alloying with 40 at.% of Ni and Zr is detrimental to the diffusion of hydrogen in the Nb membrane. However, it is well established in crystalline hydrogen permeation alloys that the resistance to hydrogen embrittlement can be improved by increasing the ratio of supporting matrix and therefore extend the durability of such membranes.

The current view and the experimental results reported by most of the literature in regard to hydrogen permeation and nanocrystalline structures is that the reduction of the grain size to the nano-scale leads to a larger grain boundary volume and other defects that contribute to alternative means of diffusion of hydrogen by their excess free volume [20, 26-33]. However, the current results show that the hydrogen diffusion in the nanocrystalline sample did not increase dramatically compared to that of the crystalline sample and was in fact marginally lower. This is consistent with the work published by Heinze et al., who used a similar technique to determine the hydrogen permeation. They reported two diffusion mechanisms when testing for hydrogen diffusion in Pd – 23 % Ag alloys, where the diffusion in the grain boundaries was found to be slower than the diffusion in the bulk, as generally observed in pure Pd samples [34]. This difference was attributed to the interactions between diffusing hydrogen and impurities in the grain boundaries [34]. The hydrogen atoms were reported to diffuse through the grain boundaries when the grain size was below 40 nm and through intragranular diffusion when the grain size was above 100

CHAPTER 6. EFFECT OF NANO-SCALE GRAIN REFINEMENT
ON THE HYDROGEN PERMEATION PERFORMANCE
OF Nb-Ni-Zr MEMBRANES

nm [21-24]. At higher hydrogen concentration, the hydrogen diffusion at the grain boundaries of the nanostructured sample is likely to increase as reported in other nanostructured membranes [27, 28]. However, the hydrogen concentration involved in the present case is not considered low, and the potential increase in hydrogen diffusion with increasing hydrogen concentration is likely to be moderate.

6.4.3 Effect of nanostructure on hydrogen permeability

The nanocrystalline sample brings the best of the amorphous and crystalline properties together. The nanocrystalline sample is found to have a high hydrogen diffusivity, which is marginally lower than the crystalline sample and has a hydrogen solubility one order of magnitude higher than the crystalline sample. The high hydrogen diffusivity ($3.70 \times 10^{-11} \text{ m}^2/\text{s}$ at RT) in the nanocrystalline sample, compared to the amorphous sample ($9.47 \times 10^{-12} \text{ m}^2/\text{s}$ at RT), is attributed to the formation of small bcc-Nb grains, which allow hydrogen to travel through lattice diffusion. The higher hydrogen solubility could be attributed to the high percentage of grain boundary volume, which is considered to be amorphous in nanocrystalline materials [20, 26, 27] and the report of a similar trend of high hydrogen solubility in Ni- and Fe-based amorphous alloys by Dos Santos and Miranda [13, 16].

Hydrogen permeability of an alloy membrane is highly composition dependent and it is common belief in Nb-based alloy membranes that the bcc-Nb phase is the preferential diffusion path of hydrogen. A larger volume fraction of bcc-Nb phase has been reported to result in higher hydrogen permeability [35-37]. The niobium content in the $\text{Nb}_{20}\text{Ni}_{40}\text{Zr}_{40}$ alloy membrane is considered low. On the other hand, the hydrogen permeability in amorphous Nb-Ni-Zr alloys has been reported to be dependent on the zirconium content. High zirconium content led to an increased hydrogen permeability, which is attributed to the preferential interaction of hydrogen with zirconium and the increase in the bond length of the Zr-Zr atoms upon hydrogenation [38]. Consequently the current alloy composition, of $\text{Nb}_{20}\text{Ni}_{40}\text{Zr}_{40}$, favours hydrogen permeation in an amorphous state as opposed to one in a crystalline state. The novelty in the work presented is that it has been shown that a reduction

CHAPTER 6. EFFECT OF NANO-SCALE GRAIN REFINEMENT
ON THE HYDROGEN PERMEATION PERFORMANCE
OF Nb-Ni-Zr MEMBRANES

in grain size to the nano-scale leads to an improvement in hydrogen permeation not only by increased hydrogen diffusion, as widely believed, but also by increased hydrogen solubility.

6.4.4 Effect of microstructure on the stability of membranes

The hydrogen concentrations for the amorphous (0.103 H/M) and nanocrystalline (0.097 H/M) Nb₂₀Ni₄₀Zr₄₀ alloys were found to be lower than that of the crystalline alloy (0.232 H/M). They were found to be within 7 % of one another and about half of the hydrogen concentration in the crystalline alloy. Based on the review of the work of Yukawa et al. in Chapter 2 [39-41], it is suggested that the hydrogen concentration within alloy membranes is a key parameter to their resistance to hydrogen embrittlement. As discussed in Section 2.6, a low hydrogen concentration within the membrane is desirable for a better resistance to hydrogen embrittlement. A critical ductile to brittle transition was reported to occur in Nb at hydrogen concentrations above H/M = 0.25 [39] and it is recommended to design alloy membranes that can operate without exceeding this hydrogen concentration threshold. The c-Nb₂₀Ni₄₀Zr₄₀ samples tested reached a hydrogen concentration of 0.232, which is just below this critical hydrogen level, and did not suffer from hydrogen embrittlement.

An interesting observation is that the amorphous and nanocrystalline membranes have hydrogen concentrations about half that of the crystalline membrane, which is consistent with a report that amorphous membranes were quite resistant to hydrogen embrittlement compared to some crystalline membranes [42]. Even though the amorphous sample had a low hydrogen concentration present, the effect of hydrogen on the thermal stability of metallic glasses have been reported in several articles and Bowman described that the exothermic reactions between hydrogen and most metallic glasses that can absorb large amounts of the gas release additional energy, which may lead to crystallization or decomposition [43].

The novelty is that the nanocrystalline membrane managed a similarly low hydrogen concentration. This implies that improvement in the resistance to hydrogen embrittlement in crystalline Nb₂₀Ni₄₀Zr₄₀ alloy membranes is possible by reducing the grain size to a nano-

CHAPTER 6. EFFECT OF NANO-SCALE GRAIN REFINEMENT
ON THE HYDROGEN PERMEATION PERFORMANCE
OF Nb-Ni-Zr MEMBRANES

scale. Based on the current results, this can be attributed to the higher hydrogen solubility coefficient of the nanocrystalline membrane ($39.7 \text{ mol H}_2/\text{m}^3\text{Pa}^{0.5}$) compared to that of the crystalline membrane ($3.4 \text{ mol H}_2/\text{m}^3\text{Pa}^{0.5}$). The higher hydrogen solubility coefficient not only allows a faster hydrogen adsorption at the upstream surface of the membrane, but also a faster desorption of hydrogen at the downstream surface. This discourages the hydrogen from building up in the alloy and keeps the hydrogen concentration low, therefore improving the membrane's resistance to hydrogen embrittlement.

6.5 Summary

The hydrogen permeability, solubility and diffusivity have been measured for a $\text{Nb}_{20}\text{Ni}_{40}\text{Zr}_{40}$ alloy in order to investigate the effect of microstructural changes on the hydrogen solubility and diffusivity during hydrogen permeation, more specifically the effect of nanostructure on hydrogen permeation. The $\text{Nb}_{20}\text{Ni}_{40}\text{Zr}_{40}$ alloy was tested in an amorphous state, with a microstructure at a nano-scale and at a micro-scale after heating to 923 K and 1173 K respectively. The hydrogen permeation is calculated from the steady-state hydrogen permeation flux and the thickness of the sample. It is found that the hydrogen permeability of the sample with a nanostructure is the highest, about twice that of the amorphous sample and one order of magnitude higher than the crystalline sample. Even though the n-sample and the a-sample have higher hydrogen permeabilities, the hydrogen diffusivity and solubility states of each are very different. The effective hydrogen diffusivity was related to the time lag required to achieve steady state hydrogen permeation flux. The a-sample is found to have the highest hydrogen solubility, followed by the n-sample and lastly the c-sample. The c-sample is found to have the highest hydrogen diffusivity, similar to that of the n-sample and the a-sample was the lowest. It was shown that the improvement in hydrogen permeation in the samples with a nanostructure was not solely based on improved hydrogen diffusivity, when compared to the amorphous sample, but also due to the improved hydrogen solubility brought about by the larger volume fraction of grain boundaries. The enhanced hydrogen solubility of the nanocrystalline membrane also helped improve its resistance to hydrogen embrittlement by lowering the hydrogen concentration in the membrane during the hydrogen permeation test.

6.6 References

- [1] D. R. Arantes, X. Y. Huang, C. Marte and R. Kirchheim, *Acta Metallurgica and Materialia*, 41 (1993) 3215
- [2] C. Marte and R. Kirchheim, *Scripta Materialia*, 37 (1997) 1171
- [3] G. Alefeld and J. Volkl, *Hydrogen in Metals*, (Springer-Verlag, Berlin, 1978) Vols. 1, pp 321
- [4] M. A. V. Devanathan and Z. Stachurski, *Proceedings of the Royal Society A*, 270 (1962) 90
- [5] M. A. V. Devanathan, O. N. R. Tech. Rep. No. ONR/551/22/NR036-028 (1961) Feb 28.
- [6] J.Y. Yang, C. Nishimura and M. Komaki, *Journal of Membrane Science*, 309 (2008) 246
- [7] C. Nishimura, M. Komaki, S. Hwang and M. Amano, *Journal of Alloys and Compounds*, 330-332 (2002) 902
- [8] Y. Zhang, J. Lu, R. Maeda and C. Nishimura, *Materials Transactions*, Vol. 49, No. 4 (2008) 754
- [9] T.M. Adams and J. Mickalonis, *Materials Letters*, 61 (2007) 817
- [10] K. Ishikawa, T. Takano, T. Matsuda and K. Aoki, *Applied Physics Letters*, 87, (2005) 081906
- [11] H. X. Tang, K. Ishikawa and K. Aoki, *Materials Transactions*, Vol. 49, No. 10 (2008) 2220
- [12] H. Wipf, *Physica Scripta*, T94 (2001) 43
- [13] D. S. Dos Santos, P. E. V. Miranda, *Journal of Material Science*, 32 (1997) 6311
- [14] N. Eliaz, D. Eliezer, *Advanced Performance Materials*, 6 (1999) 5
- [15] K. Suzuki, *Journal of Less Common Metals*, 89 (1983) 183
- [16] D. S Dos Santos, P. E. V. Miranda, *International Journal of Hydrogen Energy*, 23 (1998) 1011

CHAPTER 6. EFFECT OF NANO-SCALE GRAIN REFINEMENT
ON THE HYDROGEN PERMEATION PERFORMANCE
OF Nb-Ni-Zr MEMBRANES

- [17] B. S. Liu, W. D. Zhang, W. L. Dai, J. F. Deng, C. Sheng, S. Y. Zhou, *Journal of Membrane Science*, 135 (1997) 33
- [18] S. Hara, N. Hatakeyama, N. Itoh, H. Kimura, A. Inoue, *Journal of Membrane Science*, 211 (2003) 149
- [19] T. H. Jang, J. Y. Lee, *Journal of Non-Crystalline Solids*, 116 (1990) 73
- [20] M. Hirscher, J. Mossinger, H. Kronmuller, *Journal of Alloys and Compounds*, 231 (1995) 267
- [21] J. J. Kim, D. A. Stevenson, *Journal of Non-Crystalline Solids*, 101 (1988) 187
- [22] Q. Y. Wu, J. Xu, X. K. Sun, Z. Hu, *Journal of Material Science and Technology*, 13 (1997) 443
- [23] M. Amano, M. Komaki, C. J. Nishimura, *Journal of Less-Common Metals*, 172 (1991) 727
- [24] E. Shimizu, K. Aoki, T. J. Matsumoto, *Journal of Alloys and Compounds*, 295 (1999) 526
- [25] K. F. Kelton, T. K. Croat, A. K. Gangopadhyay, L. Q. Xing, A. L. Greer, M. Weyland, X. Li, K. Rajan, *Journal of Non-Crystalline Solids*, 317 (2003) 71
- [26] H. Gleiter, *Physica Status Solidi B*, 172 (1992) 41
- [27] H. Gleiter, *Progress in Materials Science*, 33 (1989) 223
- [28] H. Gleiter, *Acta Materialia*, 48 (2000) 1
- [29] R. Kirchheim, *Physica Scripta*, T94 (2001) 58
- [30] K. J. Bryden, J. Y. Ying, *Materials Science and Engineering A*, 204 (1995) 140
- [31] K. J. Bryden, J. Y. Ying, *Nanostructured Materials*, 9 (1997) 485
- [32] K. J. Bryden, J. Y. Ying, *Journal of Membrane Science*, 203 (2002) 29
- [33] M. Hirscher, J. Mossinger, H. Kronmuller, *Nanostructured Materials*, 6 (1995) 635
- [34] S. Heinze, B. Vuillemin, J. C. Colson, P. Giroux and D. Leterq, *Solid State Ionics*, 122 (1999) 51
- [35] K. Ishikawa, S. Tokui, K. Aoki, *Intermetallics*. 17 (2009) 109

CHAPTER 6. EFFECT OF NANO-SCALE GRAIN REFINEMENT
ON THE HYDROGEN PERMEATION PERFORMANCE
OF Nb-Ni-Zr MEMBRANES

- [36] T. Wong, K. Suzuki, M. Gibson, K. Ishikawa, K. Aoki, L.L. Jones, *Scripta Materialia*, 62 (2010) 582
- [37] K. Hashi, K. Ishikawa, T. Matsuda and K. Aoki, *Journal of Alloys and Compounds*, 368 (2004) 215
- [38] M. Nishida, M. Matsuda, Y. Shimada, K. Takashima, K. Ishikawa, K. Aoki, *Journal of Physics: Conference Series*, 144 (2009) 01210
- [39] H. Yukawa, M. Morinaga, T. Nambu, Y. Matsumoto, *Materials Science Forum*, 654-656 (2010) 2827
- [40] G. X. Zhang, H. Yukawa, T. Nambu, Y. Matsumoto, M. Morinaga, *International Journal of Hydrogen Energy*, 35 (2010) 1245
- [41] H. Yukawa, G. X. Zhang, N. Watanabe, M. Morinaga, T. Nambu, Y. Matsumoto, *Journal of Alloys and Compounds*, 476 (2009) 102
- [42] S. Hara, S. Sakaki, N. Itoh, H. M. Kimura, K. Asami, A. Inoue, *Journal of Membrane Science*, 164 (2000) 289
- [43] R. C. Bowman, Jr., *Materials Science Forum*, 31 (1988) 197

Chapter 7

Potential of Cu-Nb Alloys as Hydrogen Permeation Membranes

7.1 Introduction

Much of the current research on cost-effective alternative hydrogen-permeable membranes is focused on Nb-based alloys with a duplex microstructure [1–10]. In addition to its high hydrogen transport, body centred cubic Nb (bcc-Nb) is also known for its elemental superconducting behaviour below 9.2 K at atmospheric pressure. Due to these properties Nb has been used widely in commercial superconducting wires. This chapter investigates the potential of Cu-Nb alloys as hydrogen permeation membranes.

The Cu–Nb alloys with which this chapter is concerned are examples of such superconducting wires. These Cu–Nb superconductors have been studied thoroughly from a metallurgical and superconducting perspective [11–18]. Based on the foundational work laid back in the 1980s and 1990s, it is known that Cu–Nb alloys are very good at electron conduction and have good mechanical properties. It has been demonstrated that multifilamentary Cu–Nb composites can be best produced by consumable arc casting and subsequent drawing of the cast ingot into wires [11,12]. Hence, the potential to mass-produce this type of alloy has been demonstrated. What signifies the Cu–Nb alloy system as a potential candidate for hydrogen permeation membranes is that it has a microstructure

analogous to the Nb–Ti–Ni hydrogen permeation membranes, i.e. the presence of a hydrogen-permeable Nb phase embedded in a supporting secondary matrix. Although the hydrogen permeation behaviour of Cu–Nb multifilamentary composites is yet to be investigated in detail, the hydrogen embrittlement resistance of a Cu–20 vol.% Nb alloy has been studied by Spitzig et al. [14]. They reported that the mechanical properties of the Cu–20 vol.% Nb alloys did not suffer significantly when exposed to an equivalent amount of hydrogen that would have caused damage to pure Nb. The fact that these tests were carried out at low temperatures, where hydrogen embrittlement due to hydride formation is expected, suggests that the Cu–Nb alloys have high resistance to hydrogen embrittlement. Poor resistance to hydrogen embrittlement is a common limitation in several Nb-based alloy membranes and this therefore earmarks Cu-Nb alloys as promising candidates for hydrogen permeation membranes.

The primary aim of this chapter is to investigate the hydrogen permeation behaviour of Cu–Nb composites and thereby discuss the potential of these well-established superconductors as a novel hydrogen permeation membrane. Two types of Cu-Nb alloys that were specifically developed and studied for their superconducting properties will be investigated in this chapter. The first type is an as-cast Cu-Nb alloy that was supplied by Emeritus Professor J. D. Verhoeven and Dr. L. L. Jones from Ames laboratories USDOE at the Iowa State University (US). The second type is a Cu/Nb/Cu nanofibre wire supplied by Prof. L. Thilly and Dr. F. Lecouturier from the University of Poitiers and the ‘Laboratoire National des Champs Magnétiques Pulsées’ of CNRS-UPS-INSA (France) respectively.

7.2 As cast Cu-Nb alloys

7.2.1 Sample preparation and methodology

Attempts to make the Cu-Nb alloys by using the conventional arc melting technique failed due to the immiscibility of Nb and Cu. It was therefore required to source the samples from

Ames laboratory. Both the as-cast Cu–15 vol.% Nb and rolled Cu–20 vol.% Nb alloys were prepared by a technique called ‘*consumable arc casting*’. Figure 7.1 shows an example of the ingots that were prepared by the conventional arc melting. The ingot appears to be inhomogeneous because of the segregation of the Nb and Cu melts. Unlike the conventional arc melting, the consumable arc casting technique uses a double melt processing procedure to enhance ingot homogeneity. More details of this preparation technique can be found in Section 3.5.1 and elsewhere [11–13]. The sample preparation methods of the Cu-Nb samples were similar to that described in Chapter 3 and the hydrogen permeation test conditions similar to that described in Section 5.2.



Figure 7.1. Cu-Nb ingot prepared by a conventional arc melting technique.

The in-situ high pressure XRD characterization of the sample in vacuum and in a hydrogen atmosphere was done with the kind help of Prof. K. Aoki and Prof. K. Ishikawa at their research laboratory at the Kitami Institute of Technology in Hokkaido (Japan). The Pd coated sample was placed in the chamber of a heating furnace that was subsequently evacuated to below 10^{-2} Pa. The X-ray diffraction patterns were taken at room temperature before being heated to various temperatures under vacuum. The maximum temperature the samples were heated to was 723 K. X-ray diffraction patterns were taken under vacuum prior to the introduction of hydrogen at temperature, T_H . Hydrogen gas was then introduced in the chamber until an isostatic pressure of 0.5 MPa was reached. The X-ray diffraction

patterns were then taken under constant hydrogen pressure at the highest temperature followed by scans taken at decreasing temperature intervals.

7.3 Results

The XRD patterns of the as-cast Cu-15 vol.% Nb sample and the rolled Cu-20 vol.% Nb sample are shown in Figure 7.2 (a) and (b), respectively. The intensity ratio for the fcc-Cu reflection peaks in Figure 7.2 (a) is consistent with that of the literature value (JCPDS PDF file number 00-004-0836), indicating that the as-cast Cu-15 vol.% Nb sample is free of texture. However, the intensity ratio of Cu (200) to Cu (111) reflection peaks for the rolled Cu-20 vol.% Nb sample is clearly higher than that in the PDF reference mentioned above. This indicates that a (100) texture effect is induced in the rolled Cu-20 vol.% Nb sample. The set of four reflection peaks observed in each of the two XRD patterns are consistent with those of bcc-Nb with PDF file number 00-016-0001, and no traces of intermetallic compounds are observed. The phases present in the two samples are consistent with the binary Cu-Nb alloy system. When the reflection peaks of Nb (110) and Cu (111) are compared, a higher Nb to Cu peak ratio is observed in the Cu-20 vol.% Nb sample as opposed to the Cu-15 vol.% Nb sample.

The SEM images of the as-cast and rolled Cu-Nb alloys can be seen in Figure 7.3 (a) and (b), respectively. In both cases, the microstructure consists of the Nb phase surrounded by a Cu matrix. It is evident from the SEM image for the rolled Cu-Nb alloy that the Nb grains are slightly elongated, presumably because of the mild texture effect in the rolled sample. The grain size in the rolled sample was also found to be about 30-40 % smaller than that in the as-cast sample.

The temperature dependence of hydrogen permeability (Φ) for the as-cast Cu-15 vol.% Nb and rolled Cu-20 vol.% Nb alloys is shown in the form of an Arrhenius plot in Figure 7.4. The Φ of pure Pd is included for reference [12].

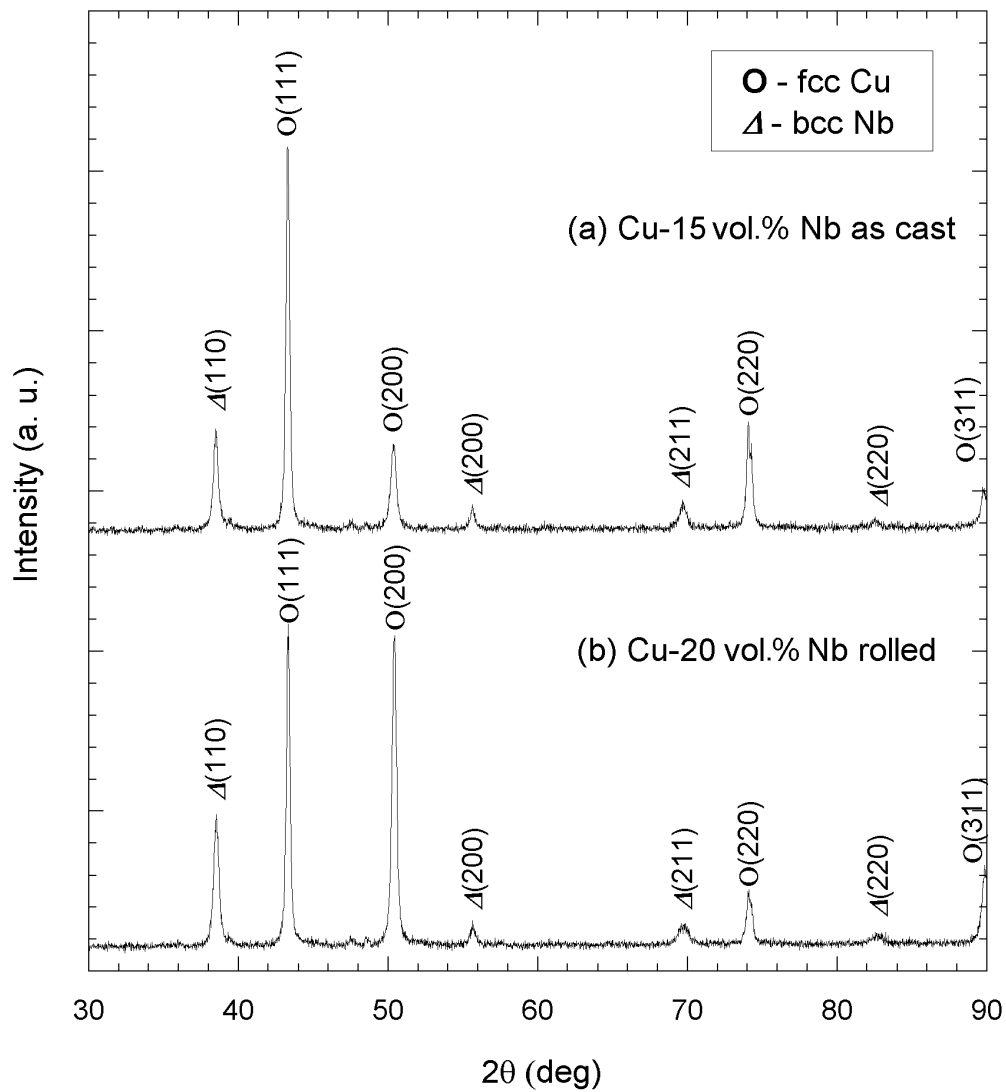


Figure 7.2. X-ray diffraction patterns of (a) Cu–15 vol.% Nb as-cast and (b) Cu–20 vol.% Nb rolled alloys.

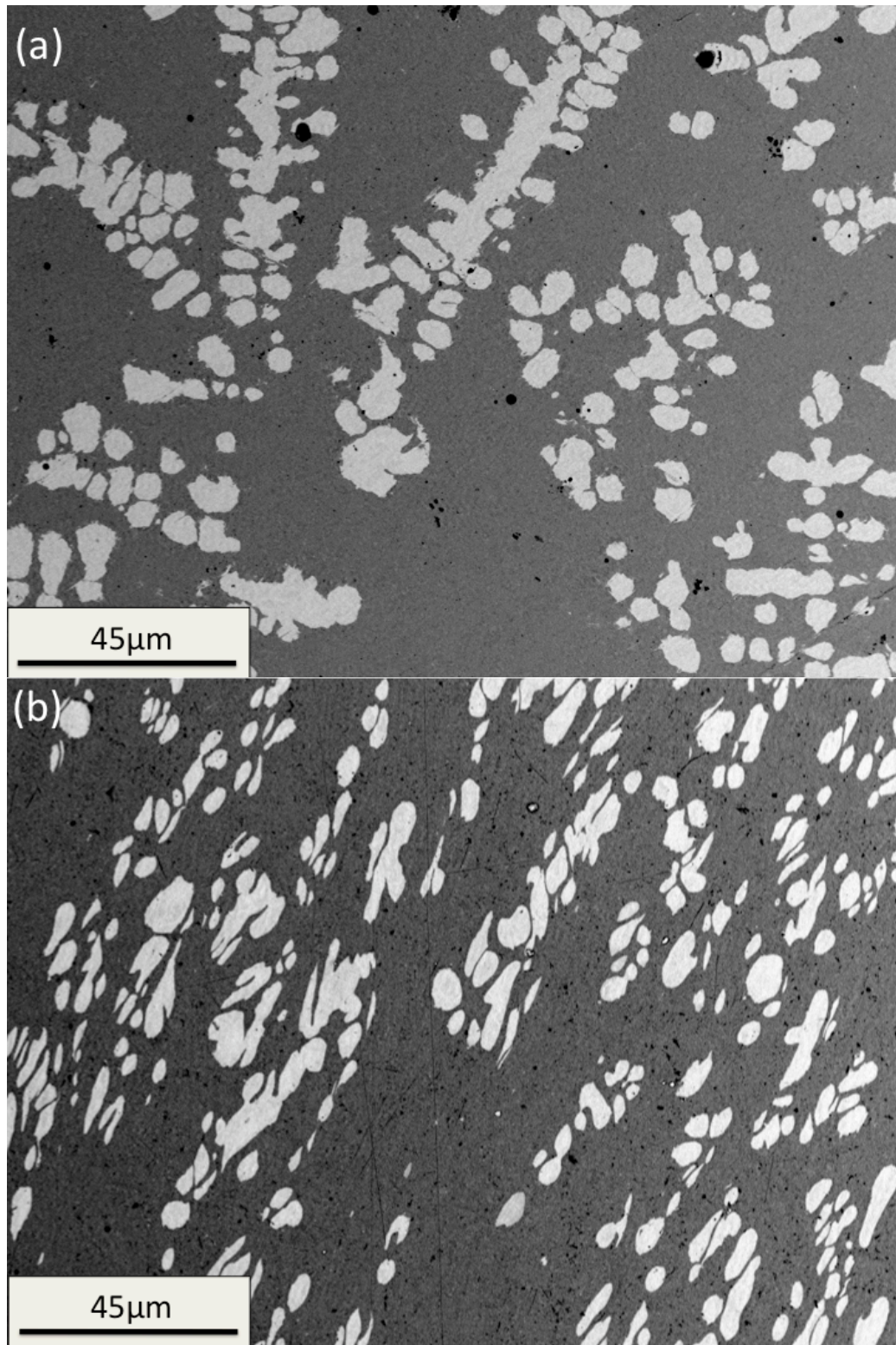


Figure 7.3. Scanning electron micrographs of (a) as-cast Cu-15 vol. % Nb and (b) rolled Cu-20 vol. % Nb samples. The scanned surfaces correspond to the membrane plane perpendicular to the hydrogen permeation path.

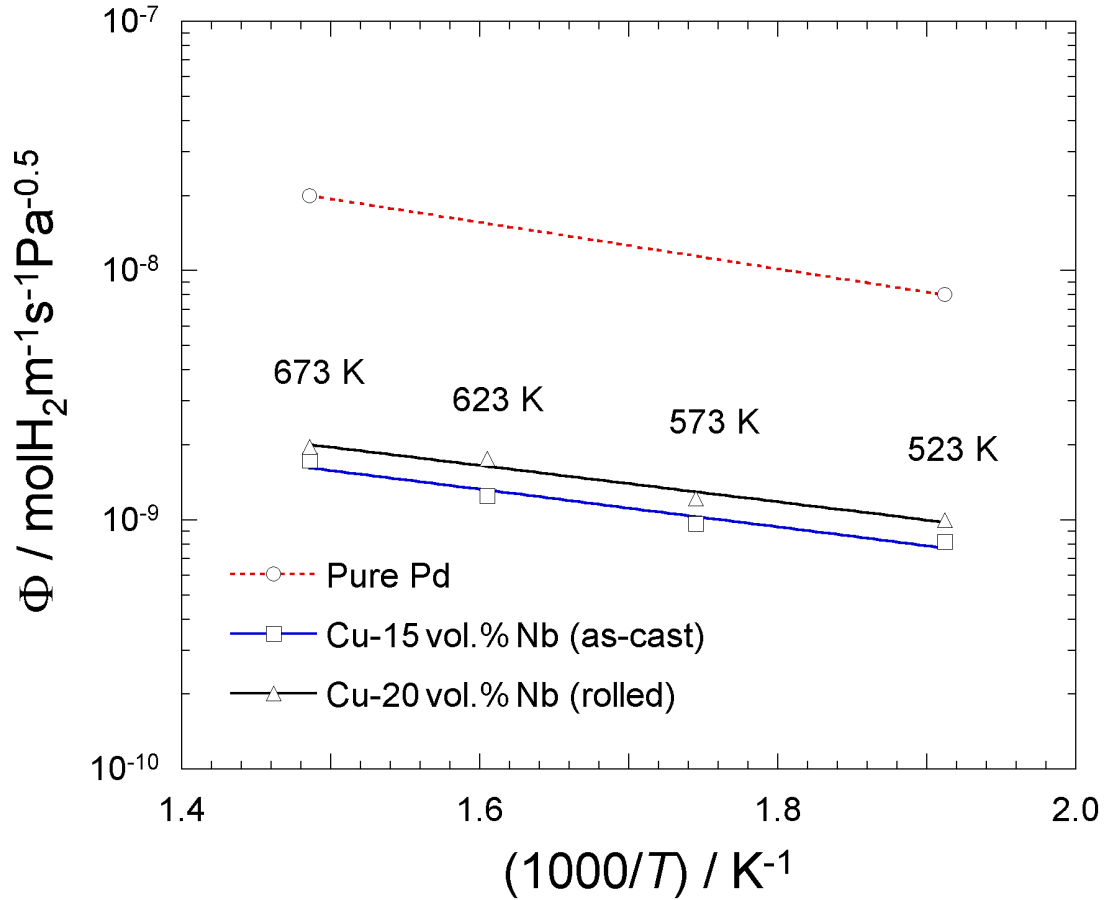


Figure 7.4. Temperature dependence of hydrogen permeability Φ for the as-cast Cu-15 vol. % Nb and rolled Cu-20 vol. % Nb alloys. The Φ of pure Pd [12] is also plotted for comparison.

The appearance of the Cu-20 vol.% Nb rolled sample after the hydrogen permeation test is shown in Figure 7.5. The alloy membrane appears to be free of cracks, suggesting that this particular alloy is resistant to hydrogen embrittlement.

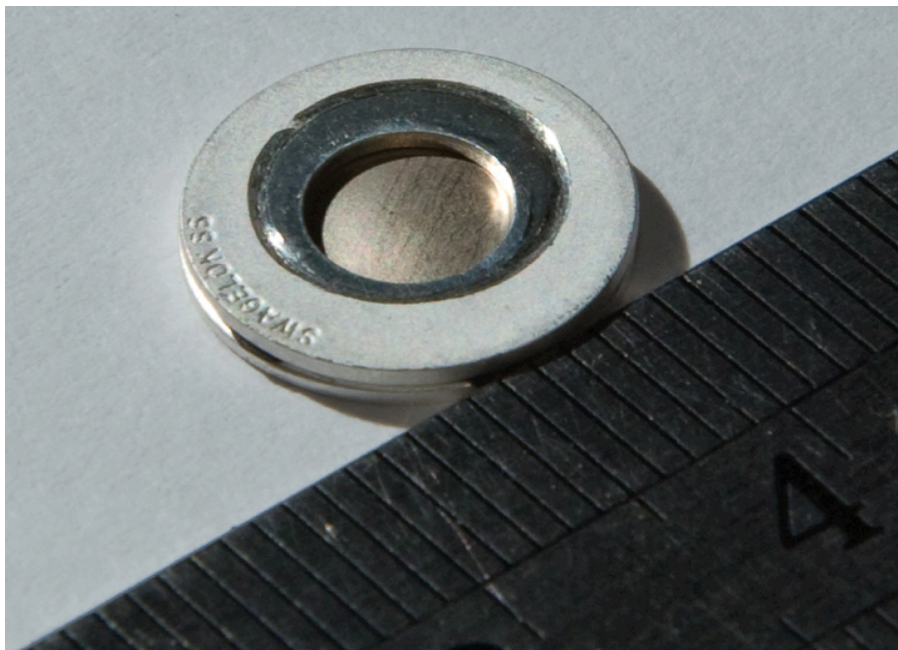


Figure 7.5. Appearance of the Cu–20 vol.% Nb rolled sample after the hydrogen permeation test. The sample is sandwiched between two silver-coated stainless steel gaskets of 12 mm diameter.

The in-situ XRD patterns of Pd coated as-cast Cu–15 vol.% Nb membranes acquired under vacuum at different temperatures can be observed in Figure 7.6. The reflection peaks of bcc-Nb and fcc-Cu phases on the three patterns are consistent with those observed in Figure 7.2. The reflection peaks of the fcc-Pd phase observed on the patterns acquired at 298 and 523 K are consistent with those of fcc-Pd with PDF file number 00-005-0681. These three phases are observed to be distinct from one another with no trace of intermetallic compounds below 523 K. At 723 K, the Nb and Cu peaks are still present, but it can also be observed that the Pd peaks at 40.1° and 46.6° have disappeared and new peaks have appeared at angles of 42.7° , 49.7° and 72.9° . These new peaks correspond to a $\text{Cu}_{3.18}\text{Pd}_{0.82}$ phase (PDF number 04-001-7353), indicating that the Pd coating has alloyed with Cu. The Cu peaks are observed to shift slightly to a lower angle with increasing temperature, reflecting the lattice expansion due to heating. The same phenomenon can be observed in Pd peaks but is not obvious in the Nb peaks. This may be attributed to the lower

thermal expansion of Nb, which has a melting point at least 1000 K higher than those of Pd and Cu.

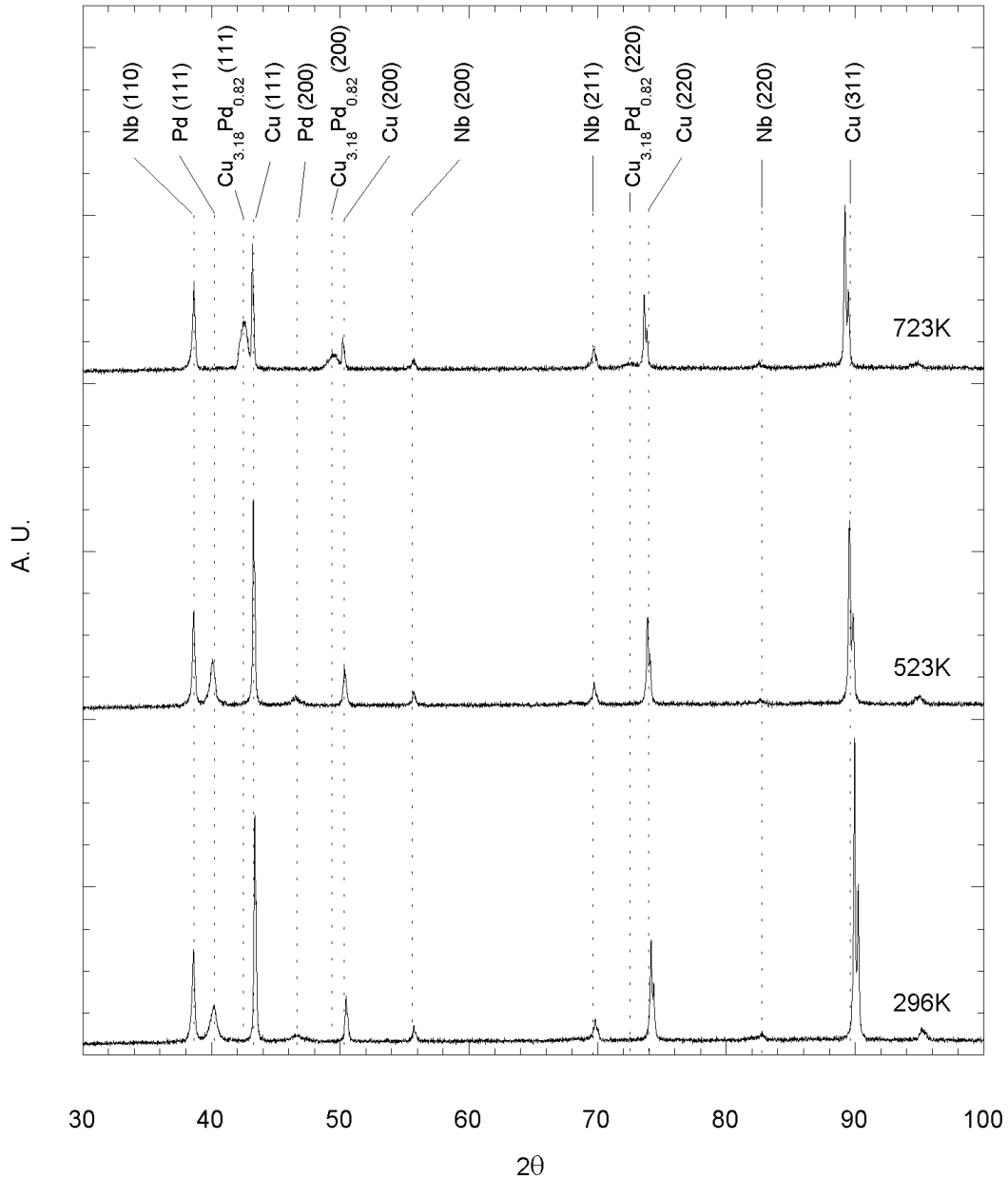


Figure 7.6. XRD traces of a Pd coated as-cast Cu–15 vol.% Nb membrane under vacuum with increasing temperature to a maximum of 723 K.

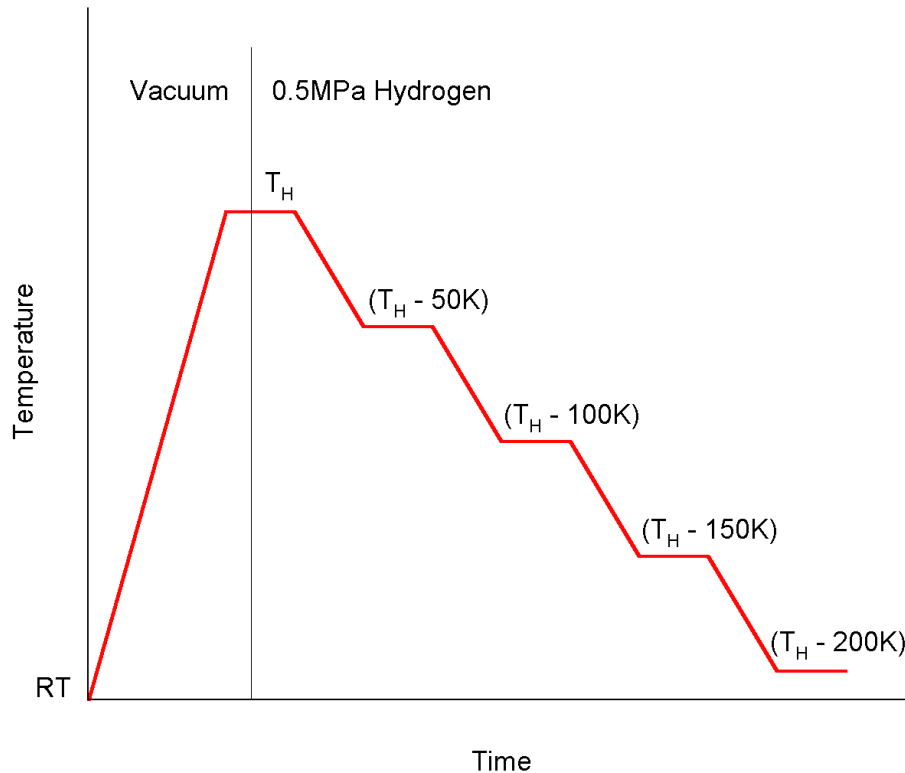


Figure 7.7. Schematic chronological diagram of the in-situ XRD analysis of the as-cast Cu–15 vol.% Nb membranes to a maximum temperature (T_H) in a hydrogen atmosphere of 0.5 MPa and under vacuum.

The relationship between temperature and time during the in-situ XRD analysis of the membranes is shown schematically in Figure 7.7. The samples were first heated to a maximum temperature (T_H) under vacuum before hydrogen was introduced and the hydrogen pressure was maintained at 0.5 MPa.

The in-situ XRD patterns of a Pd coated as-cast Cu–15 vol.% Nb membrane with a maximum temperature (T_H) of 573 K in a 0.5 MPa hydrogen atmosphere can be seen in Figure 7.8. Despite the presence of hydrogen, the Cu reflection peaks remain unchanged during the cooling to 423 K in a hydrogen atmosphere. The bcc-Nb reflection peaks observed previously under a vacuum condition (Figure 7.6) were replaced by reflection peaks corresponding to a NbH phase (PDF file number 00-0391167) when hydrogen was introduced. This is expected due to the affinity Nb has for hydrogen. The fcc-Pd reflection peaks are present at 573 K and 523 K, but as the temperature decreases to 473 K and below,

the Pd peaks disappear and new peaks appear at 38.5° and 78.5° . These new reflection peaks corresponds to a $\text{PdH}_{0.66}$ phase (PDF number 01-089-0943). This indicates that the catalytic Pd coating deteriorates into hydrides below 523 K.

The in-situ X-ray traces of a Pd coated as-cast Cu-15 vol.% Nb sample with $T_H = 723$ K in 0.5 MPa hydrogen atmosphere are shown in Figure 7.9. The reflection peaks from bcc-Nb and fcc-Cu are present in all the traces. However, the fcc-Pd reflection peaks are absent from these XRD traces because of the formation of $\text{Cu}_{3.18}\text{Pd}_{0.82}$ during the initial heating process at 723 K in a vacuum. These traces are similar to those present in Figure 7.6, where a similar sample was heated under vacuum. It can be observed that upon cooling, the $\text{Cu}_{3.18}\text{Pd}_{0.82}$ (111) and Cu (220) reflection peaks shift systematically to a higher angle, reflecting the lattice contraction due to cooling. On the other hand, the NbH (111) peak shows a small shift to a lower angle, indicating that lattice expansion takes place during cooling. This lattice expansion can be attributed to an increasing hydrogen concentration with decreasing temperature.

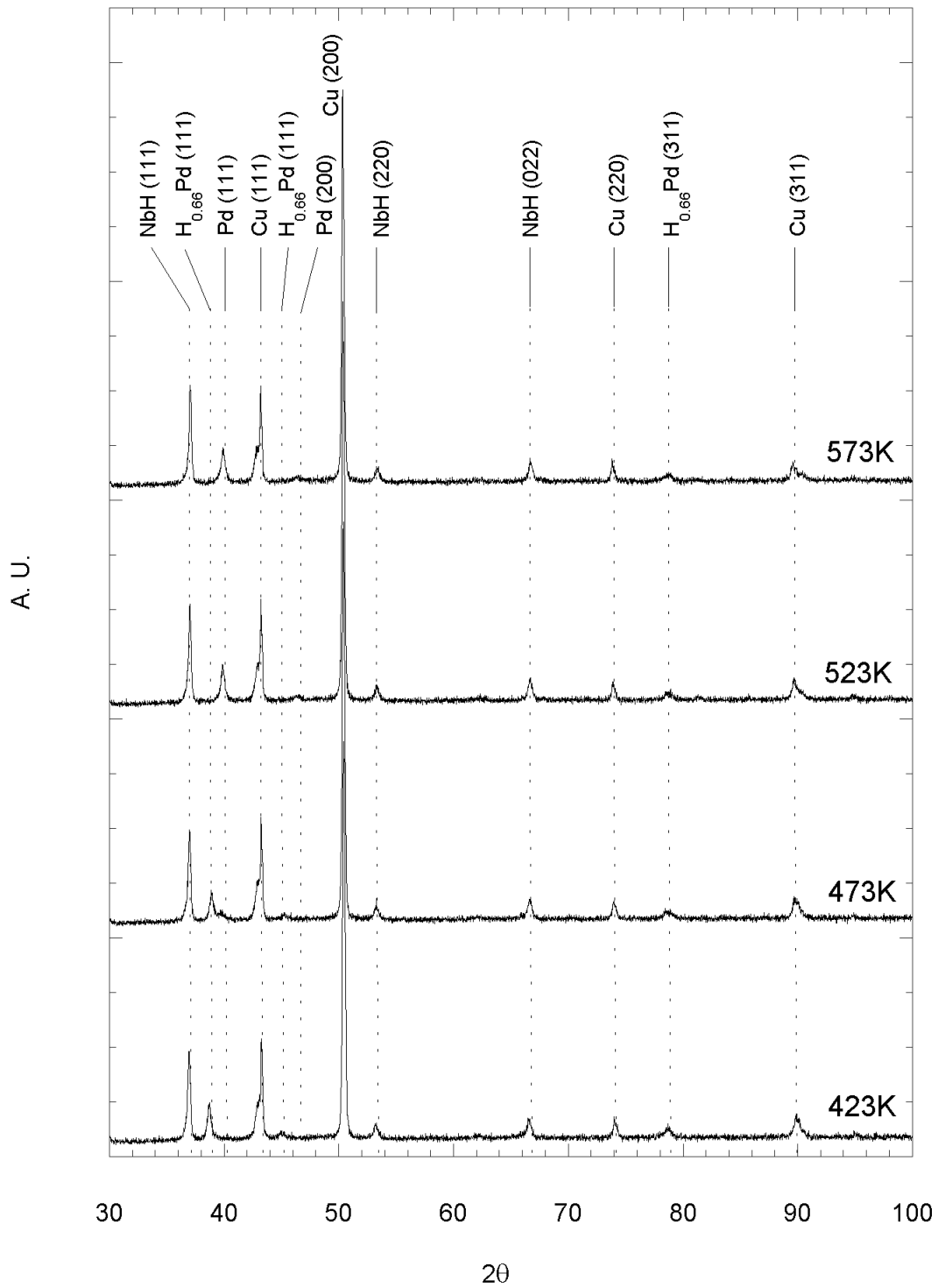


Figure 7.8. XRD traces of a Pd coated as-cast Cu-15 vol.% Nb membrane with maximum temperature, $T_H = 573$ K in 0.5 MPa hydrogen atmosphere.

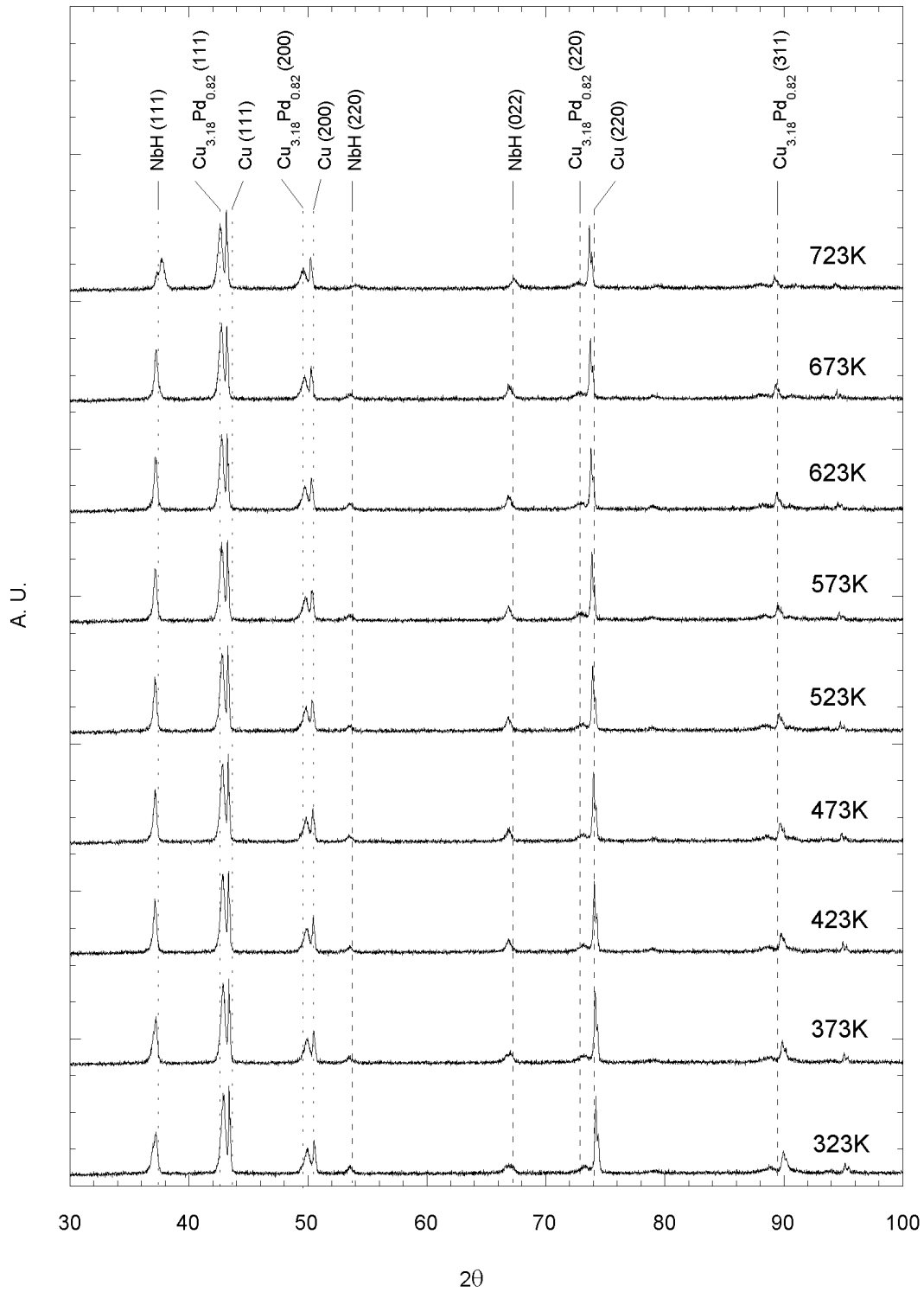


Figure 7.9. XRD traces of a Pd coated as-cast Cu-15 vol.% Nb membrane with maximum temperature, $T_H = 723$ K in 0.5 MPa hydrogen atmosphere.

The change in lattice parameter of the fcc-Cu phase of the Pd coated as-cast Cu–15 vol.% Nb alloy in vacuum and in hydrogen atmosphere at different temperatures is illustrated in Figure 7.10. These lattice parameters were obtained from the XRD traces in Figures 7.6 and 7.9 based on the method described in Section 3.3.5.

$$\frac{\Delta l}{l_o} = \alpha_1 \cdot \Delta T \quad (7.3)$$

The coefficient of linear thermal expansion was calculated by using the following equation, where Δl is the change in lattice parameter, l_o the original lattice parameter, ΔT the change in temperature and α_1 the coefficient of linear thermal expansion. It can be observed that the fcc-Cu phase experiences thermal lattice expansion with increasing temperature. The average coefficient of linear thermal expansion of the Cu phase in vacuum was calculated to be $13.6 \pm 2.8 \times 10^{-6} / \text{K}$, which is within the range of the coefficient of linear thermal expansion of pure Cu ($16.5 \pm 0.2 \times 10^{-6} / \text{K}$) in the literature [19], given the experimental error. The lattice parameter of Cu is unaffected by the hydrogen atmosphere, as there is little difference between the lattice parameters of Cu in the hydrogen atmosphere and in vacuum. This indicates the potential of Cu to resist hydrogen embrittlement.

The change in lattice parameter of the Nb phase in the as-cast Cu–15 vol.% Nb alloys in vacuum as a function of temperature from room temperature to 723 K is shown in Figure 7.11. It can be observed that the bcc-Nb phase experiences lattice expansion with increasing temperature under vacuum. The average coefficient of linear thermal expansion was calculated using Equation 7.3 and was found to be $7.0 \pm 1.9 \times 10^{-6} / \text{K}$. This calculated value is within the range of the literature value for the coefficient of linear thermal expansion of pure bcc-Nb ($7.2 \pm 0.1 \times 10^{-6} / \text{K}$) [19].

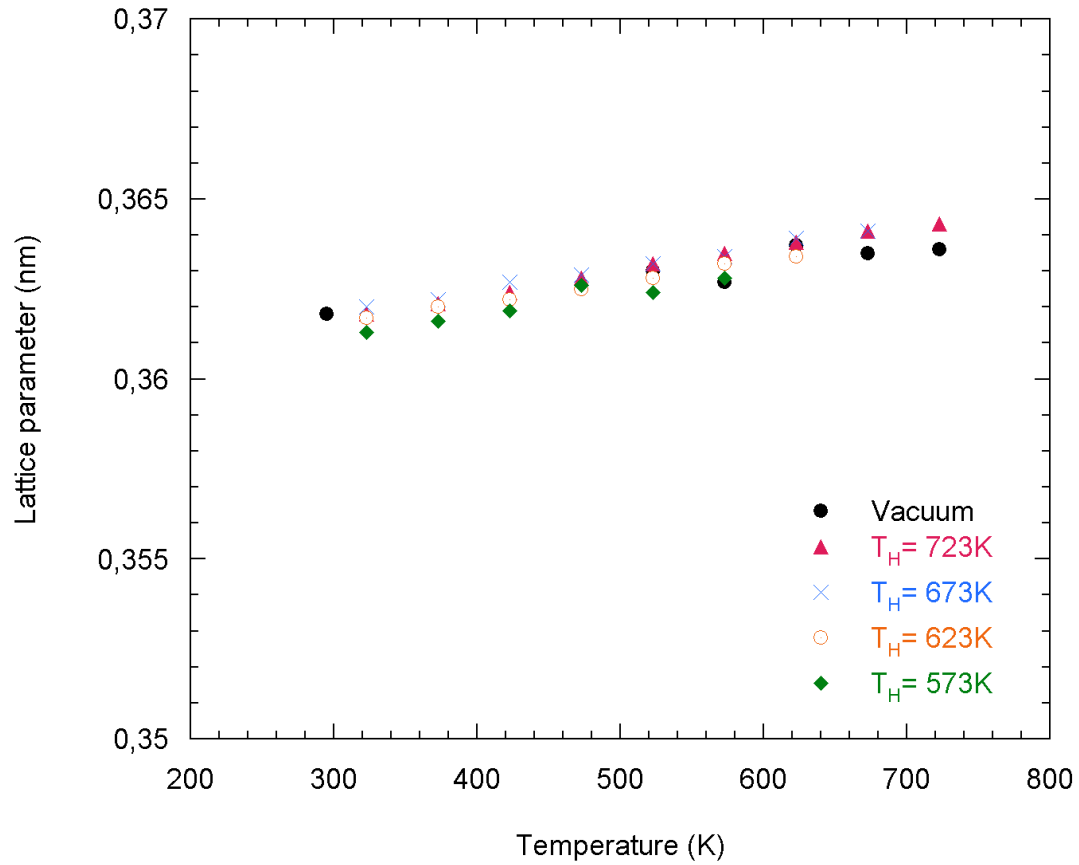


Figure 7.10. Lattice parameter of the Cu phase of the Pd coated as-cast Cu–15 vol.% Nb alloy in vacuum and hydrogen atmosphere when heated to various maximum temperatures (T_H).

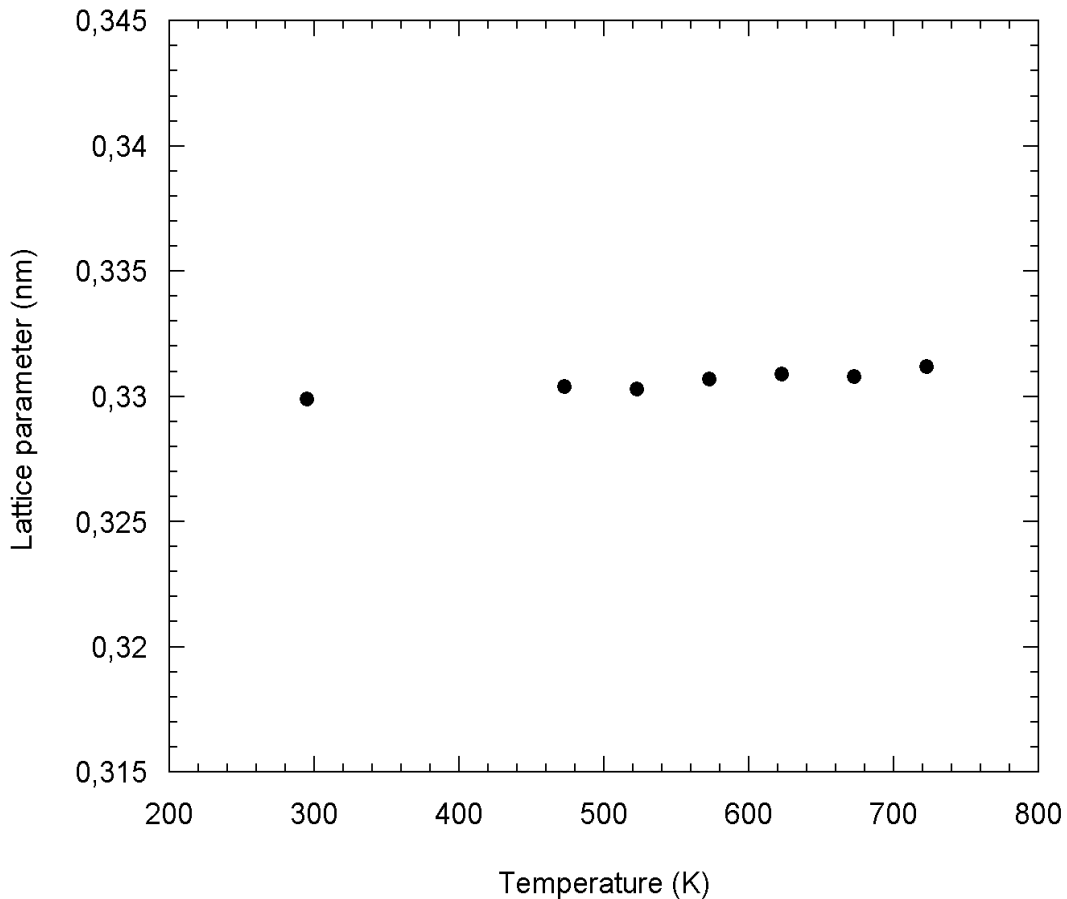


Figure 7.11. Lattice parameters of the bcc-Nb phase for the as-cast Cu–15 vol.% Nb alloy when heated from room temperature to 723 K in vacuum.

The change in lattice parameter of the NbH phase observed in Figures 7.8 and 7.9 when T_H is 573 to 723 K is shown in Figure 7.12. The lattice parameter of the NbH phase for $T_H = 573, 623$ and 673 K increases with decreasing temperature. This can be attributed to an increase in the hydrogen concentration within the NbH phase, which will be discussed further in Section 7.4.2, which looks into the effect of H on the Nb and Cu phases. However, the sample heated to 723 K shows a different trend and the lattice parameter of the NbH phase decreases with decreasing temperature below 500 K. This suggests that the hydrogen absorption rate upon cooling depends on T_H .

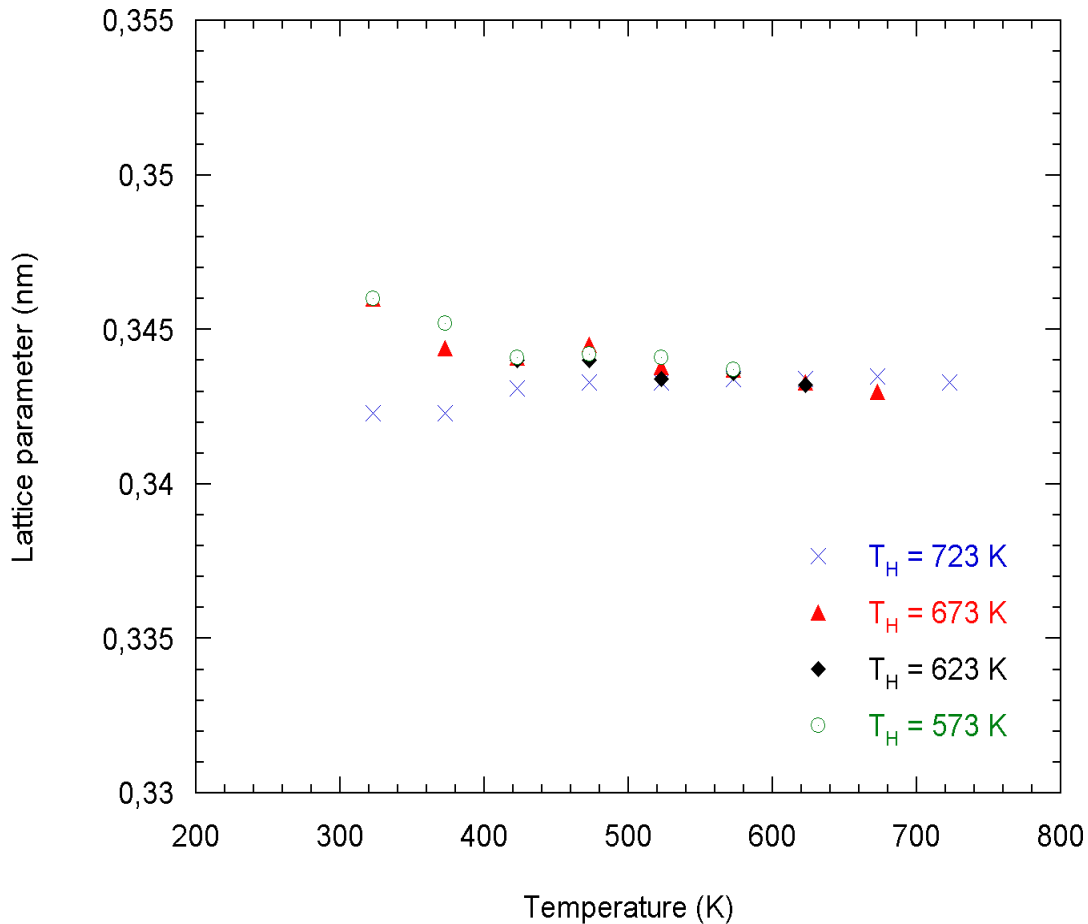


Figure 7.12. Lattice parameter of the NbH phase for the as-cast Cu–15 vol.% Nb alloys when heated in a 0.5 MPa hydrogen atmosphere to various maximum temperatures (T_H).

The lattice parameter of the Pd coating on the as-cast Cu–15 vol.% Nb alloy in vacuum and in a 0.5 MPa hydrogen atmosphere at $T_H = 573$ K is shown in Figure 7.13. The lattice expansion due to heating can be observed in the Pd phase under vacuum. The coefficient of linear thermal expansion of Pd in vacuum calculated from the patterns is $12.8 \pm 1.8 \times 10^{-6} / \text{K}$. This value is consistent with the literature value for pure Pd ($11.8 \pm 0.2 \times 10^{-6} / \text{K}$). Estimation of the lattice parameter for the Pd phase in a hydrogen atmosphere at $T_H > 573$ K was not possible because of the disappearance of the Pd phase due to the formation of a Cu-Pd phase. Under a H_2 atmosphere in a temperature range between 523 K and 573 K, the 2θ angle of reflection peaks Pd (111) and Pd (220) are observed to remain unchanged. Under vacuum, the Pd (111) and Pd (220) peaks showed no change in 2θ angle in the temperature range of 523 K and below, as shown in Figure 7.6. However, an

appreciable lattice expansion occurs when Pd is exposed to a hydrogen atmosphere at 473 K and below. The lattice expansion from around 0.389 nm to about 0.403 nm is seen in the plots in Figure 7.13. This lattice expansion is consistent with the formation of fcc-Pd-hydride, $\text{PdH}_{0.66}$, which was previously identified in Figure 7.8 by XRD analysis and has been reported elsewhere by Jamieson et al. [20].

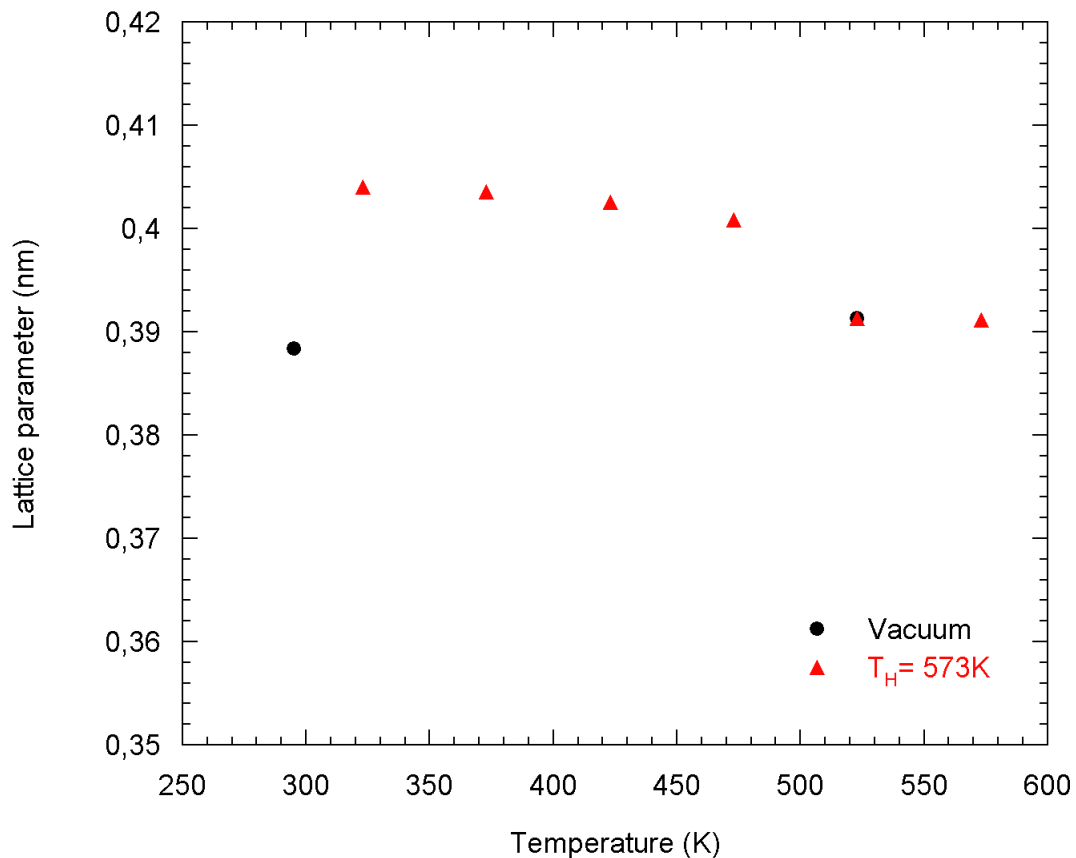


Figure 7.13. Lattice parameter of the Pd phase of the as-cast Cu–15 vol.% Nb alloy in vacuum and hydrogen atmosphere when $T_H = 573\text{ K}$. The lattice parameter of $\text{PdH}_{0.66}$ phase is observed below 473 K when cooled from $T_H = 573\text{ K}$.

7.4 Discussion

7.4.1 Potential of Cu-Nb alloys for hydrogen permeation applications

The Φ of the as-cast Cu-15 vol.% Nb and rolled Cu-20 vol.% Nb are 1.7×10^{-9} and 1.93×10^{-9} [$\text{molH}_2\text{m}^{-1}\text{s}^{-1}\text{Pa}^{-0.5}$] respectively at 673 K. Both Φ values are about 10 times smaller than that of pure Pd, as seen in Figure 7.4. The Φ values of both Cu-Nb alloys are found to increase with increasing temperature and the rolled sample was found to have a slightly higher Φ than that of the as-cast sample. Tang et al. and Ishikawa et al. reported that the hydrogen permeability of cold-rolled membranes is usually lower than that in the as-cast state and that the permeability could not only be restored but also enhanced by subsequent annealing [2, 7]. The hydrogen permeability of the rolled Cu-20 vol.% Nb sample was expected to be higher than that of the Cu-15 vol.% Nb sample due to the higher volume fraction of the hydrogen favourable Nb phase. This argument is further discussed in Section 7.4.4.2. Based on the work reported by Tang et al. and Ishikawa et al., the marginally higher Φ of Cu-20 vol.% Nb may be attributed to the effect of rolling and the annealing effect of testing the samples at elevated temperatures for hydrogen permeation [2, 7]. A past study by Tang et al. on the effect of annealing and how the microstructural changes affect the hydrogen permeation rate of cold-rolled samples brings a case for optimism [7].

The conventional approach in designing Nb-based hydrogen permeable membranes is that Nb is the hydrogen permeable phase and this phase is embedded in a supporting matrix resistant to hydrogen embrittlement to improve its performance. Ishikawa et al. have compared the permeation properties of $\text{Nb}_{40}\text{Ni}_{30}\text{Zr}_{30}$ to those of $\text{Nb}_{39}\text{Ni}_{30}\text{Ti}_{31}$ membranes and found that $\text{Nb}_{40}\text{Ni}_{30}\text{Zr}_{30}$ had a Φ value 2.5 times higher than that of $\text{Nb}_{39}\text{Ni}_{30}\text{Ti}_{31}$ even though both had a similar volume fraction of Nb and similar microstructures [8]. The higher Φ was believed to be due to hydrogen permeating through Zr. A similar argument based on the hydrogen permeability of the matrix phase may be used to explain the difference in Φ between the Nb-Ni-Zr and Cu-Nb alloys. However, the hydrogen permeability of the rolled

Cu-20 vol.% Nb is about 15 times lower than that of Nb₂₀Ni₄₀Zr₄₀ even though the volume fraction of Nb is about the same. It is difficult to attribute such a large Φ difference to the hydrogen diffusion through Zr alone. There could also be other factors influencing the Φ of the Nb₂₀Ni₄₀Zr₄₀ such as the larger density of grain boundaries and phase boundaries present. Nb₂₀Ni₄₀Zr₄₀ has a small primary phase (Nb,Zr) surrounded by a fine eutectic structure (NiZr + Nb,Zr) unlike the Cu-20 vol.% Nb which has its primary phase (Nb) surrounded by a single phase copper matrix.

An interesting aspect of the Cu-Nb alloy is that it consists of two simple solid solutions with negligibly small solubility limits. This simple binary alloy system can smooth the progress of fundamental work, for instance the investigation on the effect of the microstructure, such as grain size, phase boundaries and grain boundaries on the diffusivity and solubility of hydrogen in the membranes. The Cu-Nb alloy system is also a very malleable and ductile alloy system, which provides a broad scope regarding the control of the microstructure by severe plastic deformation, which is a well-established approach to nano-scale microstructural grain refinement. Both the Cu-15 vol.% Nb and Cu-20 vol.% Nb samples were tested in a pressure range of 0.15-0.5 MPa and did not fail. Figure 7.5 shows that the thinner rolled Cu-20 vol.% Nb sample deformed plastically into a small dome shape during the test, which shows that this particular alloy system is resistant to hydrogen embrittlement and remains ductile in a hydrogen atmosphere unlike other Nb-based alloys [8, 21]. The mechanical strength and resistance to hydrogen embrittlement of this Cu-Nb alloy system indicates good durability and could allow the use of thinner membranes. This could lead to an improvement in the flux of hydrogen passing through the membrane and to a reduction in the amount of material required for each membrane. Besides the technical potential benefit, the other savings would be on the cost of raw material as Cu is about 3 times cheaper than Ni and Ti, and 25 times cheaper than Zr. After these preliminary findings, the discussion of the in-situ X-ray analysis on the different phases, in vacuum and in a hydrogen atmosphere, is conducted below.

7.4.2 Effect of hydrogen on Nb and Cu phases

The increase in the Nb lattice parameter upon exposure to the hydrogen atmosphere because of hydrogen absorption can be seen in Figure 7.11. This is consistent with the common knowledge that Nb is highly permeable to hydrogen [2-9]. Figure 7.15 shows the equilibrium phase diagram of an Nb-H alloy system as reported by J.F. Smith [22]. Near the top section of Figure 7.15, a red line indicated by a small arrow denotes the temperature dependence of the equilibrium hydrogen content in bcc-Nb for a pressure of 1 bar. The lattice parameter of NbH is observed to increase with decreasing temperature in Figure 7.12, which indicates that the hydrogen content in NbH has a negative temperature dependence. This experimental result is consistent with the Nb-H phase diagram in Figure 7.14, where the hydrogen concentration also shows negative temperature dependence at a constant hydrogen pressure of 1 bar as shown by the red line. The lattice parameter of NbH when exposed to hydrogen in Figure 7.12 is consistent with that of the α' phase reported by Zabel and Peisl [23], as shown in Figure 7.15.

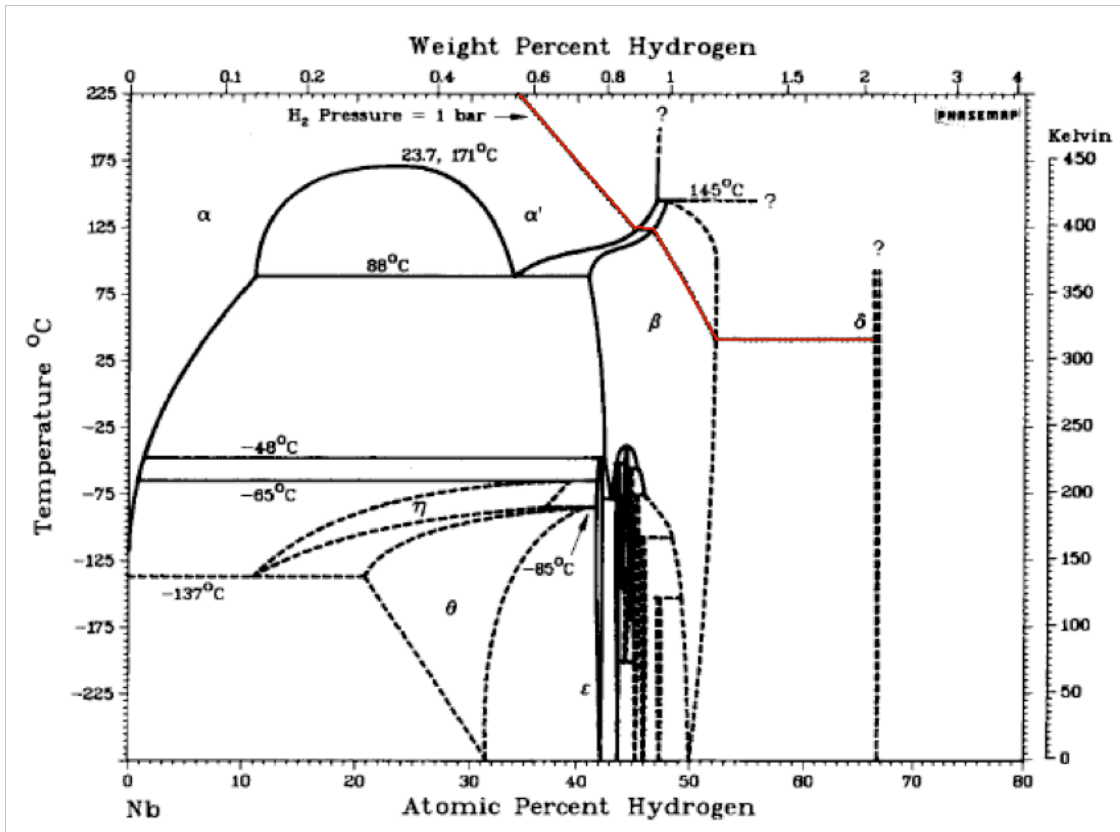


Figure 7.14. Nb-H phase diagram by J.F. Smith [22]

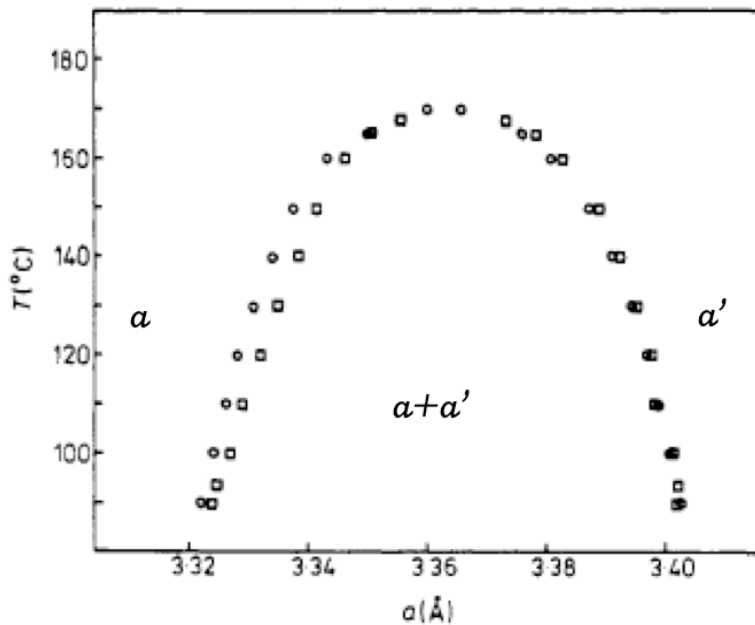


Figure 7.15. Lattice parameters of α - α' phase boundaries in Nb wire samples at various temperatures [23]. The lattice parameter of the NbH phase observed is in the α' phase region.

The presence of the α' phase is observed on the indexed XRD traces in Figures 7.8 and 7.9. The α' NbH phase observed in Figure 7.8 can be reversibly transformed to pure Nb when the sample is dehydrogenated under vacuum after the test for a period of 10 min at a temperature of 673 K. This method of dehydrogenating structurally sound Nb-based metallic membranes after a successful test is a common procedure used to prevent the formation of hydride and cracking. This is confirmed by XRD analysis of the sample after the dehydrogenation procedure as shown in Figure 7.16. Figure 7.17 shows the hydrogen pressure to hydrogen concentration isotherms in the Nb-H system as reported by S. Komjathy [24] and it can be observed that in a temperature range of 723-523 K and a pressure of 750mm Hg (equivalent to a pressure of 0.1 MPa), the H concentration range is between 0.5-0.75 H/Nb. The XRD data in Figure 7.16 shows that after the dehydrogenation process the NbH phase transforms back to a pure Nb phase, indicating the reversibility of the phase transformation using this method. Figure 7.16 also shows that the Pd coating forms a Cu-rich Cu-Pd phase after the dehydrogenation process at 673 K. The Pd catalyst is further discussed in Section 7.4.3.1. The resistance of the membrane to cracking after exposure to hydrogen at both elevated and room temperature is further discussed in the current section.

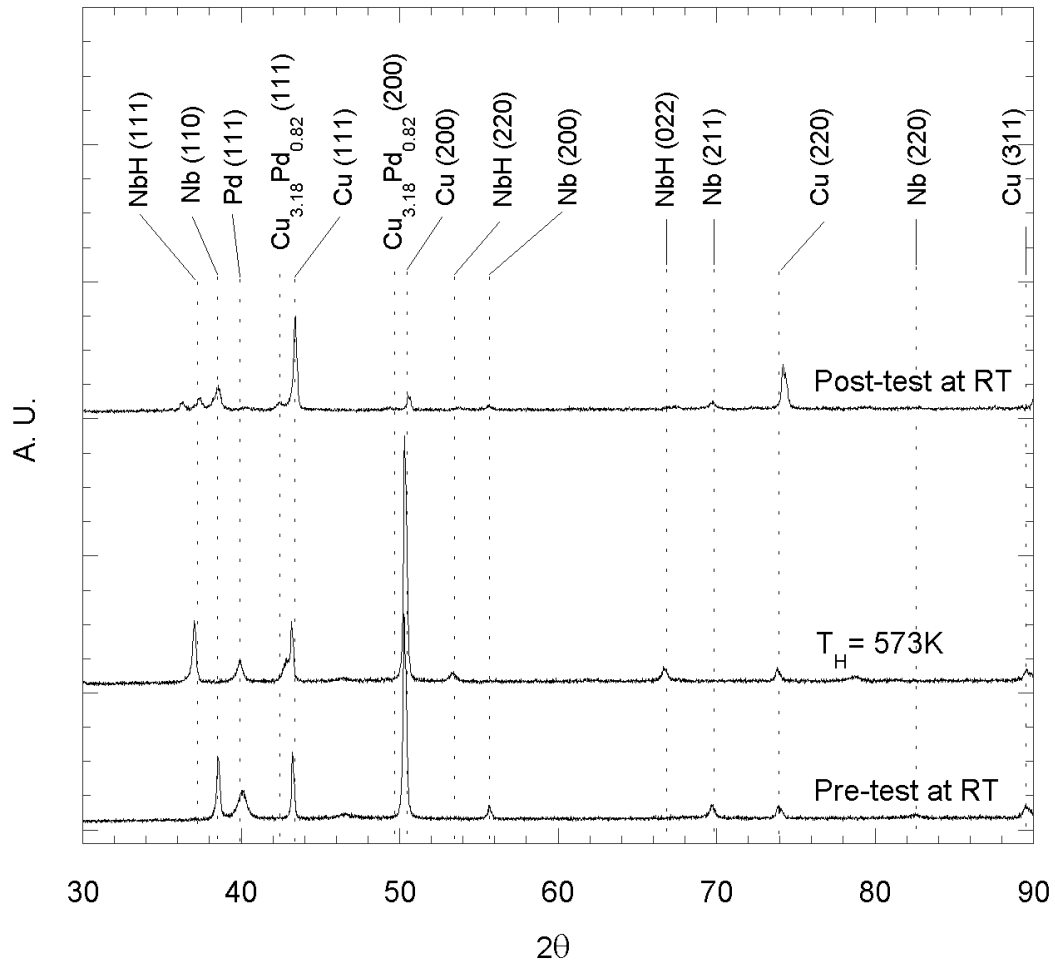


Figure 7.16. XRD of as-cast Cu-15 vol.% Nb alloy at room temperature before the test, during H permeation test at $T_H = 573\text{K}$ and at room temperature after the dehydrogenation procedure after the H permeation test.

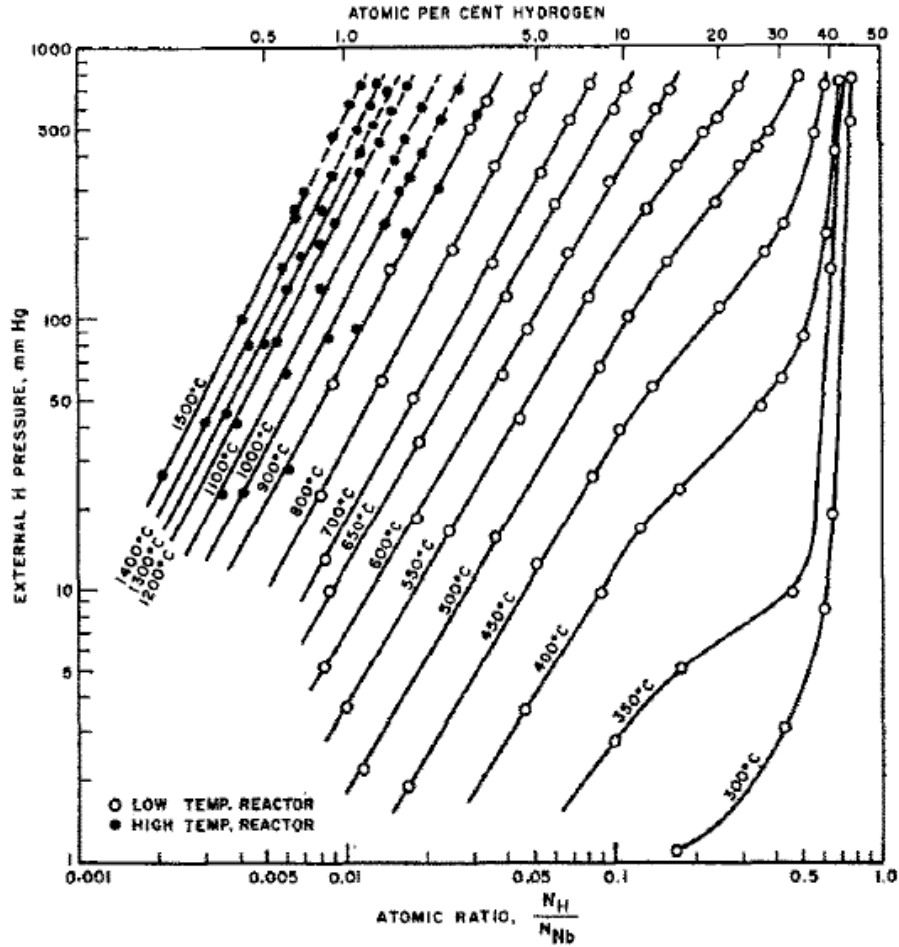


Figure 7.17. Hydrogen pressure to hydrogen concentration isotherms in Nb-H system by S. Komjathy [24].

Three arguments can be made for the observed resistance of the Cu-Nb alloy to hydrogen embrittlement. The first argument is based on the work of Yukawa et al. [26-27]. They proposed that a balancing act must be maintained between the hydrogen concentration gradient, ΔC , and resistance to hydrogen embrittlement to maximize the hydrogen flux through the membrane. The hydrogen flux, J , is known to be governed by Fick's first law, i.e.,

$$J = D \frac{\Delta C}{d} \quad (7.4)$$

Where D is the diffusion coefficient, d is the sample thickness and ΔC is the difference in concentration at the inlet and outlet side of the membrane. Nambu et al. and Yukawa et al. have recommended an ideal maximum hydrogen concentration of 0.25 H/M to avoid hydrogen embrittlement [27, 28]. From Figure 7.17, the H concentration in the Nb phase for the current experimental conditions associated with the Cu-Nb membranes should be 0.6 – 0.8 H/M. This is based on the assumption that H is only permeating through Nb and not Cu, as observed in Figure 7.10. It must be noted that the H concentration in Nb may be lower than that estimated, based on the second argument in the next paragraph on the work of Shibano et al. [29]

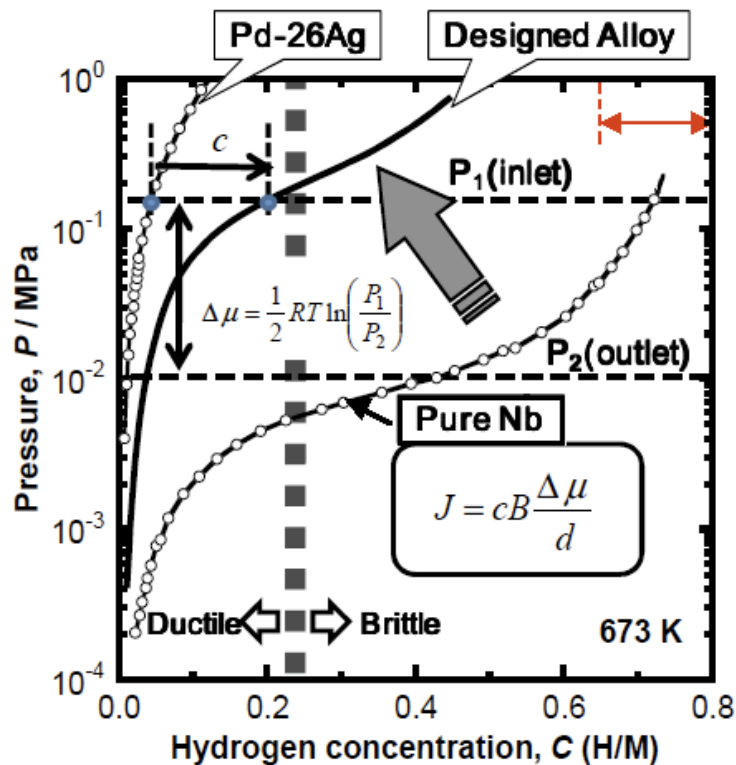


Figure 7.18. Schematic PCT diagram of Nb-based and Pd-based hydrogen permeable alloys by Yukawa et al. [26]. The red dot shows the H concentration of the Nb-Cu alloy at 673 K under an isostatic pressure of 0.5 MPa.

In Figure 7.18, Yukawa et al. reported a ductile to brittle transition region at a hydrogen concentration of 0.23 H/M [26]. A red line with double arrows is included in this figure to show the H concentration range of H in the Nb alloy between 573 to 673 K under

an isostatic pressure of 0.5 MPa based on the information from Figure 7.17. According to the work of Yukawa et al., it can be argued that the Nb phase in the Cu-Nb alloy is expected to fracture in a brittle manner [26]. However, in the present case a good resistance to hydrogen embrittlement was achieved, including ductile deformation of some thin membranes (~ 0.1 mm) tested under hydrogen atmosphere as shown in Figure 7.5 and no cracks were detected. This contradictory hydrogen embrittlement behavior of the Cu-Nb alloy membrane to the prediction by Yukawa et al. can be attributed to the unique microstructure of the Cu-Nb membranes, which is distinct from the Nb-based membranes reported by Yukawa et al. The Cu-Nb membranes have a duplex microstructure of a Nb-rich phase embedded in a supporting matrix resistant to hydrogen embrittlement, while the designed Nb-based alloy membrane described in Figure 7.18 consists mainly of a Nb rich solid solution with minor alloying elements. In the current study, the presence of the Cu supporting matrix is shown to allow for a higher hydrogen concentration in the Nb phase without failure of the membrane. The low H permeability of the Cu matrix is an advantage for this alloy as it preserves the structural integrity of the membrane from hydrogen embrittlement and gives the Nb-based duplex membrane a relatively high ductility in a hydrogen atmosphere, even at 373 K. The H concentration in Cu is nearly zero and the lattice expansion in H as shown in Fig. 7.10 does not deviate from the sample tested in vacuum. This behaviour is attributed to a low H solubility in Cu, which is due to the fact that the $H_2 + Cu$ system is a typical example of an activated system for the dissociation process as described by Kroes et al. [30]. The poor absorption of H in Cu is also reported to be due to its negative enthalpy of solution for hydrogen absorption [31]. Both Pd and Nb have a positive enthalpy of solution for hydrogen absorption, which facilitates the absorption of H in these elements and makes them likely to form hydrides [31].

The second argument is based around a similar study by Shibano et al. [29] on the Nb-Ti-Ni alloy system, where it was proposed that the resistance to hydrogen embrittlement is improved by the presence of the TiNi phase in the eutectic matrix. The shape memory TiNi phase is reported to deform to accommodate the strain during the change in shape of

the primary Nb phase upon absorption of H. According to Figure 7.14, the formation of β Nb-H phase is expected to appear at temperatures below 418 K, but in Figure 7.9 no β phase is observed to form below 418 K at a H₂ pressure of 0.5 MPa, which is equivalent to 5 bar [22-25]. It is well known that for a good resistance to hydrogen embrittlement the formation of the β Nb-hydride should be avoided, as the formation of the β phase leads to a distortion in the Nb lattice due to the long-range ordering of the H interstitials [32]. The absence of the Nb-hydride β phase below 418 K can be attributed to the isostatic pressure exerted by the Cu matrix on the α' NbH particles when they expand due to the absorption of H. This isostatic stress on the Nb phase is expected to limit the maximum hydrogen concentration in the Nb phase and hinders the transformation from the Nb-H α' phase to the β phase. The role of the Cu matrix in limiting the transformation from the Nb-H α' phase to the β phase in the membrane can be explained by the following argument by Shibano et al. on a Nb-rich phase supported by a eutectic Ti-Ni matrix [29]. The resistance of the Nb-Ti-Ni membrane was attributed to the Ti-Ni matrix, which deformed to accommodate the strain generated by the Nb rich phase upon absorption of hydrogen. However, that study also revealed that micro-cracks appeared when the membrane was cooled, in similar experimental circumstances to low temperatures under hydrogen atmosphere, and that the Ti-Ni supporting matrix was subject to a strain larger than that of the Nb phase. Even though the membrane was reported to be hydrogen embrittlement resistant, the formation of micro-cracks was observed at low temperatures unlike in the current Nb-Cu alloy. Shibano et al. estimated the stress to be several GPa based on the strain they calculated from their XRD data [29]. In the present Cu-Nb alloys, the volume change associated with the phase change from the bcc-Nb to the α' face-centred orthorhombic NbH phase is calculated to be 14.2 vol. %. This would equate to a 2.5 vol. % change in the Cu phase of the Cu-15 vol.% Nb alloy, provided that the total sample volume does not change and that there is an equiaxial volume change in the Cu phase. The change in 2θ diffraction angles on the XRD pattern due to this volume change in the Cu phase is calculated to be 0.0425° at the angle of the (111)

reflection. This change in 2θ angles is within the experimental errors associated with the measurement of the Cu (111) peak, which was found to have a standard deviation of $\pm 0.035^\circ$. Therefore, in the present case it is difficult to argue unequivocally the possible strain effect in the Cu matrix. We can neither confirm nor discard the possibility that the Cu matrix is helping to improve the resistance to hydrogen embrittlement by absorbing the strain associated with the transformation of the bcc-Nb phase to the α' NbH phase.

The third possible reason for the resistance to hydrogen embrittlement of the Cu-Nb alloy membrane is based on the size of the Nb crystallites in the microstructure. Semboshi et al. have reported about the pulverization of Nb by hydrogenation when it absorbs enough hydrogen to form a large volume of β -NbH phase [32]. Concentric cracks at about 100 μm intervals were reported to form, resulting in pulverization. Optical imaging showed that the thickness of the Nb particles is about 100 μm [32]. In Figure 7.3, it can be seen that the Nb particles in the Cu-Nb membrane are about 10 μm thick, considerably thinner than the Nb particles after hydrogenation-induced pulverization. Hence, it is possible that the size of the Nb crystallites in the present Cu-Nb alloys is small enough to accommodate the strain associated with the bcc-Nb to α' NbH phase transformation without cracking. In comparison to the work of Nambu et al. and Yukawa et al. and their associated recommendations [26-28], the ability of the Cu-Nb alloy to form an α' NbH phase with a hydrogen content higher than 0.25 H/M while maintaining a good resistance to hydrogen embrittlement holds much promise for enhanced hydrogen flux across the membrane. The reasons behind this phenomenon could be because the Cu matrix is accommodating the strain of the transformation from bcc-Nb to α' NbH, the grain size of the Nb particles are small enough to avoid cracking, or a combination of both. The excellent resistance of Cu-Nb alloys to hydrogen embrittlement also allowed the testing of membranes three times thinner than the Nb-Ni-Zr alloy membranes tested in Chapters 4 and 5, which also adds to the potential of Cu-Nb alloys for improved hydrogen flux. However, the hydrogen flux

recorded was not higher than that of the thicker Nb-Ni-Zr alloy. The next section will discuss the factors affecting the hydrogen diffusivity coefficient in the Cu-Nb alloys.

7.4.3 Factors affecting the hydrogen solubility and diffusivity coefficient

The low hydrogen flux through the Nb-Cu membrane can be attributed to two main reasons. The first one is due to how the Pd coating is interacting with Cu and H, and the second reason is due to the microstructural arrangement of the highly hydrogen permeable Nb particles in the Cu matrix. These two factors are discussed further below.

7.4.3.1 Pd catalyst coating

Two phenomena were observed for the Pd catalyst coating. The first one is the interaction observed in vacuum between Cu and Pd. Figure 7.6 shows that when the sample is heated to a temperature above 573 K, the pure Pd peaks disappear and a $\text{Cu}_{3.18}\text{Pd}_{0.82}$ phase is identified to have formed by XRD analysis. Figure 7.10 shows the lattice parameter of the Cu phase measured in vacuum, which varied between 0.3617 nm and 0.363 nm with temperature. This is consistent with the literature value of a Cu-rich Cu-Pd solid solution [33]. The equilibrium phase diagram of Pd-Cu reported by Subramanian and Laughlin [33] indicates that a Cu-Pd solid solution forms over the entire solute content. The low diffusion rate of Cu in Pd at 573 K and below is a possible reason for the retention of the Pd catalytic layer observed by XRD. Given enough time, the Pd and Cu are likely to diffuse and form a Cu-Pd solid solution. The loss of the Pd catalytic layer to a Cu-Pd phase at temperatures above 573 K had a detrimental effect on the amount of H that was absorbed by Nb. Cu does not play an active role in the H permeation process and the formation of a Cu-Pd solid solution does not impact its performance as supporting matrix. However, the Pd coating is essential for the H permeation performance of Nb-based membranes. Techniques to avoid the loss of the Pd catalytic layer will be further discussed in Section 7.4.4.

The second phenomenon is observed under H atmosphere. Figure 7.8 confirms the presence of $H_{0.66}Pd$ phase at 473 K and below. It is known that the formation of Pd hydrides is not favourable to the catalytic role of Pd in membranes and according to the equilibrium phase diagram of Pd-H, Pd hydrides are likely to form at temperatures below 556 K depending on the H concentration in Pd [31]. Therefore, the role of Pd as a catalytic layer at temperatures ranging from 556 K and below is limited. The $H_2 + Pd$ system is a typical example of a non-activated system [25]. Hydrogen adheres to different positions of the Pd lattice, depending on the temperature and surface construction [31]. If the collision energies between H_2 and Pd are modest, like at low temperatures, the dissociation of hydrogen is possible only for certain molecules oriented in a particular direction, therefore limiting the adsorption of hydrogen in Pd [25]. At these low temperatures, it is kinetically unfavourable for the hydrogen adsorption and dissociation process to take place. Ideally, Pd would be used at a temperature above 473 K to limit the formation of hydrides and increase the adsorption of hydrogen in the membrane. However, due to the formation of a Cu-rich Cu-Pd phase at temperatures above 573 K, there is a temperature window for the most favourable operating condition of the Pd catalytic coating for this Cu-Nb alloy, which is between 473 K and 573 K. A way to allow for a larger temperature window for the operation of the Nb-Cu membrane while preserving the Pd catalytic layer is further discussed in Section 7.4.4.

7.4.3.2 Microstructural arrangement of the Nb particles

The second reason for the low hydrogen flux through the Cu-Nb membrane can be attributed to the arrangement of the Nb particles in the Cu matrix. As discussed in the literature review section, it is well established that Nb is the preferred path for hydrogen diffusion in Nb-based hydrogen permeation membranes. Figure 7.3 (a) shows that Nb can be present as large elongated particles with smaller spherical particles in their vicinity, which is conducive to hydrogen permeation. However, it can be seen in Figure 7.3 (b), that this type of arrangement is not always the case. The prevalent arrangement of dendritic and/or spherical Nb particles surrounded by a Cu matrix is not conducive to hydrogen

diffusion. Hydrogen percolates through the membrane going from regions of Nb, which has high hydrogen diffusivity, to regions of low hydrogen diffusion, i.e. the Cu matrix. The current arrangement of the Nb phase in the Cu matrix interrupts the high hydrogen diffusivity path. Therefore, Section 7.4.4 will look to at potential approaches to improve hydrogen diffusivity and hydrogen permeability in the Nb-Cu alloy membranes.

7.4.4 Potential approaches to enhance hydrogen permeability and retain the Pd catalytic layer in Cu-Nb alloy membranes

Possible approaches to enhance the hydrogen permeability of the Cu-Nb alloy are identified based on models originally used for calculating the effective thermal conductivity of heterogeneous materials.

7.4.4.1 Modelling of hydrogen permeability based on models for the thermal conductivity of heterogeneous materials

In an attempt to improve the hydrogen diffusion in the Nb-Cu alloy membranes, the microstructural arrangement of Nb discussed in Section 7.4.3.2 is developed further below. The microstructure and morphology of Nb in particular have been observed to play an important role in improving hydrogen permeation. For example, Wang et al. reported that the decomposition of the eutectic lamellar microstructure to a duplex phase by annealing led to a decrease in hydrogen permeability [21].

The steady-state heat and mass transfer rates are expressed by Fourier's law and Fick's first law, respectively, i.e.

$$q = -k \frac{dT}{dx} \quad (7.5)$$

and

$$J = -D \frac{d\phi}{dx} \quad (7.6)$$

where q is the heat flux through a material, k the thermal conductivity and $\frac{dT}{dx}$ the temperature gradient. In Fick's first law in Equation 7.6, J is the atomic flux diffusing through a material, D is the diffusion coefficient and $\frac{d\phi}{dx}$ the concentration gradient. It can be observed that the Fourier's law on conductivity is analogous to Fick's law on diffusion. This simple analogy between thermal conduction and atomic diffusion can be applied to the argument of microstructural effects on the hydrogen permeation of H in Cu-Nb membranes. The H permeation through the Nb and Cu phases may be assimilated to heat conduction in a heterogeneous material where there are more than one local thermal conductivity values in a system. Wang et al. have summarized the effective thermal conductivity for a two-component system in their report on a new approach to modelling the effective thermal conductivity of heterogeneous materials [34]. The three model systems considered by Wang et al., i.e. parallel, Maxwell Eucken and series models are shown schematically in Figure 7.19. They showed that the effective thermal conductivity (K) for these three model microstructures is as follows:

for parallel model,
$$K = v_1 k_1 + v_2 k_2 \quad (7.7)$$

for Maxwell Eucken 2 model,
$$K = \frac{k_1 v_1 + k_2 v_2 \left(\frac{3k_1}{2k_1 + k_2} \right)}{v_1 + v_2 \left(\frac{3k_1}{2k_1 + k_2} \right)} \quad (7.8)$$

and for series model,
$$K = \frac{1}{\frac{v_1}{k_1} + \frac{v_2}{k_2}} \quad (7.9)$$

where k is the thermal conductivity of a component and v the volume fraction of that component. Using the rule of models described above [34], the hydrogen permeability of the Nb-Cu alloy with different microstructural arrangements can be expressed by the

following models: (i) the series model (Φ_s), (ii) the Maxwell Eucken 2 model (Φ_m), and (iii) the parallel model (Φ_p). The thermal coefficient of the component k is substituted with the hydrogen permeation coefficient Φ , while V denotes the volume fraction which in the present case the volume fractions of Nb and Cu. Following the argument by Wang et al., [34] the hydrogen permeability for these three adapted models is described by

$$\Phi_s = \frac{1}{\frac{V_{Nb}}{\Phi_{Nb}} + \frac{V_{Cu}}{\Phi_{Cu}}} \quad (7.10)$$

$$\Phi_m = \frac{\Phi_{Cu} \cdot V_{Cu} + \Phi_{Nb} \cdot V_{Nb} \left(\frac{3\Phi_{Cu}}{2\Phi_{Cu} + \Phi_{Nb}} \right)}{V_{Cu} + V_{Nb} \left(\frac{3\Phi_{Cu}}{2\Phi_{Cu} + \Phi_{Nb}} \right)} \quad (7.11)$$

and

$$\Phi_p = \Phi_{Nb} \cdot V_{Nb} + \Phi_{Cu} \cdot V_{Cu} \quad (7.12)$$

where Φ_{Nb} and Φ_{Cu} are the hydrogen permeability of Nb and Cu, respectively. The volume fraction of Nb and Cu are designated by V_{Nb} and V_{Cu} respectively.

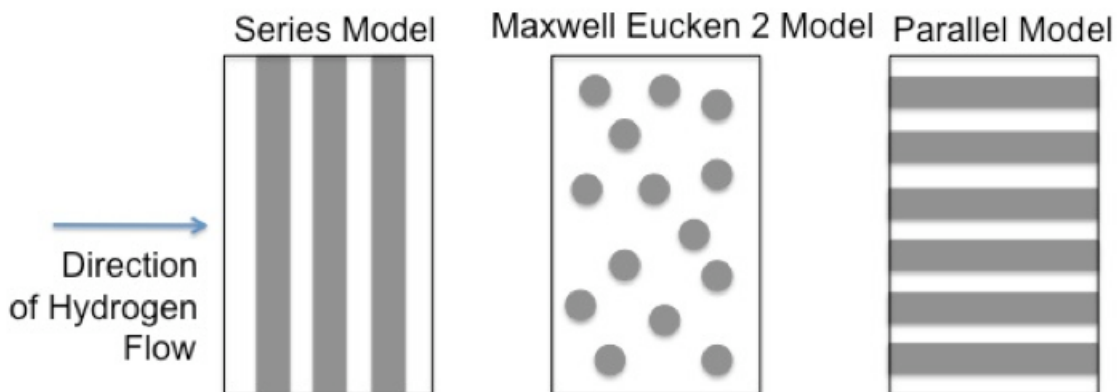


Figure 7.19. Schematic diagrams of three effective hydrogen permeability structural models for two component materials [34].

An appeal of the Cu-Nb alloy system is that Nb and Cu are immiscible in the liquid state, which after casting leads to a duplex microstructure with two distinct phases. The presence of two well-researched elements allows for more fundamental work to be done as it isolates the number of variables at play. An example of such work is seen in Figure 7.20, which shows the hydrogen permeability of pure elements with respect to the inverse of temperature.

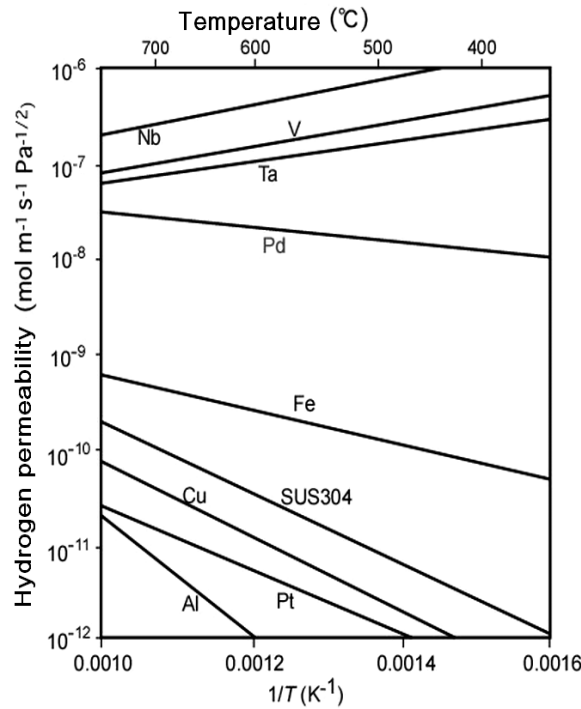


Figure 7.20. Temperature dependence of hydrogen permeability for metals, including that of Nb and Cu [1, 35].

The temperature dependence of hydrogen permeability for Nb and Cu in Figure 7.20 can be described by the least square fittings of the plots in this figure. The permeability varies by the following relationships:

$$\text{for temperature dependence of Nb: } y = 3 \times 10^{-9} e^{4.2 \times 10^3 x} \quad (7.13)$$

and

$$\text{for temperature dependence of Cu: } y = 7.42 \times 10^{-6} e^{-1.14 \times 10^4 x} \quad (7.14)$$

where y is the hydrogen permeability and x the inverse temperature. The permeability of each phase in the Cu-Nb microstructures was estimated based on these relationships. The local permeability values were then used in conjunction with Equations 7.10, 7.11 and 7.12 to model the overall hydrogen permeability of the composite alloy with various microstructural arrangements.

The calculated hydrogen permeability of Cu-Nb alloys at 723 K and 523 K as a function of Nb content is shown in Figure 7.21. The calculation was based on the series, Maxwell Eucken 2 and parallel models. Temperatures of 723 K and 523 K were chosen as they are at the higher and lower end of the commonly used temperature range for testing the hydrogen permeability of metallic membranes. The hydrogen permeability of a given Cu-Nb alloy at an intermediate temperature between 723 K and 523 K is expected to fall between the values obtained at these two temperatures. It can be observed that the hydrogen permeation coefficient increases with increasing Nb content in any of the three models. This behaviour is consistent with what has been reported by groups working on Nb-based crystalline metallic membranes [5, 36]. A large increase in Φ is observed in the model where the Nb and Cu are arranged in parallel.

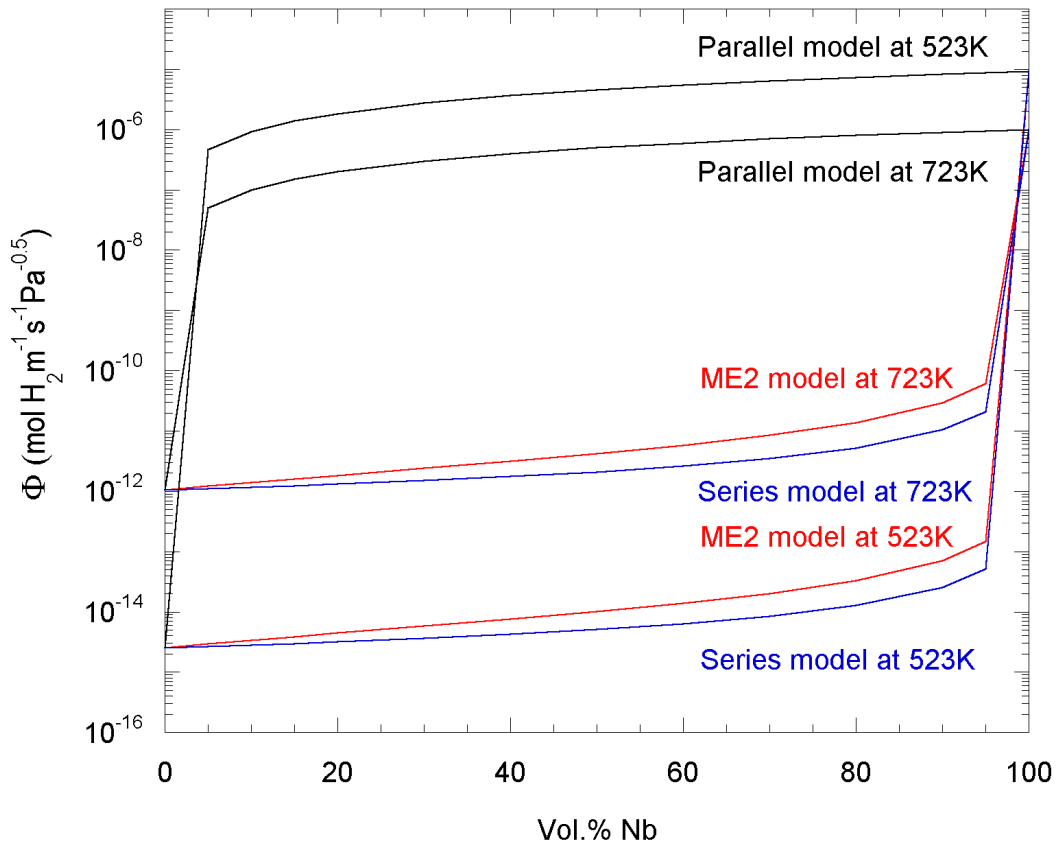


Figure 7.21. The calculated hydrogen permeability of the Cu-Nb alloy with varying Nb content at 523 K and 723 K based on the series, Maxwell Eucken 2 and parallel models.

The magnitude of this increase is unprecedented and carries much promise. Figure 7.22, which compares the simulation results of a Cu-15 vol.% Nb alloy to the experimental results of the as-cast Cu-15 vol.% Nb and pure Pd, helps put the current results in perspective. A Cu-15 vol.% Nb alloy arranged in parallel has the potential to have a Φ one order of magnitude higher than that of pure Pd at 673 K and two orders of magnitude higher at 523 K. The experimental as-cast results for a Cu-15 vol.% Nb alloy has a Φ in between that of the model arranged in parallel and in series. Based on the microstructure of the as-cast results for a Cu-15 vol.% Nb alloy observed in Figure 7.3 (a), the most representing model is expected to be the ME2 model. However, it is possible that a mixture of the ME2 and parallel model exist in the membrane if a long enough Nb particle was present in the membrane going from the high hydrogen pressure side to the other, therefore leading to an increase in Φ . Another possible reason is that the hydrogen permeation measuring apparatus

was approaching its limit in measuring the low hydrogen flux through the membrane and the real Φ of the Cu-15 vol.% Nb membrane could be closer to that of the ME2 and series models.

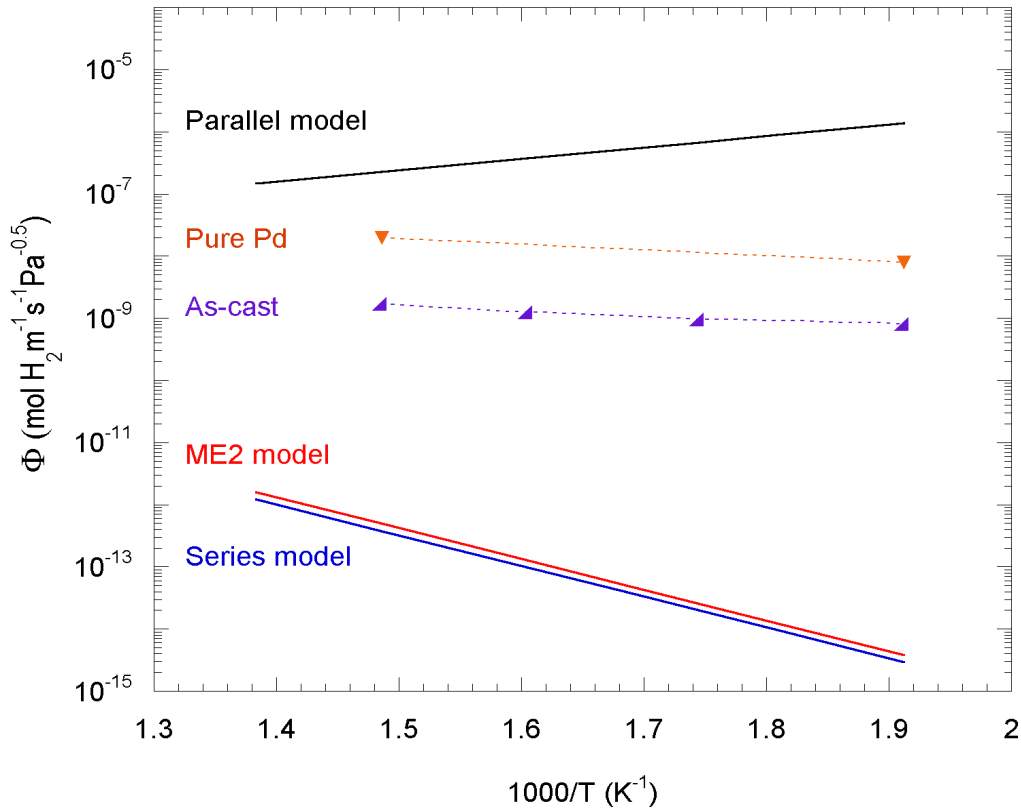


Figure 7.22. The temperature dependence of hydrogen permeability for the series, Maxwell Eucken 2 and parallel models for a Cu-15 vol.% Nb alloy and the experimental results of the as-cast Cu-15 vol.% Nb and pure Pd.

The following section will further discuss two possible approaches to increase the hydrogen permeability in the Cu-Nb alloy membrane based on the modelling results of Figures 7.21 and 7.22.

7.4.4.2 Increasing the Nb content in the Cu-Nb alloys

A more conventional approach to improve hydrogen permeability in the Nb-based alloy membranes would be to increase the Nb content. In the case of Cu-Nb alloys this approach is expected to result in higher hydrogen permeability as it is known that the diffusion of hydrogen in pure Nb is about twenty times higher than in Cu, and also because hydrogen

solubility is higher in Nb than in Cu. The molar concentration of hydrogen in Nb at 573 K is reported to be 600000 times larger than that in Cu at the same pressure [11]. Luo et al. have successfully used this approach in Nb-Ti-Co and Nb-Ti-Ni alloy membranes and confirmed that by increasing the Nb content an increase in Φ is observed in each case [5, 36]. This approach is supported by Figure 7.21, which shows that the hydrogen permeability increases with increasing Nb content in all three models of the Cu-Nb alloy.

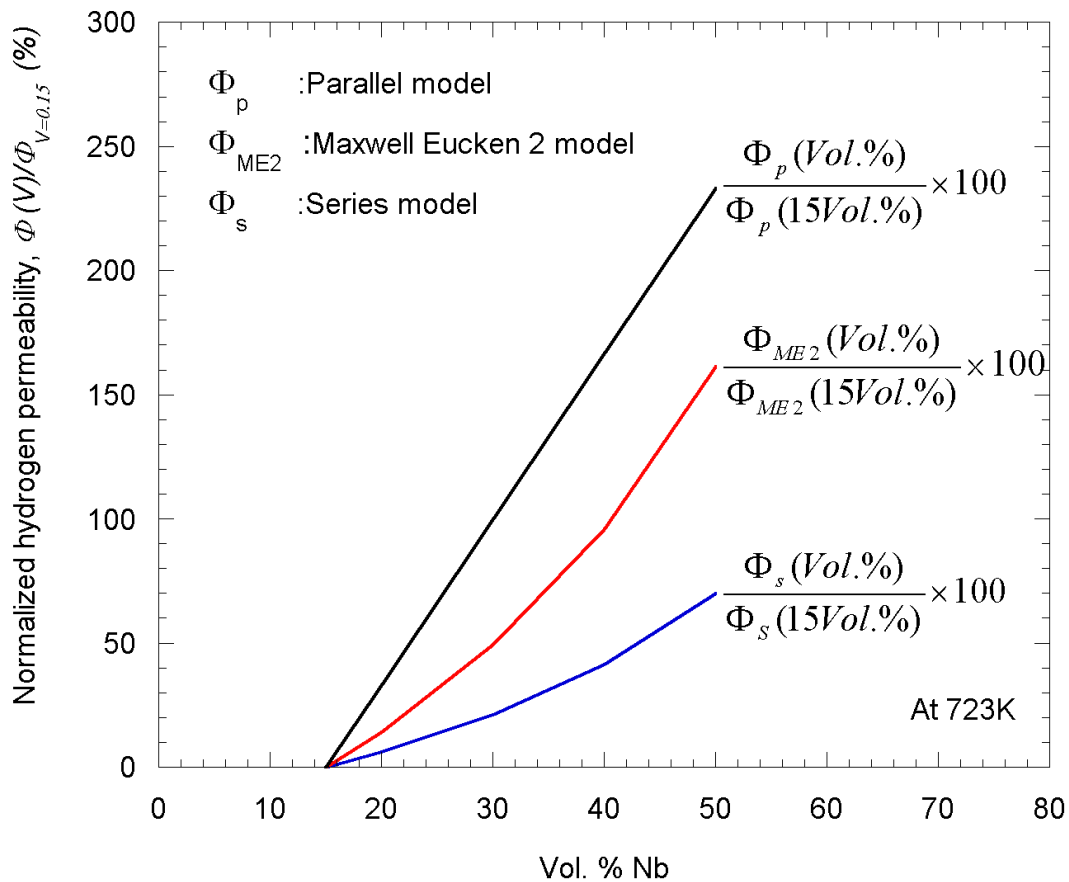


Figure 7.23. The increase in Φ with increasing Nb content in Cu when compared to Cu-15 vol.% Nb based on the parallel, Maxwell Eucken 2 and series models at 723 K.

The change in the calculated Φ as a function of Nb content is shown in Figure 7.23. The value in this diagram is normalized by the value at 15 vol.% Nb ($\Phi_{V=15\%}$), which is the alloy composition of one of the two Cu-Nb membranes investigated. It can be observed that an increase in Nb content is beneficial to all three models. However, the increase in Φ with

increasing Nb content is more pronounced in the model where the Nb and Cu phases are arranged in parallel. For example at Cu-30 vol.% Nb, the increase in the model in parallel is 100 %, while in the Maxwell Eucken 2 model it is increased by 49 % and 21 % in the model arranged in series. These models are compared to the experimental results in Figure 7.4, where the Φ of the rolled Cu-20 vol.% Nb and as-cast Cu-15 vol.% Nb samples were found to be $1.93 \times 10^{-9} \text{ molH}_2\text{m}^{-1}\text{s}^{-1}\text{Pa}^{-0.5}$ and $1.7 \times 10^{-9} \text{ molH}_2\text{m}^{-1}\text{s}^{-1}\text{Pa}^{-0.5}$, respectively, at 673 K. The difference in Φ between these two samples was found to be 13.5 %. This is consistent with the 14.4 % increase in Φ calculated with the Maxwell Eucken 2 model for an increase of Nb content from 15 vol.% to 20 vol.% shown in Figure 7.23. The Maxwell Eucken 2 appears to be the closest representation of the microstructure of the Cu-Nb alloy tested in Figure 7.4, even if variations may exist. By increasing the Nb content in the Maxwell Eucken 2 model and the series model, the increase in hydrogen permeability relies on the probability of the hydrogen percolating through more abundant Nb particle paths going from one side of the membrane to the other. On the other hand, increasing the Nb content in the parallel model leads to either a direct increase in the number of Nb outlets going from the upstream side of the membrane to the downstream side, larger Nb paths or a combination of both. It must be noted that the increase in hydrogen permeability with increasing Nb content was found to be temperature independent, as they were found to be the same at 523 K and 723 K. From this modelling exercise it can be seen that increasing the Nb content in Cu-Nb alloys, whether they follow the series, Maxwell Eucken 2 or parallel model, leads to various gains in hydrogen permeability. The most efficient microstructural arrangement for the improvement of Φ by increasing Nb content in a Cu-Nb alloy membrane is where the Nb and Cu phases are arranged in parallel to the flow of hydrogen.

The other potential advantage of a Cu-Nb binary alloy with a microstructure arranged in a similar way to the parallel model would be that the Pd coating can be directly coated on the Nb phases, which are responsible for the hydrogen diffusion, with minimal risk of Pd dissolving to form a Cu-Pd phase. It is known from the work of Hatano et al. and

Edlund et al. that the Pd catalytic coating remains stable on Nb below a temperature of 673 K [37, 38]. In other areas where the Pd will be in contact with Cu, the formation of the Cu rich Cu-Pd phase is expected to occur but with little impact on the hydrogen permeation process. From our previous work in Section 7.4.2, it has been observed that the Cu phases do not play an important part in the hydrogen permeation process and therefore do not necessitate the Pd catalytic coating.

7.4.4.3 Changing the morphology of the Nb phase in Cu-Nb alloys

From Figures 7.21, 7.22 and 7.23, it can be clearly observed that the morphology of the Nb phase and its microstructural arrangement in the Cu matrix has a significant effect on the hydrogen permeability of the binary alloys. The Φ of the Maxwell Eucken 2 model is observed to be marginally higher than that of the series model. The most significant improvement in Φ rests with the model with the Nb and Cu phases arranged in parallel to the flow of hydrogen. The difference in Φ between the models in parallel and in series varies from five orders of magnitude at 723 K to more than eight orders of magnitude at 523 K in favour of the parallel model. The large difference in hydrogen permeation rate is attributed to the microstructural difference. As shown in Section 7.4.2, bcc-Nb is the phase with high hydrogen permeability. By arranging the Nb phase in parallel to the Cu phase, a direct path for the diffusion of the protons is created. This allows the protons to quickly diffuse from one side of the membrane to the other side, thereby increasing the hydrogen permeability. Out of the three models used, arranging the Nb phase in parallel to the Cu phase is the most efficient configuration for the use of Nb in the Cu-Nb alloys for hydrogen permeation. This has the potential to lower the cost of the Cu-Nb membranes by lowering the required amount of Nb, which is more expensive than Cu. Based on the Figure 7.22, a Cu-Nb alloy with only 15 vol. % of Nb in the Cu matrix arranged in parallel is expected to have a hydrogen permeability ranging from one order to two orders of magnitude higher than that of pure Pd, depending on the temperature. The potential gain in performance at

only a fraction of the cost holds much promise for the Cu-Nb alloy membranes with a microstructure arranged in parallel.

It is also observed in Figure 7.22 that the hydrogen permeation of the Cu-Nb alloy modelled in parallel showed a differing relationship to increasing temperature when compared to the alloy modelled in series and by the Maxwell Eucken 2 model. The model in parallel is significantly more dependent on the properties of Nb, whose hydrogen permeability shows an inverse temperature dependence, unlike the Maxwell Eucken 2 and series model, which are more heavily influenced by the hydrogen permeation behaviour of the Cu matrix and thus their Φ show a positive temperature dependence. The current modelling exercise has shown the potential to improve hydrogen permeation performance of metallic membranes with Nb arranged in parallel. Arranging the phase with high hydrogen permeability in parallel to a phase resistant to hydrogen embrittlement carries the potential to increase the efficiency of the hydrogen permeation process at a fraction of the cost.

7.4.5 Preliminary tests on the potential ways to improve hydrogen permeation in the Cu-Nb alloy membranes

In an attempt to test the hydrogen permeability of Cu-Nb alloys based on the parallel model, we looked at various Cu-Nb alloys that are currently being used in other fields. A Cu/Nb/Cu multifilamentary conducting wire used in high-pulsed magnets was identified and some samples were provided courtesy of Professor Ludovic Thilly, from the Institute Pprime, CNRS-University of Poitiers, Poitiers, France, and Dr. Françoise Lecouturier from the Laboratoires National Champs Magnétiques Intenses CNRS-INSA-UJF-UPS, Toulouse, France [17, 18, 39, 40]. The Cu/Nb/Cu wires were produced by severe plastic deformation (SPD) via the accumulative drawing and bundling (ADB) process, which consists of a series of (1) annealing, (2) hot extrusion, (3) cold drawing into a hexagonal shape, and (4) cutting and bundling stages that were repeated n times ($n \leq 4$). The Cu/Nb/Cu conductor wires studied comprise a pure Cu matrix embedding N number of Nb tubes, where $N = 85^3$ Nb, indicating that the bundling and extrusion of 85 Cu/Nb/Cu tubes were repeated 3 times until

the desired microstructure was achieved. Figure 7.24 shows the arrangement of one of the Cu/Nb/Cu tube prior to the bundling and extrusion process.

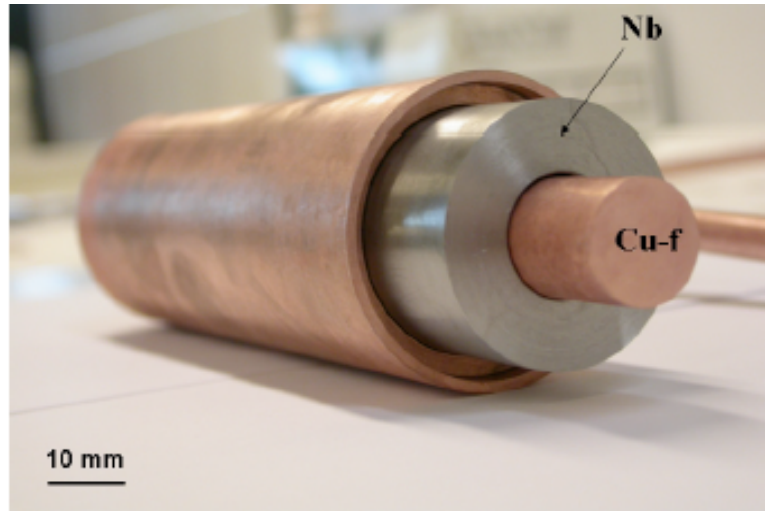


Figure 7.24. Oxygen Free High Conductivity (OFHC) Cu matrix with a bcc Nb tube filled with an OFHC Cu fiber (Cu-f) [41].

Figure 7.25 shows the SEM images of the Cu/Nb/Cu conductor wire. At low magnification in Figure 7.25 (a), several of the 85 clusters of Cu/Nb/Cu tubes can be observed. When the image is focused on one of these clusters in Figure 7.25 (b), it can be observed that one cluster is made up of 85 smaller clusters of Cu/Nb/Cu tubes. When the magnification is increased to 500X in Figure 7.25 (c) on one of the smaller clusters observed in Figure 7.25 (b), it can be observed that these smaller clusters are made up of another 85 Cu/Nb/Cu tubes that are observed to have a cross section of about 10 microns in Figure 7.25 (d). The microstructure consists of Nb tubes a few microns in diameter embedded in a multi-scale Cu matrix where the Nb nanotubes have a known distribution and the bundles are separated by channels of pure Cu. This type of microstructural arrangement of tubular Nb filaments embedded in a Cu matrix going uninterrupted from one side of the membrane to the other, is consistent with the model with Nb and Cu arranged in parallel. Therefore, this Cu/Nb/Cu multifilamentary conducting wire appears to be a suitable candidate to verify the model of the hydrogen permeation model of the Cu-Nb alloy arranged in parallel. It must be noted

that for the current application of this superconducting wire, Nb is added to the Cu conducting wire as a mechanical reinforcement, leading to improvements in the elastic limit and ultimate tensile strength [18, 39]. This is in contrast to the purpose of hydrogen permeation membranes where Nb is the main phase for hydrogen permeation and Cu is the reinforcing matrix to improve resistance to hydrogen embrittlement. The techniques used to analyze the samples are similar to the ones described in Section 7.2.1.

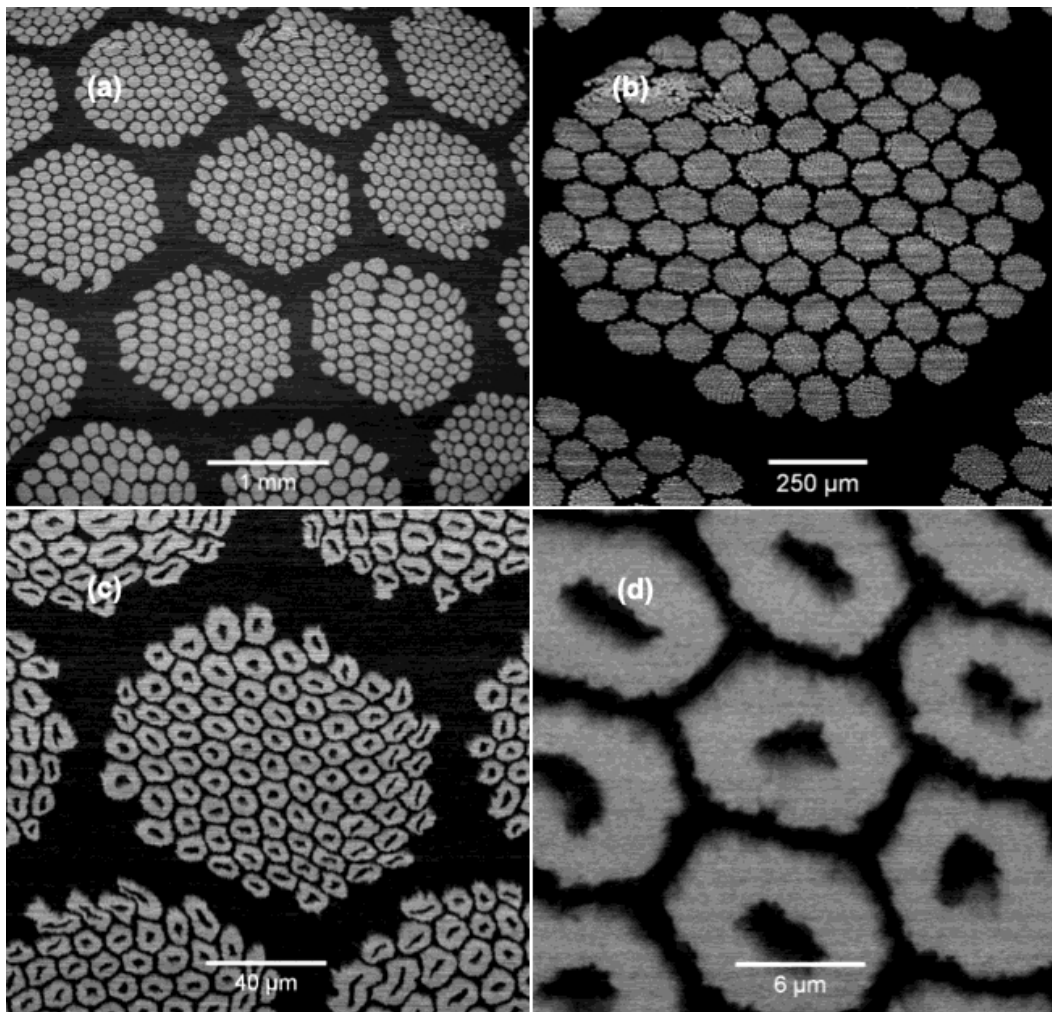


Figure 7.25. SEM images of Cu/Nb/Cu conducting wires at different magnifications (a) 20 X (b) 60 X (c) 500 X and (d) 3500 X.

The Cu/Nb/Cu multifilamentary membrane has another benefit, which solves an issue identified earlier during the test of the as-cast Cu-Nb samples. In Section 7.4.3.1, the Pd catalytic layer was observed to interact with the Cu matrix to produce a $\text{Cu}_{3.18}\text{Pd}_{0.82}$

phase. The loss of the catalytic layer is detrimental to the hydrogen permeation process. In the present case where the Cu and Nb are arranged in parallel, the Pd layer is in direct contact with the Nb tubular filament and therefore does not form a Cu-Pd phase in the area where the Pd coating is directly above the Nb. Figures 7.26 and 7.27 show the SEM images of a Pd coated Cu/Nb/Cu sample taken after annealing to 673 K in vacuum at a magnification of 3500X and 7000X, respectively. The white particles on the surface were identified by EDX analysis to be Cu-Pd phases and the darker background was found to be the Pd rich coating.

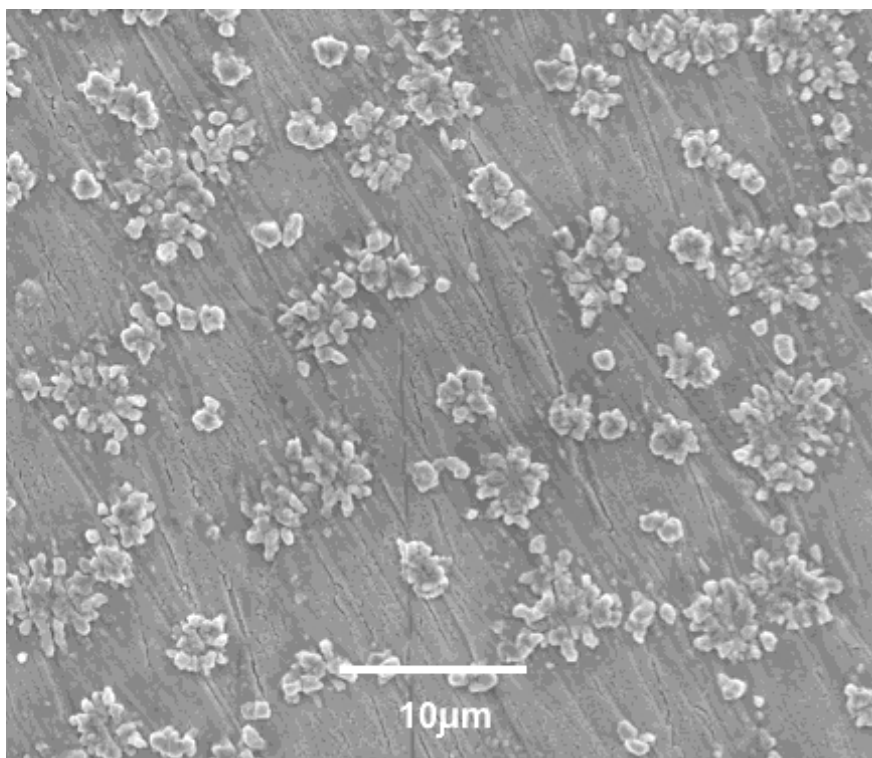


Figure. 7.26. SEM image of Pd coated Cu/Nb/Cu sample after annealing to 673 K in vacuum at a magnification of 3500X.

Figures 7.26 and 7.27 show that the Pd coating still interacts with the Cu matrix in the area directly above the Cu matrix and forms a Cu-Pd phase, but retains its integrity in the area directly above the cross-section of the tubular Nb filaments. The lighter coloured Cu-Pd phase can be observed on the surface of the Pd coating. Energy dispersive X-ray spectroscopy analysis was employed to chemically analyze the surface of the sample in

Figures 7.26 and 7.27. The Pd, Cu and Nb concentrations of the particles and the matrix parts obtained by EDX analysis are summarized in Table 7.1. The chemical composition on the light coloured particle confirms the presence of a copper rich Cu-Pd phase, while the darker coating is identified as a Pd rich solid solution.

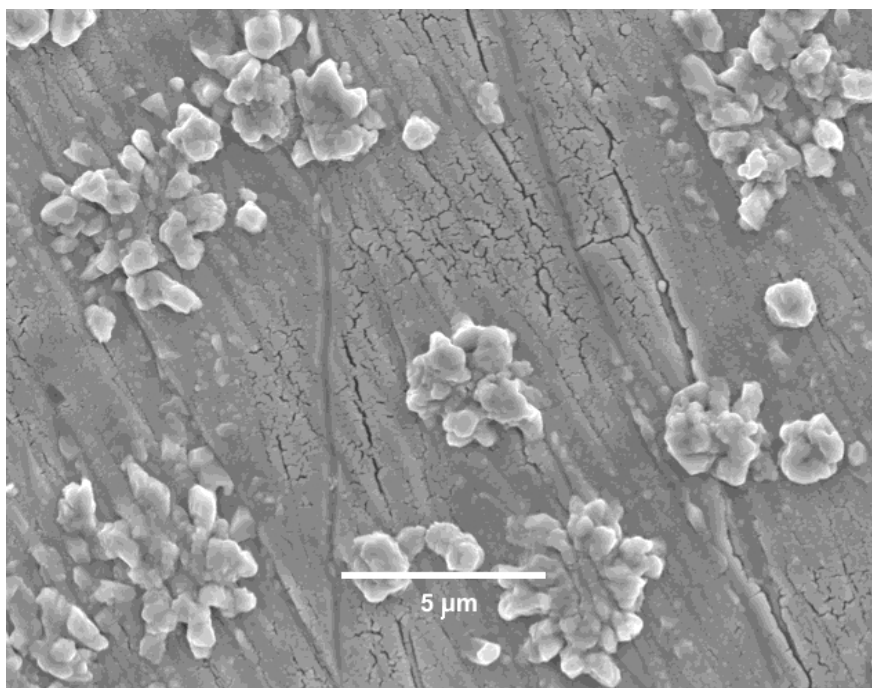


Figure 7.27. SEM image of Pd coated Cu/Nb/Cu sample after annealing to 673 K in vacuum at a magnification of 7000X. The white particles on the surface are the Cu-Pd phases and the darker background is the Pd coating.

Table 7.1. Composition of the particles formed on the surface of the Pd coating obtained by energy dispersive X-ray spectroscopy.

Marker position on	Pd (at. %)	Cu (at. %)	Nb (at. %)
Darker matrix	72.4	15.5	12.1
Lighter coloured particle	38.58	61.4	0

The fact that the Nb phase is the hydrogen permeable phase with high hydrogen diffusion coefficient, it is imperative to maintain the catalytic Pd coating on its surface for high hydrogen solubility and therefore retain a high hydrogen permeation coefficient. By

arranging the Nb and Cu particles in parallel to the direction to the flow of hydrogen, it is now possible to preserve the Pd coating directly in contact with the Nb filaments and therefore maintain a high hydrogen solubility coefficient at both surfaces of the membrane.

The hydrogen permeation test of the Cu/Nb/Cu multifilamentary membranes, with an alloy composition corresponding to Cu-20 vol. % Nb were carried out but no permeation data was obtained due to the fracture of the samples. Figure 7.28 shows the SEM image of this sample after the permeation test. The secondary electron image shows that the cracks appear at the interface of the largest Cu-Cu hexagonal sections, whereas the interface of the smaller Cu-Cu hexagonal sections and the Cu-Nb sections remain intact. This difference is attributed to the fact that the smaller hexagonal Cu-Cu sections went through the whole process of annealing, hot extrusion, cold drawing, cutting and bundling, respectively, whereas the manufacturing process for the larger hexagonal Cu-Cu sections was stopped at the hot extrusion stage as otherwise the cross-sectional area of the wire would be too small for hydrogen permeation testing. The cold drawing process would have mechanically improved the Cu-Nb interface. However, I believe that the omission of the annealing process played a major role in the failure of the membrane. Cu alloys have been reported to have a range of responses to a hydrogen environment. Philips and Graves reported that varying amounts of oxygen in an oxygen free high conductivity (OFHC) Cu is enough to cause hydrogen embrittlement [42]. The fact that OFHC Cu was the only type of Cu used in the current samples tested and that the drawing and bundling processes were done in normal atmosphere make this hypothesis the most plausible cause for the hydrogen embrittlement cracking observed. It must be noted that the Cu/Nb/Cu multifilamentary wire has been specially developed to have extraordinary strength in tension in a natural atmosphere [17], but has not been optimized for the current hydrogen permeation experimental conditions, which involve compressive and shear stresses.

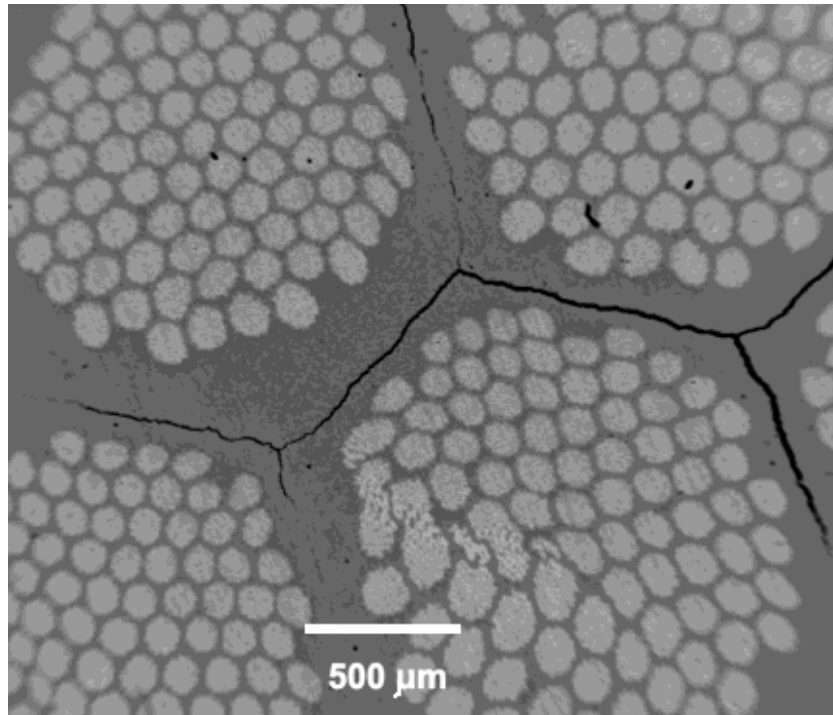


Figure 7.28. SEM image of cracked Cu/Nb/Cu multifilamentary membrane in secondary electron image mode after the hydrogen permeation test.

The current Cu/Nb/Cu multifilamentary alloy with Cu and Nb arranged in parallel holds the promise of significantly higher hydrogen permeability and preservation of the catalytic Pd coating over the as-cast Cu-Nb alloy. Further work can be done to investigate and mitigate the formation of cracks developing along the Cu-Cu interface, for example a possible investigation of the effect of annealing on the crack formation at the Cu-Cu interface. Other possible alternatives would be to look at producing the Cu/Nb/Cu samples in a controlled atmosphere that is free from oxygen or to cast molten Cu around Nb filaments before hot drawing to the desired cross sectional area followed by annealing.

7.5 Summary

This study explores for the first time the idea of using Cu-Nb superconductor wires as potential candidates for the use as hydrogen permeation membranes. The samples tested consist of a bcc-Nb phase embedded in a Cu matrix. The as-cast Cu-15 vol.% Nb and rolled Cu-20 vol.% Nb samples have a Φ of 1.7×10^{-9} and 1.93×10^{-9} molH₂m⁻¹s⁻¹Pa^{-0.5} at 673 K respectively. As discussed, even though the Φ obtained is one order of magnitude lower than that of pure Pd, there is plenty of scope to further improve these preliminary hydrogen permeability results. From a durability perspective, both Cu-20 vol.% Nb and Cu-15 vol.% Nb were found to be mechanically strong, hydrogen embrittlement resistant and ductile. Fundamentally, the Cu-Nb is a binary alloy system with a simple microstructure and thus carries a lot of potential as a model for exploring and understanding the effect of microstructure on hydrogen permeability.

An XRD in-situ analysis technique was used to look at the mechanisms involved during the hydrogen permeation in as-cast and rolled Cu-15 vol.% Nb alloys. Based on the lattice expansion observed in vacuum for the Cu and Nb phase, the coefficient of linear thermal expansion of Cu and Nb were calculated and found to be consistent with the literature values of pure Cu and Nb respectively. The formation of NbH in the Cu-Nb alloy membrane when exposed to H at elevated temperatures indicates that Nb is the phase that is primarily responsible for the permeation of hydrogen. Below 423 K Nb is found to form α' NbH. There is also evidence that Cu is responsible for the resistance to hydrogen embrittlement of the Cu-Nb alloy as its matrix is found to be unaffected by the hydrogen atmosphere below 623 K with no change in lattice parameters. This indicates that H is not permeating Cu and therefore limits the risk of H embrittlement. The catalytic Pd coating is found to form a Cu rich Cu-Pd phase in areas in direct contact with the Cu matrix at temperatures above 573 K. The loss of the catalytic Pd layer is not favourable for H permeation. Pd was also found to form Pd-H at temperatures below 523 K, therefore creating a limited temperature window for the operation of the membrane.

To circumvent this issue of the Pd coating reacting with the Cu matrix and also to potentially improve the hydrogen permeability coefficient of the membrane, a modelling exercise was carried out to investigate the effect of altering the morphology of the Nb and Cu phases in the Cu-Nb alloy. Based on the simulation, it was found that Nb and Cu phases arranged in parallel to the direction of the flow of hydrogen compared to one arranged in series, would yield gains varying from five to eight orders of magnitude at 723 K and 523 K respectively. The simulation also showed that the hydrogen permeability of a Cu-15 vol.% Nb alloy membrane following the parallel model would be between 1 to 2 orders of magnitude higher than that of pure Pd membranes at 723 K and 523 K respectively. A well-known method to improve hydrogen permeability of Nb-based alloy membranes is to increase the Nb content. The models confirms that increasing the Nb content will lead to an increase in hydrogen permeation coefficient whether the Nb and Cu phases are arranged in parallel, series or according to the Maxwell Eucken 2 model. An interesting finding is that arranging the Nb and Cu phases in parallel would yield the most efficient increase in hydrogen permeation coefficient with increasing Nb content. The models of the Cu-Nb alloy with phases arranged in parallel indicate that it follows the unique hydrogen permeation characteristics of Group V elements, which is to have an increasing hydrogen permeability with decreasing temperature. This has positive implications in improving the efficiency of these membranes.

A Cu/Nb/Cu multifilamentary conducting wire used in high-pulsed magnets was identified as a suitable candidate to test the model of arranging Nb and Cu in parallel. After testing in a hydrogen atmosphere to 673 K, the catalytic Pd coating was found to react with Cu in areas directly in contact with Cu, but remained intact in areas directly above the Nb phase. The integrity of the catalyst on the primary hydrogen permeable phase, Nb, at 673 K significantly increases the operational temperature of the Cu-Nb alloy membrane system. The Cu/Nb/Cu multifilamentary conducting wire cracked during hydrogen permeation test. The cracks occurred at the larger Cu-Cu hexagonal interface, which is attributed to the manufacturing process that was stopped at the hot extrusion stage to allow for a large

enough cross-sectional area for hydrogen permeation. The current Cu/Nb/Cu alloy is specially designed for high tensile strength but is yet to be optimized for hydrogen permeation conditions. The Cu/Nb/Cu alloy membrane has shown that the operational temperature range is now similar to that of other alloy based membranes by preserving the integrity of the Pd catalytic coating even at high temperature. The resistance to hydrogen embrittlement in the as-cast Cu-Nb membrane also highlights the potential durability of this alloy system. Based on the models and the evidence so far, the Cu-Nb alloys that follow the parallel model hold much promise in terms of resistance to hydrogen embrittlement and high hydrogen permeability at low Nb content, which would have a strong bearing on the viability of such membranes.

7.6 References

- [1] R.E. Buxbaum, A.B. Kinney, *Industrial and Engineering Chemistry Research*. 35 (1996) 530
- [2] K. Ishikawa, S. Tokui, K. Aoki, *Intermetallics* 17 (2009) 109
- [3] K. Hashi, K. Ishikawa, T. Matsuda, K. Aoki, *Journal of Alloys and Compounds*. 425 (2006) 284
- [4] K. Hashi, K. Ishikawa, T. Matsuda, K. Aoki, *Journal of Alloys and Compounds*. 368 (2004) 215
- [5] W. Luo, K. Ishikawa, K. Aoki, *Journal of Alloys and Compounds*. 407 (2006) 115
- [6] K. Kishida, Y. Yamaguchi, K. Tanaka, H. Inui, S. Tokui, K. Ishikawa, K. Aoki, *Intermetallics*. 16 (2008) 88
- [7] H. Tang, K. Ishikawa, K. Aoki, *Materials Transactions*. 48 (2007) 2454
- [8] K. Ishikawa, T. Takano, T. Matsuda, K. Aoki, *Applied Physics Letters*. 87 (2005) 081906
- [9] T. Takano, K. Ishikawa, T. Matsuda, K. Aoki, *Materials Transactions*. 45 (2004) 3360
- [10] J.W. Phair, R. Donelson, *Industrial and Engineering Chemistry Research*. 45 (2006) 5657
- [11] J.D. Verhoeven, E.D. Gibson, F.A. Schmidt, D.K. Finnemore, *Journal of Materials Science*. 15 (1980) 1449
- [12] J.D. Verhoeven, F.A. Schmidt, E.D. Gibson, W.A. Spitzig, *Journal of Metals*. 38 (1986) 20
- [13] J.D. Verhoeven, W.A. Spitzig, F.A. Schmidt, P.D. Krotz, E.D. Gibson, *Journal of Materials Science*. 24 (1989) 1015
- [14] W.A. Spitzig, D.T. Peterson, F.C. Laabs, *Journal of Materials Science*. 26 (1991) 2000
- [15] H.R.Z. Sandim, M.J.R. Sandim, H.H. Bernardi, J.F.C. Lins, D. Raabe, *Scripta Materialia*. 51 (2004) 1099
- [16] Y.C. Wang, A. Misra, R.G. Hoagland, *Scripta Materialia*. 54 (2006) 1593

CHAPTER 7. POTENTIAL OF Cu-Nb ALLOYS AS
HYDROGEN PERMEATION MEMBRANES

- [17] V. Vidal, L. Thilly, F. Lecouturier, P.O. Renault, *Scripta Materialia*. 57 (2007) 245
- [18] V. Vidal, L. Thilly, S. Van Petegem, U. Stuhr, F. Lecouturier, P.O. Renault, H. Van Swygenhoven, *Scripta Materialia*. 60 (2009) 171
- [19] ASM International, ASM Ready Reference: *Thermal properties of metals*. Product code: 06702G
- [20] H. C. Jamieson, G. C. Weatherly and F. D. Manchester, *Journal of Less Common metals*. 50 (1976) 85
- [21] W. Wang, K. Ishikawa, K. Aoki, *Journal of Membrane Science*. 351 (2010) 65
- [22] J. F. Smith: *Binary Alloy Phase Diagram*, Eds. T. B. Massalski, J. L. Murray, L. H. Bennett and H. Baker, (ASM, Metals Park, OH, 1983) pp. 1271.
- [23] H. Zabel and J. Peisl, *Journal of Physics F: Metal Physics*. Vol. 9 No. 7 (1979) 1461
- [24] S. Komjathy, *Journal of Less Common metals*. 2 (1960) 466
- [25] F. D. Manchester, *Journal of Alloys and Compounds*. 330-332 (2002) 8
- [26] H. Yukawa, M. Morinaga, T. Nambu and Y. Matsumoto, *Materials Science Forum*. Vols. 654-656 (2010) 2827
- [27] H. Yukawa, T. Nambu and Y. Matsumoto, *Defect and Diffusion Forum*. Vols. 312-315 (2011) 506
- [28] T. Nambu, K. Shimizu, Y. Matsumoto, R. Rong, N. Watanabe, H. Yukawa, M. Morinaga and I. Yasuda, *Journal of Alloys and Compounds*. 446-447 (2007) 558
- [29] J. Shibano, Y. Yamamoto, M. Kobayashi, K. Ishikawa, K. Aoki, *Key Engineering Materials*. 353-358 (2007) 655
- [30] G. J. Kroes, A. Gross, E. J. Baerends, M. Scheffler, D. A. McCormack, *Accounts of Chemical Research*. 35 (2002) 193
- [31] H. Wipf, *Physica Scripta*. T94 (2001) 43
- [32] S. Semboshi, N. Masahashi, T. J. Konno, S. Hanada, *Metallurgical and Materials Transactions A*. Vol. 37A (2006) 1301
- [33] P. R. Subramanian and D. E. Laughlin, *Journal of Phase Equilibria*. 12 (1991) 231

CHAPTER 7. POTENTIAL OF Cu-Nb ALLOYS AS
HYDROGEN PERMEATION MEMBRANES

- [34] J. F. Wang, J. K. Carson, M. F. North, D. J. Cleland, International Journal of Heat and Mass Transfer. 49 (2006) 3075
- [35] R. E. Buxbaum and T. L. Marker, J. Membrane Sci., 85 (1993) 29
- [36] W. Luo, K. Ishikawa, K. Aoki, International Journal of Hydrogen Energy. 37 (2012) 12793
- [37] Y. Hatano, K. Ishiyama, H. Homma, K. Watanabe, Journal of Alloys and Compounds. 446-447 (2007) 539
- [38] D.J. Edlund and J. McCarthy, Journal of Membrane Science. 107 (1995) 147
- [39] J. B. Dubois, L. Thilly, F. Lecouturier, P. Olier, and P. O. Renault, IEEE Transactions on Applied Superconductivity. Vol. 22, No. 3 (2012) 6900104
- [40] M. J. R. Sandim, H. R. Z. Sandim, D. Stamopoulos, R. A. Renzetti, M. G. das Virgens, and L. Ghivelder, IEEE Transactions On Applied Superconductivity. Vol. 16, No. 2 (2006) 1692
- [41] V. Vidal, Ph.D. dissertation, l'Institut National des Sciences Appliquées de Toulouse, 2006, *Optimization of the mechanical properties of Cu/X (X= Nb or Ta) nanofilamentary conductors by the study of elementary mechanisms of deformation*, Fig. 2.1 (b) 'Cas des conducteurs Cu/Nb/Cu'
- [42] A. Philips and D. B. Graves, Transactions of the American Institute of Mining, Metallurgical and Petroleum Engineers, 143 (1941) 322

Chapter 8

Conclusions and Future Work

8.1 Conclusions

The formation of amorphous in the Nb-Ni-Zr and the Nb-Ti-Co systems by the melt-spinning technique was found to be highly composition dependent. The $(\text{Nb}_{90}\text{Zr}_7\text{Ni}_3)_{1-x}(\text{Ni}_{50}\text{Zr}_{50})_x$ alloys with Nb contents below 45 at. % and the eutectic Nb-Ti-Co alloy yielded amorphous ductile ribbons. The Nb-Ni-Zr alloy system was found to be an easier alloy system to produce amorphous and ductile wide ribbons. The formation range of amorphous in the $(\text{Nb}_{90}\text{Zr}_7\text{Ni}_3)_{1-x}(\text{Ni}_{50}\text{Zr}_{50})_x$ alloy system was observed to be in the hypereutectic region, which was explained by the presence of an asymmetric coupled zone skewed towards the NiZr phase.

Two decomposition behaviors were observed in the Nb-Ni-Zr alloys. The $(\text{Nb}_{90}\text{Zr}_7\text{Ni}_3)_{1-x}(\text{Ni}_{50}\text{Zr}_{50})_x$ alloys with a higher niobium content, Nb \sim 45 – 20 at. %, had a two-step crystallization reaction while those with a Nb content of \sim 18 – 9 at. % showed a single-step crystallization reaction. The nanoscale grain refinement of a NiZr and bcc-Nb microstructure was obtained for $(\text{Nb}_{90}\text{Zr}_7\text{Ni}_3)_{1-x}(\text{Ni}_{50}\text{Zr}_{50})_x$ ribbons with Nb content between 45 – 20 at. % after heating to 923 K and subsequent coarsening of the Nb and NiZr duplex structure was observed in samples heated to 1173 K.

Annealing was found to be beneficial to the Φ of Nb-Ni-Zr alloys, which were on average 2 times greater than that of their respective as-cast samples. The resistance to hydrogen embrittlement showed no marked improvement after annealing. SEM analysis of

the fracture surface revealed that there were two main mechanisms of crack propagation, namely transgranular and intergranular cracking. The modes of fracture were found to be composition dependent with samples with high Nb content suffering from transgranular cracking and those with low Nb content from intergranular cracking. The mode of fracture was found to be unaffected by annealing.

The hydrogen permeability of a chemically identical Nb-based alloy separation membrane in an amorphous, nanocrystalline and crystalline state was reported for the first time. The hydrogen permeability of the Nb₂₀Ni₄₀Zr₄₀ sample with a nanostructure was found to be the highest, about twice as high as that of the amorphous sample and one order of magnitude higher than the crystalline sample. It was shown that the improvement in hydrogen permeation in the samples with a nanostructure was not solely based on improved hydrogen diffusivity, when compared to the amorphous sample, but also due to improved hydrogen solubility. The enhanced hydrogen solubility of the nanocrystalline membrane also helped improve its resistance to hydrogen embrittlement by lowering the hydrogen concentration in the membrane during the hydrogen permeation test.

For the first time the idea of using Cu-Nb alloys as potential candidates for hydrogen permeation membranes is proposed. The samples tested consist of a bcc-Nb phase embedded in a Cu matrix. The as-cast Cu-15 vol.% Nb and rolled Cu-20 vol.% Nb samples have a Φ of 1.7×10^{-9} and 1.93×10^{-9} molH₂m⁻¹s⁻¹Pa^{-0.5} at 673 K respectively. As discussed, even though the Φ obtained is one order of magnitude lower than that of pure Pd, there is plenty of scope to further improve these preliminary hydrogen permeability results. From a durability perspective, both Cu-20 vol.% Nb and Cu-15 vol.% Nb were found to be mechanically strong, hydrogen embrittlement resistant and ductile. Fundamentally, the Cu-Nb is a binary alloy system with a simple microstructure and thus carries a lot of potential as a model for exploring and understanding the effect of microstructure on hydrogen permeability. XRD in-situ analysis revealed a lattice expansion observed in the Nb phase when exposed to hydrogen, indicating that Nb is the phase that is primarily responsible for the permeation of hydrogen. The Cu matrix was found to be unaffected by the hydrogen

atmosphere below 623 K with no change in lattice parameters. The catalytic Pd coating was found to form a Cu rich Cu-Pd phase in areas in direct contact with the Cu matrix at temperatures above 573 K. Pd was also found to form Pd-H at temperatures below 523 K, therefore creating a limited temperature window for the operation of the membrane.

To circumvent this issue of the Pd coating reacting with the Cu matrix and also to potentially improve the hydrogen permeability coefficient of the membrane, a modelling exercise was carried out to investigate the effect of altering the morphology of the Nb and Cu phases in the Cu-Nb alloy. Based on the simulation, it was found that Nb and Cu phases arranged in parallel to the direction of the flow of hydrogen compared to one arranged in series, would yield gains varying from five to eight orders of magnitude at 723 K and 523 K respectively. The simulation also showed that the hydrogen permeability of a Cu-15 vol.% Nb alloy membrane following the parallel model would be between 1 to 2 orders of magnitude higher than that of pure Pd membranes at 723 K and 523 K respectively. A well-known method to improve hydrogen permeability of Nb-based alloy membranes is to increase the Nb content. The models confirm that increasing the Nb content will lead to an increase in hydrogen permeation coefficient whether the Nb and Cu phases are arranged in parallel, series or according to the Maxwell Eucken 2 model. The simulation showed that arranging the Nb and Cu phases in parallel would yield the most efficient increase in hydrogen permeation coefficient with increasing Nb content. The models of the Cu-Nb alloy with phases arranged in parallel indicate that it follows the unique hydrogen permeation characteristics of Group V elements, which show increasing hydrogen permeability with decreasing temperature. This has positive implications in improving the efficiency of these membranes.

A Cu/Nb/Cu multifilamentary conducting wire used in high-pulsed magnets was identified as a suitable candidate to test the model of arranging Nb and Cu in parallel. After testing in a hydrogen atmosphere to 673 K, the catalytic Pd coating was found to react with Cu in areas directly in contact with Cu, but remained intact in areas directly above the Nb phase, thus providing a solution to the problem previously identified. The integrity of the

catalyst on the primary hydrogen permeable phase, Nb, at 673 K significantly increases the operational temperature of the Cu-Nb alloy membrane system. The Cu/Nb/Cu alloy membrane has shown that the operational temperature range is now similar to that of other alloy based membranes by preserving the integrity of the Pd catalytic coating even at high temperature. The resistance to hydrogen embrittlement in the as-cast Cu-Nb membrane also highlights the potential durability of this alloy system. Based on the models and the evidence so far, the Cu-Nb alloys that follow the parallel model hold much promise in terms of resistance to hydrogen embrittlement and high hydrogen permeability at low Nb content, which would have a strong bearing on the viability of such membranes.

8.2 Future work

Two experiments regarding this project are suggested for future works. Firstly, further research into the temperature dependence of the hydrogen permeation properties of the $\text{Nb}_{20}\text{Ni}_{40}\text{Zr}_{40}$ alloy membrane in an amorphous, crystalline and nanocrystalline state, and secondly, optimize the resistance to hydrogen embrittlement along the Cu-Cu interface in the Cu/Nb/Cu multifilamentary alloy.

- Confirmation of Arrhenius behaviour in the amorphous and nanocrystalline $\text{Nb}_{20}\text{Ni}_{40}\text{Zr}_{40}$ alloy membrane

In Section 6.3 and 6.4, the hydrogen permeability of the c- $\text{Nb}_{20}\text{Ni}_{40}\text{Zr}_{40}$ alloy membrane annealed to 1173 K showed an Arrhenius relationship when compared to the values obtained from literature of a similar crystalline alloy tested at higher temperatures. However, this Arrhenius relationship comparison was not possible for the amorphous and nanocrystalline alloy membrane as the experimental data were obtained at room temperature only. To observe whether the amorphous and nanocrystalline $\text{Nb}_{20}\text{Ni}_{40}\text{Zr}_{40}$ alloy membranes obey the Arrhenius relationship, this experiment is suggested. In Chapter 2, amorphous metal membranes have been reported to display non-Arrhenius behaviour of hydrogen diffusion. It will be interesting to observe whether the nanocrystalline alloy membrane

follows the Arrhenius behaviour of its crystalline counterpart or non-Arrhenius behaviour usually associated with amorphous alloys.

- Improvement of the hydrogen embrittlement resistance of the Cu-Cu interface in Cu-Nb alloys

The Cu/Nb/Cu multifilamentary conducting wire tested is specially designed for high tensile strength but is yet to be optimized for hydrogen permeation conditions. Further work can be done to mitigate the formation of cracks developing along the Cu-Cu interface in the Cu/Nb/Cu alloy and optimize the manufacturing processes for hydrogen permeation applications. For example the effect of annealing on the crack formation and/or producing Cu/Nb/Cu in a controlled oxygen free atmosphere could be investigated. An alternative approach would be to eliminate the Cu-Cu interface by casting molten Cu around Nb filaments, which is feasible due to the large temperature difference between the melting points of the two elements. This can be followed by hot drawing to reduce the size of the Nb filaments and the cross sectional area.

APPENDIX

Acronyms

ASTM: American society for testing and materials

a: amorphous

bcc: body centred cubic

c: crystalline

Co: Cobalt

Cu: Copper

Cu-f: Copper fibre

DTA: Differential thermal analyzer

EDX: Energy dispersive X-ray

ETM: Early transition metals

Fcc: face centred cubic

FWHM: Full width half maximum

GFA: Glass forming ability

H: Hydrogen

K: Kelvin

KIT: Kitami institute of technology

LTM: Late transition metals

ME2: Maxwell Eucken 2

n: nanocrystalline

Nb: Niobium

Ni: Nickel

OFHC: Oxygen free high conductivity

PCT: Pressure composition temperature

PIPS: Precision ion polishing system

PSA: Pressure swing adsorption

RT: Room temperature

SEM: Scanning electron microscope

TEM: Transmission electron microscope

Ti: Titanium

TTT: Time temperature transformation

USA: United States of America

USDOE: United States department of energy

XRD: X-ray diffraction

Zr: Zirconium